A CAA Primer for Practicing Engineers

Dr. Christopher Tam
Department of Mathematics
Florida State University

April 2008

Final Report for Period 1 Oct 2006 - 30 Sep 2007

ARNOLD ENGINEERING DEVELOPMENT CENTER
ARNOLD AIR FORCE BASE, TENNESSEE
AIR FORCE MATERIEL COMMAND
UNITED STATES AIR FORCE

NOTICES

When U. S. Government drawings, specifications, or other data are used for any purpose other than a definitely related Government procurement operation, the Government thereby incurs no responsibility nor any obligation whatsoever, and the fact that the Government may have formulated, furnished, or in any way supplied the said drawings, specifications, or other data, is not to be regarded by implication or otherwise, as in any manner licensing the holder or any other person or corporation, or conveying any rights or permission to manufacture, use, or sell any patented invention that may in any way be related thereto.

Qualified users may obtain copies of this report from the Defense Technical Information Center.

References to named commercial products in this report are not to be considered in any sense as an endorsement of the product by the United States Air Force or the Government.

DESTRUCTION NOTICE

For unclassified, limited documents, destroy by any method
that will prevent disclosure or reconstruction of the document.
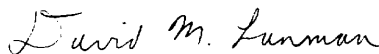
APPROVAL STATEMENT

This report has been reviewed and approved.

S. Bancroft

STEVEN A. BANCROFT
Program Manager
Technology Division
704th Test Systems Group

Approved for publication:

FOR THE COMMANDER

David M. Lanman

DAVID M. LANMAN
Director, Technology Division
704th Test Systems Group

	Form Approved
REPORT DOCUMENTATION PAGE	*OMB No. 0704-0188*

The public reporting burden for this collection of information is estimated to average 1 hour per response, including the time for reviewing instructions, searching existing data sources, gathering and maintaining the data needed, and completing and reviewing the collection of information. Send comments regarding this burden estimate or any other aspect of this collection of information, including suggestions for reducing the burden, to Department of Defense, Washington Headquarters Services, Directorate for Information Operations and Reports (0704-0188), 1215 Jefferson Davis Highway, Suite 1204, Arlington, VA 22202-4302. Respondents should be aware that notwithstanding any other provision of law, no person shall be subject to any penalty for failing to comply with a collection of information if it does not display a currently valid OMB control number.
PLEASE DO NOT RETURN YOUR FORM TO THE ABOVE ADDRESS

1. REPORT DATE (DD-MM-YYYY)	2. REPORT TYPE	3. DATES COVERED (From – To)
xx-04-2008	Final Report	1 Oct 2006 - 30 Sep 2007

4. TITLE AND SUBTITLE	5a. CONTRACT NUMBER
A CAA Primer for Practicing Engineers	ATA-06-18, ATA-07-288
	5b. GRANT NUMBER
	5c. PROGRAM ELEMENT NUMBER

6. AUTHOR(S)	5d. PROJECT NUMBER
Dr. Christopher Tam	AEDC Job 11808
Department of Mathematics	**5e. TASK NUMBER**
Florida State University	
	5f. WORK UNIT NUMBER

7. PERFORMING ORGANIZATION NAME(S) AND ADDRESS(ES)	8. PERFORMING ORGANIZATION REPORT NO.
C.W.K. Tam, 2127 Orleans Drive, Tallahassee FL 32308-5924	AEDC-TR-08-2

9. SPONSORING/MONITORING AGENCY NAME(S) AND ADDRESS(ES)	10. SPONSOR/MONITOR'S ACRONYM(S)
Arnold Engineering Development Center/XRS, MS 9013, Arnold AFB TN 37389	AEDC/XRS
	11. SPONSOR/MONITOR'S REPORT NUMBER(S)

12. DISTRIBUTION/AVAILABILITY STATEMENT

Statement A: Approved for public release; distribution is unlimited.

13. SUPPLEMENTARY NOTES

Available in the Defense Technical Information Center (DTIC).

14. ABSTRACT

This is a CAA (computational aeroacoustics) primer written specifically for AEDC. This is not a document written for research in CAA. It is to be a user's guide for practicing engineers who have responsibilities of solving (through prediction) or resolving (through better understanding) aeroacoustics problems by extensive computation. Oftentimes, established codes that may or may not have been designed for aeroacoustics applications are used. For this reason, the accuracy and validity of the computed solution may be in question. In this situation, this document serves to provide a reference to a proper CAA approach. CAA problems are very different from CFD (computational fluid dynamics) problems. In some situations, special CAA treatments are required that are not encountered in CFD. Such methods are, therefore, not available in standard CFD or numerical analysis references. This document is to offer a discussion of a variety of CAA methods, most of which are developed only relatively recently.

15. Subject Terms

aeroacoustics computation

16. SECURITY CLASSIFICATION OF:			17. LIMITATION OF ABSTRACT	18. NUMBER OF PAGES	19A. NAME OF RESPONSIBLE PERSON
A. REPORT	**B. ABSTRACT**	**C. THIS PAGE**			Steven A. Bancroft, AEDC/XRS
Unclassified	Unclassified	Unclassified	Unclassified	157	**19B. TELEPHONE NUMBER** *(Include area code)* 931-454-6418

Standard Form 298 (Rev. 8/98)
Prescribed by ANSI Std. 739.18

PREFACE

This is a CAA (computational aeroacoustics) primer written specifically for AEDC. This is not a document written for research in CAA. It is to be a user's guide for practicing engineers who have responsibilities of solving (through prediction) or resolving (through better understanding) aeroacoustics problems by extensive computation. Oftentimes, established codes that may or may not have been designed for aeroacoustics applications are used. For this reason, the accuracy and validity of the computed solution may be in question. In this situation, this document serves to provide a reference to a proper CAA approach. CAA problems are very different from CFD (computational fluid dynamics) problems. In some situations, special CAA treatments are required that are not encountered in CFD. Such methods are, therefore, not available in standard CFD or numerical analysis references. This document is to offer a discussion of a variety of CAA methods, most of which are developed only relatively recently. It is hoped that one of these methods is what is required.

The objectives of this primer are:

1. To provide an easy-to-access beginners reference to CAA methodology (no prior knowledge of CFD or advanced numerical analysis is required).

2. To serve as a resource book of CAA methods for practicing engineers.

In deciding what to include in this primer, it is felt that some theories are necessary to provide a starting point and a solid foundation for any discussion of numerical methods. They will not be excessive. Practical users may choose to pass over some of these sections. In writing this primer, the intent is not to offer an in-depth treatment of CAA topics. Rather, the aim is to provide a broad coverage of many possible computational and modeling methods engineers might find useful sometime in their career. Each topic will be covered to a reasonable, hopefully sufficient, depth for understanding and implementation. CAA is a dynamic field. New problems and methods are constantly added to the literature. It would, therefore, become necessary to limit the scope of this primer to methods that are sufficiently well established at this time.

Christopher Tam
Tallahassee, Florida

A CAA PRIMER FOR PRACTICING ENGINEERS

TABLE OF CONTENTS

8. MULTI-SCALES PROBLEMS

9. IMPEDANCE BOUNDARY CONDITION

1. INTRODUCTION

To obtain a stable and accurate numerical solution/simulation of an unsteady flow or an aeroacoustics problem, four basic computational elements are required. They are

1. A high resolution, least dispersive and dissipative computational scheme.

2. A well designed computation grid.

3. A set of high quality boundary conditions.

4. An effective artificial selective damping or filtering scheme and strategy.

Aeroacoustics problems usually involve propagation of acoustic waves over long distances. For this reason, numerical dispersion would cause the waveform to spread out in space leading to significant degradation of the quality of the solution. Furthermore, dispersion will mean that the computed waves propagate at a different speed than that of the original governing partial differential equations. Numerical dissipation contributes to damping of the waves. Over long propagation distance, this could have disastrous effects on the computed solution.

No computation could yield a high quality solution unless it is done on a well-designed grid. The grid lines provide the directions along which discretized approximation of spatial derivatives is made. Most computational aeroacoustics (CAA) problems involve more than one length scale. When this is the case, different size grid in different parts of the computational domain should be used to provide adequate spatial resolution.

The amplitude of acoustic disturbances is usually very small compared to that of the fluid flow. A CAA solution is, therefore, prone to various kinds of numerical pollution. When the outgoing acoustic waves reach the boundary of a computation domain, they would be reflected back into the computation domain and thus contaminating the computed solution. To avoid this boundary reflection problem, radiation boundary conditions are usually imposed at the outer edge of the computational domain to assist the waves to exit without significant back reflection. The Navier-Stokes equations or the Euler equations support entropy and vorticity waves in addition to acoustic waves. These waves could also be reflected back as acoustic waves at the outer boundary of a computation domain unless a set of high quality outflow boundary conditions is imposed. Numerical boundary treatment is vital to a successful CAA computation even though its importance has not been emphasized as strongly in computational fluid dynamics (CFD).

It is known that second and high order computation schemes, inevitably, would support spurious short waves. These waves are generated at boundaries, discontinuities and by nonlinearities. Experience indicates that the most prevalent and troublesome spurious short waves are the grid-to-grid oscillations. These waves have a wavelength of two mesh spacings. In addition to polluting the computed solution, when accumulated in a local region, grid-to-grid

5

oscillations often lead to numerical instability. It is, therefore, extremely important to add artificial selective damping or filtering to remove the spurious short waves.

In a recent review article on CAA, Tam (2004) presented a list of the challenges CAA must overcome but are not necessarily required of CFD. In selecting a method to use, it appears to be useful to take these challenges into consideration. For this reason, the list is reproduced below.

a. Aeroacoustics problems typically involve frequency range that spreads over a wide bandwidth. Numerical resolution of the high frequency waves with extremely short wavelength becomes a formidable obstacle to accurate numerical simulation.
b. Acoustic waves usually have small amplitudes. They are very small compared to the mean flow. Oftentimes, the sound intensity is five to six orders smaller. To compute sound waves accurately, a numerical scheme must have extremely low numerical noise.
c. In most aeroacoustics problems, interest is in the sound waves radiated to the far field. This requires a solution that is uniformly valid from the source region all the way to the measurement point at many acoustic wavelengths away. Because of the long propagation distance, computational aeroacoustics schemes must have minimal numerical dispersion and dissipation. Also, it should propagate the waves at the correct wave speeds and is isotropic irrespective of the orientation of the computation mesh.
d. Computation domain is inevitably finite in size. For aerodynamics or fluid mechanics problems, flow disturbances, generally, tend to decay very fast away from a body or their source of generation. They, therefore, are usually small at the boundary of the computation domain. Acoustic waves, on the other hand, decay very slowly and actually reach the boundaries of a finite computation domain. To avoid the reflection of outgoing sound waves back into the computation domain and thus contaminates the solution, radiation and outflow boundary conditions must be imposed at the artificial exterior boundaries to assist the waves to exit smoothly. For standard computational fluid dynamics (CFD) problems, such boundary conditions are usually not required.
e. Aeroacoustics problems are archetypical examples of multiple-scales problems. The length scale of the acoustic source is usually very different from the acoustic wavelength. That is, the length scale of the source region and that of the acoustic far field region can be vastly different. Computational aeroacoustic methods must be designed to deal with problems with greatly different length scales in different parts of the computational domain.

2. DISCRETIZATION SCHEMES

CAA is related to CFD which has had a lot of success in solving fluid mechanics problems. It is, therefore, inevitable for many investigators to apply CFD methods to CAA problems. We will first briefly review CFD based methods that have been used (some with and others without modifications or improvements) for solving CAA problems. Then we will do a more in depth review of methods that were developed primarily for CAA applications.

2.1 Spectral, Finite Element and Finite Volume Methods.

Spectral methods (Canuto *et al*., 1987) involve approximations of the solution by Fourier series or orthogonal polynomials. These approximations are reported to be very accurate for smooth functions. (Kopriva, 1990) demonstrated by numerical examples that spectral methods may have spectrally small dispersion and dissipation errors which makes them suitable for linear aeroacoustics problems. Traditional spectral formulations were costly and inflexible because of the global polynomial nature of the approximation. To overcome these disadvantages, spectral multi-domain methods were introduced (Patera, 1984; Kopriva, 1986). In the multi-domain method, complex geometries are subdivided into multiple elements. Spectral approximation is applied on each subdomain. Local resolution can be controlled by changing the size of the elements or by varying the order of the polynomials. Recently, improved discontinuous spectral methods were developed (Kopriva *et al*., 1996a,b) that add flexibility and ease of implementation. Analysis of the dispersion and dissipation properties of the discontinuous Galerkin method based on a highly structures grid can be found in the work of Hu *et al*. (1999). Applications of spectral methods to benchmark aeroacoustics problems were offered by Kopriva (1995), Bismuti (1997) and Rasetarinera (2000). Stanescu *et al*. (1999) performed multi-domain spectral computations of sound radiation from ducted fans. Atkins *et al*. (1997a) developed a quadrature-free form of the discontinuous Galerkin method on unstructured grids. Atkins (1997b) and Lockard (2000) applied the method to problems involving acoustic scattering and sound radiation from shear layers.

A widely used CFD algorithm is the finite volume method. However, generally speaking, finite volume methods are low order and hence are prone to incur dispersive errors. Recently, several investigators (Nance, 1996; Loh *et al* 1996) attempted to improve the dispersion characteristics of finite volume schemes. They incorporate the optimization ideas of the DRP (dispersion relation preserving) scheme into their method. They provide numerical examples to demonstrate the improvement.

An interesting method that is akin to finite element and finite volume methods was proposed by Chang *et al*., 1995, 1999. They refer to their method as the space-time conservation element and solution element (CE/SE) method. In this method, all the dependent variables and their derivatives are considered as unknowns. Flux conservation is enforced in the space-time Euclidean space. Through numerical examples, it has been shown that the CE/SE formulation could result in a computational scheme with very low numerical dissipation.

2.2 Finite Difference Schemes

Recently, a number of high-order finite-difference algorithms with large resolved bandwidth in wavenumber space has been developed. They include the DRP scheme (Tam & Webb, 1993a), optimized explicit scheme (Zingg *et al*., 1993, 1996), the compact scheme (Lele, 1992; Davis, 1991, 1995; Haras *et al*., 1994; Kim *et al*., 1996; Fung *et al*., 1996; Hixon, 1998a), improved MacCormack schemes (Gotleib *et al*., 1976; Bayliss *et al.*, 1985; Hixon *et al*., 1997a,b, 1998b), optimized upwind schemes (Lockard, 1995; Li, 1997; Zhuang *et al*., 2002) and leapfrog-type schemes (Thomas *et al*., 1993; Roe, 1998).

It is important to point out that CAA or more generally wave propagation problems involve the interplay between space and time. Just spatial discretization alone (all the schemes cited above) does not constitute a working computational algorithm. A temporal discretization is necessary. In most algorithms, spatial and temporal discretizations are performed independently. However, there are methods in which space and time discretizations are coupled as a single stage computation. These coupled methods have not received general acceptance and have almost no impact on CAA application. For this reason, these specialized methods will not be further discussed in this report.

2.3 Wave Number Analysis

One advantage CFD based methods have is that they have been developed through extensive use, not just simply trials and errors alone. A good deal of experience has been acquired over the years in the use of many popular methods. Traditional CFD methods were not designed for wave propagation computation. Within the framework of CFD there is no rigorous mathematical method to analyze the dispersion and dissipation characteristics of a scheme. Most CFD methods were developed using no more than Taylor series truncation. Taylor series truncation provides only order of magnitude estimates. It is believed that it is fair to say there is no rigorous mathematical support for many CFD methods. For instance, a search through the literature indicates that even the idea of upwinding, a crucial concept in CFD, has no rigorous mathematical underpinning. But, there is no doubt that upwinding, if done right, works. It is not too far-fetch to say that there is a high degree of empiricism in CFD.

In a recent review article on CAA, Tam (2004) pointed out that one of the most significant differences between traditional CFD and CAA methodology is the method of error analysis. In CFD, the standard way to assess the quality of a scheme is by the order of Taylor series truncation. It is generally assumed that a fourth-order scheme is better than a second-order scheme, that, in turn, is better than a first order scheme. But all these are qualitative not quantitative. There is no way to find out by order of magnitude analysis how many mesh points per wavelength are needed to achieve, say, a half-percent accuracy in a computation. Traditional numerical analysis also does not provide a way to quantify wave propagation errors. Dispersion and dissipation errors are often erroneously linked to the phase velocity and amplification factor.

The development of wave number analysis, through the use of Fourier-Laplace transforms, has provided a firm mathematical foundation for error analysis in CAA (Tam, 2004). Wave number analysis shows that it is not the order of a scheme that is important. It is the resolved bandwidth of a scheme in wave number space that is important. As far as numerical wave propagation error is concerned, wave number analysis shows that phase velocity is totally irrelevant. Rather, it is the group velocity and the dependence of $d\bar{\alpha}/d\alpha$ and $d\bar{\omega}/d\omega$ (where $\bar{\alpha}(\alpha)$ and $\bar{\omega}(\omega)$ are the wave number and angular frequency of a scheme and α and ω are the true wave number and angular frequency of the original partial differential equations) of the scheme on wave number that are important. In wave propagation, space and time play an important partnership role. The relationship is all encoded in the dispersion function. Thus a dispersion-relation-preserving scheme would automatically guarantee not only a numerically accurate solution but also the number of wave modes (acoustic, vorticity and entropy) and their characteristics supported by the computation scheme are identical to those of the original partial

differential equations. Wave number analysis has opened a way for the development of many optimized schemes (e.g., Tam & Webb, 1993; Lockard *et al.*, 1995; Kim & Lee, 1996; Zhuang & Chen, 1998, 2002; Li, 1997; Orlin et al,1997; Gaitande & Shang, 1997; Lee & Soo, 2002). It provides an understanding of the existence and characteristics of spurious short waves. Such knowledge allows the design of very effective artificial selective damping stencils (Tam *et al.*, 1993) and filters (Visbal & Gaitande, 2001). Wave number analysis, together with the dispersion relation of the discretized equations, offer a simple quantitative method for analyzing numerical stability of CAA algorithms (see Tam & Webb, 1993). Such an analysis is crucial to the selection of the size of time marching step.

2.4 Numerical Schemes for Spatial Discretization

In CAA, there are two methods which are truly original. They are the DRP scheme of Tam & Webb (1993) and the compact scheme of Lele (1992). Both methods have spawned a host of other schemes. The formulas of these schemes are now provided below.

2.4.1 The DRP Scheme

The DRP Scheme is an explicit optimized central difference scheme. A widely used version of this scheme is the 7-point stencil DRP scheme,

$$\left(\frac{\partial f}{\partial x}\right)_\ell \approx \frac{1}{\Delta x}\sum_{j=-3}^{3} a_j f_{\ell+j} \ , \qquad a_{-j} = -a_j$$

Two of the coefficients of a_j are chosen so that the finite difference approximation is accurate to the fourth order. The remaining coefficient is used as an optimized parameter to minimize the integrated error between $\overline{\alpha}$ and α over a wide band of wave number. This results in an approximation with a larger resolved bandwidth than the standard sixth order central difference scheme. The coefficients of the seven point DRP scheme are,

$a_0 = 0.0$ $a_1 = -a_{-1} = 0.77088238051822552$
$a_2 = -a_{-2} = -0.166705904414580469$ $a_3 = -a_{-3} = 0.02084314277031176$

For higher resolution, Tam (2004) provided the coefficients of a 15-point stencil DRP scheme. The stencil coefficients are,

$$. \qquad a_0 = 0.0$$

$$a_1 = -a_{-1} = 9.1942501110343045059277722885 \ D-1$$
$$a_2 = -a_{-2} = -3.5582959926835268755667642401 \ D-1$$
$$a_3 = -a_{-3} = 1.5251501608406492469104928679 \ D-1$$
$$a_4 = -a_{-4} = -5.9463040829715772666828596899 \ D-2$$
$$a_5 = -a_{-5} = 1.9010752709508298659849167988 \ D-2$$
$$a_6 = -a_{-6} = -4.3808649297336481851137000907 \ D-3$$
$$a_7 = -a_{-7} = 5.3896121868623384659692955878 \ D-4$$

2.4.2 Variants of the DRP Scheme

The optimized operator of Zingg *et al*. (1993, 1996) has also a seven-point stencil. The discretization is divided into a central-difference part approximating the derivative and a symmetric part providing artificial dissipation of spurious numerical waves,

$$\left(\partial f / \partial x\right)_l \approx \left(\sum_{j=1}^{3} a_j (f_{l+j} - f_{l-j})\right)/\Delta x + \left(d_0 f_l + \sum_{j=1}^{3} d_j (f_{l+j} + f_{l-j})\right)/\Delta x$$

The coefficients a_j and d_j are calculated so that the approximation is formally first-order accurate and the four remaining coefficients are used as optimization parameters to minimize the maximum phase and amplitude errors for waves resolved with at least ten points per wavelength. The scheme is not optimized for group velocity. The stencil coefficients are,

$$d_0 = 0.1$$
$$a_1 = 0.75996126 \qquad d_1 = -0.076384622$$
$$a_2 = -0.15812197 \qquad d_2 = 0.03228962$$
$$a_3 = 0.018760895 \qquad d_3 = -0.0059049989$$

Lockard *et al*. (1995) developed an explicit high-bandwidth upwind finite-difference operator. Coefficients of the eight-point stencil were determined by minimizing the real part of the weighted error between $\overline{\alpha}$ and α, and by controlling the high-frequency damping through biasing the imaginary part into a favorable direction. The operator was derived from averaging optimized seven-point central-difference and upwind ($N = 4$, $M = 2$) operators. The stencil coefficients are,

$$a_{-4} = 0.01039302092790538$$
$$a_{-3} = -0.08469749427253499$$
$$a_{-2} = 0.34203118305695955$$
$$a_{-1} = -1.05268128383328493$$
$$a_0 = 0.2872741244042224$$
$$a_1 = 0.58616247381945879$$
$$a_2 = -0.0981442816633705$$

$a_3 = 0.00966225756064431$

The explicit optimized upwind scheme of Zhuang *et al*. (2002) is formally fourth-order accurate with a seven-point non-symmetric stencil

$$\left(\partial f / \partial x\right)_l \approx (1 / \Delta x)\sum_{j=-N}^{M} a_j f_{l+j}$$

where $M = 4$, $N = 2$ for waves propagating to the left or $M = 2$, $N = 4$ for waves traveling to the right. The two free coefficients are used to minimize the integrated error between the real part of the numerical number $\mathrm{Re}(\overline{\alpha})$ and the physical wavenumber α, and to shift numerical dissipation to the high-wavenumber range by controlling the distribution of the imaginary part $\mathrm{Im}(\overline{\alpha})$. Li (1997) presented a number of wavenumber-extended upwind-biased finite-difference schemes of second- to eighth-order. The coefficients of optimized upwind scheme of Zhuang *et al* are,

$a_{-4} = 0.0161404967151$

$a_{-3} = $ -0.12282127902

$a_{-2} = 0.455332277706$

$a_{-1} = $ -1.2492595882615

$a_0 = 0.5018904380193$

$a_1 = 0.4399321927296$

$a_2 = $ -0.04121453788895

2.4.3 The Compact Scheme

The optimized "spectral-like" compact scheme of Lele (1992) is a pentadiagonal scheme with a seven-point stencil given by,

$$\beta D_{l-2} + \eta D_{l-1} + D_l + \eta D_{l+1} + \beta D_{l+2} \approx$$
$$c \frac{f_{l+3} - f_{l-3}}{6\Delta x} + b \frac{f_{l+2} - f_{l-2}}{4\Delta x} + a \frac{f_{l+1} - f_{l-1}}{2\Delta x}$$

where D_l denotes the spatial derivative $(\partial f / \partial x)_l$ at the mesh node l. Coefficients of the approximation are computed with three constraints imposed on the numerical wave number to provide better resolution of the high wave number range. The stencil coefficients are,

$\eta = 0.5771439 \qquad a = 1.3025166$

$\beta = 0.0896406 \qquad b = 0.99355$

$\qquad\qquad\qquad\quad c = 0.03750245$

2.4.4 Variants of the Compact Scheme

The work of Lele (1992) spawned an entire family of optimized compact schemes. Several of such schemes were proposed by Haras *et al*. (1994) who followed an approach similar to that of Tam *et al*. (1993a) and computed stencil coefficients by minimizing the integrated error between numerical and physical wavenumbers $\bar{\alpha}$ and α. The tridiagonal scheme with a five-point stencil has the form

$$\eta\, D_{l-1} + D_l + \eta\, D_{l+1} \approx b\, \frac{f_{l+2} - f_{l-2}}{4\Delta x} + a\, \frac{f_{l+1} - f_{l-1}}{2\Delta x}$$

This form is particularly attractive because of the reduced cost of matrix inversion. One set of coefficients for the scheme is provided below.

$$\eta = 0.3534620435 \qquad a = 1.566965775$$
$$b = 0.1399583152$$

Hixon (1998a) derived a new class of compact schemes that obtain high-order accuracy while using a very small stencil. In Hixon's approach the derivative operator D_l was split into forward, D_l^F, and backward, D_l^B, operators as $D_l = (D_l^F + D_l^B)/2$, and the discretized equations were written in the compact form,

$$a\, D_{l+1}^F + (1 - a - c)\, D_l^F + c D_{l-1}^F \approx$$
$$\left(b f_{l+1} - (2b - 1) f_l - (1 - b) f_{l-1} \right) / \Delta x$$
$$c\, D_{l+1}^B + (1 - a - c)\, D_l^B + a D_{l-1}^B \approx$$
$$\left((1 - b) f_{l+1} + (2b - 1) f_l - b f_{l-1} \right) / \Delta x$$

Coefficients of Hixon's six-order scheme are $a = 1/2 - 1/2\sqrt{5}$, $b = (1/6 + a^2)/a$, $c = 0$. The stencil is reduced to three points and the tridiagonal matrix is replaced by two bidiagonal matrices. Hixon did not attempt a wave number based optimization which could potentially improve the wave propagation properties of the scheme.

2.4.5 Comparison in Wave Number Space

Assuming that the time part of the computation is done exactly, waves with $d\bar{\alpha}/d\alpha > 1$ $(d\bar{\alpha}/d\alpha < 1)$ propagate at speeds that are faster (slower) than the wavespeed of the governing equations. Because of the difference in group velocity for different wavenumbers, the wavepacket will disperse in time. Lockard *et al* (1995) and Zingg *et al* (1996, 2000) based the analysis of numerical dispersion on phase velocity errors of a finite-difference discretization when, in fact, dispersion errors of a dispersive system are determined by the group velocity (Whitham, 1974).
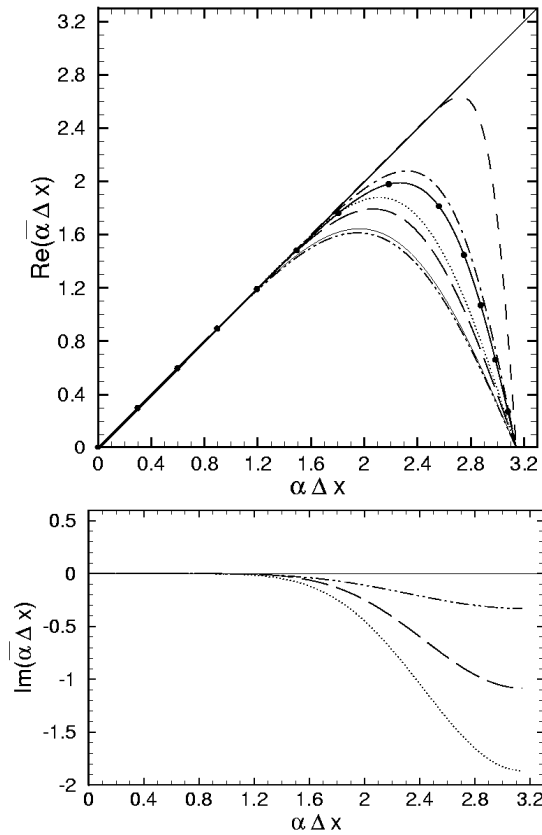
Figure 2.1. $\bar{\alpha}\Delta x$ vs $\alpha\Delta x$ relation for finite-difference operators: DRP (Tam, 1993a) ————— ; explicit optimized (Zingg, 1996) $-\cdot\cdot-\cdot\cdot-$;   optimized compact   (Lele, 1992); $-~-~-~-$; optimized compact (Haras, 1994) $-\cdot-\cdot-$; prefactored 6th -order compact (Hixon, 1998a) ——•—— ; optimized upwind (Zhuang, 2002) ………; optimized upwind (Lockard, 1995) —— —— —— .

Fig. 2.1 shows the dependence of $\bar{\alpha}\Delta x$ on $\alpha\Delta x$ for the seven schemes: DRP (Tam, 1993a), explicit optimized (Zingg, 1996), pentadiagonal "spectral-like" compact (Lele, 1992), tridiagonal optimized compact (Haras, 1994), prefactored 6th-order compact (Hixon, 1998a), explicit optimized upwind (Zhuang, 2002), explicit high-bandwidth upwind (Lockard, 1995). Figure 2.2a shows $\text{Re}(d\bar{\alpha}/d\alpha)-1$ vs. $\alpha\Delta x$, and Fig. 2.2b plots $E_{group} = |\,\text{Re}(d\bar{\alpha}/d\alpha)-1|$ as a function of the wavelength measured in points per wavelength (PPW). E_{group} reflects errors in group velocity of the numerical schemes . Clearly, the optimized compact scheme of Lele exhibits the best wave propagation performance. It is capable of resolving very short waves, the error E_{group} is below 0.4% even for waves with the wavelength of only three PPW. However, this exceptional performance is achieved at the price of inverting a pentadiagonal matrix. For the optimized tridiagonal compact scheme of Haras E_{group} is less than 0.4% for waves with the wavelength of at least five PPW. Schemes of Lockard, Hixon and Zhuang require six to seven PPW, and the DRP

scheme needs seven PPW for E_{group} to be below 0.4%. Eight PPW is necessary for E_{group} of the scheme of Zingg be less than 0.4%.
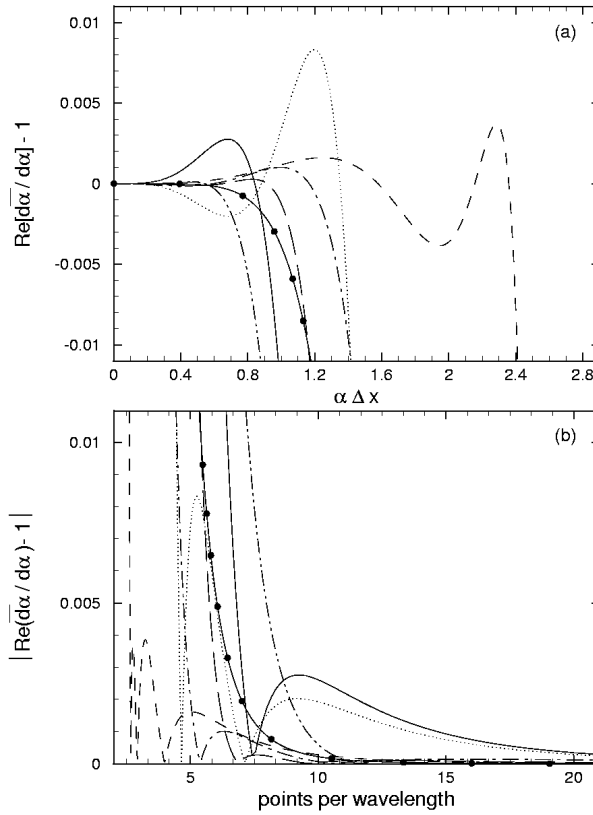

Figure 2.2. (a) $Re(d\overline{\alpha}/d\alpha)-1$ vs. $\overline{\alpha}\Delta x$, and (b) $|Re[d(\overline{\alpha}\Delta x)/d(\alpha\Delta x)]-1|$ vs. points per wavelength for finite-difference operators: DRP (Tam, 1993a) ——— ; explicit optimized (Zingg, 1996) $- \cdot \cdot -$ $\cdot \cdot -$; optimized compact (Lele, 1992) $- - - -$; optimized compact (Haras, 1994) $- \cdot - \cdot -$; prefactored six-order compact (Hixon, 1998a) ——•— ; optimized upwind (Zhuang, 2002) ………; optimized upwind (Lockard, 1995) — — —

The three schemes of Zingg, Zhuang and Lockard have a non-zero imaginary part of $\overline{\alpha}\Delta x$ (Fig. 2.1) that, if negative, add numerical dissipation to the scheme. The dissipation was added, explicitly by Zingg and implicitly through upwinding by Lockard and Zhuang, to damp out short spurious numerical waves.

2.5 Numerical Schemes for Temporal Discretization

There are fundamental differences between space and time. For instance, space extends from negative infinity to positive infinity while time only increases in one direction. These differences require finite difference approximation of time derivative to be different from spatial derivatives.

In general, there are two ways to form a discretized approximation of time derivative. They are the single time step method and the multi-level time discretization method. In this chapter, the single time step method will be discussed briefly. The multi-level discretization method will be discussed in greater details. One major difference between single time step method and multi-level methods is that, for wave propagation problems, the latter, when properly implemented, may lead to dispersion-relation-preserving (DRP) schemes.

2.5.1 Single Time Step Method: Runge-Kuta Scheme

One of the most popular time marching methods is the Runge-Kutta (RK) scheme. The RK scheme is based on Taylor series truncation. A widely used RK scheme is the 4th order method. To illustrate the basic approach of the RK method, let the time axis be divided into increments of Δt. Suppose the solution of a differential equation,

$$\frac{d\mathbf{u}}{dt} = \mathbf{F}(\mathbf{u}), \tag{2.1}$$

where $\mathbf{u}$ and $\mathbf{F}$ are vectors, at time level n is known. To find the solution at the next time level $(n+1)$, four evaluations of the derivative function $\mathbf{F}$ are performed (4th order RK). These intermediate evaluations provide indirectly the high-order derivatives of $\mathbf{u}$ so that a matching of high-order terms in Δt in a Taylor series expansion becomes possible. The following is a very general form of the fourth order RK scheme.

$$\mathbf{u}^{(n+1)} = \mathbf{u}^{(n)} + \sum_{j=1}^{4} w_j \mathbf{k}_j \tag{2.2}$$

$$\mathbf{k}_1 = \mathbf{F}(\mathbf{u}^{(n)})\Delta t$$
$$\mathbf{k}_2 = \mathbf{F}(\mathbf{u}^{(n)} + \beta_2\mathbf{k}_1)\Delta t$$
$$\mathbf{k}_3 = \mathbf{F}(\mathbf{u}^{(n)} + \beta_3\mathbf{k}_2)\Delta t$$
$$\mathbf{k}_4 = \mathbf{F}(\mathbf{u}^{(n)} + \beta_4\mathbf{k}_3)\Delta t$$

Superscript (n) indicates the time level. The constants β_2, β_3, β_4, w_1, w_2, w_3 and w_4 are chosen so that when the left and right side of Eq. (2.2) are expanded in Taylor series for small Δt, they are matched to order $(\Delta t)^4$. For the standard 4th order scheme, the constants are assigned the following values,

$$\beta_2 = \beta_3 = \frac{1}{2}, \qquad \beta_4 = 1.0, \qquad w_1 = w_4 = \frac{1}{6}, \qquad w_2 = w_3 = \frac{1}{3}$$

It is known that the above choice is not unique. Other choices are possible within the requirement that the Taylor series expansions of Eq. (2.2) are matched to terms involving $(\Delta t)^4$. An alternative choice proposed by Hu *et al.* (1996) called the Low-Dissipation Low-Dispersion Runge-Kutta (LPDRK) scheme is widely used in CAA. Instead of considering the time discretization of Eq. (2.1), attention is focused on discretizing the time derivative of the convective wave equation,

$$\frac{\partial u}{\partial t} + c\frac{\partial u}{\partial x} = 0 \tag{2.4}$$

Suppose the spatial derivative of Eq. (2.4) is approximated by a high-order finite difference scheme. The Fourier transform of the finite difference equation is,

$$\frac{d\tilde{u}}{dt} = -ic\overline{\alpha}\tilde{u} \tag{2.5}$$

where $\tilde{u}$ is the Fourier transform of u and $\overline{\alpha}(\alpha)$ is the wave number of the spatial finite difference approximation of $\partial/\partial x$.

Now if the 4th order RK scheme (2.2) is applied to Eq. (2.5), it is easy to find, after some algebra, that the time marching scheme becomes

$$u^{(n+1)} = u^{(n)}\left[1 + \sum_{j=1}^{4} c_j\left(-ic\overline{\alpha}\Delta t\right)^j\right] \tag{2.6}$$

where

$$c_1 = \sum_{j=1}^{4} w_j, \qquad c_2 = \sum_{j=2}^{4} w_j\beta_j \tag{2.7}$$

$$c_3 = w_3\beta_3\beta_2 + w_4\beta_4\beta_3, \qquad c_4 = w_4\beta_4\beta_3\beta_2$$

It is a simple matter to show that for the standard 4th order RK scheme $c_j = (1/j!)$.

According to LDDRK, the constants c_j's are assigned the values,

$$c_1 = 1.0, \quad c_2 = 0.5, \quad c_3 = 0.162997, \quad c_4 = 0.0407574 \tag{2.8}$$

This choice is motivated by numerical stability consideration and the desire to use the largest Δt permissible. It turns out the choice also keeps the numerical dispersion low as pointed out by Tam (2004). That LDDRK is a low dispersion scheme will be discussed in section 3.

To implement the LDDRK scheme, it is necessary to find a set of numerical values of β_j and w_j's when the c_j's are given by Eq. (2.8). To keep the scheme close to the standard 4th order scheme, a simple way is to keep the values of β_j the same as the standard scheme and determine the values of w_j by solving Eq. (2.7) as a linear system of equations.

2.5.2 Four-Level DRP Scheme

Tam & Webb (1993a) developed an optimized four-level Adams-Bashforth-type time-marching scheme that advances the solution f from time level n to time level (n+1) as,

$$f^{(n+1)} - f^{(n)} = \Delta t \sum_{j=0}^{3} b_j (df/dt)^{(n-j)} \tag{2.9}$$

By applying the Laplace transform with zero initial conditions to Eq. (2.9) it is easy to show that the effective angular frequency of the time-marching scheme (2.9) is given by,

$$\overline{\omega}\Delta t = i\left(e^{-i\omega\Delta t} - 1\right)\Big/ \sum_{j=0}^{3} b_j \, e^{ij\omega\Delta t} \tag{2.10}$$

Three of the four coefficients b_j $(j = 1, 2, 3)$ are chosen so that the scheme is formally third-order accurate. The remaining coefficient b_0 is used as an optimization parameter to minimize a weighted integral error between $\overline{\omega}$ and ω. Eq. (2.10) yields four roots of $\omega\Delta t$ for each value of $\overline{\omega}\Delta t$. Only one root with nearly zero imaginary part, ω_{good}, gives a good approximation of the desired relation $\overline{\omega} = \omega$ over the range $\overline{\omega}\Delta t < 0.4$. The scheme is numerically stable if all of the roots have a negative imaginary part. This determines the stability limit $R_{DRP} = 0.41$ $(\omega\Delta t \leq R_{DRP})$ of the scheme (2.9). The coefficients of the scheme are,

$$b_0 = 2.302558088383$$
$$b_1 = -2.4910075998482$$
$$b_2 = 1.5743409331815$$
$$b_3 = -0.38589142217162$$

3. NUMERICAL DISPERSION AND DISSIPATION OF HIGH-ORDER SCHEMES: THEORETICAL ANALYSIS

It is well known that high order schemes are subjected to dispersion and dissipation errors. A theoretical analysis of the origin of numerical dispersion and dissipation is briefly presented below.

3.1 Wave Number and Angular Frequency of High Order Schemes

In a recent review article, Tam (2004) showed that discretized equations, invariably, behaved mathematically like a dispersive wave system, even though the waves supported by the original partial differential equations were non-dispersive. This is an extremely important point and should be clearly understood by all CAA investigators and users. Let us illustrate this by considering the solution of the simple convective wave equation,

$$\frac{\partial u}{\partial t} + c\frac{\partial u}{\partial x} = 0 \tag{3.1}$$

and initial condition

$$t = 0 \qquad u(x, 0) = \Phi(x)$$

To find the nature of the waves supported by this equation, we may perform a Fourier-Laplace transform to this equation. The Fourier transform of a function $f(x)$, denoted by $\hat{f}(\alpha)$, and its inverse are defined by

$$\hat{f}(\alpha) = \frac{1}{2\pi} \int_{-\infty}^{\infty} f(x) e^{-i\alpha x} dx, \quad f(x) = \int_{-\infty}^{\infty} \hat{f}(\alpha) e^{+i\alpha x} d\alpha.$$

The Laplace transform of a function $g(t)$, denoted by $\bar{g}(\omega)$, and its inverse are defined by

$$\bar{g}(\omega) = \frac{1}{2\pi} \int_{0}^{\infty} g(t) e^{i\omega t} dt, \quad g(t) = \int_{\Gamma} \bar{g}(\omega) e^{-i\omega t} d\omega$$

where α and ω are the wave number (Fourier transform variable) and angular frequency (Laplace transform variable). Γ is a contour in the upper half ω-plane parallel to the real axis, above all poles and singularities of $\bar{g}(\omega)$.

The Fourier-Laplace transform of (1) leads to,

$$(\omega - c\alpha)\tilde{u} = \frac{i\hat{\Phi}(\alpha)}{2\pi} \tag{3.2}$$

where $\tilde{u}$ is the Fourier-Laplace transform of u. $\hat{\Phi}(\alpha)$ is the Fourier transform of initial condition $u(x,0)$. Thus $\tilde{u}$ is given by,

$$\tilde{u} = \frac{i\hat{\Phi}(\alpha)}{2\pi(\omega - c\alpha)}. \tag{3.3}$$

The poles of Eq. (3.3) are found by setting the denominator to zero. This yields,

$$\omega = c\alpha. \tag{3.4}$$

Eq. (3.4) gives the relationship between wave number and angular frequency. It is called the dispersion relation. According to dispersive wave theory (Whitham, 1974), all wave propagation characteristics of the partial differential equation are encoded in the dispersion relation. The group velocity or wave speed is given by $d\omega/d\alpha$. In the case of Eq. (3.1), by using dispersion relation (3.4), the group velocity is,

$$\frac{d\omega}{d\alpha} = c \tag{3.5}$$

so that all wave components propagate with the same speed. That is to say, the waves supported by the convective wave equation are nondispersive.
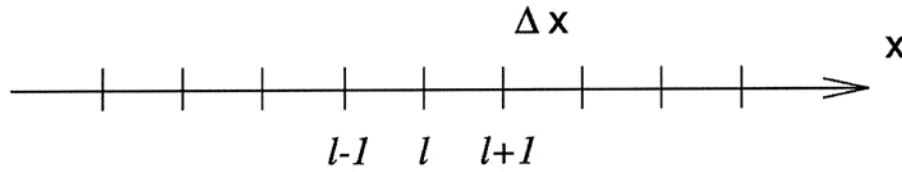
Figure 3.3 A uniform mesh of spacing Δx

Now we may convert Eq. (3.1) into a discretized system on a uniform mesh as shown in Fig. 3.3 by first approximating the x-derivative at the ℓth mesh point by a standard central difference quotient or by the DRP scheme (Tam & Webb, 1993) with a stencil of $(2N+1)$ points; i.e.,

$$\left(\frac{\partial u}{\partial x}\right)_\ell \cong \frac{1}{\Delta x}\sum_{j=-N}^{N}a_j u_{\ell+j}; \quad \left(a_j = -a_{-j}\right). \tag{3.6}$$

Eq. (3.6) is a relationship for a set of discrete mesh points on the x-axis (see Fig. 1). We may now generalize this relationship and regard it to hold true for any set of points spaced at Δx apart on the x-axis. This generalizes Eq. (3.6) to

$$\frac{\partial u}{\partial x}(x) \cong \frac{1}{\Delta x}\sum_{j=-N}^{N}a_j u(x+j\Delta x). \tag{3.7}$$

In Eq. (3.7) x is an arbitrary point on the x-axis. By setting $x = x_\ell$ in Eq. (3.7), Eq. (3.6) is recovered. Eq. (3.7) is a finite difference relation of a continuous variable. By taking the Fourier transform of Eq. (3.7) it is straightforward to find with the help of the Shifting Theorem,

$$i\alpha\hat{u} \cong i\overline{\alpha}\hat{u} \tag{3.8}$$

where

$$\overline{\alpha} = \frac{-i}{\Delta x}\sum_{j=-N}^{N}a_j e^{ij\alpha\Delta x} = \frac{2}{\Delta x}\sum_{j=1}^{N}a_j \sin(\alpha\Delta x). \tag{3.9}$$

The α on the left side of Eq. (3.8) is the wave number arising from the transform of the x-derivative. The $\overline{\alpha}$ on the right side may, therefore, be interpreted as the wave number of the finite difference
scheme. It is to be noted that for central difference approximation $\overline{\alpha}$ is real when α is real.

Once the a_j's are known, the relationship between α, the true wave number, and $\overline{\alpha}$, the wave number of the finite difference scheme, may be calculated by Eq. (3.9). For the standard central difference schemes, the a_j's are determined by using truncated Taylor series expansion for the terms on the right side of Eq. (3.6). For the DRP scheme of Tam & Webb (1993), the a_j's are found by minimizing the square of the difference between $\overline{\alpha}\Delta x$ and $\alpha\Delta x$ over a large band of wave numbers; i.e., minimizing $E = \int_0^\eta |\overline{\alpha}\Delta x - \alpha\Delta x|^2 d(\alpha\Delta x)$. Fig. 3.2 shows the dependence of $\overline{\alpha}\Delta x$ on $\alpha\Delta x$ over the interval $-\pi \leq \alpha\Delta x \leq \pi$ for the standard 6th order central difference scheme, the 7-point stencil and the 15-point stencil DRP schemes. The coefficients of the 15-point stencil DRP scheme are given in the appendix. For low wave numbers, $\overline{\alpha}\Delta x$ is nearly equal to $\alpha\Delta x$. For

instance, for the 7-point stencil DRP scheme, $\overline{\alpha}\Delta x$ differs from $\alpha\Delta x$ by less than 0.1% in the interval $0 \leq |\alpha\Delta x| \leq 1.05$. That is, this scheme incurs an error of less than 0.1% when 6 mesh points per wavelength is used in a computation.
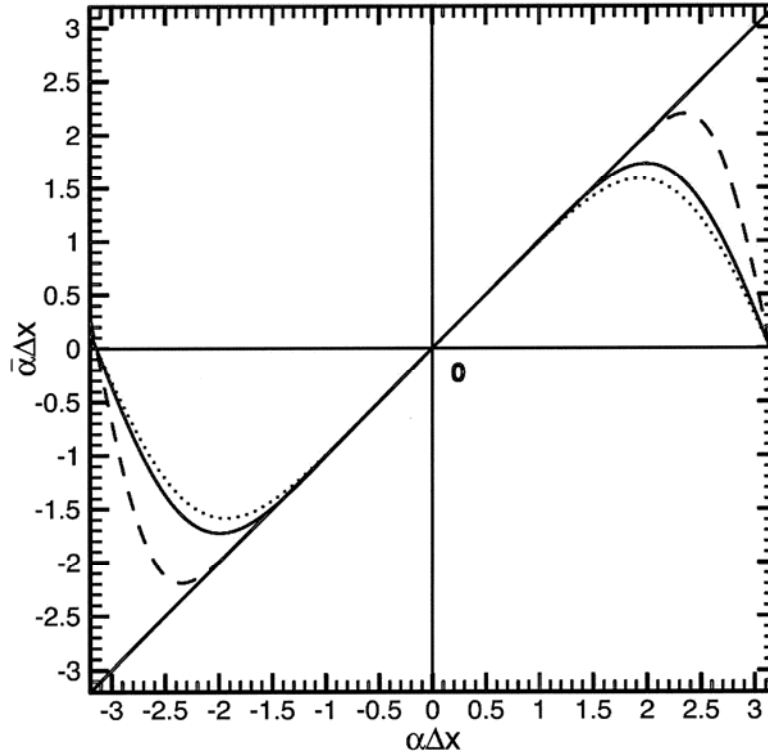

Figure 3.2. The $\overline{\alpha}\Delta x$ versus $\alpha\Delta x$ curves, ……… 6th order central difference scheme, _____ 7-point DRP scheme, - - - - - - - - 15-point DRP scheme.

Suppose an unsymmetric stencil with N points to the left and M points to the right is used to approximate the x-derivative; i.e.,

$$\left(\frac{\partial u}{\partial x}\right)_\ell \cong \frac{1}{\Delta x}\sum_{j=-N}^{M} a_j u_{\ell+j}, \qquad N \neq M. \tag{3.10}$$

It is easy to find by taking the Fourier transform of the generalized form of Eq. (3.10) that the corresponding wave number relationship between $\overline{\alpha}\Delta x$ and $\alpha\Delta x$ is

$$\overline{\alpha}\Delta x = -i\sum_{j=-N}^{M} a_j e^{ij\alpha\Delta x}. \tag{3.11}$$

We note that for real α, $\overline{\alpha}$ is complex. The significance of stencil wave number $\overline{\alpha}$ being complex will be discussed later.

Now after performing spatial discretization, Eq. (3.1) may be rewritten in the form,

$$\frac{du_\ell}{dt} = K_\ell \tag{3.12a}$$

$$K_\ell = \frac{-c}{\Delta x} \sum_{j=-N}^{N} a_j u_{\ell+j} . \tag{3.12b}$$

The time derivative of Eq. (3.12a) may be approximated by either a single step method such as the Runge-Kutta method or by a multi-step method such as the Adams-Bashforth 4-level scheme. We will consider a multi-step method. In this case $u^{(n)}$, where superscript n denotes the time level, is advanced to the $(n+1)$ time level by the formula

$$u_\ell^{(n+1)} = u_\ell^{(n)} + \Delta t \sum_{j=0}^{3} b_j K_\ell^{(n-j)} . \tag{3.13}$$

Δt is the time step. b_j's are the coefficients of the scheme. Finite difference equation (3.13) may now be generalized to one with a continuous variable following the same steps that lead to Eq. (3.7). We may apply Laplace transform to the generalized form of Eq. (3.13). On recalling that $K_\ell(t)$ is $du_\ell(t)/dt$ and that the Laplace transform of du_ℓ/dt is $-i\omega \overline{u}_\ell$, it is straightforward to obtain, assuming zero initial condition, (see Tam & Webb, 1993, for details)

$$-i\omega \overline{u}_\ell \cong -i\overline{\omega} \overline{u}_\ell \tag{3.14}$$

where $\overline{\omega}$ is given by

$$\overline{\omega} \Delta t = i \frac{\left(e^{-i\omega \Delta t} - 1\right)}{\sum\limits_{j=0}^{3} b_j e^{ij\omega \Delta t}} . \tag{3.15}$$

Since ω on the left side of Eq. (3.14) is the angular frequency of the Laplace transform of d/dt, $\overline{\omega}$ on the right side may be regarded as the angular frequency of the 4-level time matching scheme (3.13). It is easy to show numerically that $\overline{\omega} \Delta t$ is a good approximation of $\omega \Delta t$ for small $\omega \Delta t$. For the DRP scheme, the coefficients b_j of Eq. (3.13) are chosen to minimize the difference between $\overline{\omega} \Delta t$ and $\omega \Delta t$ over a band of $\omega \Delta t$. Tam & Webb (1993) found that $\overline{\omega} \cong \omega$ to a high degree of accuracy for $\omega \Delta t \leq 0.19$.

Now Eq. (3.1) may be fully discretized by first rewriting it as a system of two equations each involving only either temporal or spatial derivative

$$\frac{\partial u}{\partial t} = K$$
$$K = -c \frac{\partial u}{\partial x} .$$

The derivative of each of the above equations may be discretized according to Eq. (3.6) for spatial derivatives and Eq. (3.13) for time derivative. The fully discretized form of (1) is,

$$K_\ell^{(n)} = -\frac{c}{\Delta x} \sum_{j=-N}^{N} a_j u_{\ell+j}^{(n)}$$ (3.16a)

$$u_\ell^{(n+1)} = u_\ell^{(n)} + \Delta t \sum_{j=0}^{3} b_j K_\ell^{(n-j)}.$$ (3.16b)

This set of finite difference equations with discrete variables ℓ and n may again be generalized into a set of finite difference equations with continuous variables x and t. By taking the Fourier-Laplace transform and after some algebra, it is easy to find that the solution is (see Tam & Webb, 1993, for treatment of initial condition),

$$\tilde{u} = \frac{i\hat{\Phi}(\alpha)}{2\pi(\overline{\omega} - c\overline{\alpha})}\left(\frac{\overline{\omega}}{\omega}\right)$$ (3.17)

where $\tilde{u}$ is the Fourier-Laplace transform of the solution of Eq. (3.16). Eq. (3.17) is identical to the Fourier-Laplace transform of the solution of the original convective wave equation; i.e., Eq. (3.3), if $\overline{\omega}$ and $\overline{\alpha}$ in Eq. (3.17) are replaced by ω and α. The dispersion relation of the waves supported by Eq. (3.16) is given by the zeros of the denominator of Eq. (3.17), namely,

$$\overline{\omega}(\omega) = c\overline{\alpha}(\alpha).$$ (3.18)

This is formally the same as the dispersion relation of the original partial differential equation; i.e., Eq. (3.4), provided $\overline{\omega}$ is replaced by ω and $\overline{\alpha}$ is replaced by α. It can be shown (see Tam & Webb, 1993) that the above discretized procedure will always lead to a formal preservation of the dispersion relation even for multi-dimensional problems governed by the linearized Euler equations. For this reason, the scheme is referred to as dispersion-relation-preservation (DRP). Since $\overline{\omega} \cong \omega$ and $\overline{\alpha} \cong \alpha$ are true for small $\omega\Delta t$ and $\alpha\Delta x$, the dispersion relation of Eq. (3.16) is a good approximation of that of Eq. (3.1). This guarantees that the solution of finite difference equation (3.16) should be a good approximation of the exact solution if the solution contains only low frequency or long waves (we will refer this as the resolved wave number range). Outside the resolved wave number range, the dispersion relation of the discretized equation is no longer a good approximation of that of the original equation. As a result, the finite difference solution will differ significantly from the exact solution.

Now even in the resolved wave number range, the group velocity $d\omega/d\alpha$ of dispersion relation (3.18) is not a constant equal to c. The waves supported by the finite difference approximation is dispersive. This turns out to be a general property of almost all discretized approximations. On the other hand, we now know the Fourier-Laplace transform of the exact solution of the finite difference approximation. This allows us to analyze quantitatively the various types of errors introduced by finite difference approximation. With such understanding and knowledge of the errors incurred, we are in a position to tailor the computational algorithm to meet the accuracy needed by the physical problem.

3.2. Origin of Numerical Dispersion

The exact solution of the finite difference approximation of Eq. (3.1) using the DRP scheme is given by the inverse transform of Eq. (3.17),

$$u(x,t) = \frac{i}{2\pi} \int_{-\infty}^{\infty} \int_{\Gamma} \frac{\hat{\Phi}(\alpha)}{(\overline{\omega} - c\overline{\alpha})} \frac{\overline{\omega}}{\omega} e^{i(\alpha x - \omega t)} d\omega \, d\alpha. \tag{3.19}$$

The double integral may be evaluated by first calculating the contributions of the poles in the ω-plane. The poles are given by the zeros of the denominator of the integrand, that is, the roots of,

$$\overline{\omega}(\omega) = c\overline{\alpha}(\alpha). \tag{3.20a}$$

Eq. (3.20a) is the dispersion relation; same as Eq. (3.18). For a four level time marching scheme, there would be four poles; $\omega = \omega_j(\alpha)$, $j = 1,2,3,4$. One of the poles has $\text{Im}(\omega)$ nearly equal to zero. This is the pole that corresponds to the physical solution. The other poles lead to solutions that are heavily damped.

Numerical dispersion can arise from spatial or temporal discretization. We will first consider spatial discretization alone. For this purpose, we will let $\Delta t \to 0$, that is, we treat time exactly. This is equivalent to replacing $\overline{\omega}$ by ω in Eq. (3.19) so that the expression for the exact solution of the spatially discretized equation (3.1) is,

$$u(x,t) = \frac{i}{2\pi} \int_{-\infty}^{\infty} \int_{\Gamma} \frac{\hat{\Phi}(\alpha)}{\omega - c\overline{\alpha}(\alpha)} e^{i(\alpha x - \omega t)} d\omega \, d\alpha.$$

Dispersion relation (3.20a) now simplifies to

$$\omega = c\overline{\alpha}(\alpha). \tag{3.20b}$$

The integrand has a pole at $\omega = c\overline{\alpha}(\alpha)$. On deforming the inverse contour Γ to pick up this pole in the ω-plane, it is easy to find through the use of the Residue Theorem

$$u(x,t) = \int_{-\infty}^{\infty} \hat{\Phi}(\alpha) e^{i\left(\alpha\frac{x}{t} - \omega\right)t} \bigg|_{\omega = c\overline{\alpha}(\alpha)} d\alpha. \tag{3.21}$$

Now for large t (with x/t fixed), the α-integral of Eq. (3.21) may be evaluated by the method of stationary phase (see e.g., Ablowitz & Fokas, Chapter 6). The stationary phase point $\alpha = \alpha_s$ is given by the zero of the derivative of the phase function $\Psi = (\alpha(x/t) - \omega(\alpha))$ with respect to α. This leads to

$$\frac{d\omega}{d\alpha} = c\frac{d\overline{\alpha}(\alpha)}{d\alpha}\bigg|_{\alpha=\alpha_s} = \frac{x}{t}, \tag{3.22}$$

which yields α_s as a function of x/t. The asymptotic solution is

$$u(x,t) \underset{t \to \infty}{\sim} \left(\frac{2\pi}{\left| c\overline{\alpha}''(\alpha_s) \right| t} \right)^{\frac{1}{2}} \hat{\Phi}(\alpha_s) e^{i\left[\alpha_s \frac{x}{t} - c\overline{\alpha}(\alpha_s) \right] t + i\frac{\pi}{4} \text{sgn}(-c\overline{\alpha}'')} \qquad (3.23)$$

where $\text{sgn}(z)$ is the sign of z.

In wave propagation theory (Whitham, 1974) $d\omega/d\alpha$ in Eq. (3.22) is called the group velocity. Since $x = (d\omega/d\alpha)t$, it is the propagation speed of the component of the solution with wave number α in the $x-t$ diagram. Now ω and α are related by Eq. (3.20b). In general $d\overline{\alpha}/d\alpha$ is not a constant equal to 1, different wave number of the initial disturbances will propagate with a slightly different speed. Because of the different propagation speed a wave packet will spread out or disperse in space as it propagates. Even a small difference in group velocity can manifest into serious dispersion over a long time or a long distance of propagation. This is the origin of numerical dispersion.

In the more general case of solution Eq. (3.19), when both spatial and temporal discretization are used, the group velocity may be calculated by implicit differentiation of Eq. (3.20a). This gives,

$$\frac{d\omega}{d\alpha} = \frac{c \dfrac{d\overline{\alpha}}{d\alpha}}{\dfrac{d\overline{\omega}}{d\omega}} . \qquad (3.24)$$

Eq. (3.24) indicates that numerical dispersion can be the result of imperfect spatial discretization; i.e., $d\overline{\alpha}/d\alpha \neq 1$ or imperfect temporal discretization; i.e., $d\overline{\omega}/d\omega \neq 1$. We will defer the consideration of imperfect time discretization later as it is quite involved. We will now illustrate the effect of dispersion due to spatial discretization by a numerical example.

For the convective wave equation (3.1), Eq. (3.22) reveals that the variation in group velocity is caused by the variation of the slope of the $\overline{\alpha}\Delta x$ versus $\alpha\Delta x$ curve. Fig. 3.3 shows the $d\overline{\alpha}/d\alpha$ versus $\alpha\Delta x$ curves for a number of schemes. Notice that the $d\overline{\alpha}/d\alpha$ curve for the 7-point stencil DRP scheme has a peak at $\alpha\Delta x = 0.67$ at which $d\overline{\alpha}/d\alpha = 1.00276$. That is, the wave component with $\alpha\Delta x = 0.67$ (wave with 9.38 mesh points per wavelength) will propagate faster than the exact wave speed $d\overline{\alpha}/d\alpha = 1.0$ by about 0.3%. Suppose in a computation, the waves propagate over a distance of 400 mesh points. In this case, when the main part of the wave packet reaches $x = 400$, the wave component with $\alpha\Delta x = 0.67$ will reach $x = 401.1$. Under these circumstances, numerical dispersion would just be noticeable as wave dispersion exceeds one mesh point. On the other hand, if the standard 6th order scheme is used instead, severe numerical dispersion will result when the main wave reaches $x = 400$. Waves in the wave number range of $\alpha\Delta x > 0.6$, having group velocity less than 1.0 would form trailing waves.
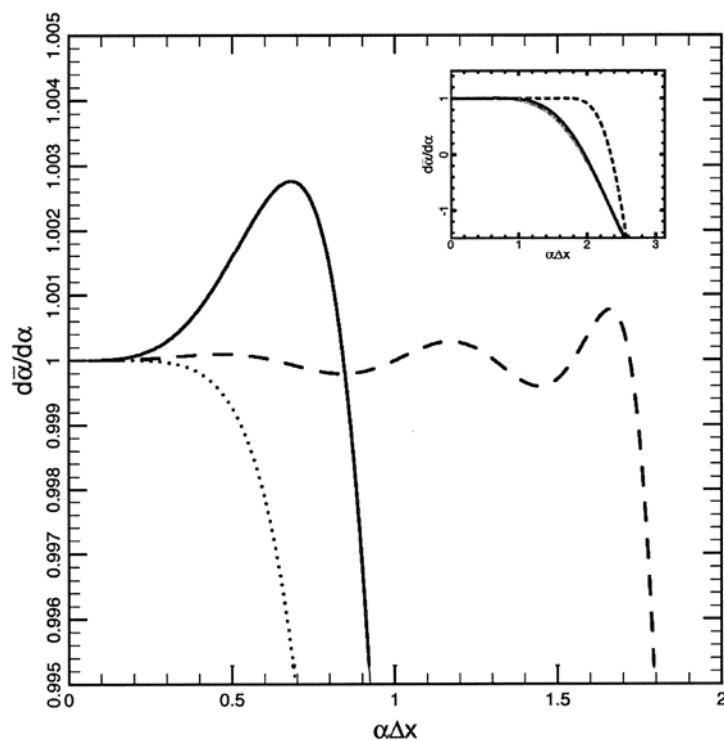
Figure 3.3. The $d\bar{\alpha}/d\alpha$ vs. $\alpha\Delta x$ curves, …….. 6th order central difference scheme , _____ 7-point DRP scheme, - - - - - - - - 15-point DRP scheme.
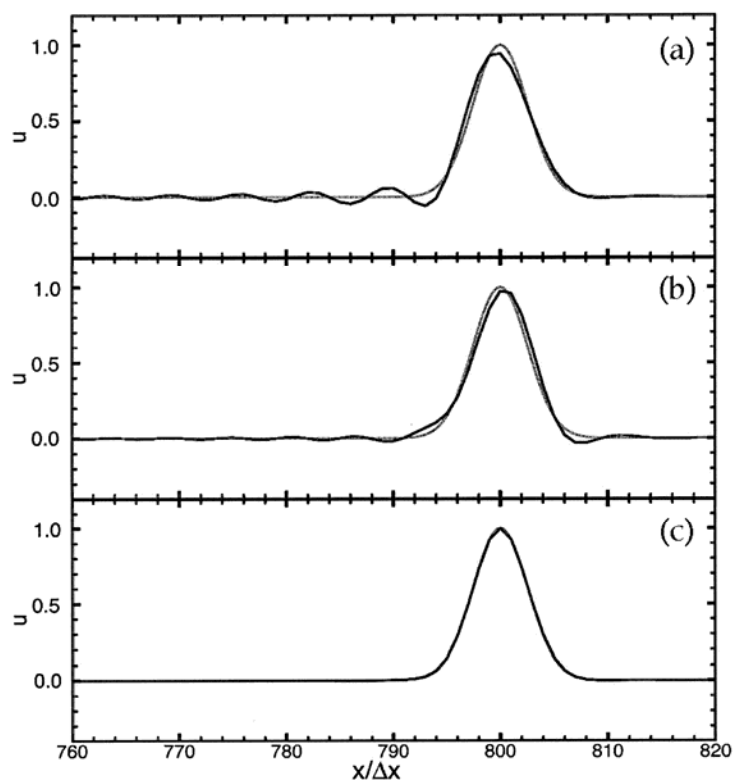

Figure 3.4. Comparison between computed solutions and exact solution for the one dimensional convective wave equation. (a) 6th order central difference scheme, (b) 7-point DRP schems, (c) 15-point DRP scheme.

A relevant question to ask is how to reduce numerical dispersion due to spatial discretization. This can be done by using a scheme with a larger stencil. Fig. 3.3 shows the $d\overline{\alpha}/d\alpha$ curve for the 15-point stencil DRP scheme. For $\alpha\Delta x < 1.73$, the group velocity differs from 1.0 by no more than 0.1%. Thus if the wave packet of the solution contains only waves with wave number $\alpha\Delta x < 1.73$, then there will be no observable numerical dispersion even after the wave packet propagates over a distance of up to 1000 mesh points. As a concrete example, Fig. 3.4 shows the computed solution of the convective wave equation (3.1) with initial condition in the form of a Gaussian with a half-width of 3 mesh spacings,

$$u(x,0) = e^{-(\ln 2)\left(\frac{x}{3\Delta x}\right)^2}$$

(3.25)

using the standard 6th order scheme, the 7-point stencil and the 15-point stencil DRP scheme. It is easy to see that there is significant numerical dispersion (with extensive trailing waves) when computed by the standard 6th order scheme. The 7-point stencil DRP scheme is better. Both schemes, having the same stencil size, require the same amount of computation. The solution by the 15-point stencil is even better. For all intents and purposes, the solution is identical numerically to the exact solution.

It is worthwhile to point out that numerical dispersion is the result of the variation of the group velocity of a numerical scheme. Unfortunately, in some textbooks it is linked erroneously to the phase velocity of the computation scheme. Phase velocity and group velocity are not the same. In fact, they can have opposite signs so that phase velocity and group velocity can propagate in opposite directions. From Fig. 3.3, it is easy to see that $d\overline{\alpha}/d\alpha$ for the standard 6th order central difference scheme as well as the 7-point stencil DRP scheme is negative for $\alpha\Delta x > 2.0$. In other words, for short waves with $\alpha\Delta x > 2.0$, the phase velocity is positive but the waves propagate backward because the group velocity is negative.

3.3. Numerical Dispersion Arising from Temporal Discretization

As was pointed out in the last section, computation schemes that have dispersion-relation-preserving property will exhibit numerical dispersion due to temporal discretization if $d\overline{\omega}/d\omega$ of the angular frequency relationship $\overline{\omega}(\omega)$ is not equal to 1.0. Most single time step schemes, such as the Runge-Kutta method, do not have dispersion-relation-preserving property. However, they do lead to numerical dispersion. For schemes of this type, there is no general way to derive the dispersion relation. To illustrate this point, let us again consider numerical solution of convective wave equation (3.1) by finite difference. We will use a 15-point stencil DRP scheme to approximate the spatial derivative. This spatial scheme can accurately resolve waves with as few as 3.6 mesh points per wavelength so that unless an acoustic pulse has extremely narrow half-width, there is negligible dispersion due to spatial discretization. The Fourier transform of the discretized form of Eq. (3.1) is,

$$\frac{d\hat{u}}{dt} = f(\hat{u})$$

(3.26a)

where

$$f(\hat{u}) = -ic\overline{\alpha}(\alpha)\hat{u}.$$

(3.26b)

Now suppose we discretize the time derivative of Eq. (3.26) by the 4th order Runge-Kutta scheme with time step Δt. The time marching scheme, as discussed in section 2.4.6 is,

$$
\begin{aligned}
K_1 &= f\left(\hat{u}^{(n)}\right)\Delta t \\
K_2 &= f\left(\hat{u}^{(n)} + \beta_2 K_1\right)\Delta t \\
K_3 &= f\left(\hat{u}^{(n)} + \beta_3 K_2\right)\Delta t \\
K_4 &= f\left(\hat{u}^{(n)} + \beta_4 K_3\right)\Delta t \\
\hat{u}^{(n+1)} &= \hat{u}^{(n)} + \sum_{j=1}^{4} w_j K_j .
\end{aligned}
\tag{3.27}
$$

Substitution of Eq. (3.26b) into Eq. (3.27), the time marching finite difference equation for $\tilde{u}^{(n)}$ is found to be,

$$
\hat{u}^{(n+1)} = \hat{u}^{(n)}\left[1 + \sum_{j=1}^{4} c_j \left(-ic\overline{\alpha}\Delta t\right)^j\right]
\tag{3.28}
$$

where

$$
c_1 = \sum_{j=1}^{4} w_j, \quad c_2 = \sum_{j=2}^{4} w_j \beta_j,
$$
$$
c_3 = w_3 \beta_3 \beta_2 + w_4 \beta_4 \beta_3, \quad c_4 = w_4 \beta_4 \beta_3 \beta_2
\tag{3.29}
$$

It is a simple matter to show that for the Standard RK scheme $c_j = 1/j!$. For the LDDRK scheme of Hu *et al* (1996) the following values are assigned, $c_1 = 1.0$, $c_2 = 0.5$, $c_3 = 0.162997$, $c_4 = 0.0407574$

Now Eq. (3.28) can be readily generalized into a finite difference equation with a continuous variable. By applying Laplace transform to the difference equation, it is easy to find that the dispersion relation of the finite difference algorithm of the convective wave equation discretized temporally by a 4th order Runge-Kutta scheme is,

$$
e^{-i\omega\Delta t} = \left[1 + \sum_{j=1}^{4} c_j \left(-ic\overline{\alpha}\Delta t\right)^j\right].
\tag{3.30}
$$

By differentiating Eq. (3.30) with respect to α, the following formula for the group velocity is derived,

$$\frac{d\omega}{d\alpha} = \frac{c\sum_{j=1}^{4} jc_j\left(-ic\overline{\alpha}\Delta t\right)^{j-1}}{\left[1+\sum_{j=1}^{4} c_j\left(-ic\overline{\alpha}\Delta t\right)^{j}\right]}\frac{d\overline{\alpha}}{d\alpha}. \qquad (3.31)$$

Since $d\omega/d\alpha$ is not a constant equal to c even if $d\overline{\alpha}/d\alpha=1.0$, numerical dispersion is introduced by the use of the Runge-Kutta scheme. A plot of $\mathrm{Re}(d\omega/d\alpha)$ as a function of $c\alpha\Delta t$ ($\overline{\alpha}=\alpha$ assumed) for the LDD Runge-Kutta scheme of Hu *et al.* (1996) is given as one of the curves in Fig. 3.6. Notice that the group velocity drops below c for $c\alpha\Delta t > 0.5$. The group velocity is less than the exact wave speed by 0.2% or more for $c\alpha\Delta t > 0.65$. Waves in this range will form trailing waves after propagating over a distance of approximately 600 mesh points.
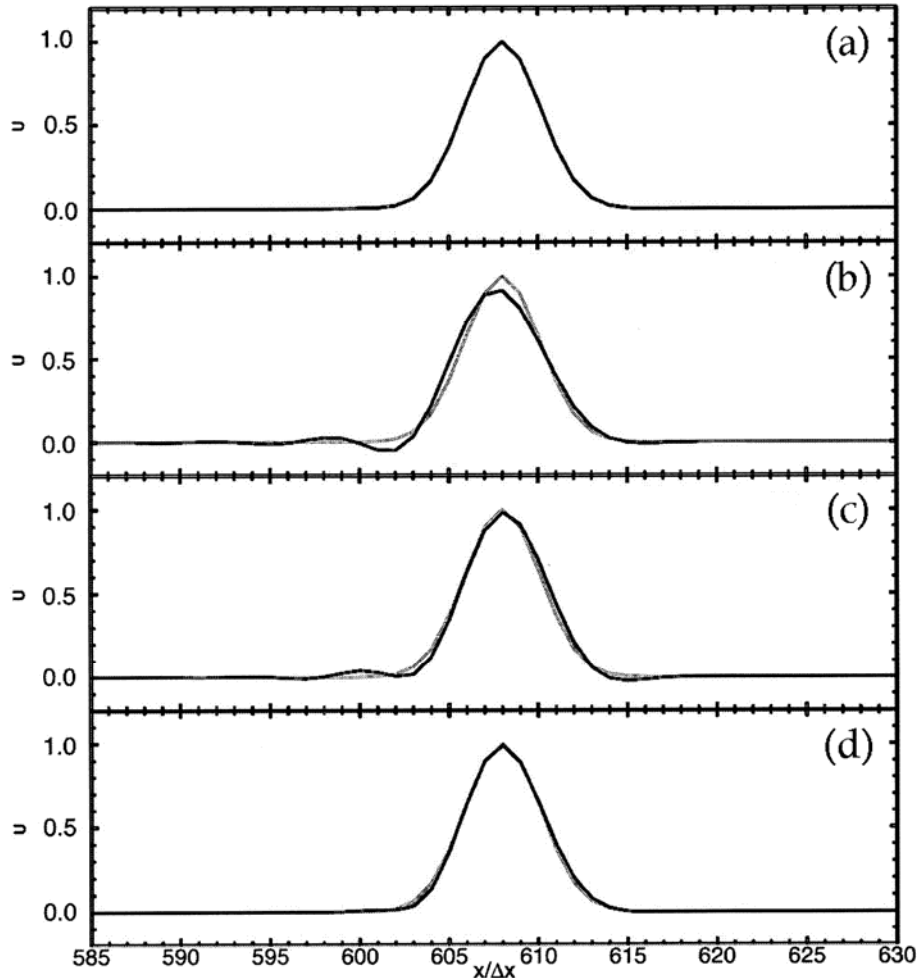

Figure 3.5. Waveform of Gaussian pulse with half-width = 2.5 Δx after propagating a distance of 608 mesh spacings. (a) Δt/Δx=0.25, standard 4th order Runge-Kutta scheme, (b) Δt/Δx=0.76, standard 4th order Runge-Kutta scheme, (c) Δt/Δx=0.76, LDD Runge-Kutta scheme of

Hu *et al* (1996), (d) Δt/Δx=0.19, 4-level DRP scheme.

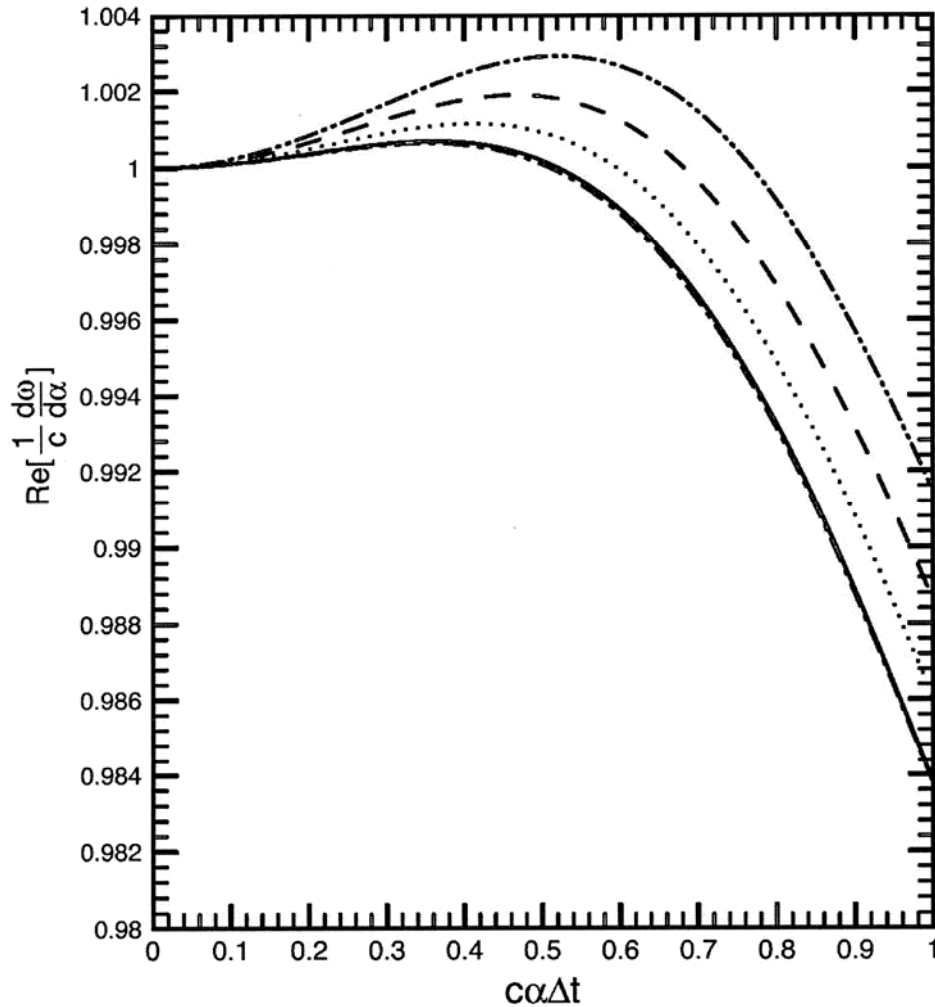Figure 3.6. Optimized group velocity of the convective wave equation.
-.-.-.-.-.-.-.- , η=0.6, ..., η=0.7,
———————, η=0.8, –..–..–..–..–..– η=0.9
_____ , Hu *et al* LDD Runge-Kutta scheme.

To illustrate numerical dispersion due to temporal discretization, we will consider the solution of Eq. (3.1) with initial condition,

$$t = 0, \quad u(x,0) = \exp\left[-(\ln 2)\left(\frac{x}{2.5\Delta x}\right)^2\right]$$

(3.32)

using the 15-point stencil DRP scheme for spatial discretization and the standard 4th order Runge-Kutta scheme for temporal discretization. For convenience, we will set $c = 1$. The computed results are shown in Fig. 3.5. Figure 3.5a shows the computed waveform after the

pulse has propagated a distance of 608 mesh spacings using a very small time step $\Delta t = 0.25\Delta x$. The computed result is indistinguishable from the exact solution. Figure 3.5b shows the computed result when a larger Δt, $\Delta t = 0.76\Delta x$, is used. There is no question that the pulse is slightly dispersed. The cause is temporal discretization. For comparison purpose, Fig. 3.5c shows the computed waveform using the LDD Runge-Kutta scheme of Hu *et al.* (1996) with $\Delta t = 0.76\Delta x$. There is definitely an improvement using this scheme. However, there are still some trailing waves, a manifestation of numerical dispersion. For initial condition (3.32), a small fraction of the initial pulse has wave number larger than $\alpha\Delta x = 0.855$ corresponding to $\alpha\Delta t = 0.65$. This part of the initial spectrum will propagate slower according to the group velocity curve of Fig. 3.6. They show up as trailing waves. Finally, Fig. 3.5d shows the computed result of the 4-level time marching DRP scheme of Tam & Webb (1993). The 4-level scheme computes the derivative function once per step. The single step Runge-Kutta scheme computes the derivative function four times per step. Thus to compare the results based on nearly the same workload, the time step of the DRP is taken to be a quarter of that of the Runge-Kutta schemes; i.e., $\Delta t = 0.19\Delta x$. As can be seen, the results of Figs. 3.5b, c and d seem to indicate that the DRP scheme has less dispersion due to temporal discretization.

  At the present time, there is no question that the Runge-Kutta scheme is the most popular time discretization method. In the literature, many articles can be found proposing some slight modifications to the original formulation to reduce storage requirement or to improve computing time or to improve accuracy. Most of the proposals were strictly on time marching without considering linkage to spatial discretization as is necessary in wave propagation problems. Hu *et al.* (1996) appear to be the first to optimize the constants of the Runge-Kutta scheme based on the convective wave equation (3.1). They derived a formula for the amplification of the equation. They then chose the constants to minimize the difference between the exact amplification factor and the amplification factor when Runge-Kutta scheme was used. They called their scheme low-dissipation low-dispersion (LDD) Runge-Kutta scheme. As far as wave propagation is concerned, the physical meaning of amplification factor is not clear. There is no question that amplification factor is important in numerical stability consideration. It also has something to do with numerical dissipation and phase error. But any direct linkage to wave propagation has not been established. Its direct relationship to numerical dispersion is also unclear. However, numerical examples such as that shown in Fig. 3.5., indeed, confirm that the use of LDDRK scheme reduces dispersion error. An explanation will be offered later.

 For certain wave propagation problems, minimizing dispersion error could be an important consideration. To do so, one might choose the free parameters or constants of the Runge-Kutta scheme to minimize the difference between the group velocity and the exact velocity of propagation of the governing wave equation. For the simple convective wave equation, the group velocity is given by Eq. (3.31). Suppose in Eqs. (3.28) and (3.29) we set $c_1 = 1$ and $c_2 = 0.5$ but allow c_3 and c_4 to be free parameters. We may then choose c_3 and c_4 to minimize the square of the difference between the group velocity and the exact wave speed c over a band of wave number. We will assume that the spatial discretization is exact; i.e., $\overline{\alpha} = \alpha$. Thus, c_3 and c_4 are chosen to minimize the following integral,

$$E = \int_0^{\pi} \left| \frac{1}{c} \frac{d\omega}{d\alpha} - 1 \right|^2 d(\alpha\Delta t). \qquad (3.33)$$

Note: When all the c_j's are known, one may keep β_j to be the same as the standard Runge-Kutta scheme and find w_j's by solving Eq. (3.29) as a linear system.

η (eq. (3.33))	c_3	c_4
0.6	0.163168	4.07351 E-02
0.7	0.161940	4.04090 E-02
0.8	0.160545	4.00390 E-02
0.9	0.158992	3.96280 E-02
Hu *et al.* (1996)	0.162997	4.07574 E-02
Standard 4th order RK	0.166667	4.16667 E-02

TABLE 1 Values of parameter c_3 and c_4.

Table 1 gives the values of c_3 and c_4 for different choices of η. The group velocity $\mathrm{Re}(d\omega/d\alpha)$ as a function of $c\alpha\Delta t$ corresponding to these choices of c_3 and c_4 are plotted in Fig. 3.6. It is clear from this figure that by using a large η the minimization procedure forces a large band of wave number to have group velocity closer to c. However, it is a feature of mean squared minimization that this also leads to a larger overshoot. So one might select a compromise between a larger bandwidth with normalized group velocity closer to 1.0 and a smaller overshoot. Plotted also in Fig. 3.6 is the group velocity curve of the LDDRK scheme of Hu *et al.* It turns out it is almost identical to that of the choice $\eta = 0.6$. This is strictly a coincidence! But this appears to offer an explanation of why the LDDRK scheme does not incur excessive numerical dispersion error arising from temporal discretization.

3.4. Origin of Numerical Dissipation

Discretization of a partial differential equation into a finite difference equation, generally, leads to numerical dissipation in addition to numerical dispersion. Let us again illustrate this by considering solving the convective wave equation (3.1) using a large stencil finite difference scheme. Suppose we approximate the spatial derivative by a finite difference quotient and solve time exactly. The exact solution of the semi-discretized problem is again given by Eq. (3.19) except that $\overline{\omega}$ is to be replaced by ω; i.e.,

$$u(x,t) = \frac{i}{2\pi} \int_{-\infty}^{\infty} \int_{\Gamma} \frac{\hat{\Phi}(\alpha)}{\omega - c\overline{\alpha}(\alpha)} e^{i(\alpha x - \omega t)} d\omega \, d\alpha. \tag{3.34}$$

The integrand has a pole at $\omega = c\overline{\alpha}(\alpha)$ in the ω-plane. By means of the Residue Theorem, the ω-integral may be evaluated to give,

$$u(x,t) = \int_{-\infty}^{\infty} \hat{\Phi}(\alpha) e^{i(\alpha x - c\overline{\alpha}(\alpha)t)} d\alpha. \tag{3.35}$$

Now whether the numerical solution is damped or not depends critically on whether a central difference stencil or an unsymmetric difference stencil is used. If a central difference

stencil is used, then $\overline{\alpha}(\alpha)$ is a real function for real α. In this case, Eq. (3.35) represents a dispersive wave packet without being damped in time. If an unsymmetric stencil is used, then $\overline{\alpha}(\alpha)$ is complex for real α (see Eq. (3.11)). In this case, the solution is damped in time provided $\mathrm{Im}(c\overline{\alpha})$ is negative for all α. The time rate of damping for wave with wave number α is given by $c\,\mathrm{Im}[\overline{\alpha}(\alpha)]$. For many popular numerical schemes $c\,\mathrm{Im}(\overline{\alpha})$ is negative. Such schemes have built-in numerical damping. The damping rate can be calculated precisely once the stencil size and stencil coefficients are known.

It is worthwhile to point out that it is possible c and $\mathrm{Im}(\overline{\alpha})$ have the same sign. In this case, the numerical solution will grow exponentially in time leading to numerical instability. Therefore, a necessary condition for numerical stability is

$$c\,\mathrm{Im}\big[\overline{\alpha}(\alpha)\big] < 0, \quad -\pi \leq \alpha\Delta x \leq \pi. \tag{3.36}$$

Eq. (3.36) is the upwinding requirement. It is easy to show numerically that only upwind unsymmetric stencils could satisfy condition (3.36). The upwinding requirement is extremely important when solving the full Euler equations. The Euler equations support several modes of waves (acoustic, vorticity and entropy waves). The upwinding condition must be satisfied by each wave mode if the numerical solution is to remain stable.

Temporal discretization also introduces numerical damping. The damping rate can be determined quantitatively from the dispersion relation. Because $\overline{\omega}(\omega)$ is complex, the root $\omega = \omega(\alpha)$ of $\overline{\omega}(\omega) = c\overline{\alpha}(\alpha)$ has an imaginary part even when $\overline{\alpha}(\alpha)$ is real for real α. For the convective wave equation, the exact solution of the fully discretized system is given by Eq. (3.19). The integrals may be evaluated by the Residue Theorem. This leads to the replacement of ω by $\omega = \omega(\alpha)$, the root of $\overline{\omega}(\omega) = c\overline{\alpha}(\alpha)$. Since $\omega(\alpha)$ is now complex, the solution is damped in time. The time rate of damping for wave component with wave number α is $\mathrm{Im}[\omega(\alpha)]$.

A simple way to reduce numerical damping due to temporal discretization is to use a smaller Δt. To see why reducing time step size would reduce numerical damping, let us assume that a spatial discretization scheme is chosen so that the problem would be solved accurately by using N mesh points per wavelength. In other words, if λ is the shortest wavelength, the scheme is designed to resolve, then $\lambda/\Delta x > N$. This yields, in terms of wave number, $2\pi/N > \overline{\alpha}_{\text{largest}}\Delta x$. Now $\overline{\omega}$ is related to $\overline{\alpha}$ by the dispersion relation (3.20a), thus

$$\frac{2\pi}{N}c\left(\frac{\Delta t}{\Delta x}\right) > \overline{\omega}_{\text{largest}}\Delta t. \tag{3.37}$$

By choosing $\Delta t/\Delta x$ small, $\overline{\omega}_{\text{largest}}\Delta t$ would be confined to a range that is closer to zero. For most temporal marching schemes, including the Runge-Kutta method, the DRP scheme, the $\overline{\omega}\Delta t$ versus $\omega\Delta t$ relation is such that $\mathrm{Im}(\overline{\omega}\Delta t)$ and hence $\mathrm{Im}(\omega\Delta t)$ becomes smaller when $\overline{\omega}\Delta t$ is closer to zero. It follows that the roots of Eq. (3.18) i. e. $\omega(\alpha)$ would be nearly real when Δt is reduced. This means that the temporal damping rate $\mathrm{Im}[\omega(\alpha)]$ would be reduced.

4. STABILITY OF NUMERICAL SCHEMES

4.1 Choice of time step

How to choose a time step to ensure the numerical solution of Euler equation is numerically stable is of critical importance. To illustrate how this can be done, the case of small amplitude disturbances superimposed on a uniform mean flow of density ρ_0, pressure p_0 and velocity u_0 in the x-direction (see Fig. 4.1) is considered. The linearized Euler equation for two-dimensional disturbances is:

$$\frac{\partial \mathbf{U}}{\partial t} + \frac{\partial \mathbf{E}}{\partial x} + \frac{\partial \mathbf{F}}{\partial y} = \mathbf{H} \tag{4.1}$$

where

$$\mathbf{U} = \begin{bmatrix} \rho \\ u \\ v \\ p \end{bmatrix}, \qquad \mathbf{E} = \begin{bmatrix} \rho_0 u + \rho u_0 \\ u_0 u + \frac{p}{\rho_0} \\ u_0 v \\ u_0 p + \gamma p_0 u \end{bmatrix}, \qquad \mathbf{F} = \begin{bmatrix} \rho_0 v \\ 0 \\ \frac{p}{\rho_0} \\ \gamma p_0 v \end{bmatrix}.$$

The nonhomogeneous term $\mathbf{H}$ on the right side of Eq. (4.1) represents distributed time-dependent sources.
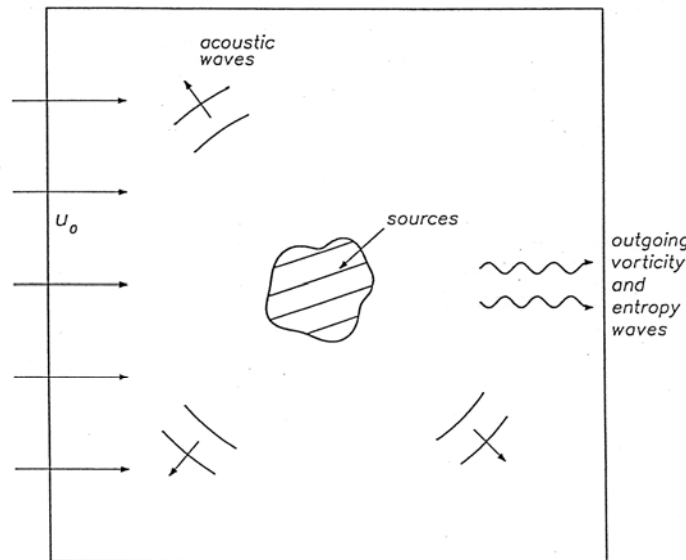
Figure 4.1. Acoustic, vorticity and entropy wave sources in a uniform flow.

The Fourier-Laplace transform $\widetilde{f}(\alpha,\beta,\omega)$ of a function $f(x,y,t)$ is related to the function by:

$$\widetilde{f}(\alpha,\beta,\omega) = \frac{1}{(2\pi)^3} \int_0^\infty \int_{-\infty}^\infty \int_{-\infty}^\infty f(x,y,t) e^{-i(\alpha x + \beta y - \omega t)} dx \, dy \, dt$$

$$f(x, y, t) = \int_{\Gamma} \int \int_{-\infty}^{\infty} \tilde{f}(\alpha, \beta, \omega) e^{i(\alpha x + \beta y - \omega t)} d\alpha \, d\beta \, d\omega$$

In the above, the contour Γ is a line parallel to the real axis in the complex ω-plane above all poles and singularities of the integrand (see Appendix A)
.

Now, consider the general initial value problem governed by the linearized Euler equation (4.1). The initial condition at $t = 0$ is,

$$\mathbf{u} = \mathbf{u}_{initial}(x, y) \tag{4.2}$$

The general initial value problem for arbitrary nonhomogeneous source term $\mathbf{H}$ can be solved formally by Fourier-Laplace transforms. As shown in Appendix A, the Laplace transform of a time derivative is,

$$\frac{1}{2\pi} \int_0^\infty \frac{\partial \mathbf{u}}{\partial t} e^{i\omega t} dt = -\frac{1}{2\pi} \mathbf{u}_{initial} - i\omega \tilde{\mathbf{u}} \tag{4.3}$$

The Fourier-Laplace transform of Eq. (4.1) is a system of linear algebraic equations that may be written in the form,

$$\mathbf{A}\tilde{\mathbf{U}} = \tilde{\mathbf{G}} \tag{4.4}$$

where

$$\mathbf{A} = \begin{bmatrix} (\omega - \alpha u_0) & -\rho_0 \alpha & -\rho_0 \beta & 0 \\ 0 & (\omega - \alpha u_0) & 0 & -\frac{\alpha}{\rho_0} \\ 0 & 0 & (\omega - \alpha u_0) & -\frac{\beta}{\rho_0} \\ 0 & -\gamma p_0 \alpha & -\gamma p_0 \beta & (\omega - \alpha u_0) \end{bmatrix} \tag{4.4a}$$

and $\tilde{\mathbf{G}} = i[\tilde{\mathbf{H}} + (\tilde{\mathbf{U}}_{initial} / 2\pi)]$ represents the sum of the transforms of the source term and the initial condition.

It is easy to show that the eigenvalues λ and eigenvectors $\mathbf{X}_j$ ($j = 1, 2, 3, 4$) of matrix $\mathbf{A}$ are:

$$\lambda_1 = \lambda_2 = (\omega - \alpha u_0) \tag{4.5}$$

$$\lambda_3 = (\omega - \alpha u_0) + a_0 (\alpha^2 + \beta^2)^{\frac{1}{2}} \tag{4.6}$$

$$\lambda_4 = (\omega - \alpha u_0) - a_0 (\alpha^2 + \beta^2)^{\frac{1}{2}} \tag{4.7}$$

$$
\mathbf{X}_1 = \begin{bmatrix} 1 \\ 0 \\ 0 \\ 0 \end{bmatrix}, \qquad
\mathbf{X}_2 = \begin{bmatrix} 0 \\ \beta \\ -\alpha \\ 0 \end{bmatrix}, \qquad
\mathbf{X}_3 = \begin{bmatrix} \frac{1}{a_0^2} \\ \frac{-\alpha}{\rho_0 a_0 (\alpha^2 + \beta^2)^{1/2}} \\ \frac{-\beta}{\rho_0 a_0 (\alpha^2 + \beta^2)^{1/2}} \\ 1 \end{bmatrix}, \qquad
\mathbf{X}_4 = \begin{bmatrix} \frac{1}{a_0^2} \\ \frac{\alpha}{\rho_0 a_0 (\alpha^2 + \beta^2)^{1/2}} \\ \frac{\beta}{\rho_0 a_0 (\alpha^2 + \beta^2)^{1/2}} \\ 1 \end{bmatrix} \tag{4.8}
$$

where $a_0 = (\gamma p_0/\rho_0)^{1/2}$ is the speed of sound. The solution of Eq. (4.4) may be expressed as a linear combination of the eigenvectors:

$$
\tilde{\mathbf{U}} = \frac{C_1}{\lambda_1} \mathbf{X}_1 + \frac{C_2}{\lambda_2} \mathbf{X}_2 + \frac{C_3}{\lambda_3} \mathbf{X}_3 + \frac{C_4}{\lambda_4} \mathbf{X}_4. \tag{4.9}
$$

The coefficient vector $\mathbf{C}$, having elements C_j ($j = 1$ to 4), is given by:

$$
\mathbf{C} = \mathbf{X}^{-1} \tilde{\mathbf{G}}. \tag{4.10}
$$

$\mathbf{X}^{-1}$ is the inverse of the fundamental matrix:

$$
\mathbf{X}^{-1} = \begin{bmatrix}
1 & 0 & 0 & -\frac{1}{a_0^2} \\
0 & \frac{\beta}{(\alpha^2 + \beta^2)} & -\frac{\alpha}{(\alpha^2 + \beta^2)} & 0 \\
0 & -\frac{1}{2} \frac{\rho_0 a_0 \alpha}{(\alpha^2 + \beta^2)^{1/2}} & -\frac{1}{2} \frac{\rho_0 a_0 \beta}{(\alpha^2 + \beta^2)^{1/2}} & \frac{1}{2} \\
0 & \frac{1}{2} \frac{\rho_0 a_0 \alpha}{(\alpha^2 + \beta^2)^{1/2}} & \frac{1}{2} \frac{\rho_0 a_0 \beta}{(\alpha^2 + \beta^2)^{1/2}} & \frac{1}{2}
\end{bmatrix}. \tag{4.11}
$$

Eq. (4.9) represents the decomposition of the solution into the entropy wave, $\mathbf{X}_1$, the vorticity wave, $\mathbf{X}_2$, and the two modes of acoustic waves, $\mathbf{X}_3$ and $\mathbf{X}_4$. Now each wave solution will be considered individually.

a. The Entropy Wave

The entropy wave consists of density fluctuations alone; i.e., $u = v = p = 0$. By inverting the Fourier-Laplace transform, it is straightforward to find that ρ is given by:

$$
\rho(x,y,t) = \int_\Gamma \int \int_{-\infty}^{\infty} \frac{C_1}{(\omega - \alpha u_0)} e^{i(\alpha x + \beta y - \omega t)} d\alpha \, d\beta \, d\omega. \tag{4.12}
$$

The zero of the denominator gives rise to a pole of the integrand. The relationship between ω, α and β arising from this zero is the dispersion relation. In this case, it is

$$
\lambda_1 = (\omega - \alpha u_0) = 0. \tag{4.13}
$$

b. The Vorticity Wave

The vorticity wave consists of velocity fluctuations alone. That is, there are no pressure and density fluctuations associated with this wave mode ($p = \rho = 0$). By inverting the Fourier-Laplace transforms, it is found,

$$\begin{bmatrix} u \\ v \end{bmatrix} = \int_\Gamma \int_{-\infty}^{\infty} \int \begin{bmatrix} \beta \\ -\alpha \end{bmatrix} \frac{C_2(\alpha,\beta)}{(\omega - \alpha u_0)} e^{i(\alpha x + \beta y - \omega t)} d\alpha \, d\beta \, d\omega. \tag{4.14}$$

The dispersion relation is

$$\lambda_2 = (\omega - \alpha u_0) = 0.$$

c. The Acoustic Wave

The acoustic waves involve fluctuations in all the physical variables. The dispersion relation is given by

$$\lambda_3 \lambda_4 = (\omega - \alpha u_0)^2 - a_0^2(\alpha^2 + \beta^2) = 0. \tag{4.15}$$

The formal solution may be found by inverting the Fourier-Laplace transforms. After some algebra, the formal solution may be written as,

$$\begin{bmatrix} \rho \\ p \end{bmatrix} = \int_\Gamma \int_{-\infty}^{\infty} \int \frac{\rho_0 a_0^2(\alpha \tilde{G}_2 + \beta \tilde{G}_3) + (\omega - \alpha u_0)\tilde{G}_4}{(\omega - \alpha u_0)^2 - a_0^2(\alpha^2 + \beta^2)} \begin{bmatrix} \frac{1}{a_0^2} \\ 1 \end{bmatrix} e^{i(\alpha x + \beta y - \omega t)} d\alpha \, d\beta \, d\omega. \tag{4.16}$$

$$\begin{bmatrix} u \\ v \end{bmatrix} = \int_\Gamma \int_{-\infty}^{\infty} \int \frac{[(\omega - \alpha u_0)(\alpha \tilde{G}_2 + \beta \tilde{G}_3)/(\alpha^2 + \beta^2)] + (\tilde{G}_4/\rho_0)}{(\omega - \alpha u_0)^2 - a_0^2(\alpha^2 + \beta^2)} \begin{bmatrix} \alpha \\ \beta \end{bmatrix} e^{i(\alpha x + \beta y - \omega t)} d\alpha \, d\beta \, d\omega. \tag{4.17}$$

Recall that the Fourier-Laplace transform of the DRP scheme is formally the same as that of the original Euler equations (with α, β, ω replaced by $\bar{\alpha}$, $\bar{\beta}$, $\bar{\omega}$, respectively). Thus by modifying Eq. (4.16) accordingly, the pressure associated with the acoustic waves computed by the DRP scheme is given by,

$$p(x,y,t) = \int_\Gamma \int_{-\infty}^{\infty} \int \frac{\left[\rho_0 a_0^2(\bar{\alpha}\tilde{G}_2 + \bar{\beta}\tilde{G}_3) + (\bar{\omega} - \bar{\alpha}u_0)\tilde{G}_4\right]}{(\bar{\omega} - \bar{\alpha}u_0)^2 - a_0^2(\bar{\alpha}^2 + \bar{\beta}^2)} e^{i(\alpha x + \beta y - \omega t)} d\alpha \, d\beta \, d\omega \tag{5.39}$$

where $\bar{\alpha}(\alpha)$, $\bar{\beta}(\beta)$ and $\bar{\omega}(\omega)$ and its inverse $\omega = \omega(\bar{\omega})$ are given in section 2. From the theory of Laplace transform it is well known that for large t the dominant contribution to the ω-integral comes from the residue of the pole of the integrand which has the largest imaginary part in the

complex ω-plane. In Eq. (4.18) the pole corresponding to the outgoing acoustic wave is given implicitly by

$$\overline{\omega}(\omega) = \overline{\alpha}(\alpha)u_0 + a_0\left(\overline{\alpha}^2(\alpha) + \overline{\beta}^2(\beta)\right)^{\frac{1}{2}}$$
(4.19)

As has been discussed in section 2.5.2, for a given $\overline{\omega}$ there are four values of ω. Thus there are four wave solutions associated with the $\overline{\omega}$ pole of Eq. (4.19); three of which are spurious. Let the roots be denoted by ω_k ($k = 1, 2, 3, 4$) with ω_1 corresponding to the physical acoustic wave. On completing the contour in the lower half ω-plane by a large semi-circle, by the residue theorem, the pressure field given by Eq. (4.18) becomes,

$$p(x,y,t) = \sum_{k=1}^{4} -(2\pi i)\left[\int_{-\infty}^{\infty}\int \frac{\left[\rho_0 a_0^2\left(\overline{\alpha}\widetilde{G}_2 + \overline{\beta}\widetilde{G}_3\right) + \left(\overline{\omega} - \overline{\alpha}u_0\right)\widetilde{G}_4\right]}{2\left(\overline{\omega} - \overline{\alpha}u_0\right)\frac{d\overline{\omega}}{d\omega}}\bigg|_{\omega=\omega_k} e^{i(\alpha x + \beta y)}\,d\alpha\,d\beta\right]e^{-i\omega_k t}$$
(4.20)

To obtain numerical stability, a sufficient condition is

$$\mathrm{Im}(\omega_k) \le 0, \qquad k = 1,\ 2,\ 3,\ 4.$$
(4.21)

It is to be noted from Fig. 3.2 that for arbitrary values of α and β the inequalities

$$\overline{\alpha}\Delta x < 1.75, \qquad \overline{\beta}\Delta y < 1.75$$
(4.22)

hold true. Substitution of Eq. (4.22) into Eq. (4.19) and upon multiplying by Δt it is found

$$\overline{\omega}\Delta t \le \frac{1.75 a_0}{\Delta x}\left[M + \left(1 + \left(\frac{\Delta x}{\Delta y}\right)^2\right)^{\frac{1}{2}}\right]\Delta t$$
(4.23)

where M is the Mach number. From section 2.5.2 it appears that if $|\overline{\omega}\Delta t|$ is less than 0.41 then all the roots of ω_k, especially the spurious roots, are damped. Therefore to ensure numerical stability it is sufficient by Eq. (4.23) to restrict Δt to less than $\Delta t_{\max}$ where $\Delta t_{\max}$ is given by

$$\Delta t_{\max} = \frac{0.41}{1.75\left[M + \left(1 + \left(\frac{\Delta x}{\Delta y}\right)^2\right)^{1/2}\right]}\frac{\Delta x}{a_0}.$$
(4.24)

Similar analysis for the entropy and the vorticity wave modes of the finite difference scheme yields the following criterion for numerical stability:

$$\Delta t < \frac{0.4}{1.75 M}\frac{\Delta x}{a_0}.$$
(4.25)

Eq. (4.24) is a more stringent condition than Eq. (4.25). Therefore, for $\Delta t < \Delta t_{max}$ the DRP scheme would be numerically stable.

4.2 Artificial Selective damping

To fix ideas, consider the initial value problem associated with the linearized Euler equations in one space dimension without mean flow. The dimensionless linearized momentum and energy equations are:

$$\frac{\partial u}{\partial t} + \frac{\partial p}{\partial x} = 0 \tag{4.26}$$

$$\frac{\partial p}{\partial t} + \frac{\partial u}{\partial x} = 0. \tag{4.27}$$

For simplicity, consider the following initial conditions,

$$t = 0 \qquad u = 0 \tag{4.28}$$

$$p = f(x). \tag{4.29}$$

It is easy to verify that the exact solution of (7.1) to (7.4) is,

$$p = \frac{1}{2}\left[f(x-t) + f(x+t)\right]. \tag{4.30}$$

This solution suggests that half the initial pressure pulse propagates to the left and the other half to the right at the speed of sound (unity in dimensionless units).

Now consider the "boxcar" initial condition,

$$f(x) = H(x + M) - H(x - M) \tag{4.31}$$

where M is a large positive number and $H(x)$ is the unit step function. The wave number spectrum of initial condition (4.31) extends well beyond the range $-\pi < \alpha < \pi$. A considerable fraction of the spectrum falls in the short wave range. This offers an excellent example on the wave propagation characteristics of the short waves of finite difference schemes. From Eq. (4.30), the exact solution is,

$$p(x,t) = \frac{1}{2}\left[H(x-t+M) - H(x-t-M)\right] + \frac{1}{2}\left[H(x+t+M) - H(x+t-M)\right]. \tag{4.32}$$

It is of interest to find out what happens when the problem is solved by the 7-point stencil DRP scheme. On discretizing Eqs. (4.26) and (4.27) according to the DRP scheme, the resulting finite difference equations are,

$$E_l^{(n)} \quad = \quad -\sum_{j=-3}^{3} a_j p_{l+j}^{(n)}$$

$$F_l^{(n)} \quad = \quad -\sum_{j=-3}^{3} a_j u_{l+j}^{(n)}$$

$$u_l^{(n+1)} \quad = \quad u_l^{(n)} + \Delta t \sum_{j=0}^{3} b_j E_l^{(n-j)}$$

$$p_l^{(n+1)} \quad = \quad p_l^{(n+1)} + \Delta t \sum_{j=0}^{3} b_j F_l^{(n-j)}$$

(4.33)

The initial conditions corresponding to Eqs. (4.28) and (4.31) are,

$$u_\ell^{(n)} = 0, \qquad\qquad\qquad\qquad n \le 0$$
$$p_\ell^{(n)} = \begin{cases} H(l+M) \; - \; H(l-M), & n = 0 \\ 0, & n < 0 \end{cases}$$

(4.34)
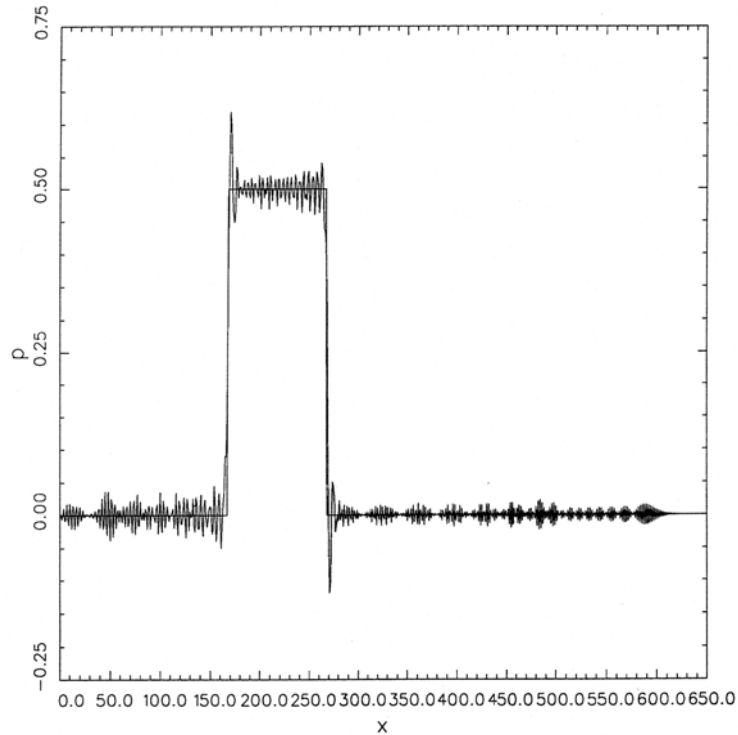
Figure 4.2. Pressure waveform initiated by boxcar initial condition at 2000 time steps.

Fig. 4.2 shows the numerical solution with the boxcar initial condition ($M = 50$). As can be seen, the solution is badly contaminated by short waves. The lead waves are the grid-to-grid oscillatory waves. The envelope of the amplitude of the short waves oscillates spatially (giving

the appearance of lumps of waves). The longer dispersive waves are trailing the main pulse solution.

This example clearly shows that short waves are pollutants of numerical solutions. They can be generated by discontinuous initial or boundary conditions. To render numerical solutions acceptable, a way must be found to suppress or eliminate the short waves without interfering with the long waves.

Short waves are spurious numerical contaminants of a computed solution. To improve the quality of a numerical solution, it is imperative that they be automatically removed from the computation as soon as they are generated. A way to remove short waves is to add artificial selective damping terms to the finite difference equations. For this method to be acceptable, the damping terms must selectively damp out the short waves and have minimal effect on the long waves.

4.2.1. The Basic Concept

Suppose a damping term, D(x), is added to the right side of the momentum equation of the linearized Euler equations in dimensional form,

$$\frac{\partial u}{\partial t} + \frac{1}{\rho_0}\frac{\partial p}{\partial x} = D(x). \tag{4.35}$$

Let the spatial derivative be approximated by the 7-point stencil DRP scheme. The discretized form of Eq. (4.35) is,

$$\frac{du_\ell}{dt} + \frac{1}{\rho_0 \Delta x}\sum_{j=-3}^{3} a_j p_{\ell+j} = D_\ell. \tag{4.36}$$

It will now be assumed that D_ℓ is proportional to the values of u_ℓ within the stencil. Let d_j be the weight coefficients. Eq. (4.36) may be written as

$$\frac{du_\ell}{dt} + \frac{1}{\rho_0 \Delta x}\sum_{j=-3}^{3} a_j p_{\ell+j} = -\frac{\nu}{(\Delta x)^2}\sum_{j=-3}^{3} d_j u_{\ell+j} \tag{4.37}$$

where ν is the artificial kinematic viscosity. $\nu/(\Delta x)^2$ has the dimension of $(\text{time})^{-1}$, so that d_j's are pure numbers. Now d_j's are to be chosen so that the artificial damping would be effective mainly for high wave number or short waves.

The Fourier transform of the generalized form of Eq. (4.37) is,

$$\frac{d\tilde{u}}{dt} + \ldots = -\frac{\nu}{(\Delta x)^2}\tilde{D}(\alpha \Delta x)\tilde{u} \tag{4.38}$$

where

$$\tilde{D}(\alpha\Delta x) = \sum_{j=-3}^{3} d_j e^{ij\alpha\Delta x}. \qquad (4.39)$$

On ignoring the terms not shown in Eq. (4.38), the solution is,

$$\tilde{u} \sim e^{-\frac{\nu}{(\Delta x)^2}\tilde{D}(\alpha\Delta x)t}. \qquad (4.40)$$

Since $\tilde{D}(\alpha\Delta x)$ depends on the wave number, the damping will vary with wave number. It is desirable for $\tilde{D}$ to be zero or small for small $\alpha\Delta x$ but large for large $\alpha\Delta x$. This can be done by choosing d_j's appropriately. But one must be careful to make sure that the damping term would not cause undamping or numerical instability. The purposes of the following three conditions that are to be imposed on $\tilde{D}$ are self-evident.

1. $\tilde{D}(\alpha\Delta x)$ should be a positive even function of $\alpha\Delta x$. The even function condition is assured by setting $d_{-j} = d_j$. Thus

$$\tilde{D}(\alpha\Delta x) = d_0 + 2\sum_{j=-3}^{3} d_j \cos(j\alpha\Delta x) \qquad (4.41)$$

2. There should be no damping for long waves. That is, $\tilde{D}(\alpha\Delta x) \to 0$ as $\alpha\Delta x \to 0$. This requires,

$$d_0 + 2\sum_{j=1}^{3} d_j = 0 \qquad (4.42)$$

3. For convenience, $\tilde{D}(\alpha\Delta x)$ may be normalized so that

$$\tilde{D}(\pi) = 1 \qquad (4.43)$$

The right side of Eq. (4.39) is a truncated Fourier cosine series. To ensure that $\tilde{D}(\alpha\Delta x)$ is small when $\alpha\Delta x$ is small but becomes large when $\alpha\Delta x \to \pi$, one may use a Gaussian function centered at $\alpha\Delta x = \pi$ with half-width σ as a template for choosing the Fourier coefficients d_j. This is done by determining d_j such that the integral

$$\int_0^{\beta} \left[\tilde{D}(\alpha\Delta x) - e^{-\ln 2\left(\frac{\alpha\Delta x - \pi}{\sigma}\right)^2} \right]^2 d(\alpha\Delta x)$$

is a minimum subjected to conditions (4.42) and (4.43). The upper limit of the integral β is a parameter that may be adjusted to yield the most desirable properties for $\tilde{D}$. For example, the coefficients of a very useful damping curve for problems involving discontinuous solution are ($\sigma=0.3\pi$, $\beta=0.65\pi$),

$$d_0 \quad = \quad 0.3276986608$$

$$d_1 \quad = \quad d_{-1} \quad = \quad -0.235718815$$

$$d_2 \quad = \quad d_{-2} \quad = \quad 0.0861506696$$

$$d_3 \quad = \quad d_{-3} \quad = \quad -0.014811847$$

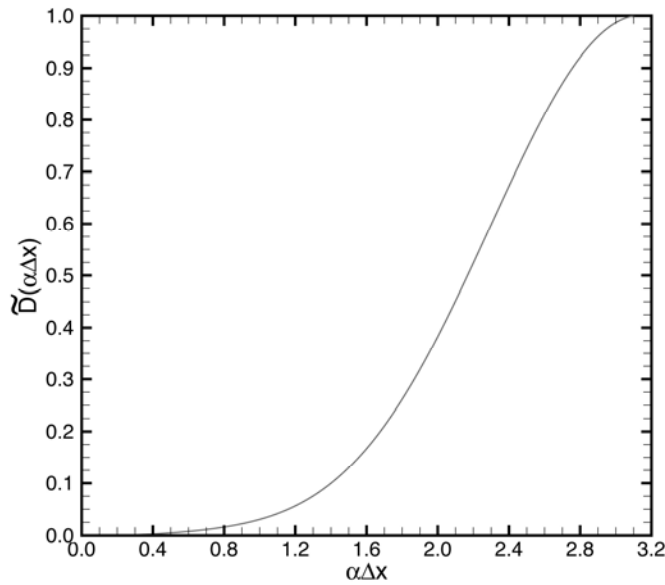A plot of $\tilde{D}$ versus $\alpha\Delta x$ for this choice is shown in Fig. 4.3.

Figure 4.3. Damping curve. 7-point stencil, $\sigma = 0.3\pi$.

4.2.2. Numerical Example

To illustrate the effectiveness of artificial selective damping, consider again the simple wave problem with discontinuous initial condition. On incorporating artificial selective damping to the DRP scheme, the finite difference equations are,

$$u_\ell^{(n+1)} \;=\; u_\ell^{(n)} + \Delta t \sum_{j=0}^{3} b_j E_\ell^{(n-j)}$$

$$p_\ell^{(n+1)} \;=\; p_\ell^{(n)} + \Delta t \sum_{j=0}^{3} b_j F_\ell^{(n-j)}$$

$$E_\ell^{(n)} \;=\; -\sum_{j=-3}^{3} a_j p_{\ell+j}^{(n)} - \frac{1}{R_\Delta} \sum_{j=-3}^{3} d_j u_{\ell+j}^{(n)}$$

$$\hspace{10cm} (4.44)$$

$$F_\ell^{(n)} \;=\; -\sum_{j=-3}^{3} a_j u_{\ell+j}^{(n)} - \frac{1}{R_\Delta} \sum_{j=-3}^{3} d_j p_{\ell+j}^{(n)}$$

$$u_\ell^{(n)} \;=\; 0 \hspace{2cm} (n \leq 0)$$

$$p_\ell^{(n)} \;=\; \begin{cases} \left[H(\ell+M) - H(\ell-M) \right], & n = 0 \\ 0, & n < 0 \end{cases}$$

where $R_\Delta = a_0 \Delta x / \nu$ is the artificial mesh Reynolds number. In the numerical simulation below R_Δ^{-1} is given the value of 0.3.
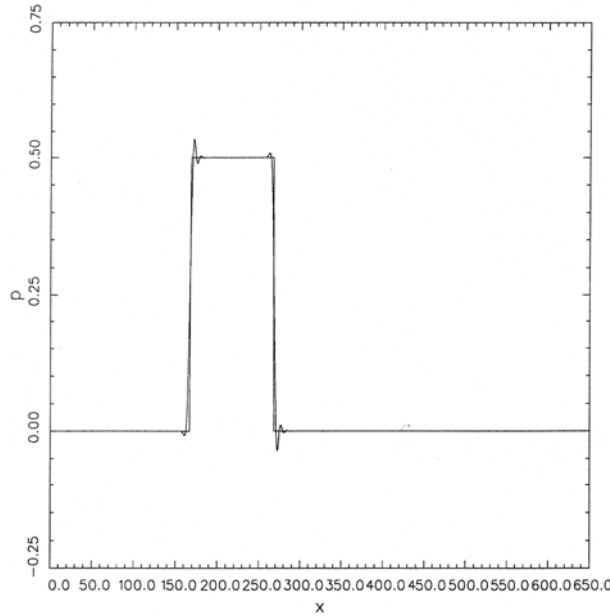
Figure 4.4. Pressure waveform initiated by boxcar initial condition
computed with artificial selective damping. t = 2000 time steps.

In the course of computing the numerical solution of Eq. (4.44), it is noticed that the short waves corresponding to grid-to-grid oscillations which are subjected to most intense damping, are damped out almost immediately after they are generated. The damping for the spurious waves with longer wave length is smaller. Their presence in the numerical solution can still be seen after 200 time steps. At $t = 500\Delta t$, they, too, are almost completely eliminated. Fig. 4.4

shows the calculated pressure waveform at $t = 2000\Delta t$. Essentially all the spurious waves, except two spikes, have been damped out. The computed solution is now a reasonably good approximation of the exact boxcar solution. Of course, the finite difference solution is not perfect. It does not faithfully reproduce the sharp discontinuities. Each discontinuity is spread over a distance of about 5 to 6 mesh spacings. This is close to the minimum wavelength that the scheme can resolve.

4.2.3 Other Damping stencils

The $\sigma = 0.3\pi$ 7-point damping stencil with damping function shown in Fig. 4.3 is primarily designed for problems with discontinuities or shocks. Because of the steep gradients involved, strong damping over a wide band of wave number is necessary. But even in problems for which the solutions are shock and discontinuity free, short spurious waves are often generated. Wall boundaries, mesh size change interfaces and regions with steep gradients are potential sources of short waves. For this reason, it is a good practice to add a small amount of background artificial selective damping to a computation. Also because of the need to use backward difference stencils at the boundary region of a computation domain, the numerical solution is subjected to weak numerical instability. These instabilities usually manifest themselves in the form of grid-to-grid oscillations with very gradual increase in amplitude. This type of weak instability can easily be suppressed by the addition of artificial selective damping.

For general background damping for which only short waves need to be removed, the following $\sigma = 0.2\pi$ 7-point damping stencil is recommended. The stencil coefficients are,

7-point damping stencil ($\sigma = 0.2\pi$)

$$
\begin{aligned}
d_0 &= 0.2873928425 \\
d_1 = d_{-1} &= -0.2261469518 \\
d_2 = d_{-2} &= 0.1063035788 \\
d_3 = d_{-3} &= -0.0238530482
\end{aligned}
$$

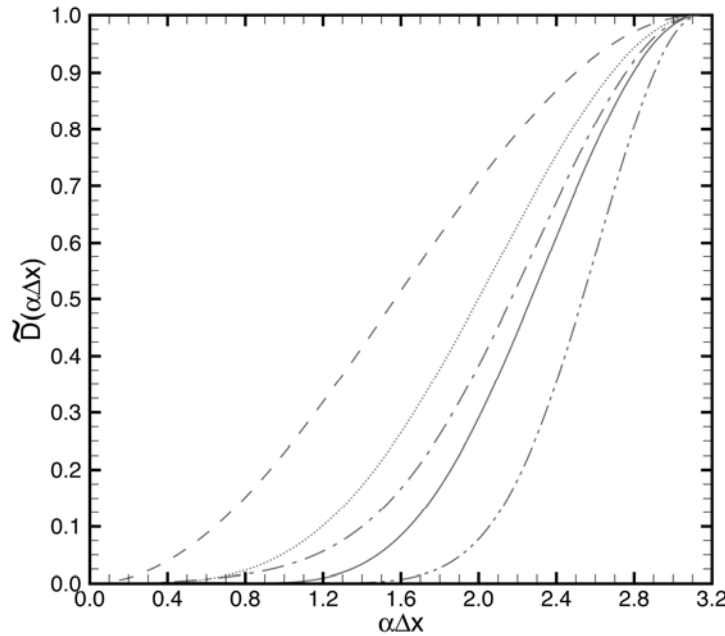The damping function of this damping stencil is shown in Fig. 4.5.

Figure 4.5. Damping functions $\tilde{D}(\alpha\Delta x)$. ——— 7-point stencil ($\sigma = 0.2\pi$), —·—·— 7-point stencil ($\sigma = 0.3\pi$), ······· 5-point stencil, – – – – 3-point stencil, —··—··— 15-point stencil.

When very high resolution is required, the 15-point stencil DRP scheme is often used. In this case, a 15-point damping stencil will be needed. The following is a set of damping coefficients for such a stencil.

15-point damping stencil

$$d_0 = 0.2042241813072920$$
$$d_1 = d_{-1} = -0.1799016298200503$$
$$d_2 = d_{-2} = 0.1224349282118140$$
$$d_3 = d_{-3} = -6.3456279827554890E-02$$
$$d_4 = d_{-4} = 2.4341225689340974E-02$$
$$d_5 = d_{-5} = -6.5519987489327603E-03$$
$$d_6 = d_{-6} = 1.1117554451990776E-03$$
$$d_7 = d_{-7} = -9.0091603462069583E-05$$

The damping curve is shown in Fig. 4.5.

4.3 Artificial Damping At Surfaces of Discontinuity

A surface of discontinuity such as a wall is a potential source of spurious waves. Thus it is important to incorporate artificial selective damping near such a surface to suppress the generation of these waves.

Near a horizontal wall, there is not enough room for a 7-point central damping stencil in the vertical direction for mesh points in the two rows adjacent to the wall (see Fig. 4.6). Only smaller symmetric stencil can fit in the limited space. The following are stencil coefficients for 5-point and 3-point stencils that have been used extensively with satisfactory results.

5-point damping stencil

$$d_0 = 0.375$$
$$d_1 = d_{-1} = -0.25 .$$
$$d_2 = d_{-2} = 0.0625$$

3-point damping stencil

$$d_0 = 0.5$$
$$d_1 = d_{-1} = -0.25$$

The damping curves for these stencils are shown in figure 4.5. These smaller damping stencils impose a non-negligible damping on the long waves. They should not be used as general damping stencils over the entire computational domain. Experience indicates that when used only near a wall or at the outside boundary of a computational domain, they do not cause excessive damping to the physical solution.

For general background damping, the use of an inverse mesh Reynolds number, R_Δ^{-1}, of 0.05 or slightly less has been found to be satisfactory. The amount of damping is sufficient to remove spurious short waves in most problems. For viscous fluid, additional damping near a wall especially at a sharp corner (see Fig. 4.6) is often necessary. To impose extra damping, a simple but effective way is to use a Gaussian distribution of R_Δ^{-1} in the direction normal to the wall. The peak value of the Gaussian is at the wall. A good choice of the half width of the Gaussian is 3 or 4 mesh spacings. For instance, along the wall y = 0 in Fig. 4.6, an additional inverse mesh Reynolds number distribution of the form.

$$R_\Delta^{-1} = 0.15\, e^{-(\ln 2)(\frac{y}{4\Delta y})^2} H(y) \tag{4.45}$$

where H(y) is the unit step function, may be incorporated into the artificial selective damping terms of the computation scheme. The highest value of R_Δ^{-1} at the wall may be larger than 0.1 as indicated above. A similar distribution of inverse mesh Reynolds number distribution may also be imposed adjacent to the wall at x = 0.
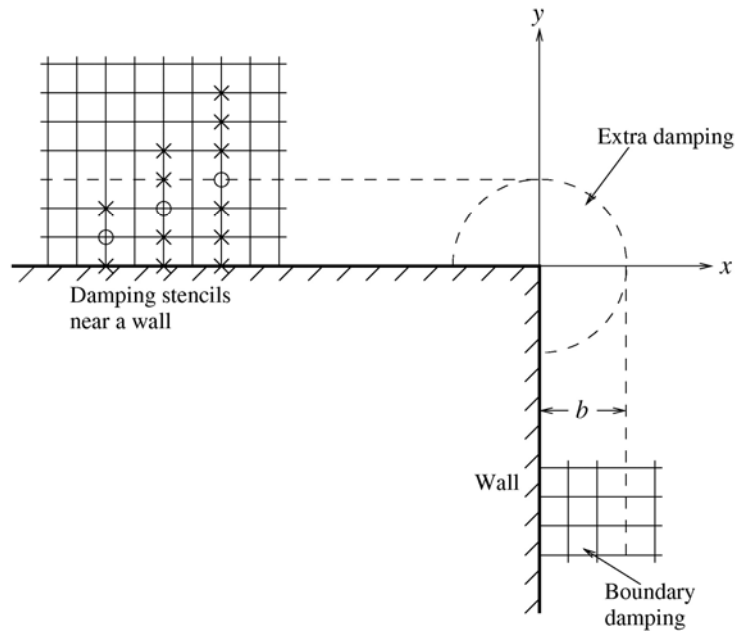
Figure 4.6 Artificial selective damping and damping stencils near a wall and at a sharp corner.

At a sharp corner, as shown in Fig. 4.6, large amount of artificial selective damping is required to stabilize the computation. This may be implemented by using an inverse mesh Reynolds number distribution at the corner point in the form of a multi-dimensional Gaussian function,

$$R_\Delta^{-1} = 0.3\, e^{-\ln 2 \left[\frac{x^2 + y^2}{16\Delta x^2}\right]} \tag{4.46}$$

At the present time, there is no formal guideline in setting the amplitude of the Gaussian function at the corner point. This value has to be adjusted in each problem until a satisfactory value is selected.

5. EXTERIOR BOUNDARY CONDITIONS FOR OPEN DOMAIN PROBLEMS

A computational domain is inevitably finite. A finite computation domain introduces a set of artificial boundaries. There are two basic reasons why exterior boundary conditions are needed at the artificial boundaries. First, exterior boundary conditions must reproduce the effect of the outside world exerted on the flow inside the computation domain. Since only the computed results inside the computation domain are known, it is, generally, not possible to know the outside influence. For this reason, a computation domain is often taken as large as possible so that all sources are inside. This will minimize possible external influence.

Another reason for imposing exterior boundary conditions is to avoid the reflection of out going disturbances back into the computation domain and thus contaminating the computed solution. One way to avoid reflection is to construct boundary conditions in such a way as to

allow the smooth exit of all disturbances. An alternative way is to develop absorbing boundary conditions. This type of boundary condition consists of an absorbing layer which absorbs or dissipates all outgoing disturbances as they traverse the layer.

There are a variety of exterior boundary conditions. Some are very effective. Others are not. Several types of exterior boundary conditions are considered below.

5.1 Characteristic Boundary Conditions

A number of investigators developed radiation boundary conditions using one-dimensional characteristics. They include Porter and Coakley (1972), Hedstrom (1979), Chakravarthy (1983), Scott and Hankey (1985), Thompson (1987, 1990), Poinsot and Lele (1992), Atkins and Casper (1994), Baum et.al. (1994), Ferm (1995), Kim and Lee (1997, 2000), Berthet et. al. (2000), Hixon (2000), and Bruneau and Creuse (2001). When one-dimensional characteristics are used, the waves are implicitly assumed to be one-dimensional, and oriented normal to the boundary. Thus, waves impinging on the boundary at other angles are partially or wholly reflected back into the computational domain. Experience indicates that one dimensional characteristic boundary conditions often lead to excessive reflection and should not be used when quality results are required.

5.2 Boundary Conditions Based on Operator Expansion

It is possible to develop boundary conditions rigorously through the use of Fourier-Laplace transforms. However, to express the boundary conditions in physical space, the inverse transforms cannot be performed analytically nor can be efficiently performed computationally. To transform the exact nonlocal boundary condition to an approximate, local boundary condition, rational function approximations may be employed. This methodology was used by Engquist and Majda (1977, 1979) for the wave equation, and Giles (1990) attempted to extend it to the linearized Euler equations. Colonius, et. al. (1993), used a Giles-type analysis to devise boundary conditions for the Navier-Stokes equations. An improved form of the rational approximations was given for the linearized Euler equations by Goodrich and Hagstrom (1996, 1997) and Hagstrom (1996), using auxiliary functions to extend the boundary condition to arbitrarily high accuracy in time. Rowley and Colonius (2000) extended this type of analysis to account for numerical accuracy at the boundaries. In general, this type of boundary conditions lead to a complicated hierarchy set of boundary conditions. The implementation of the set of boundary condition is non-trivial and numerical results are not impressive.

5.3 Asymptotic Boundary Conditions

When disturbances supported by the Euler equations propagate far away from the sources, they become outgoing waves. Outgoing waves are highly simplified solutions when compared to solution in the near field. The simplified form allows them to be used as the basis to form exterior asymptotic boundary conditions.

There are two ways to derive asymptotic boundary conditions. The first way is to partition the governing equations into a sequence of high order operators giving a sequence of

theoretically more accurate boundary conditions. This strategy was first exploited by Bayliss and Turkel (1980, 1982a, 1982b). Higdon (1986,1987) reduced the higher-order operators to a series of one-dimensional operators that are applied at various angles to the boundary. Using a series of auxiliary functions, Hagstrom and Hariharan devised a method to apply the higher-order operators while only requiring low-order derivatives (e.g., Hagstrom and Hariharan (1988, 1997, 1998) and Hariharan and Hagstrom (1990)).

A different way to formulate asymptotic boundary conditions was pioneered by Tam and Webb (1993). They obtained formal solutions of the linearized Euler equations by Fourier-Laplace transforms. The solutions clearly identify three sets of waves. They are the acoustic waves, the entropy waves and the vorticity waves. Since the entropy and vorticity waves are convected downstream by the mean flow, it becomes obvious that one should separate inflow from outflow boundary conditions. Inflow boundaries have only outgoing acoustic waves. Outflow boundaries have outgoing entropy and vorticity waves as well as acoustic waves. The discovery of the need to impose different inflow and outflow boundary conditions represents a major difference between the two approaches in formulating exterior boundary conditions. Tam and Webb succeeded in deriving the asymptotic solution of the outgoing acoustic, entropy and vorticity waves through asymptotic evaluation of the inversion integrals. The forms of these solutions in two dimensions with a uniform mean flow in the x-direction are,

(i) Acoustic waves

$$
\begin{bmatrix} \rho \\ u \\ v \\ p \end{bmatrix} = \frac{F\left(\dfrac{r}{V(\theta)} - t, \theta\right)}{r^{1/2}} \begin{vmatrix} 1/a^2 \\ \hat{u}(\theta) \\ \hat{v}(\theta) \\ 1 \end{vmatrix} + O(r^{-3/2})
$$

where (r, θ) are the polar coordinates. $V(\theta) = u_0 \cos\theta + a_0 (1 - M^2 \sin^2\theta)^{1/2}$, M is the mean flow Mach number and a_0 is the speed of sound.

(ii) Vorticity waves $\qquad \rho = p = 0$

$$
\begin{bmatrix} u \\ v \end{bmatrix} = \begin{bmatrix} \dfrac{\partial \Psi}{\partial y} \\ -\dfrac{\partial \Psi}{\partial x} \end{bmatrix}
$$

where $\qquad \Psi = \begin{cases} \Psi(x - u_0 t, y) & x \to +\infty \\ 0 & x \to -\infty \end{cases}$

(iii) Entropy waves $\qquad u = v = 0$

$$\rho = \begin{cases} \chi(x - u_0 t, y) & x \to +\infty \\ 0 & x \to -\infty \end{cases}$$

The functions F, Ψ and χ are arbitray. u_0 is mean flow velocity.

A set of radiation or inflow boundary conditions may be found by eliminating F from the acoustic wave solution by cross differentiation,

$$\left(\frac{1}{V(\theta)} \frac{\partial}{\partial t} + \frac{\partial}{\partial r} + \frac{1}{2r} \right) \begin{vmatrix} \rho \\ u \\ v \\ p \end{vmatrix} = 0 + O(r^{-5/2})$$

In the outflow region, the outgoing disturbances consist of a combination of the three sets of waves given above. It is, however, possible to eliminate the unknowns F, Ψ and χ and upon using the linearized momentum equation of Euler equations to obtain the following set of outflow boundary conditions.

$$\frac{\partial \rho}{\partial t} + u_0 \frac{\partial \rho}{\partial x} = \frac{1}{a_0} \left(\frac{\partial p}{\partial t} + u_0 \frac{\partial p}{\partial x} \right)$$

$$\frac{\partial u}{\partial t} + u_0 \frac{\partial u}{\partial x} = -\frac{1}{\rho_0} \frac{\partial p}{\partial x}$$

$$\frac{\partial v}{\partial t} + u_0 \frac{\partial v}{\partial x} = -\frac{1}{\rho_0} \frac{\partial p}{\partial y}$$

$$\frac{1}{V(\theta)} \frac{\partial p}{\partial t} + \cos\theta \frac{\partial p}{\partial x} + \sin\theta \frac{\partial p}{\partial y} + \frac{p}{2r} = 0$$

For slightly non-uniform mean flow, Tam and Dong (1996) extended the above approach to derive a more general set of outflow boundary conditions. One significant feature of their boundary condition is that it allows the mean flow to slightly adjust itself. In this way a precise mean flow need not be known *a priori* .

5.4 Absorbing Boundary Conditions

There are many types of "absorbing layers" for the purpose of annihilating the outgoing disturbances. A brief review of two types of these absorbing layers will first be given below. Attention will, however, be concentrated on "Perfectly Matched Layers (PML)" as it is the most successful.

5.4.1 Grid Stretching and Numerical Filtering

Attenuation of the solution may be achieved by purely numerical means. One such approach is to create a sponge layer (Colonius et al, 1993) in which the grids are stretched and

coarsened. When an out-going wave enters the sponge layer, it becomes under-resolved in the coarsened grid. As most numerical schemes have built-in provision to damp out unresolved waves, the out-going disturbances are attenuated through numerical dissipation.

The attenuation of the numerical solution can be enhanced by applying low-pass numerical filters inside the sponge or exit zone and thus reducing its length. In Colonius *et al* (1993) a five-point explicit filter operation was enforced. In Visbal and Gaitonde (2001), implicit high-order filters were used. Visbal and Gaitonde noted that since grid stretching could cause high frequency grid-to-grid oscillations, high order filters should be applied to the solution in the physical domain as well. Examples were presented by Visbal and Gaitonde where grid stretching could even be done non-smoothly when combined with high-order filters

5.4.2 Artificial Dissipation and Damping

Another way to absorb out-going disturbances is to create and append an absorbing zone to the physical computationa domain in which the governing equations are modified to mimic a physical dissipation mechanism. The advantage of using a physical analogy is that the modified equations will likely mathematically well posed.

For the Euler or Navier-Stokes equations, an artificial damping term can be easily introduced as follows,

$$\frac{\partial \mathbf{u}}{\partial t} = L(\mathbf{u}) - \upsilon_a (\mathbf{u} - \mathbf{u}_0)$$

where u is the solution vector and L(u) denotes the spatial operators of the governing equations. υ_a is the artificial damping coefficient. u_0 is the target value in the absorbing zone. One advantage of this approach is that no numerical instability would be created in the absorbing layer. The value of the artificial damping coefficient may be tuned for maximum effectiveness in a specific problem.

5.4.3. Perfectly Matched Layer (PML) as an Absorbing Boundary Condition

Perfectly Matched Layer (PML) was invented by Berenger (1994, 1996) as an absorbing boundary condition for computational electromagnetics. The idea is to enclose a computational domain by a PML. In the PML, a modified set of governing equations is used. The modified equations, as designed, have the unusual characteristics that when an outgoing disturbance impinges on the interface between the computational domain and the absorbing layer, no wave is reflected back. In other words, all outgoing disturbances are transmitted into the absorbing layer where they are damped out.

Hu (1996) was the first to apply PML successfully to aeroacoustic problems governed by the linearized Euler equations. In the beginning, the linearization was done over a uniform mean flow. Recently Hu (2005) had extended his work to nonuniform mean flow. Tam *et al.* (1998) analyzed the original version of the PML equations. They pointed out that those equations supported spatially growing unstable solutions. This is due to the fact that in the presence of a mean flow, the PML equations give rise to dispersive waves. In the original version of PML, a small band of these waves has phase velocity in opposite direction to the group velocity. Spatial damping in the PML is associated with the direction of the phase velocity. As a result, these waves grow in amplitude as they propagate across the PML instead of being damped. Hu (2001, 2004) has since resolved this instability problem. In this chapter, the more recent PML equations developed by Hu are presented and analyzed.

A. Derivation of the PML equation

The PML equation for the linearized Euler equation (linearized over a uniform mean flow in the *x*-direction) may be derived following three basic steps. To make the discussion of each of these steps as simple as possible, two-dimensional problems in Cartesian coordinates will first be considered. Let L be the length scale, a_0 (sound speed of the uniform mean flow) be the velocity scale, L/a_0 be the time scale, ρ_0 (gas density of mean flow) be the density scale and $\rho_0 a_0^2$ be the pressure scale. The dimensionless linearized Euler equation may be written in the form

$$\frac{\partial \mathbf{U}}{\partial t} + \mathbf{A}\frac{\partial \mathbf{U}}{\partial x} + \mathbf{B}\frac{\partial \mathbf{U}}{\partial y} = 0 \tag{5.1}$$

where

$$\mathbf{U} = \begin{vmatrix} \rho \\ u \\ v \\ p \end{vmatrix}, \qquad \mathbf{A} = \begin{vmatrix} M & 1 & 0 & 0 \\ 0 & M & 0 & 1 \\ 0 & 0 & M & 0 \\ 0 & 1 & 0 & M \end{vmatrix}, \qquad \mathbf{B} = \begin{vmatrix} 0 & 0 & 1 & 0 \\ 0 & 0 & 0 & 0 \\ 0 & 0 & 0 & 1 \\ 0 & 0 & 1 & 0 \end{vmatrix}$$

M is the Mach number of the mean flow.

The first step is to make a change of variables from (x,y,t) to $(\bar{x},\bar{y},\bar{t})$. The variables are related by

$$\bar{x} = x, \qquad \bar{y} = \left(1 - M^2\right)^{\frac{1}{2}} y, \qquad \bar{t} = t + \frac{Mx}{1 - M^2}. \tag{5.2}$$

This transformation is necessary to make the PML equation stable. The linearized Euler equation now becomes,

$$\left(\mathbf{I} + \frac{M}{1 - M^2}\mathbf{A}\right)\frac{\partial \mathbf{U}}{\partial \bar{t}} + \mathbf{A}\frac{\partial \mathbf{U}}{\partial \bar{x}} + \left(1 - M^2\right)^{\frac{1}{2}}\mathbf{B}\frac{\partial \mathbf{U}}{\partial \bar{y}} = 0. \tag{5.3}$$

In Eq. (5.3), $\mathbf{I}$ is the identity matrix, On assuming, for the time being, a time dependence of $e^{-i\bar{\omega}\bar{t}}$, Eq. (5.3) may be rewritten as,

$$-i\overline{\omega}\left(\mathbf{I}+\frac{M}{1-M^2}\mathbf{A}\right)\hat{u}+\mathbf{A}\frac{\partial\hat{\mathbf{u}}}{\partial\overline{x}}+\left(1-M^2\right)^{\frac{1}{2}}\mathbf{B}\frac{\partial\hat{u}}{\partial\overline{y}}=0 \tag{5.4}$$

where $\mathbf{u}(x,y,t)=\hat{\mathbf{u}}(x,y)e^{-i\overline{\omega}t}$.

The second step is to introduce damping into the equation through a so-called *complex change of variables*. Let $\sigma_x(x)>0$, $\sigma_y(y)>0$ be the absorption coefficients. The complex change of variables is to let

$$\overline{x}\to\overline{x}+\frac{i}{\overline{\omega}}\int^{\overline{x}}\sigma_x(x)\,dx, \qquad \overline{y}\to\overline{y}+\frac{i}{\overline{\omega}}\int^{\overline{y}}\sigma_y(y)\,dy$$

so that

$$\frac{\partial}{\partial\overline{x}}\to\frac{1}{1+\dfrac{i\sigma_x}{\overline{\omega}}}\frac{\partial}{\partial\overline{x}}, \qquad \frac{\partial}{\partial\overline{y}}\to\frac{1}{1+\dfrac{i\sigma_y}{\overline{\omega}}}\frac{\partial}{\partial\overline{y}}.$$

On performing the complex change of variables on Eq. (5.4), it becomes.

$$-i\overline{\omega}\left(\mathbf{I}+\frac{M}{1-M^2}\mathbf{A}\right)\hat{\mathbf{u}}+\frac{1}{1+\dfrac{i\sigma_x}{\overline{\omega}}}\mathbf{A}\frac{\partial\hat{\mathbf{u}}}{\partial\overline{x}}+\frac{(1-M^2)^{\frac{1}{2}}}{1+\dfrac{i\sigma_y}{\overline{\omega}}}\mathbf{B}\frac{\partial\hat{\mathbf{u}}}{\partial\overline{y}}=0. \tag{5.5}$$

The final step is to recast Eq. (5.5) back into the original physical variables. This may be done by first multiplying the equation by $[1+(i\sigma_x/\overline{\omega})][1+(i\sigma_y/\overline{\omega})]$. Also it is convenient to introduce an auxiliary variable of $\hat{q}$ defined by

$$\hat{\mathbf{q}}=\frac{i}{\overline{\omega}}\hat{\mathbf{u}}. \tag{5.6}$$

This yields,

$$\left(\mathbf{I}+\frac{M}{1-M^2}\mathbf{A}\right)\left(-i\overline{\omega}+\sigma_x\right)\hat{\mathbf{u}}+\mathbf{A}\frac{\partial\hat{\mathbf{u}}}{\partial\overline{x}}+\sigma_y\hat{\mathbf{u}}+\sigma_y\mathbf{A}\left(\frac{-i\overline{\omega}M}{1-M^2}\hat{\mathbf{q}}+\frac{\partial\hat{\mathbf{q}}}{\partial\overline{x}}\right)$$
$$+\sigma_x\sigma_y\left(\mathbf{I}+\frac{M}{1-M^2}\mathbf{A}\right)\hat{\mathbf{q}}+\sigma_x\left(1-M^2\right)^{\frac{1}{2}}\mathbf{B}\frac{\partial\hat{\mathbf{q}}}{\partial\overline{y}}+\left(1-M^2\right)^{\frac{1}{2}}\mathbf{B}\frac{\partial\hat{\mathbf{u}}}{\partial\overline{y}}=0 \tag{5.7}$$

upon restoring the time dependence and switching back to the original (x,y,t) coordinate system, Eq. (5.7) becomes

$$\frac{\partial\mathbf{u}}{\partial t}+\mathbf{A}\frac{\partial\mathbf{u}}{\partial x}+\mathbf{B}\frac{\partial\mathbf{u}}{\partial y}+\left(\sigma_x+\sigma_y\right)\mathbf{u}+\sigma_y\mathbf{A}\frac{\partial\mathbf{q}}{\partial x}+\sigma_x\mathbf{B}\frac{\partial\mathbf{q}}{\partial y}$$
$$+\sigma_x\sigma_y\mathbf{q}+\sigma_x\frac{M}{1-M^2}\mathbf{A}\left(\mathbf{u}+\sigma_y\mathbf{q}\right)=0 \tag{5.8}$$

where

$$\frac{\partial\mathbf{q}}{\partial t}=\mathbf{u}. \tag{5.9}$$

Eqs. (5.8) and (5.9) are the PML equations for rectangular computational domain as shown in Figure 5.1.

It is worthwhile to point out that the auxiliary variable **q** is needed only in the PML domains. This is because the spatial derivative $\partial \mathbf{q}/\partial x$ disappears for the PML equation when $\sigma_y = 0$ and similarly $\partial \mathbf{q}/\partial y$ disappears when $\sigma_x = 0$. Thus $\partial \mathbf{q}/\partial x$ is required only in a horizontal PML and $\partial \mathbf{q}/\partial y$ is required only a vertical PML. In short, there is no need to compute nor store **q** in the Euler computation domain.

Figure 5.1. A Cartesian computational domain governed by the linearized
Euler equations enclosed by PML's

B. Perfectly matching and stability consideration

Perfect matching between the solutions of the PML equations and the linearized Euler equations is one of the most important properties of a PML. It is, however, not obvious from the derivation that the governing PML equations actually possess this unusual characteristic. Here, it is intended to confirm perfect matching. For this purpose, consider the interface between the Euler computational domain and the vertical PML on the right side of Fig. 5.1. If will now be assumed that the computational domain is large compared to the size of the outgoing disturbances, so that the interface may be regarded as infinite in extent in the *y*-direction as shown in Fig. 5.2. For convenience, a Cartesian coordinate system centered at the interface will be used. In the Euler domain, the linearized Euler equation (5.1) when written out in full becomes,

$$\frac{\partial \rho}{\partial t} + M\frac{\partial \rho}{\partial x} + \frac{\partial u}{\partial x} + \frac{\partial v}{\partial y} = 0$$

$$\frac{\partial u}{\partial t} + M\frac{\partial u}{\partial x} + \frac{\partial p}{\partial x} = 0$$

$$\frac{\partial v}{\partial t} + M\frac{\partial v}{\partial x} + \frac{\partial p}{\partial y} = 0 \qquad (5.10)$$

$$\frac{\partial p}{\partial t} + M\frac{\partial p}{\partial x} + \frac{\partial u}{\partial x} + \frac{\partial v}{\partial y} = 0$$
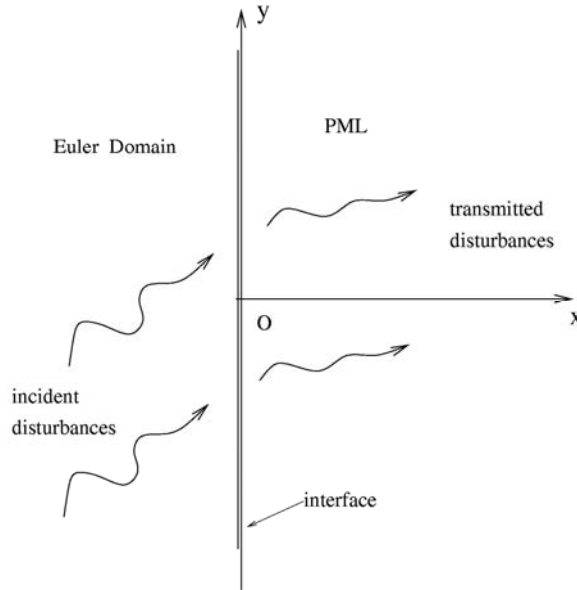
Figure 5.2. The interface region between the Euler computational domain and the PML on the right.

To allow the most general incident disturbances to impinge on the interface, one may choose to apply Fourier transform in y and Laplace transform in t to Eq. (5.10). This reduces Eq. (5.10) to a system of ordinary differential equations in x in the form (a ~ is used to indicate a Fourier-Laplace transformed variable),

$$-i\omega\tilde{\rho} + M\frac{d\tilde{\rho}}{dx} + \frac{d\tilde{u}}{dx} + i\beta\tilde{v} = 0$$

$$-i\omega\tilde{u} + M\frac{d\tilde{u}}{dx} + \frac{d\tilde{p}}{dx} = 0$$

$$-i\omega\tilde{v} + M\frac{d\tilde{v}}{dx} + i\beta\tilde{p} = 0 \qquad (5.11)$$

$$-i\omega\tilde{p} + M\frac{d\tilde{p}}{dx} + \frac{d\tilde{u}}{dx} + i\beta\tilde{v} = 0$$

In Eq. (5.11), β is the Fourier transform variable and ω is the Laplace transform variable. Eq. (5.11)) is a fourth-order differential system in x. Four linearly independent solutions can easily be found. They are given below.

55

(a) Entropy waves

$$\tilde{u} = \tilde{v} = \tilde{p} = 0, \qquad \tilde{\rho} = A(\beta,\omega)e^{i(\omega/M)x}. \tag{5.12}$$

The amplitude function $A(\beta,\omega)$ is arbitrary.

(b) Vorticity waves

$$\tilde{\rho} = \tilde{p} = 0, \qquad \tilde{u} = B(\beta,\omega)e^{i(\omega/M)x}, \qquad \tilde{v} = -\frac{\omega}{M\beta}B(\beta,\omega)e^{i(\omega/M)x}. \tag{5.13}$$

The amplitude function $B(\beta,\omega)$ is arbitrary.

(c) Acoustic waves

$$\begin{bmatrix} \tilde{\rho} \\ \tilde{u} \\ \tilde{v} \\ \tilde{p} \end{bmatrix} = C(\beta,\omega) \begin{vmatrix} (\omega - \lambda_+ M) \\ \lambda_+ \\ \beta \\ (\omega - \lambda_+ M) \end{vmatrix} e^{i\lambda_+ x}. \tag{5.14}$$

The amplitude function $C(\beta,\omega)$ is arbitrary and

$$\lambda_+ = \frac{-\omega M + \left[\omega^2 - \beta^2(1 - M^2)\right]^{\frac{1}{2}}}{1 - M^2}.$$

The branch cuts of the square root function in the ω-plane are shown in Fig. 5.3. Eq. (5.14) gives the acoustic waves that propagate or spread to the right. The left propagating acoustic wave solution is obtained by replacing the square root function by its negative value. It is to be noted that for acoustic waves that propagate to the far field, λ_+ must be real. This requires $\omega^2 > \beta^2 (1 - M^2)$. The components for which $\omega^2 < \beta^2 (1 - M^2)$ are nonpropagating acoustic near field. They decay exponentially with increasing x.
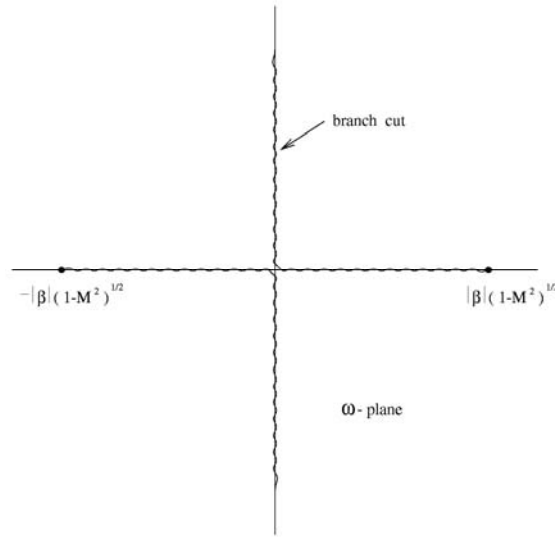
Figure 5.3. Branch cuts for the square root function $\left[\omega^2 - \beta^2(1 - M^2)\right]^{1/2}$ in the complex ω-plane.

The most general disturbances that exit the Euler domain on the right side to enter the PML are represented by a combination of entropy, vorticity and acoustic waves. It turns out the PML equation supports a similar set of wave solutions. The PML equation when written out in full are,

$$\frac{\partial \rho}{\partial t} + M\frac{\partial \rho}{\partial x} + \frac{\partial u}{\partial x} + \frac{\partial}{\partial y}(v + \sigma_x q_3) + \sigma_x \rho + \frac{\sigma_x M}{1 - M^2}(M\rho + u) = 0$$

$$\frac{\partial u}{\partial t} + M\frac{\partial u}{\partial x} + \frac{\partial p}{\partial x} + \sigma_x u + \frac{\sigma_x M}{1 - M^2}(Mu + p) = 0$$

$$\frac{\partial v}{\partial t} + M\frac{\partial v}{\partial x} + \frac{\partial p}{\partial y} + \sigma_x \frac{\partial q_4}{\partial y} + \sigma_x v + \frac{\sigma_x M^2}{1 - M^2}v = 0$$

$$\frac{\partial p}{\partial t} + M\frac{\partial p}{\partial x} + \frac{\partial u}{\partial x} + \frac{\partial v}{\partial y} + \sigma_x \frac{\partial q_3}{\partial y} + \sigma_x p + \frac{\sigma_x M}{1 - M^2}(u + Mp) = 0$$

$$\frac{\partial q_3}{\partial t} = v$$

$$\frac{\partial q_4}{\partial t} = p$$

(5.15)

The Fourier-Laplace transform of Eq. (5.15) in y and t is,

$$-i\omega\tilde{\rho} + M\frac{d\tilde{\rho}}{dx} + \frac{d\tilde{u}}{dx} + i\beta\tilde{v}\left(\tilde{v} - \sigma_x\frac{\tilde{v}}{i\omega}\right) + \frac{\sigma_x}{1-M^2}(\tilde{\rho} + M\tilde{u}) = 0$$

$$-i\omega\tilde{u} + M\frac{d\tilde{u}}{dx} + \frac{d\tilde{p}}{dx} + \frac{\sigma_x}{1-M^2}(\tilde{u} + M\tilde{p}) = 0$$

$$-i\omega\tilde{v} + M\frac{d\tilde{v}}{dx} + i\beta\tilde{p} - \sigma_x\frac{\beta}{\omega}\tilde{p} + \frac{\sigma_x}{1-M^2}\tilde{v} = 0 \qquad (5.16)$$

$$-i\omega\tilde{p} + M\frac{d\tilde{p}}{dx} + \frac{d\tilde{u}}{dx} + i\beta\tilde{v} - \sigma_x\frac{\beta}{\omega}\tilde{v} + \frac{\sigma_x}{1-M^2}(\tilde{p} + M\tilde{u}) = 0$$

It should be pointed out that at the interface $x = 0$, the y and t dependence of the transmitted waves must be the same as those of the incident waves. This requires that β and ω in Eq. (5.16) are the same as those in Eq. (5.11). Eq.(5.16) is a fourth-order differential system in x. The four linearly independent solutions can easily be verified to be as follows

(a) Entropy waves

$$\tilde{u} = \tilde{v} = \tilde{p} = 0, \qquad \tilde{\rho} = \overline{A}(\beta,\omega)e^{(i\omega - \frac{\sigma_x}{1-M^2})\frac{x}{M}} \qquad (5.17)$$

where $\overline{A}(\beta,\omega)$ is arbitrary. By comparing Eq. (5.12) and Eq. (5.17), it is clear by setting $\overline{A}(\beta,\omega) = A(\beta,\omega)$ the entropy wave solution in the PML will match perfectly the entropy wave solution of the Euler domain at the interface $x = 0$. There is no reflected wave. Also Eq. (5.17) indicates that any entropy waves transmitted into the PML will be damped spatially with a damping rate of $\sigma_x/[M(1 - M^2)]$ in the x-direction

(b) Vorticity waves

$$\tilde{\rho} = \tilde{p} = 0, \qquad \tilde{u} = \overline{B}(\beta,\omega)e^{(i\omega - \frac{\sigma_x}{1-M^2})\frac{x}{M}}, \qquad \tilde{v} = \frac{\omega}{M\beta}\overline{B}(\beta,\omega)e^{(i\omega - \frac{\sigma_x}{1-M^2})\frac{x}{M}} . \qquad (5.18)$$

By comparing Eq. (5.13) and Eq. (5.18), it is obvious that by setting $\overline{B}(\beta,\omega) = B(\beta,\omega)$ the vorticity waves in the Euler domain is completely transmitted into the PML without reflection at the interface $x = 0$. In the PML, the spatial damping rate for the vorticity waves is the same as that of the entropy waves.

(c) Acoustic waves

$$\begin{bmatrix} \tilde{\rho} \\ \tilde{u} \\ \tilde{v} \\ \tilde{p} \end{bmatrix} = \overline{C}(\beta,\omega)\begin{bmatrix} (\omega - \lambda_+ M) \\ \lambda_+ \\ \beta \\ (\omega - \lambda_+ M) \end{bmatrix}e^{i\lambda x} \qquad (5.19)$$

where $\overline{C}(\beta,\omega)$ is arbitrary and $\lambda = \lambda_+ + \dfrac{i\sigma_x}{\omega(1-M^2)}\left[\omega^2 - \beta^2(1-M^2)\right]^{\frac{1}{2}}$

By comparing Eq. (5.14) and Eq. (5.19), it is possible to conclude that there is perfect matching between the acoustic waves incident on the interface at $x = 0$ and the transmitted acoustic waves in the PML. Perfect matching is achieved by setting $\overline{C}(\beta,\omega) = C(\beta,\omega)$. This is true not only for propagating acoustic waves for which $\omega^2 > \beta^2(1-M^2)$. It is also true for non-propagating near field components with $\omega^2 < \beta^2(1-M^2)$. The spatial damping rate in the PML is equal to $\dfrac{i\sigma_x}{\omega(1-M^2)}\left[\omega^2 - \beta^2(1-M^2)\right]^{\frac{1}{2}}$ in the x-direction.
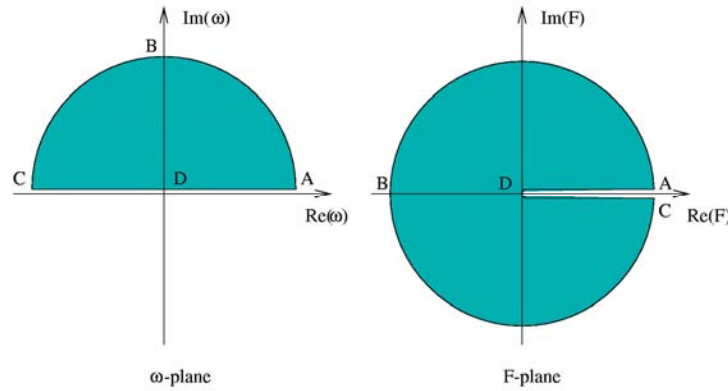
Figure 5.4. Mapping of the upper half ω-plane on to the F-plane

It was mentioned before that the first version of PML equations were unstable. Now, it is easy to show that PML equation (5.5) does not support unstable solution. To prove this assertion, one is required to show that there is no unstable acoustic wave solution in the PML. The simplest way to complete the proof is to take the Fourier transform of Eq. (5.16) in x. Eq. (5.16) is a homogeneous system. It is straightforward to find the condition for non-trivial solution is given by setting the determinant of the coefficient matrix to zero. This gives, after some algebraic simplifications,

$$F(\omega) = \frac{\beta^2}{1-M^2} \tag{5.20}$$

where

$$F(\omega) = \frac{\omega^2}{\left(1-M^2\right)^2} - \frac{\omega^2}{\left(\omega+i\sigma_x\right)^2}\left(\alpha + \frac{M\omega}{1-M^2}\right)^2. \tag{5.21}$$

In Eq. (5.21), α is the Fourier transform variable for x. Eq. (5.20) is the dispersion relation for the acoustic waves supported by the PML equations. To prove that there is no unstable acoustic wave solution, it is sufficient to show that Eq. (5.20) has no roots in the upper half ω-plane for arbitrary α and β. This can be done by mapping the upper half ω-plane into the complex F-plane. Fig. 5.4 gives the image in the F-plane. Notice that there is no value in the upper half ω-plane that makes F real and positive. Therefore, Eq. (5.20) cannot be satisfied as the right side of the equation is real and positive. Since both the entropy and vorticity waves are damped waves, therefore, PML equation (5.5) would only have damped wave solutions.

C. PML in three dimensions

In three dimensions, the linearized Euler equations may be written in a matrix form as

$$\frac{\partial \mathbf{u}}{\partial t} + \mathbf{A}\frac{\partial \mathbf{u}}{\partial x} + \mathbf{B}\frac{\partial \mathbf{u}}{\partial y} + \mathbf{C}\frac{\partial \mathbf{u}}{\partial z} = 0 \tag{5.22}$$

where

$$\mathbf{u} = \begin{vmatrix} \rho \\ u \\ v \\ w \\ p \end{vmatrix}, \quad \mathbf{A} = \begin{vmatrix} M & 1 & 0 & 0 & 0 \\ 0 & M & 0 & 0 & 1 \\ 0 & 0 & M & 0 & 0 \\ 0 & 0 & 0 & M & 0 \\ 0 & 1 & 0 & 0 & M \end{vmatrix}, \quad \mathbf{B} = \begin{vmatrix} 0 & 0 & 1 & 0 & 0 \\ 0 & 0 & 0 & 0 & 0 \\ 0 & 0 & 0 & 0 & 1 \\ 0 & 0 & 0 & 0 & 0 \\ 0 & 0 & 1 & 0 & 0 \end{vmatrix}, \quad \mathbf{C} = \begin{vmatrix} 0 & 0 & 0 & 1 & 0 \\ 0 & 0 & 0 & 0 & 0 \\ 0 & 0 & 0 & 0 & 0 \\ 0 & 0 & 0 & 0 & 1 \\ 0 & 0 & 0 & 1 & 0 \end{vmatrix}. \tag{5.23}$$

A straightforward application of the method of Section A yields the following PML equations.

$$\frac{\partial \mathbf{u}}{\partial t} + \mathbf{A}\frac{\partial \mathbf{u}_1}{\partial x} + \mathbf{B}\frac{\partial \mathbf{u}_2}{\partial y} + \mathbf{C}\frac{\partial \mathbf{u}_3}{\partial z} + \mathbf{u}_4 + \frac{\sigma_x M}{1-M^2}\mathbf{A}\mathbf{u}_1 = 0 \tag{5.24}$$

where

$$\begin{aligned} \mathbf{u}_1 &= \mathbf{u} + (\sigma_y + \sigma_z)\mathbf{q}_1 + \sigma_y\sigma_z\mathbf{q}_2 \\ \mathbf{u}_2 &= \mathbf{u} + (\sigma_z + \sigma_x)\mathbf{q}_1 + \sigma_z\sigma_x\mathbf{q}_2 \\ \mathbf{u}_3 &= \mathbf{u} + (\sigma_x + \sigma_y)\mathbf{q}_1 + \sigma_x\sigma_y\mathbf{q}_2 \\ \mathbf{u}_4 &= (\sigma_x + \sigma_y + \sigma_z)\mathbf{u} + (\sigma_y\sigma_z + \sigma_z\sigma_x + \sigma_x\sigma_y)\mathbf{q}_1 + \sigma_x\sigma_y\sigma_z\mathbf{q}_2 \end{aligned}$$

The auxiliary variables $\mathbf{q}_1$ and $\mathbf{q}_2$ are given by

$$\frac{\partial \mathbf{q}_1}{\partial t} = \mathbf{u}, \qquad \frac{\partial \mathbf{q}_2}{\partial t} = \mathbf{q}_1. \tag{5.25}$$

Notice that the absorption coefficients σ_x, σ_y and σ_z are arbitrary functions of x, y and z, respectively. Again as in the two-dimensional case, the auxiliary variables need to be computed only in the PML regions.

5.5 Incoming Disturbances

In many aeroacoustics problems, there are disturbances that enter the computational domain through the outer boundary. For example, in computing the scattering characteristics of an object, acoustic waves must be allowed to pass through the boundary of a computational domain in a specified direction and intensity. The scattering phenomenon produces scattered waves. These waves are radiated in all directions. They propagate to the far field as outgoing waves through the boundary of the computational domain. In this case, the boundary condition of the computational domain must take on the responsibility of generating the incoming sound. At the same time, they also serve as radiation boundary conditions for the scattered waves. To handle the dual role, a Split-Variable method has been developed. The essence of this method is discussed below.

The equations governing the propagation of small amplitude disturbances are the linearized Euler equations. Both the incoming disturbances and the outgoing scattered waves are solutions of these equations. However, in a scattering problem, incoming disturbances are known or specified, whereas the scattered outgoing waves are unknown. To illustrate the basic concept of the split-variable method, consider a two-dimensional problem with a uniform mean flow velocity u_0 in the x-direction. It will be assumed that the incoming sound waves enter the computational domain from the left boundary as shown in Fig. 5.5. The variables associated with the incoming waves are labeled by a subscript 'in' and variables associated with the outgoing scattered waves are labeled by a subscript 'out'. In the left boundary region of the computational domain, the total variables are the direct sum of the incoming and outgoing disturbances; i.e.,

$$
\begin{bmatrix} \rho \\ u \\ v \\ p \end{bmatrix} = \begin{bmatrix} \rho_{in} \\ u_{in} \\ v_{in} \\ p_{in} \end{bmatrix} + \begin{bmatrix} \rho_{out} \\ u_{out} \\ v_{out} \\ p_{out} \end{bmatrix}
\tag{5.26}
$$

In Eq. (5.26) the variables associated with the incoming disturbances are known. They are prescribed by the physical problem. The aim is to compute the outgoing scattered waves. In the boundary region (see Fig. 5.5), the outgoing acoustic waves are governed by the radiation boundary condition. That is,

$$
\left[\frac{1}{V(\theta)} \frac{\partial}{\partial t} + \cos\theta \frac{\partial}{\partial x} + \sin\theta \frac{\partial}{\partial y} + \frac{1}{2\left(x^2 + y^2\right)^{\frac{1}{2}}} \right] \begin{bmatrix} \rho_{out} \\ u_{out} \\ v_{out} \\ p_{out} \end{bmatrix} = 0 + 0\left(r^{-\frac{5}{2}}\right)
\tag{5.27}
$$

where $V(\theta) = [u_0 \cos\theta + (a_0^2 - u_0^2 \sin^2\theta)^{1/2}]$ and a_0 is the speed of sound.
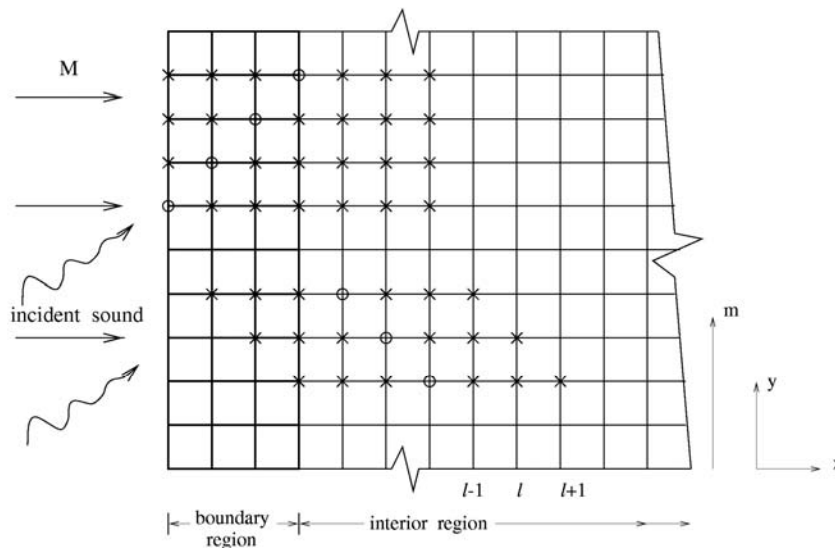
Figure 5.5. Computational mesh showing the boundary and the interior regions and the 7-point stencils for the DRP scheme. Incident sound waves enter the computational domain on the left.

In the interior region, the small amplitude disturbances are governed by the linearized Euler equations. They are

$$\frac{\partial \mathbf{U}}{\partial t} + \frac{\partial \mathbf{E}}{\partial x} + \frac{\partial \mathbf{F}}{\partial y} = 0$$

(5.28)

$$\text{where} \quad \mathbf{U} = \begin{bmatrix} \rho \\ u \\ v \\ p \end{bmatrix}, \quad \mathbf{E} = \begin{bmatrix} \rho_0 u + \rho u_0 \\ u_0 u + p/\rho_0 \\ u_0 v \\ u_0 p + \gamma p_0 u \end{bmatrix}, \quad \mathbf{F} = \begin{bmatrix} \rho_0 v \\ 0 \\ p/\rho_0 \\ \gamma p_0 v \end{bmatrix}$$

It is to be noted that the distinction between incoming and outgoing waves is lost once the point of interest is not in the boundary region of the computational mesh.

To compute the numerical solution, Eq. (5.28) is discretized by the 7-point stencil DRP scheme. These discretized equations are used to determine the full physical variables (ρ,u,v,p) in the interior region. At the same time Eq. (5.27) is discretized again by the 7-point stencil DRP scheme. These discretized equations are used to calculate the outgoing waves $(\rho_{out},u_{out},v_{out},p_{out})$. They are applied only in the boundary region. But before the computation can be implemented, one must recognize that once the 7-point stencil DRP scheme is applied to Eq. (5.27), the finite difference stencil in the x-direction would extend outside the boundary region into the interior region as shown in Fig. 5.5. In the interior region, only the full variables (ρ,u,v,p) are computed. But $(\rho_{out},u_{out},v_{out},p_{out})$ are needed at the extended stencil points to support the computation. To find these quantities, one may use Eq. (5.26). Since the incoming disturbances are known, the outgoing wave variables can be found by subtracting the incoming disturbance variables from the full variables at mesh points near the outer boundary of the interior region.

Now in computing the full variables (ρ,u,v,p) in the interior region, one would encounter a similar problem. For mesh points in the three columns closest to the boundary region, the 7-point stencil will extend into the boundary region where only the outgoing disturbances are computed. To find the values of the full variables in the boundary region, one may again use Eq. (5.26) by adding the known incoming disturbances to the computed outgoing waves. In this way, the variables in the entire computational domain can be marched forward in time. It is straightforward to see that the split variable method essentially converts the boundary region into a source of the incoming disturbances. At the same time it acts as radiation boundary condition for the outgoing scattered waves.

5.6. Nonlinearized Outflow Boundary Conditions

In many CAA simulations, the boundary of the computation domain cuts across an outflow. An example is the case of simulating jet noise generation. Since numerical boundary conditions

imposed at the outflow boundary must reproduce all the external effects on the flow field inside the computational domain, the outflow boundary is usually placed sufficiently far downstream of the nozzle exit to avoid significant upstream influence of the jet flow left outside. In the jet noise simulation problem, as in many other problems, the mean flow is not known *a priori*. The numerical boundary conditions are required to capture the mean flow as well as being transparent to the outgoing acoustic, vorticity and entropy waves.

Presently, many CAA boundary conditions are formulated under the assumption that the mean flow is known. Their main concern is to avoid any reflection of the outgoing unsteady disturbances. Dong (1997) recognized the need for CAA outflow boundary conditions to be capable of capturing the mean flow correctly as well. He proposed a set of asymptotic outflow boundary conditions based on sink/source flows. In two dimensions, they are,

$$
\frac{1}{a_\infty}\frac{\partial \rho}{\partial t}+\frac{\partial \rho}{\partial r}+\frac{2}{r}(\rho-\rho_\infty)=0
$$

$$
\frac{1}{a_\infty}\frac{\partial u}{\partial t}+\frac{\partial u}{\partial r}+\frac{u}{r}=0
$$

$$
\frac{1}{a_\infty}\frac{\partial v}{\partial t}+\frac{\partial v}{\partial r}+\frac{v}{r}=0 \tag{5.29}
$$

$$
\frac{1}{a_\infty}\frac{\partial p}{\partial t}+\frac{\partial p}{\partial r}+\frac{2}{r}(p-p_\infty)=0
$$

where r is the radial distance in polar coordinates. p_∞, ρ_∞ and a_∞ are the ambient pressure, density and sound speed, respectively. Dong derived this set of outflow boundary conditions by noting that the asymptotic solution of a time independent localized source in two dimensions, denoted by an overbar, is

$$
\overline{\rho}=\rho_\infty-\frac{Q^2}{8\pi^2\gamma p_\infty r^2}+O\!\left(\frac{1}{r^4}\right)
$$

$$
\overline{v}_r=\frac{Q}{2\pi^2\rho_\infty r}+O\!\left(\frac{1}{r^3}\right) \tag{5.30}
$$

$$
\overline{p}=p_\infty-\frac{Q^2}{8\pi^2\rho_\infty r^2}+O\!\left(\frac{1}{r^4}\right)
$$

where Q is the source strength, γ is the ratio of specific heats and v_r is the radical velocity component. It is easy to verify that Eq. (5.30) is a solution of Eq. (5.29) to order $O(r^{-4})$. On the other hand, the asymptotic solution of outgoing acoustic waves in two dimensions without mean flow is,

$$
\begin{bmatrix} \rho \\ u \\ v \\ p \end{bmatrix} = \frac{F\left(\frac{r}{a_\infty} - t, \theta\right)}{r^{\frac{1}{2}}} \begin{bmatrix} \dfrac{1}{a_\infty^2} \\ \dfrac{\hat{u}(\theta)}{\rho_\infty a_\infty} \\ \dfrac{\hat{v}(\theta)}{\rho_\infty a_\infty} \\ 1 \end{bmatrix} + O\left(r^{\frac{3}{2}}\right). \tag{5.31}
$$

By substitution of Eq. (5.31) into Eq. (5.29), it is easy to find that Eq. (5.29) is satisfied to order $O(r^{-3/2})$. It has been pointed out that (9.6) is very similar to the asymptotic boundary conditions discussed previously. The major difference is in the numerical coefficients of the $1/r$ terms. It is straightforward to see that the asymptotic solution of the mean flow of a localized source and that of the outgoing acoustic waves have different dependence on r. Eq. (5.29) as an outflow boundary condition is a reasonable compromise.

Outflow boundary condition Eq. (5.29) may be generalized to three dimensions. The corresponding equations in spherical polar coordinates (R,θ,ϕ) are,

$$
\begin{aligned}
\frac{1}{a_\infty}\frac{\partial \rho}{\partial t} + \frac{\partial \rho}{\partial R} + \frac{3(\rho - \rho_\infty)}{R} &= 0 \\
\frac{1}{a_\infty}\frac{\partial u}{\partial t} + \frac{\partial u}{\partial R} + \frac{2u}{R} &= 0 \\
\frac{1}{a_\infty}\frac{\partial v}{\partial t} + \frac{\partial v}{\partial R} + \frac{2v}{R} &= 0 \\
\frac{1}{a_\infty}\frac{\partial w}{\partial t} + \frac{\partial w}{\partial R} + \frac{2w}{R} &= 0 \\
\frac{1}{a_\infty}\frac{\partial p}{\partial t} + \frac{\partial p}{\partial R} + \frac{3(p - p_\infty)}{R} &= 0
\end{aligned}
\tag{5.32}
$$

Jet flows are not source flows. Boundary layer arguments as well as experimental measurements suggest that the static pressure across a jet far downstream is practically constant and is equal to the ambient pressure. In this case, $\bar{p} = p_\infty$ is a good mean flow pressure boundary condition. This is the steady state solution of the jet outflow boundary condition. Now if the outflow boundary conditions of section 5 are nonlinearized; i.e., replacing the linear convection term $u_0(\partial u/\partial x)$ by the full convection terms etc., it is easy to arrive at the following set of nonlinear outflow boundary conditions. Written in cylindrical coordinates (r,ϕ,x), they are

$$
\frac{\partial \rho}{\partial t} + u\frac{\partial \rho}{\partial x} + v\frac{\partial \rho}{\partial r} + \frac{w}{r}\frac{\partial \rho}{\partial \phi} = \frac{1}{a^2}\left(\frac{\partial p}{\partial t} + u\frac{\partial p}{\partial x} + v\frac{\partial p}{\partial r} + \frac{w}{r}\frac{\partial p}{\partial \phi}\right) \tag{5.33}
$$

$$
\frac{\partial u}{\partial t} + u\frac{\partial u}{\partial x} + v\frac{\partial u}{\partial r} + \frac{w}{r}\frac{\partial u}{\partial \phi} = -\frac{1}{\rho}\frac{\partial p}{\partial x} \tag{5.34}
$$

$$\frac{\partial v}{\partial t} + u \frac{\partial v}{\partial x} + v \frac{\partial v}{\partial r} + \frac{w}{r} \frac{\partial v}{\partial \phi} - \frac{w^2}{r} = -\frac{1}{\rho} \frac{\partial p}{\partial x} \tag{5.35}$$

$$\frac{\partial w}{\partial t} + u \frac{\partial w}{\partial x} + v \frac{\partial w}{\partial r} + \frac{w}{r} \frac{\partial w}{\partial \phi} + \frac{vw}{r} = -\frac{1}{\rho} \frac{1}{r} \frac{\partial w}{\partial \phi} \tag{5.36}$$

$$\frac{1}{V(\theta)} \frac{\partial p}{\partial t} + \frac{\partial p}{\partial R} + \frac{p - p_\infty}{R} = 0 \tag{5.37}$$

where $V(\theta) = u \cos \theta + a(1 - \sin^2 \theta)^{1/2}$ and $M = u/a$. $a = (\gamma p/\rho)^{1/2}$ is the speed of sound. (R, θ, ϕ) are the spherical polar coordinates with the polar axis coinciding with the centerline of the jet. For the mean flow, $p = p_\infty$ is a solution for Eq. (5.37). Eqs. (5.34) to (5.36) are identical to the momentum equations of the Euler equations. They should yield the correct velocity field. For time independent solution, Eq. (5.33) reduces to

$$u \frac{\partial \rho}{\partial x} + v \frac{\partial \rho}{\partial r} + \frac{w}{r} \frac{\partial \rho}{\partial \phi} = 0. \tag{5.38}$$

Eq. (5.38) is the same as $\rho =$ constant along a streamline. This should be reasonably good for jet flow far downstream where there is no intense mixing. Thus, outflow boundary conditions Eqs. (5.33) to (5.37), although originally designed for outgoing disturbances alone, are also capable of capturing the mean flow of a jet.

Now outflow boundary conditions (5.32) and boundary conditions Eq. (5.33) to (5.38) are very different. Each is designed specifically for a class of outflows. If the mean flow is source-like, then use Eq. (5.32)). On the other hand, if the mean flow is jet-like, then Eq. (5.33) to (5.38) would be more appropriate.

5.7 Testing of Boundary Conditions

There are many tests of boundary condition performance in the literature, but only a representative few will be mentioned here. Scott et. al. (1993) investigated the effect of the outflow boundary on the computed results for a nonlinear Navier-Stokes calculation of a supersonic jet with small perturbations introduced at the inflow boundary. By comparing the growth rate of the disturbances in the jet shear layer, the effect of the outflow boundary condition can be assessed. In this work, two characteristic-type boundary conditions were considered as well as an asymptotic radiation boundary condition. All boundary conditions performed adequately in this test case, though there were outflow reflections visible in some of the figures.

In Hixon et. al. (1995), the relatively simple problem of a point monopole in a uniform mean flow was calculated using the linearized Euler equations. For this linear test with acoustic waves impinging on the boundary at all angles of incidence, this work found the Tam and Webb radiation boundary conditions performed well, while the Thompson 1-D characteristic boundary condition gave an unacceptably high level of error.

In a continuation of Scott, et. al.'s (1993) work on jet outflow boundary conditions, Hayder and Turkel (1995) tested boundary conditions for a nonlinear jet flow calculation. In this later test, a wider range of boundary conditions were considered: Scott-Hankey (1985), Thompson (1987, 1990), Giles (1990), Bayliss-Turkel (1982b), Hagstrom-Hariharan (1988), Roe (1989), and the Tam-Webb (1993) outflow condition; they found that the Tam-Webb and Giles boundary conditions worked equally well for this case.

Goodrich and Hagstrom (1997) tested their nonlocal-to-local boundary condition against a Perfectly Matched Layer (PML) condition on an acoustic transient problem to find that the nonlocal-to-local condition worked better; Hagstrom and Goodrich (1998) used this test case to perform a strict test of the time-accuracy of the nonlocal-to-local boundary condition.

In later work, Hixon et. al. (2000) tested Thompson (1987, 1990), Giles (1990), Hagstrom (1996), and PML boundary conditions for the benchmark problem of a vortical gust impinging on a flat-plate cascade. For this test, the results ranged from code instability (Thompson), to fairly accurate solutions (Giles and PML).

6. INTERIOR AND DUCTED DOMAIN PROBLEMS

Interior boundaries are inevitable features of practical aeroacoustic problems. Most interior boundaries are solid surfaces or impedance surfaces. Occasionally, there are problems with fluid interfaces. Because CAA problems are unsteady and may involve high frequency components, unlike CFD, a somewhat different treatment of interior boundaries is required. The development of appropriate numerical treatment of these boundaries forms a core effort in CAA.

6.1 Solid Surfaces

The ghost point method of Tam and Dong (1994) was one of the first method developed specifically for enforcing wall boundary conditions when a high order (large stencil) computational algorithm is used. The method is effective and widely used. Other methods have since been proposed by a number of investigators. For instance, Chung and Morris (1995) advocated an "impedance mismatch" method while Lockard and Morris (1998) experimented with the Thompson-type 1-D characteristic method. These methods, however, yielded mostly low quality results. Other investigators, e.g. Dadone and Grossman (1994), Dong *et al* (1997), Dadone (1998), Hixon (1999) , Dyson and Hixon (2002) for structured grids and, Balakrishnan and Fernandez (1998), Atkins and Lockard (1999) and Wang and Sun (2002) on unstructured grids, proposed a variety of methods for enforcing wall boundary conditions. So far these methods have not gained general acceptance.

On a solid surface, if the flow is viscous, the no-slip boundary conditions require,
$$\mathbf{v} = \mathbf{0} \qquad \text{on the wall}$$

where **v** is the fluid velocity. If viscous effects are unimportant or the fluid is inviscid, then, only the no-through flow boundary condition

$$\mathbf{v} \cdot \mathbf{n} = 0$$

is needed, where **n** is the unit vector normal to the surface. In the ghost point method, the computational domain is allowed to extend beyond the wall by one row of ghost points. For the no-slip boundary condition, two (three) ghost values are introduced at the ghost points if the problem is two (three) dimensional. They are the ghost values of pressure and shear stresses. These ghost values are chosen so that **v** = 0 on the wall. In the case of inviscid fluid, only the ghost value of pressure is needed. In this case, the ghost pressure is chosen to ensure the pressure gradient normal to wall surface is zero. This is equivalent to the no-through flow boundary condition. Physically, the ghost pressure and shear stresses simulate the effects of the forces exerted by a wall on the fluid. The ghost pressure prevents the fluid from flowing through the wall. The ghost shear stresses prevent the fluid from sliding past the wall surface.

For curved walls, implementation of the ghost point method depends strongly on the mesh used for computation. If a Cartesian mesh is used, then the wall surface may be approximated by linear segments between the intersections of the mesh and the wall boundary. The ghost points will not be regularly spaced. The boundary enforcement points are not on the grid points. A relatively involved procedure is needed to set up the numerical boundary treatment. Details can be found in Kurbatskii and Tam (1997). On the other hand, if a body fitted grid is used in the region adjacent to the curved wall, then the ghost point method can easily be carried out in the computation plane or volume. It is only necessary to rewrite the momentum equation with the velocity components normal and tangential to the wall as unknown. The wall boundary conditions can be enforced in nearly the same manner as the case of a flat wall aligning on a grid line in Cartesian coordinate.

6.2 Fluid Interface

When fluid layers of different densities are separated by a thin transition layer, the transition layer is often modeled by a surface of discontinuity or a fluid interface. Similarly, when a shear layer separating two fluid layers moving relative to each other is thin, it is sometimes advantageous to model it as a vortex sheet. This approximation is definitely valid when the length scale of the motion of the vortex sheet is much larger than the thickness of the shear layer. Modeling a thin shear layer by a vortex sheet avoids the need to introduce a very fine mesh in a computation.

The motion of a fluid interface or vortex sheet is governed by well established kinematic and dynamic boundary conditions. For acoustic problems, the amplitude of interface displacement is usually very small. Thus the use of linearized kinematic and dynamic boundary conditions, imposed on the undisturbed location of the interface, will suffice.

How to enforce interface boundary conditions computationally is not well established. Recently, a sound transmission problem across an interface separating two fluid layers of

different densities was included as a benchmark problem in the 4th CAA Workshop on Benchmark Problems. The problem was solved computationally by Tam and Ju (2004) using the ghost point method. In this case, the pressure and the velocity component normal to the interface are continuous, but their derivatives in the normal direction are discontinuous. For fluid interface problems, the number of ghost values is equal to the number of interface boundary conditions. The selection of ghost variables (whether pressure or velocity component) is not unique. Tam and Ju, however, was able to demonstrated numerically that as long as they are chosen appropriately the same results are obtained.

6.3. Axis Boundary Conditions

There are many aeroacoustics problems for which the use of a cylindrical coordinate system is the most natural choice for computing its solution. A simple example is the case of computing the noise from a circular jet. Another example is the numerical calculation of the propagation of acoustic waves inside a circular duct. The governing equations are the Navier-Stokes equations. When written in cylindrical coordinates, some terms of these equations with $1/r$ coefficient apparently could blow up. In other words, there is an apparent singularity (although not a true one) at the axis ($r = 0$) of the coordinate system. In this section, a way to treat such apparent singularity is discussed.

6.3.1. Linear problem involving a single azimuthal Fourier component

Acoustic problems are often linear. If the problem is linear and involves only a single azimuthal Fourier component, say the nth mode, then usually it is advantageous to separate out the azimuthal dependence by assuming that all variables have the dependence of $e^{in\phi}$. On factoring out $e^{in\phi}$, the reduced set of equations effectively becomes two-dimensional. Let the mean flow be axisymmetric. Near the x-axis, the mean flow may be assumed to be locally uniform; i.e., $u = \bar{u}$, $\bar{v} = \bar{w} = 0$, $\rho = \bar{\rho}$, $p = \bar{p}$ and $T = \bar{T}$. The linearized equations of motion are

$$\frac{\partial \rho}{\partial t} + \bar{u}\frac{\partial \rho}{\partial x} + \bar{\rho}\overline{\nabla} \cdot \mathbf{v} = 0 \tag{6.1}$$

$$\frac{\partial \mathbf{v}}{\partial t} + \bar{u}\frac{\partial \mathbf{v}}{\partial x} = -\frac{1}{\rho}\nabla p + \nu_t \nabla^2 \mathbf{v} \tag{6.2}$$

$$\bar{\rho}c_v\left(\frac{\partial T}{\partial t} + \bar{u}\frac{\partial T}{\partial x}\right) + \bar{p}\nabla \cdot \mathbf{v} = k_t \nabla^2 T \tag{6.3}$$

$$p = \bar{\rho}RT + \rho R\bar{T} \tag{6.4}$$

where ν_t and k_t are the turbulent kinematic viscosity and thermal conductivity, if the flow is turbulent; otherwise the molecular values should be used.

It can easily be shown that when Eqs. (6.1) to (6.4) are written in cylindrical coordinates (r,ϕ,x), it is an eighth-order differential system in r. Four of the solutions are bounded at $r = 0$. The other four are unbounded. Here, interest is confined to the bounded solutions alone.

In general, the velocity vector may be represented by a scalar potential Φ and vector potential, $\mathbf{A}$, that is,

$$\mathbf{v} = \nabla\Phi + \nabla \times \mathbf{A}. \tag{6.5}$$

For Eqs. (6.1) to (6.4), the solutions for the scalar and vector potentials can be obtained separately. It turns out the viscous solutions are related only to the vector potential. For convenience, the vector potential solutions will be referred to as viscous solutions.

Substitution of Eq. (6.5) into Eqs. (6.1) to (6.4), it is easy to find the governing equations for the scalar and vector potentials are,

$$\frac{\partial \rho}{\partial t} + \bar{u}\frac{\partial \rho}{\partial x} + \bar{\rho}\nabla^2\Phi = 0 \tag{6.6}$$

$$\frac{\partial \Phi}{\partial t} + \bar{u}\frac{\partial \Phi}{\partial x} = -\frac{1}{\rho}p + \nu_t\nabla^2\Phi \tag{6.7}$$

$$\bar{\rho}c_v\left(\frac{\partial T}{\partial t} + \bar{u}\frac{\partial T}{\partial x}\right) + \bar{p}\nabla^2\Phi = k_t\nabla^2 T \tag{6.8}$$

$$p = \bar{\rho}RT + \rho R\bar{T} \tag{6.9}$$

and

$$\left(\frac{\partial \mathbf{A}}{\partial t} + \bar{u}\frac{\partial \mathbf{A}}{\partial x}\right) = \nu_t\nabla^2\mathbf{A}. \tag{6.10}$$

The viscous solutions are given by $\rho = p = T = 0$, $\mathbf{v} = \nabla \times \mathbf{A}$.

A. Scalar potential solutions

General solutions of the scalar potential, Φ, may be found by applying Fourier-Laplace transforms to x and t and expanding Φ dependence in a Fourier series, that is,

$$\Phi(r,\phi,x,t) = \sum_{n=-\infty}^{\infty} \int_{-\infty}^{\infty}\int_{\Gamma} \tilde{\Phi}_n(r,k,\omega)\, e^{i(kx-\omega t+n\phi)}\, d\omega\, dk. \tag{6.11}$$

This reduces Eqs. (6.6) to (6.10) to a fourth-order differential system in r. The two solutions bounded at $r = 0$ may be expressed in terms of Bessel functions of order n. The complete solutions when written out in full are as follows:

$$\tilde{u}_n = ikJ_n(\lambda_{\pm}r), \qquad \tilde{v}_n = \frac{d}{dr}J_n(\lambda_{\pm}r)$$

$$\tilde{w}_n = \frac{in}{r}J_n(\lambda \pm r), \qquad \tilde{\rho}_n = \frac{i\bar{\rho}(\lambda_{\pm}^2 + k^2)}{(\omega - \tilde{u}k)}J_n(\lambda_{\pm}r)$$

(6.12)

$$\tilde{p}_n = \bar{p}\left[i(\omega - \bar{u}k) - v_t(\lambda_{\pm}^2 + k^2)\right]J_n(\lambda_{\pm}r)$$

$$\tilde{T}_n = \left[\frac{i(\omega - \bar{u}k)}{R} - (\lambda_{\pm}^2 + k^2)\left(\frac{i\tilde{T}}{\omega - \bar{u}k} + \frac{v_t}{R}\right)\right]J_n(\lambda_{\pm}r)$$

where

$$\lambda_{\pm} = \left[\frac{\alpha \pm (\alpha^2 + 4\beta)^{1/2}}{2} - k^2\right]^{\frac{1}{2}}$$

$$\alpha = \frac{(ik_t(\omega - \bar{u}k)/R - \bar{p} - c_v\bar{\rho}\bar{T} + ic_v\bar{\rho}v_t[(\omega - \bar{u}k)/R]}{k_t\left[(v_t/R) + i\bar{T}/(\omega - \bar{u}k)\right]}.$$

$$\beta = \frac{-\bar{\rho}c_v(\omega - \bar{u}k)^2}{Rk_t\left[(v_t/R) + i\bar{T}/(\omega - \bar{u}k)\right]}$$

B. Viscous solutions

There are two sets of viscous solutions. The first set is found by letting

$$\mathbf{A} = \psi\,\mathbf{e_x}, \qquad p = \rho = T = 0 \qquad (6.13)$$

where $\mathbf{e_x}$ is the unit vector in the *x*-direction. Again by the use of Fourier-Laplace transforms and Fourier expansion, the solution that is bounded at $r = 0$ is,

$$\tilde{p}_n = \hat{\rho}_n = \tilde{T}_n = \tilde{u}_n = 0$$

$$\tilde{v}_n = \frac{in}{r}J_n\left\{i\left[k^2 - \frac{i(\omega - \bar{u}k)}{v_t}\right]^{\frac{1}{2}}r\right\}$$

(6.14)

$$\tilde{w}_n = \frac{d}{dr}J_n\left\{i\left[k^2 - \frac{i(\omega - \bar{u}k)}{v_t}\right]^{\frac{1}{2}}r\right\}$$

The second set may be found by letting,

$$\mathbf{A} = \chi\,\mathbf{e_r} - i\chi\,\mathbf{e_\phi}, \qquad p = \rho = T = 0. \tag{6.15}$$

On following the steps before, the bounded solution, after some algebra, is found to be

$$\tilde{p}_n = \tilde{\rho}_n = \tilde{T}_n = 0$$

$$\tilde{u}_n = -i\left(\frac{d}{dr}J_{n+1}\left\{i\left[k^2 - \frac{i(\omega - \bar{u}k)}{v_t}\right]^{\frac{1}{2}}r\right\} + \frac{n+1}{r}J_{n+1}\left\{i\left[k^2 - \frac{i(\omega - \bar{u}k)}{v_t}\right]^{\frac{1}{2}}r\right\}\right)$$

$$\tilde{v}_n = -kJ_{n+1}\left\{i\left[k^2 - \frac{i(\omega - \bar{u}k)}{v_t}\right]^{\frac{1}{2}}r\right\}$$

$$\tilde{w}_n = ikJ_{n+1}\left\{i\left[k^2 - \frac{i(\omega - \bar{u}k)}{v_t}\right]^{\frac{1}{2}}r\right\}$$

(6.16)

C. Analytic continuation into the r < 0 region

The general solution is a linear combination of the scalar and vector potential solutions. The Bessel functions of these solutions can be continued analytically into the nonphysical region $r < 0$. For positive r, the analytic continuation formula for integer-order Bessel function is

$$J_n(-\xi r) = (-1)^n J_n(\xi r). \tag{6.17}$$

By means Eq. (6.17) and the preceding general solutions, it is straightforward to establish,

$$\rho_n(-r,x,t) = (-1)^n \rho_n(r,x,t)$$

$$p_n(-r,x,t) = (-1)^n p_n(r,x,t)$$

$$T_n(-r,x,t) = (-1)^n T_n(r,x,t)$$

(6.18)

$$u_n(-r,x,t) = (-1)^n u_n(r,x,t)$$

$$v_n(-r,x,t) = (-1)^{n+1} v_n(r,x,t)$$

$$w_n(-r,x,t) = (-1)^{n+1} w_n(r,x,t)$$

where ρ_n, p_n, etc. are the amplitude functions of the Fourier series expansions in ϕ.

Now Eq. (6.18) may be used to extend the solution into the nonphysical negative r region to facilitate the computation of high-order large stencil finite difference in r for points adjacent to the jet axis. That is, when a finite difference stencil extends into the negative r region, the values of the variables are found by Eq, (6.18). It is noted, however, that for $n = 1$,

$$\lim_{r \to 0} v_1(r,x,t) \neq 0, \qquad \lim_{r \to 0} w_1(r,x,t) \neq 0$$

in general. For this reason, terms such as v_1/r and w_1/r cannot be computed at the jet axis $r = 0$. It is recommended that the values of v and w and all the other variables not be computed directly by finite difference marching scheme at $r = 0$. Instead, the numerical solution at a new time level for all the other mesh points is first computed. The values of all the variables on mesh points in the region $r < 0$ are then calculated by analytical continuation. This leaves the values at $r = 0$ still to be determined. Here it is suggested that they are to be found by high-order symmetric interpolation. Once the values of all physical variables at the axis $r = 0$ are found, the computation at the new time level is completed.

6.3.2. The General Case

In using cylindrical coordinates for two or three-dimensional computation, there are two basic problems in computing the solution at and near $r = 0$. The first problem is how to approximate $\partial/\partial r$ by a finite difference quotient at mesh points close to $r = 0$. The second problem is how to calculate the solution ar $r = 0$ where there is an apparent singularity. This section addresses these two issues in the general situation.
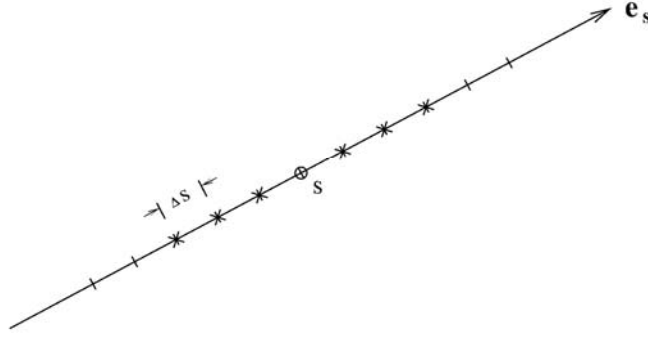
Figure 6.1. Approximating directional derivative in the $\mathbf{e_s}$ direction at s by a 7-point stencil finite difference quotient.

A. *Directional derivative*

Let $\mathbf{e_s}$ be a unit vector in the *s*-direction as shown in Fig. 6.1. To approximate $\partial/\partial s$, one may use a 7-point finite difference quotient on a line in the $\mathbf{e_s}$ direction as shown; i.e.,

$$\left(\frac{\partial \Phi}{\partial s}\right)_0 = \frac{1}{\Delta s} \sum_{j=-3}^{3} a_j \Phi_j. \tag{6.19}$$

Here, $\partial \Phi/\partial s = \mathbf{e_s} \bullet \nabla \Phi$ is the directional derivative of Φ in the $\mathbf{e_s}$ direction.

B. $\partial/\partial r$ as a directional derivative

The *r*-derivative of a variable Φ at $\theta = \theta_1$ and $r = \Delta r$ (see Figure 9.6) may be regarded as a directional derivative. That is,

$$\left.\frac{\partial \Phi}{\partial r}\right|_{\theta=\theta_1, r=\Delta r} = \mathbf{e_r}|_{\theta=\theta_1} \cdot \nabla \Phi|_{r=\Delta r}. \tag{6.20}$$

A finite difference approximation to the directional derivative of Eq. (6.20) may be formed in the same way as Eq. (6.19). Thus,

$$\left.\frac{\partial \Phi}{\partial r}\right|_{\theta=\theta_1, r=\Delta r} = \frac{1}{\Delta r} \sum_{j=-3}^{3} a_j \Phi\big((j+1)\Delta r, \theta_1\big). \tag{6.21}$$

In this way, except for $r = 0$, there is no problem in computing the solution to the discretized Navier-Stokes equations on a cylindrical coordinate mesh.
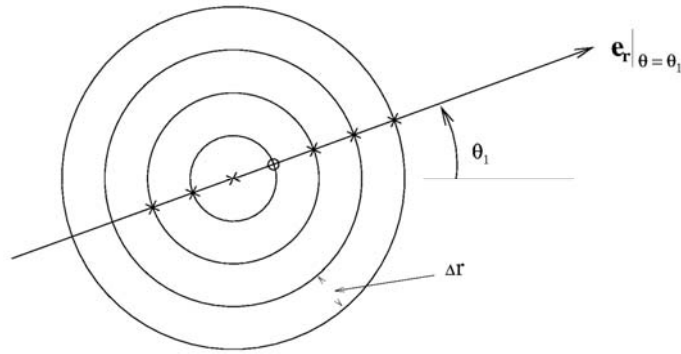
Figure 6.2. Approximating the r-derivative at $\theta = \theta_1$, r = Δr as directional derivative by a
7-point stencil finite difference quotient.

C. Variables at $r = 0$

Because the Navier-Stokes equations in cylindrical coordinates have apparent singularities at $r = 0$, the values of the flow variables cannot be advanced in time by means of the discretized form of the equations there. To find the solution at $r = 0$, a simple way is to compute first the solution at all other mesh points in the computational domain. After this is done, the values of the flow variables at r = 0 may be found by using high-order multi-dimensional optimized interpolation based on the values of all the mesh points on the first three rings of the cylindrical mesh. For this purpose, the multi-dimensional optimized interpolation method of section 7 would be very useful.

6.4 Perfectly Matched Layer for Ducted Domain
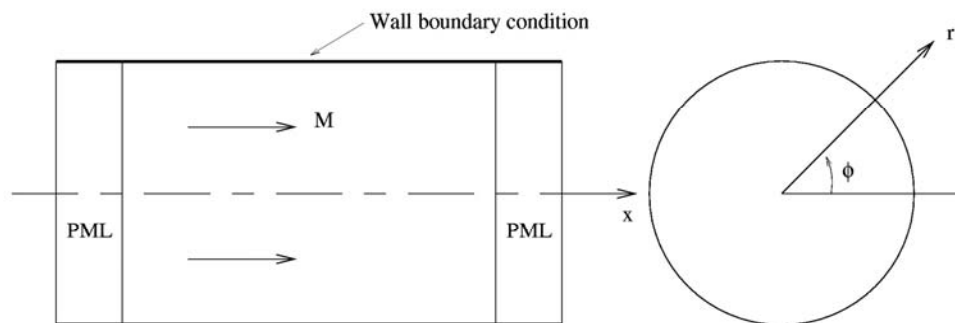
Figure 6.3. PML for circular ducted computational domain.

PML absorbing boundary conditions is especially useful in a ducted environment. It is very effective for simulating a long duct termination. Fig. 6.3 shows a computational domain inside a circular duct with rigid walls. In cylindrical coordinates, (x,r,ϕ), the linearized Euler equations may be written as,

$$\frac{\partial \mathbf{u}}{\partial t} + \mathbf{A}\frac{\partial \mathbf{u}}{\partial x} + \mathbf{B}\frac{\partial \mathbf{u}}{\partial r} + \mathbf{C}\frac{1}{r}\frac{\partial \mathbf{u}}{\partial \phi} + \frac{1}{r}\mathbf{D}\mathbf{u} = 0 \tag{6.22}$$

where

$$\mathbf{u} = \begin{vmatrix} \rho \\ u \\ v \\ w \\ p \end{vmatrix}, \quad \mathbf{A} = \begin{vmatrix} M & 1 & 0 & 0 & 0 \\ 0 & M & 0 & 0 & 1 \\ 0 & 0 & M & 0 & 0 \\ 0 & 0 & 0 & M & 0 \\ 0 & 1 & 0 & 0 & M \end{vmatrix}, \quad \mathbf{B} = \begin{vmatrix} 0 & 0 & 1 & 0 & 0 \\ 0 & 0 & 0 & 0 & 0 \\ 0 & 0 & 0 & 0 & 1 \\ 0 & 0 & 0 & 0 & 0 \\ 0 & 0 & 1 & 0 & 0 \end{vmatrix}.$$

$$\mathbf{C} = \begin{bmatrix} 0 & 0 & 0 & 1 & 0 \\ 0 & 0 & 0 & 0 & 0 \\ 0 & 0 & 0 & 0 & 0 \\ 0 & 0 & 0 & 0 & 1 \\ 0 & 0 & 0 & 1 & 0 \end{bmatrix}, \quad \mathbf{D} = \begin{bmatrix} 0 & 0 & 1 & 0 & 0 \\ 0 & 0 & 0 & 0 & 0 \\ 0 & 0 & 0 & 0 & 0 \\ 0 & 0 & 0 & 0 & 0 \\ 0 & 0 & 1 & 0 & 0 \end{bmatrix}.$$

The corresponding PML equation is

$$\frac{\partial \mathbf{u}}{\partial t} + \mathbf{A}\frac{\partial \mathbf{u}}{\partial x} + \mathbf{B}\frac{\partial \mathbf{u}_5}{\partial y} + \mathbf{C}\frac{1}{r}\frac{\partial \mathbf{u}_5}{\partial \phi} + \frac{1}{r}\mathbf{D}\mathbf{u}_5 + \mathbf{u}_6 = 0 \tag{6.23}$$

where

$$\mathbf{u}_5 = \mathbf{u} + \sigma_x \mathbf{q}_1 \quad, \quad \mathbf{u}_6 = \sigma_x \mathbf{u} \quad \text{and} \quad \frac{\partial \mathbf{q}_1}{\partial t} = \mathbf{u}.$$

In applying PML to a ducted domain, the wall boundary condition for the PML is the same as that for the Euler domain. For instance, for the rigid wall circular duct problem of Fig. 6.3, the same rigid wall boundary condition, namely $v = 0$, at $r = D/2$ is to be used in the PML regions.

In implementing PML, the damping coefficients, say, $\sigma_x(x)$, $\sigma_y(y)$ are often taken as smooth functions. A good practice is to set these functions equal to zero at the interface with Euler domain. It is also a good practice to let $\sigma_x(x)$ increase smoothly to a constant level in the main part of the PML. At the termination of the PML, the computed variables are usually exponentially small so that reflection is not a concern. However, it is a good practice to impose a standard radiation boundary condition that is of minimal cost to the computation.

7. COMPLEX GEOMETRY

Computationally, there are two general ways to treat problems with complex geometry. One way is to use unstructured grids. The other is to use overset grids. Overset grids are formed by overlapping structured grids. In this chapter, the basic idea of overset grids methodology and its implementation are discussed.

7.1 Basic Concept of Overset Grids

To illustrate the basic idea of overset grids, consider the problem of computing the scattering of acoustic waves by a solid cylinder in two dimensions. In the space around the cylinder, the coordinates of choice for computing the solution is the cylindrical polar coordinates centered at the axis of the cylinder. This coordinate system provides a set of body fitted coordinates and hence a body fitted mesh when discretized around the cylinder. One significant advantage of using body fitted grid is the relative ease in enforcing the no through flow wall boundary condition using the ghost point method or other methods. Away from the cylinder, acoustic waves propagate with no preferred direction. The natural coordinate system to use is the Cartesian coordinates. Therefore, to take into account the advantages stated, one may use a polar mesh around the cylinder and a Cartesian mesh away from the cylinder with an overlapping mesh region. The overlapping mesh region is for data transfer from one set of grid to the other and vice versa.
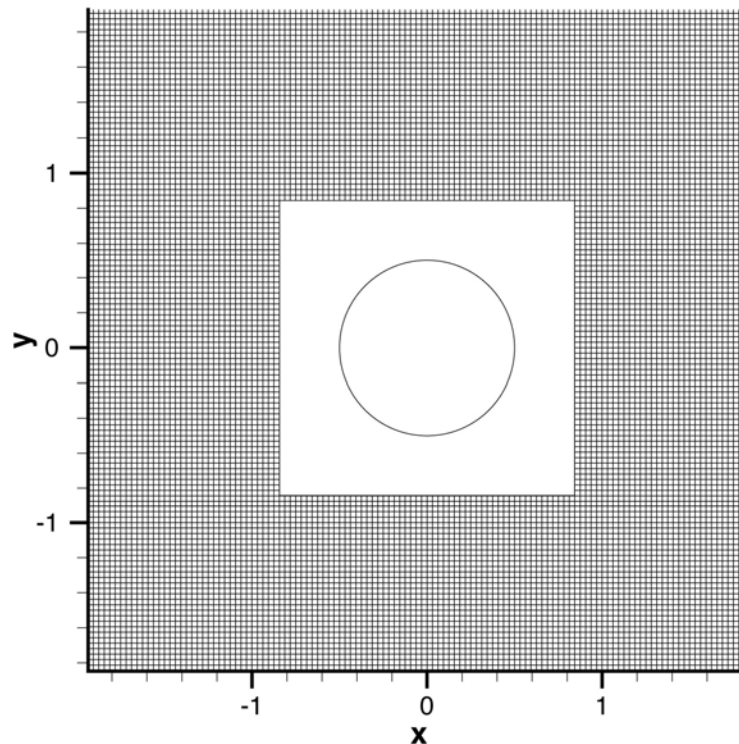
Figure 7.1. Cartesian grid used in acoustic wave scattering by a cylinder problem.
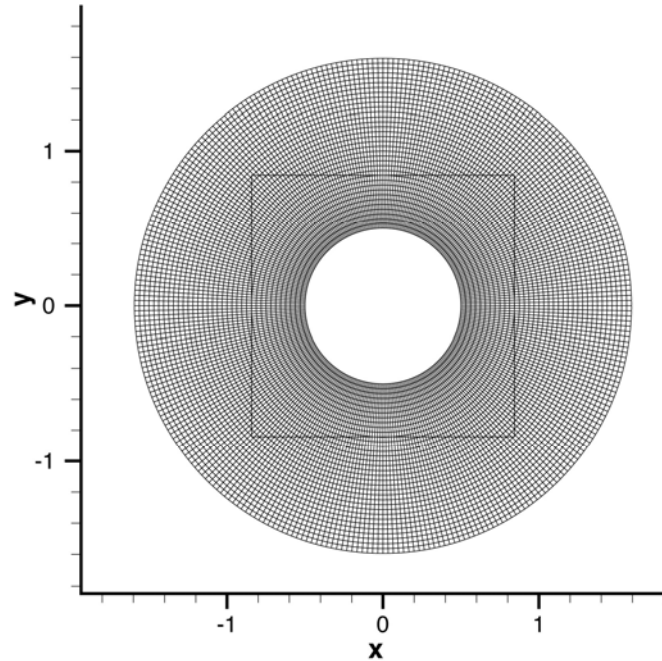
Figure 7.2. Polar grid used in acoustic wave scattering problem.
Square indicates the inner boundary of the Cartesian grid.
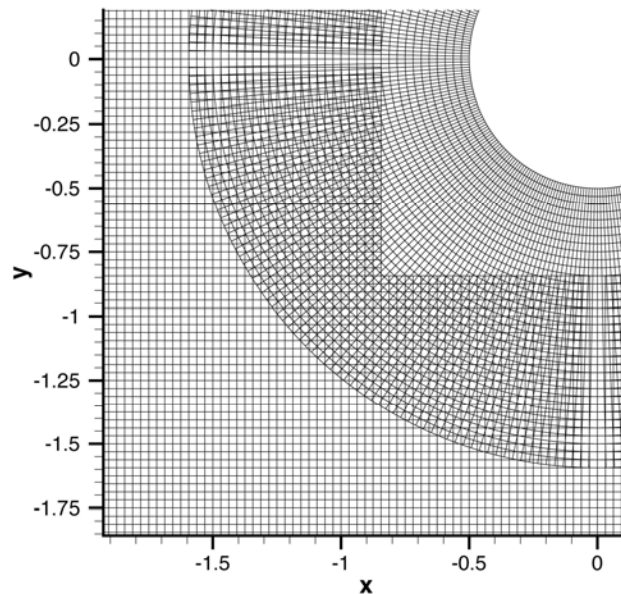
Figure 7.3. The overlapping region of the Cartesian and polar grids.

Figure 7.1 shows a Cartesian mesh with a square hole around the cylinder. For the purpose of putting all variables in dimensionless form, the diameter, D, of the cylinder is taken as length scale, speed of sound a_0 as the velocity scale, D/a_0 as the time scale, ρ_0 (the density of the undisturbed gas) as the density scale, and $\rho_0 a_0^2$ as the pressure scale. The mesh size is $\Delta x = \Delta y = 1/32$. The size of the square hole is 1.6 by 1.6. Figure 7.2 shows a polar mesh with $\Delta r = 1/32$ and $\Delta \theta = \pi/150$. The polar mesh extends to a distance of $r = 1.5$. The mesh overlap region is between the square and the outside edge of the polar mesh as shown in Fig. 7.2. Figure

77

7.3 is an enlarged view of the mesh overlap region. Both the cylindrical mesh and the Cartesian mesh are structured meshes. To compute the solution, it would be best to write the governing equations in the coordinate system used. For acoustic wave scattering problems under discussion the governing equations are the full Euler equations. In dimensionless form, they are

Cartesian coordinates

$$\frac{\partial \rho}{\partial t} + u\frac{\partial \rho}{\partial x} + v\frac{\partial \rho}{\partial y} + \rho\left(\frac{\partial u}{\partial x} + \frac{\partial v}{\partial y}\right) = 0$$

$$\frac{\partial u}{\partial t} + u\frac{\partial u}{\partial x} + v\frac{\partial u}{\partial y} + \frac{1}{\rho}\frac{\partial p}{\partial x} = 0$$

$$\frac{\partial v}{\partial t} + u\frac{\partial v}{\partial x} + v\frac{\partial v}{\partial y} + \frac{1}{\rho}\frac{\partial p}{\partial y} = 0 \qquad (7.1)$$

$$\frac{\partial p}{\partial t} + u\frac{\partial p}{\partial x} + v\frac{\partial p}{\partial y} + \gamma p\left(\frac{\partial u}{\partial x} + \frac{\partial v}{\partial y}\right) = 0$$

Polar coordinates

$$\frac{\partial \rho}{\partial t} + \frac{1}{r}\frac{\partial}{\partial r}(\rho v_r r) + \frac{1}{r}\frac{\partial(\rho v_\theta)}{\partial \theta} = 0$$

$$\frac{\partial v_r}{\partial t} + v_r\frac{\partial v_r}{\partial r} + \frac{v_\theta}{r}\frac{\partial v_r}{\partial \theta} - \frac{v_\theta^2}{r} + \frac{1}{\rho}\frac{\partial p}{\partial r} = 0$$

$$\frac{\partial v_\theta}{\partial t} + v_r\frac{\partial v_\theta}{\partial r} + \frac{v_\theta}{r}\frac{\partial v_\theta}{\partial \theta} + \frac{v_r v_\theta}{r} + \frac{1}{\rho}\frac{\partial p}{\partial \theta} = 0 \qquad (7.2)$$

$$\frac{\partial p}{\partial t} + v_r\frac{\partial p}{\partial r} + \frac{v_\theta}{r}\frac{\partial p}{\partial \theta} + \gamma p\left(\frac{1}{r}\frac{\partial v_r r}{\partial r} + \frac{1}{r}\frac{\partial v_\theta}{\partial \theta}\right) = 0$$

The solution of (7.1) is computed on the Cartesian mesh. The solution of (7.2) is computed on the polar mesh. (u,v) and (v_r,v_θ) are related by,

$$u = v_r\cos\theta - v_\theta\sin\theta$$

$$v = v_r\sin\theta + v_\theta\cos\theta$$

$$v_r = u\cos\theta + v\sin\theta$$

$$v_\theta = -u\sin\theta + v\cos\theta$$

In computing the solution, the 7-point stencil DRP scheme may be used. Since the 7-point stencil DRP scheme is a central difference scheme, the values of the computation variables of the three rows and columns of the Cartesian mesh around the square hole are not computed by the time marching scheme. They are found by interpolation from the values of the polar mesh using, say, a 16-point regular stencil. A typical stencil is shown in Fig. 7.4. For the polar mesh, the values of the computation variables at the outer three

rings are not computed. They are interpolated from the values of the Cartesian mesh using a 16-point regular stencil as shown in Fig. 7.5.
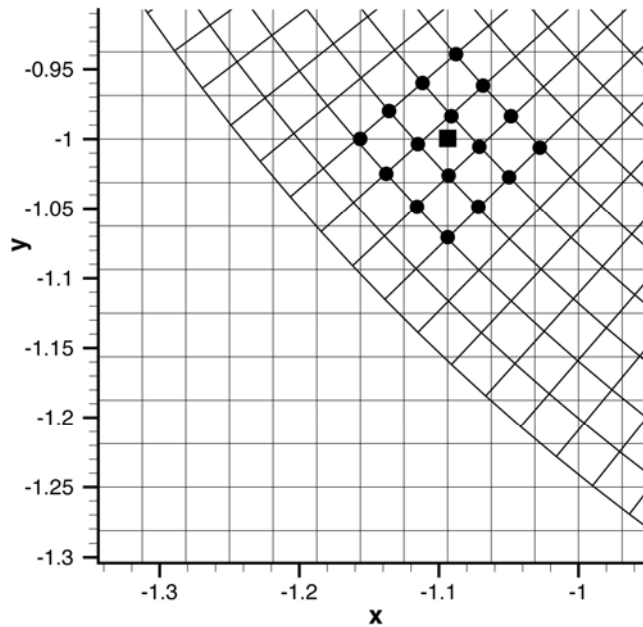

Figure 7.4. Interpolation from a polar grid to a Cartesian grid using a
16-point stencil. $\Delta x = \Delta y = \Delta r = 1/32$, $\Delta\theta = \pi/150$.
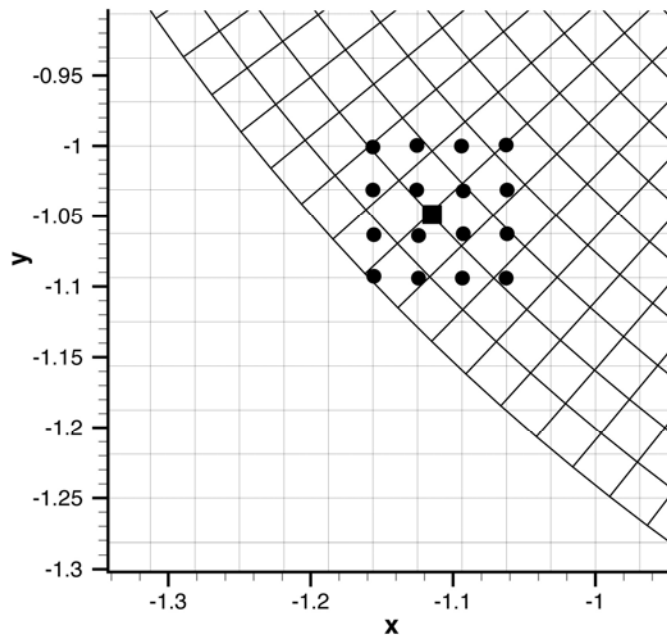

Figure7.5. Interpolation from a Cartesian grid to a polar grid using a
16-point stencil. $\Delta x = \Delta y = \Delta r = 1/32$.

Data transfer from one set of grid to the other is one of the crucial processes of overset grids method. Since a high-order scheme is used for computation in each of the structured grid, it is important for the data transfer process to retain, at least, the same accuracy. In what follows, a

highly accurate multi-dimensional interpolation scheme, suitable for use as a data transfer method, is discussed.

7.2. Optimized multi-dimensional interpolation
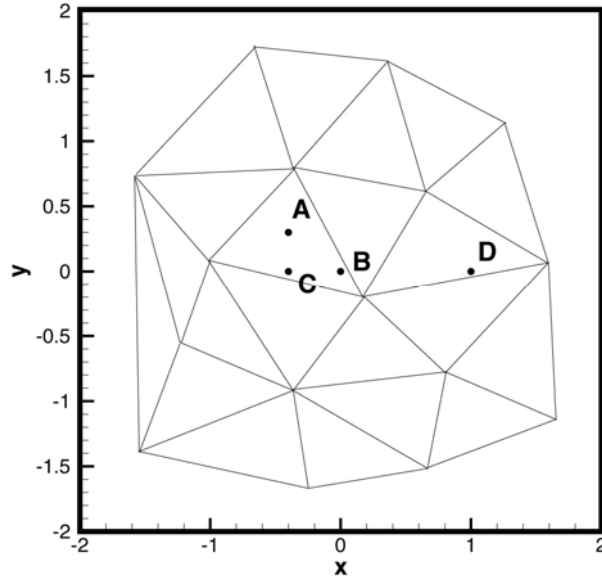
Fig. 7.6. A 16-point irregular interpolation stencil.

The idea and methodology of optimized multi-dimensional interpolation will be considered first. Numerical examples will be given later. For simplicity, only two-dimensional interpolation is discussed in detail. The generalization to three dimensions is fairly straightforward. Consider an interpolation stencil in a computational domain as shown in Fig. 7.6. Without loss of generality, the interpolation is considered for implementation in the x–y plane. However, x and y may be a set of curvilinear coordinates in the physical domain. For interpolation purpose, the values of a function $f(x,y)$ are given at the stencil points (x_j,y_j), $j = 1,2,…,N$ for an N-point stencil. The objective is to estimate the value $f(x_o,y_o)$ at a general point P at (x_o,y_o). By definition of interpolation (not extrapolation) the point P lies within the boundary of the stencil as defined by Fig. 7.6. Let d_j be the distance between neighboring points of the stencil. A useful length scale is

$$\Delta = \frac{1}{K}\sum_{j=1}^{K}d_j \qquad (7.3)$$

where K is the number of links between stencil points.

The most general interpolation formula in two dimensions has the form

$$f(x_o,y_o)=\sum_{j=1}^{N}S_j f(x_j,y_j). \qquad (7.4)$$

Different interpolation methods determine the coefficient S_j in different ways.

It will be assumed that the function $f(x,y)$ to be interpolated has a Fourier inverse transform, such that

$$f(x,y) = \int_{-\infty}^{\infty}\int_{-\infty}^{\infty} \tilde{f}(\alpha,\beta)e^{i(\alpha x + \beta y)}\,d\alpha d\beta..\tag{7.5}$$

where (α,β) are the wave numbers in the x and y direction, respectively.

Let $A(\alpha,\beta) = \left|\tilde{f}(\alpha,\beta)\right|$ and $\phi(\alpha,\beta) = \arg[\tilde{f}(\alpha,\beta)]$, Eq. (7.5) may be rewritten as

$$f(x,y) = \int_{-\infty}^{\infty}\int_{-\infty}^{\infty} A(\alpha,\beta)e^{i[\alpha x + \beta y + \phi(\alpha,\beta)]}\,d\alpha d\beta.\tag{7.6}$$

This equation may be interpreted in the sense that $f(x,y)$ is made up of a superposition of simple waves $\exp[i(ax + by + \phi(a,b))]$ with amplitude $A(\alpha,\beta)$. It is useful to define the local interpolation error, E_{local}, for wave number (α,β) as the absolute value of the difference between the left and right side of Eq. (7.4) when $f(x,y)$ is replaced by the simple wave

$$f_{\alpha\beta} = e^{i[\alpha x + \beta y + \phi(\alpha,\beta)]}.\tag{7.7}$$

Here all simple waves are assumed to have unit amplitude; i.e., $A(\alpha,\beta) = 1.0$. It is easy to find,

$$
\begin{aligned}
E_{\text{local}}^2 &= \left| e^{i(\alpha x_o + \beta y_o + \phi)} - \sum_{j=1}^{N} S_j e^{i(\alpha x_j + \beta y_j + \phi)} \right|^2 \\
&= \left| 1 - \sum_{j=1}^{N} S_j e^{i\left[\alpha\Delta\left(\frac{x_j - x_o}{\Delta}\right) + \beta\Delta\left(\frac{y_j - y_o}{\Delta}\right)\right]} \right|^2 .
\end{aligned}
\tag{7.8}
$$

The total error, E, over the region $-\kappa \le \alpha\Delta, \beta\Delta \le \kappa$, in wave number space is obtained by integrating E_{local}^2 of Eq. (7.8),

$$E^2 = \int_{-\kappa}^{\kappa}\int_{-\kappa}^{\kappa} \left| 1 - \sum_{j=1}^{N} S_j e^{i\left[\alpha\Delta\left(\frac{x_j - x_o}{\Delta}\right) + \beta\Delta\left(\frac{y_j - y_o}{\Delta}\right)\right]} \right|^2 d(\alpha\Delta)d(\beta\Delta).\tag{7.9}$$

When the function to be interpolated is a constant, which corresponds to setting $\alpha = \beta = 0$ in Eq. (7.7), it is reasonable to require the local interpolation error to be zero. By Eq. (7.8), this requirement leads to

$$\sum_{j=1}^{N} S_j - 1 = 0. \tag{7.10}$$

It is now proposed that the interpolation coefficients, S_j ($j = 1, 2,\ldots, N$) be chosen such that E^2 is a minimum subjected to constraint (7.10). This can readily be done by using the method of Lagrange multipliers. Let

$$L = \int_{-\kappa}^{\kappa} \int_{-\kappa}^{\kappa} \left| 1 - \sum_{j=1}^{N} S_j e^{i\left[\xi\left(\frac{x_j - x_0}{\Delta}\right) + \eta\left(\frac{y_j - y_0}{\Delta}\right)\right]} \right|^2 d\xi \, d\eta + \lambda \left(\sum_{j=1}^{N} S_j - 1 \right). \tag{7.11}$$

where λ is the Lagrange multiplier. The conditions for L to be a minimum are

$$\frac{\partial L}{\partial S_j} = 0, \qquad \frac{\partial L}{\partial \lambda} = 0, \qquad j = 1, 2,\ldots, N. \tag{7.12}$$

It is easy to find the condition $\partial L/\partial S_j = 0$ yields,

$$2 \text{Re} \left\{ \int_{-\kappa}^{\kappa} \int_{-\kappa}^{\kappa} e^{-i\left[\xi\frac{(x_j - x_0)}{\Delta} + \eta\frac{(y_j - y_0)}{\Delta}\right]} \left[1 - \sum_{k=1}^{N} S_k e^{i\left[\xi\frac{(x_k - x_0)}{\Delta} + \eta\frac{(y_k - y_0)}{\Delta}\right]} \right] d\xi d\eta \right\} + \lambda = 0. \tag{7.13}$$

where Re{ } is the real part of { }. Similarly it is easy to find $\partial L/\partial \lambda$ leads to,

$$\sum_{j=1}^{N} S_j - 1 = 0, \tag{7.14}$$

which is constraint (7.10).

Eqs. (7.13) and (7.14) form a linear matrix system of ($N + 1$) unknowns for S_j ($j = 1, 2,\ldots, N$) and λ. It turns out all the integrals of Eq. (7.13) can be evaluated in closed form. This allows the matrix elements to be written out explicitly. The values of S_j may be found by solving the matrix system,

$$\mathbf{AS} = \mathbf{b} \tag{7.15}$$

where vector $\mathbf{S}^{\mathbf{T}} = (S_1 \ S_2 \ S_3 \ \cdots \ S_N \ \lambda)$. Note: Superscript $\mathbf{T}$ denotes the transpose. The elements of the coefficient matrix $\mathbf{A}$ and vector $\mathbf{b}$ are given by,

$$A_{jk} = \begin{cases} 4\kappa^2, & j = k \\ \\ \dfrac{4\Delta^2}{(x_k - x_j)(y_k - y_j)} \sin\left[\kappa \dfrac{(x_k - x_j)}{\Delta}\right] \sin\left[\kappa \dfrac{(y_k - y_j)}{\Delta}\right], & j \neq k \end{cases}$$

$$(j, k = 1, 2, \ldots, N)$$

(7.16)

$$A_{j(N+1)} = \frac{1}{2}, \qquad (j = 1, 2, \ldots, N)$$

(7.17)

$$A_{(N+1)k} = 1, \qquad (k = 1, 2, \ldots, N)$$

(7.18)

$$A_{(N+1)(N+1)} = 0$$

(7.19)

$$b_j = \frac{4\Delta^2}{(x_j - x_0)(y_j - y_0)} \sin\left[\kappa \frac{(x_j - x_0)}{\Delta}\right] \sin\left[\kappa \frac{(y_j - y_0)}{\Delta}\right]$$

(7.20)

$$b_{(N+1)} = 1.$$

(7.21)

Note: In the case $x_j = x_k$ and/or $y_j = y_k$ or $x_j = x_0$ or $y_j = y_0$ the limit forms of the above formulas are to be used. Computationally, the limit forms are used wherever $|x_j - x_k| < \varepsilon$ or $|y_j - y_k| < \varepsilon$. This is discussed in Appendix A of this chapter.

It is useful to point out that A_{jk} depends on Δ and κ as well as the coordinates of the stencil points only. The coordinates of the point to be interpolated to, (x_0, y_0), appears only in b_j. Thus if many values of f are to be interpolated using the same stencil, $\mathbf{A}$ and $\mathbf{A}^{-1}$ need only be computed once.

For error estimate purposes, the following symmetry properties of the local error, given by Eq. (7.8), can easily be derived.

$$E_{\text{local}}(\alpha, \beta) = E_{\text{local}}(-\alpha, -\beta)$$

(7.22)

$$E_{\text{local}}(-\alpha, \beta) = E_{\text{local}}(\alpha, -\beta).$$

(7.23)

Thus once S_j's are found, E_{local} can be calculated by formula (7.8). Upon invoking Eqs. (7.22) and (7.23) it is sufficient to examine $E_{\text{local}}(\alpha, \beta)$ over the upper half of the $\alpha\Delta - \beta\Delta$ plane for $-\pi \leq \alpha\Delta, \beta\Delta \leq \pi$.

7.2.1. Order constraints

For small Δ, it is often desirable to require interpolation formula (7.4) to be accurate to a specified order of Taylor series expansion in Δ. This requirement imposes a set of constraints on the interpolation coefficients S_j. To find these constraints in their simplest form, first expand $f(x_j, y_j)$ about (x_o, y_o) to obtain,

$$f\left(x_j, y_j\right) = f\left(x_o, y_o\right) + \sum_{p,q} \frac{1}{p!q!}\left(\frac{\partial^{p+q} f}{\partial x^p \partial y^q}\right)_{x_0, y_0} \left(x_j - x_o\right)^p \left(y_j - y_o\right)^q. \tag{7.24}$$

On substituting (7.24) into (7.4), it is found

$$f\left(x_o, y_0\right) = f\left(x_o, y_o\right)\left(\sum_{j=1}^{N} S_j\right) + \sum_{p,q} \frac{1}{p!q!}\left(\frac{\partial^{p+q} f}{\partial x^p \partial y^q}\right)_{x_0, y_0}\left[\sum_{j=1}^{N}\left(x_j - x_o\right)^p\left(y_j - y_o\right)^q S_j\right]. \tag{7.25}$$

Thus, if Eq. (7.25) is truncated to order Δ^M, S_j must satisfy the following conditions.

$$\sum_{j=1}^{N} S_j = 1, \qquad M = 0 \tag{7.26}$$

$$\sum_{j=1}^{N}\left(x_j - x_o\right)^p\left(y_j - y_o\right)^q S_j = 0, \qquad 1 \le p + q \le M \tag{7.27}$$

From Eq. (7.25) it is easy to see that if the order of truncation is increased from $(M-1)$ to M, $(M+1)$ more constraints are added. Therefore, the total number of constraints, T, to be satisfied, if Eq. (7.24) is truncated at M^{th} order, is

$$T = 1 + 2 + 3 + \ldots + (M+1) = \frac{1}{2}(M+1)(M+2). \tag{7.28}$$

It is possible if (x_j, y_j), $j = 1, 2, \ldots, N$ are points on a highly regular grid, the total number of independent constraints given by Eqs. (7.26) and (7.27) is less than that calculated by Eq. (7.28). Degeneracy would occur when a number of x_j's or y_j's are the same. In this case, only the linearly independent constraints need to be imposed.

Now for a given interpolation stencil with a given set of points (x_j, y_j), $j = 1, 2, \ldots, N$, the interpolation coefficients S_j for the point (x_o, y_o) may be found by minimizing the total error E^2, given by Eq. (7.9), subjected to order constraints (7.26) and (7.27). This constrained minimization problem can again be easily solved by the method of Lagrange multipliers. Let

$$\mathsf{L} = \int_{-\kappa}^{\kappa}\int_{-\kappa}^{\kappa}\left|1 - \sum_{j=1}^{N} S_j e^{i\left[\xi\frac{(x_j - x_0)}{\Delta} + \eta\frac{(y_j - y_0)}{\Delta}\right]}\right|^2 d\xi\, d\eta + \lambda\left(\sum_{j=1}^{N} S_j - 1\right) + \sum_{n,m}\mu_{mn}\left[\sum_{j=1}^{N} S_j\left(x_j - x_0\right)^n\left(y_j - y_0\right)^m\right]. \tag{7.29}$$

where $n, m = 0, 1, 2,\ldots, M$; $n + m \leq M$; n and m are not both equal to zero. M is the order of truncation μ_{mn} are Lagrangian multipliers. Since the total number of constraints (T as given by Eq. (7.28)) cannot exceed the number of stencil points, it is understood that $T < N$. The conditions for a minimum are:

$$\frac{\partial L}{\partial S_j} = 0 \tag{7.30}$$

$$\frac{\partial L}{\partial \lambda} = 0 \tag{7.31}$$

$$\frac{\partial L}{\partial \mu_{mn}} = 0. \tag{7.32}$$

Again, Eqs. (7.30) to (7.32) lead to a linear matrix equation for the unknowns S_j, λ and m_{mn}. Let the transpose of the vector $\mathbf{X}$ and $\mathbf{d}$ be defined by,

$$\mathbf{X^T} = \begin{pmatrix} S_1 & S_2 & \cdots & S_N & \lambda & \mu_{10} & \mu_{01} & \mu_{20} & \mu_{11} & \mu_{02} & \cdots & \mu_{mn} & \cdots & \mu_{0M} \end{pmatrix} \tag{7.33}$$

$$\mathbf{d^T} = \begin{pmatrix} b_1 & b_2 & \cdots & b_N & 1 & 0 & 0 & 0 & \cdots & \cdots & 0 & 0 \end{pmatrix} \tag{7.34}$$

where b_j's are given by Eqs. (7.20) and (7..21). It is easy to establish by means of Eqs. (7.30) to (7.32) that $\mathbf{X}$ is the solution of the matrix equation

$$\mathbf{BX} = \mathbf{d}. \tag{7.35}$$

The coefficient matrix $\mathbf{B}$ may be partitioned into four submatrices as,

$$\mathbf{B} = \begin{vmatrix} \mathbf{A} & \mathbf{C} \\ \mathbf{C^T} & \mathbf{0} \end{vmatrix}. \tag{7.36}$$

$\mathbf{A}$ is a $(N+1)$ by $(N+1)$ square matrix. It is the same as that of Eq. (7.15). $\mathbf{C}$ is a $(N+1)$ by $(T-1)$ matrix. $\mathbf{C^T}$ is the transpose of $\mathbf{C}$. The zero matrix $\mathbf{0}$ is a square matrix of size $(T-1)$. On writing out in full the elements of matrix $\mathbf{C}$ are,

$$\mathbf{C} = \begin{vmatrix} (x_1-x_0) & (y_1-y_0) & (x_1-x_0)^2 & (x_1-x_0)(y_1-y_0) & (y_1-y_0)^2 & (x_1-x_0)^3 & (x_1-x_0)^2(y_1-y_0)\cdots(x_1-x_0)(y_1-y_0)^{M-1} & (y_1-y_0)^M \\ (x_2-x_0) & (y_2-y_0) & (x_2-x_0)^2 & (x_2-x_0)(y_2-y_0) & (y_2-y_0)^2 & (x_2-x_0)^3 & (x_2-x_0)^2(y_2-y_0)\cdots(x_2-x_0)(y_2-y_0)^{M-1} & (y_2-y_0)^M \\ \vdots & \vdots & \vdots & \vdots & \vdots & \vdots & \vdots & \vdots \\ (x_j-x_0) & (y_j-y_0) & (x_j-x_0)^2 & (x_j-x_0)(y_j-y_0) & (y_j-y_0)^2 & (x_j-x_0)^3 & (x_j-x_0)^2(y_j-y_0)\cdots(x_j-x_0)(y_j-y_0)^{M-1} & (y_j-y_0)^M \\ \vdots & \vdots & \vdots & \vdots & \vdots & \vdots & \vdots & \vdots \\ (x_N-x_0) & (y_N-y_0) & (x_N-x_0)^2 & (x_N-x_0)(y_N-y_0) & (y_N-y_0)^2 & (x_N-x_0)^3 & (x_N-x_0)^2(y_N-y_0)\cdots(x_N-x_0)(y_N-y_0)^{M-1} & (y_N-y_0)^M \\ 0 & 0 & 0 & 0 & 0 & 0 & 0 & 0 \end{vmatrix}. \tag{7.37}$$

Again once Eq. (7.35) is solved, the interpolation coefficients S_j's are found. By substituting the values of S_j's into Eq. (7.8), the local interpolation error, E_{local}, at wave number ($\alpha\Delta,\beta\Delta$) may be computed.

7.2.2. Interpolation errors in wave number space

An interpolation stencil may be regular or irregular depending on the configuration of the stencil relative to the coordinate system used for the computation. Generally speaking, interpolation error is small compared with extrapolation error. Fig. 7.6 shows a 16-point irregular interpolation stencil. For reference purposes, the coordinates of the interpolation points of this stencil are

(−0.70,1.72)
(0.34,1.58)
(1.24,1.14)
(−1.62,0.72)
(−0.38,0.79)
(0.64,0.60)
(−1.02,0.08)
(0.18, −0.20)
(1.58,0.06)
(−1.24,−0.56)
(−0.38,−0.92)
(0.80.−0.78)
(−1.56,−1.40)
(−0.26,−1.68)
(0.66,−1.52)
(1.64,−1.16)

The points to be interpolated are:

A (−0.40,0.30)
B (0.00,0.00)
C (−0.40,0.00)
D (1.00,0.00)

Fig. 7.7 shows a 16-point regular stencil in the form of a square. Interpolation error analysis for the four points *A*, *B*, *C*, *D* shown in both Figs. 7.6 and 7.7 has been carried out. The finding is that the errors for points *A*, *B* and *C* are very similar. For this reason, only the interpolation errors of *A* and *D* will be discussed. It is useful to consider point *A* as typical of all the points located around the center of the stencil and point *D* as typical of all the points located close to the boundary of the stencil.
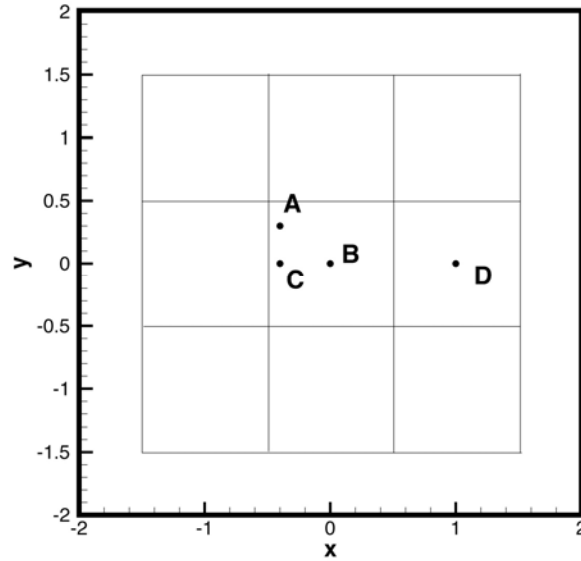
Fig. 7.7. A 16-point regular stencil in the form of a square.

Fig. 7.8 shows the local error, E_{local}, contours in the $\alpha\Delta - \beta\Delta$ plane. In calculating E_{local}, κ has been set equal to 1.2. It has been found through numerical experimentation that $\kappa = 1.2$ is a reasonably good value to use. As can readily be seen in Fig. 7.8, unlike extrapolation, there is no large error even for high wave numbers. In most aeroacoustics applications, the range of wave number that is of interest is $-1.0 \leq \alpha\Delta, \beta\Delta \leq 1.0$. In order to show error maps with more clarity, only the low wave number portion of the $\alpha\Delta - \beta\Delta$ plane is shown.
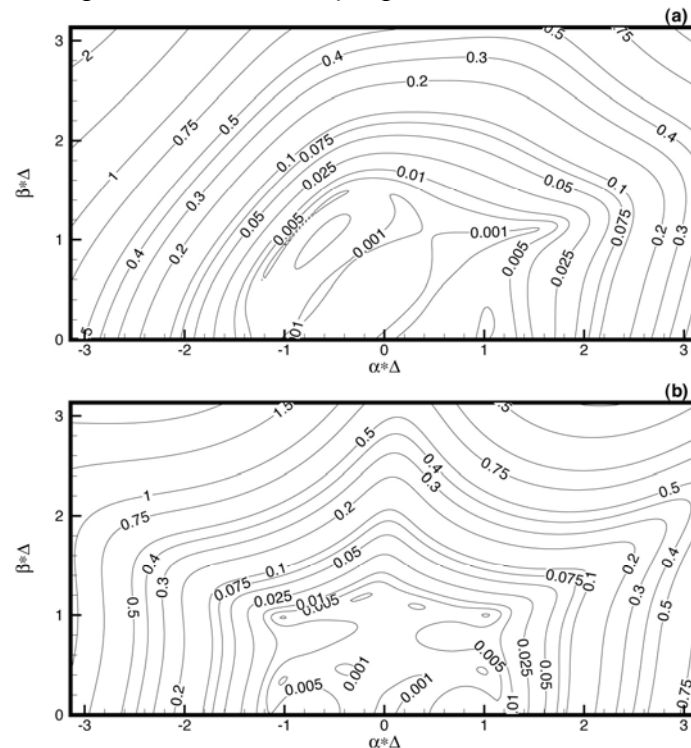
Fig. 7.8. Contours of local interpolation error, E_{local}, in the $\alpha\Delta - \beta\Delta$ plane for the irregular stencil of Fig. 7.6 using the optimized interpolation scheme. (a) at A, (b) at D.

The imposition of order constraints has a significant impact on the local error distribution in the wave number space. It is beneficial in reducing the error in the low wave number region. On the other hand, imposing high order constraint tends to increase error in the high wave number region.
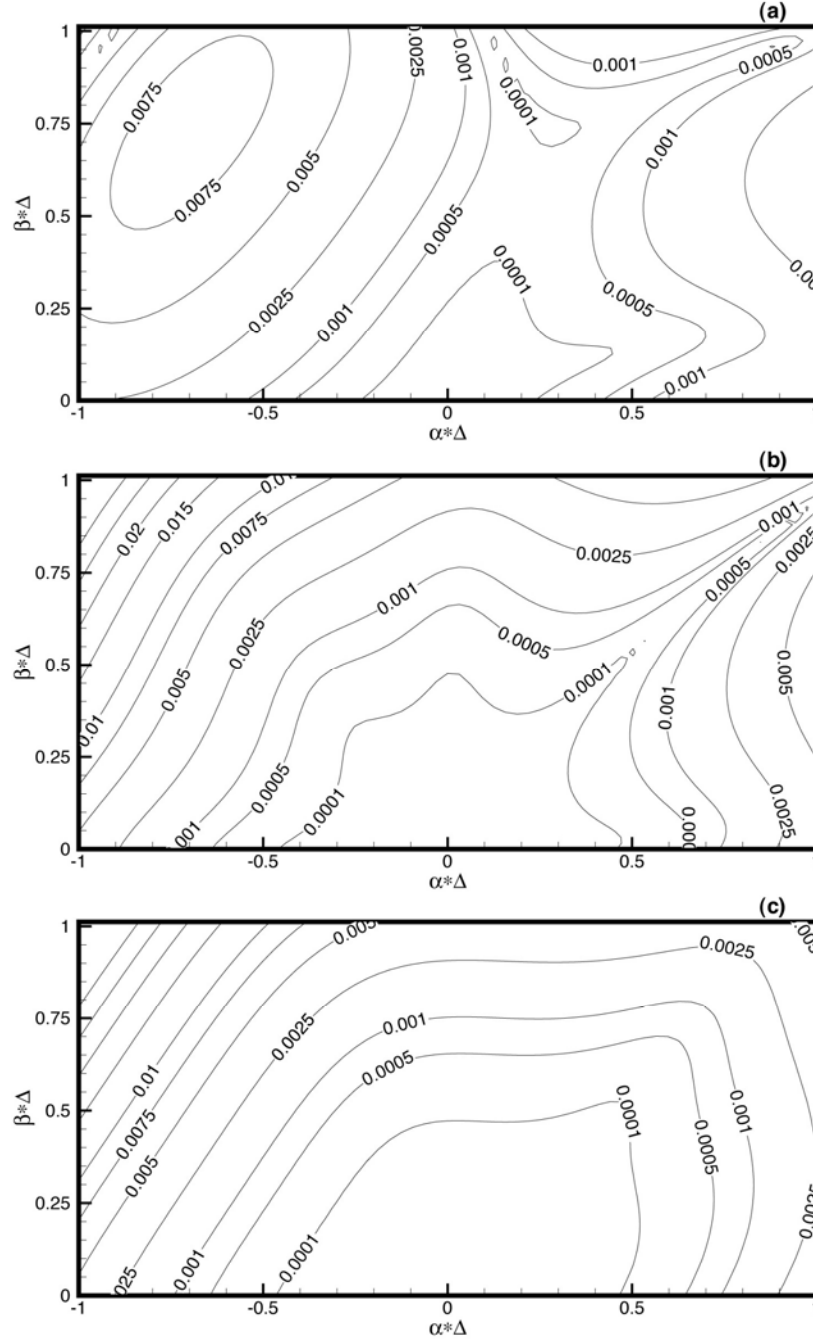
Fig. 7.9. Contour maps of interpolation error, E_{local}, at A using the irregular stencil with order constraints. (a) Second order. (b) Third order. (c) Fourth order.
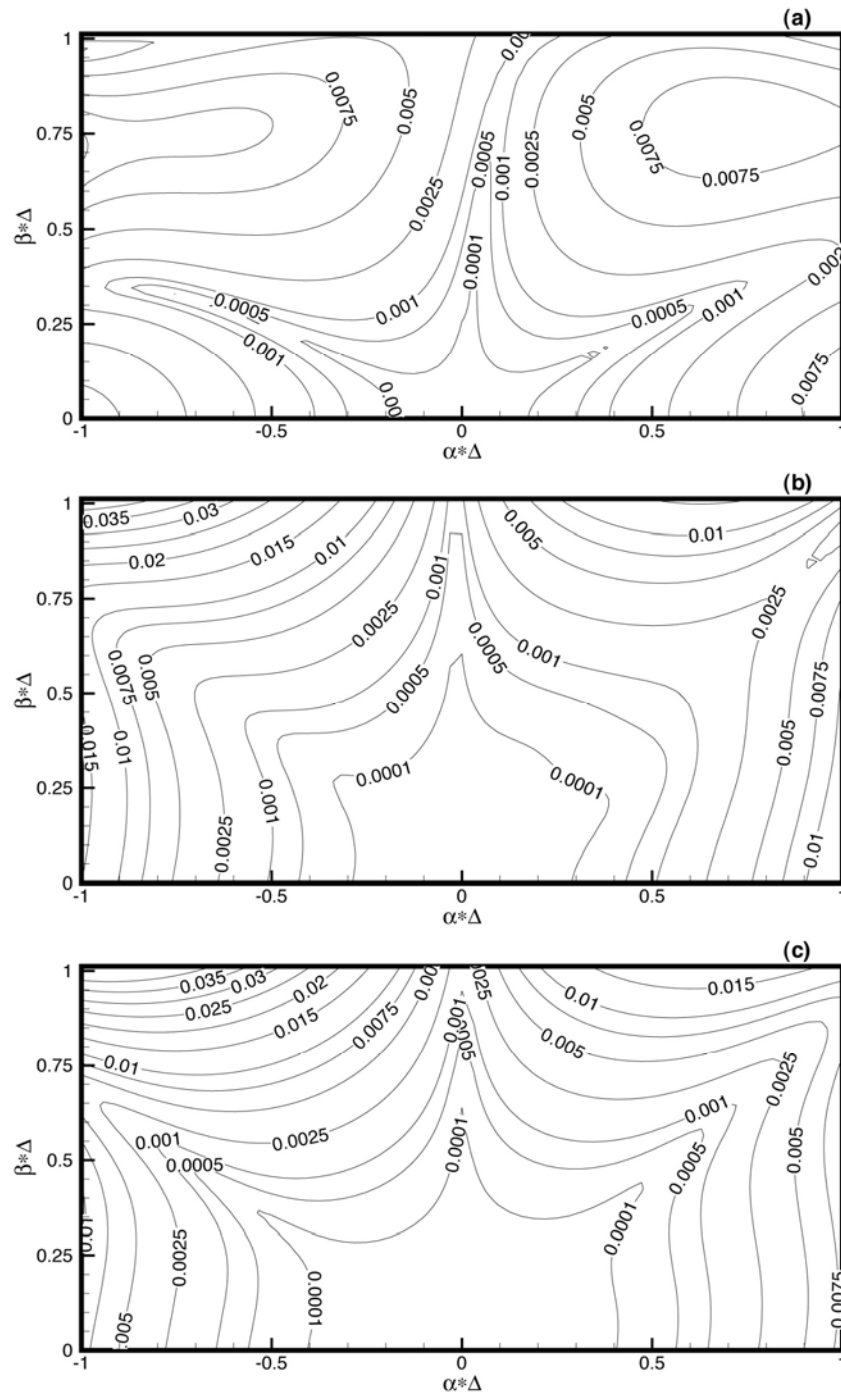
Fig. 7.10. Contour maps of interpolation error, E_{local}, at D using the irregular stencil with order constraints. (a) Second order. (b) Third order. (c) Fourth order.

Figs. 7.9a,b,c show the error contour distributions in the $\alpha\Delta - \beta\Delta$ plane for interpolation to point A using the irregular stencil of Fig. 7.6. Figure 7.9a is obtained with the imposition of a 2nd order constraint. Figs. 7.9b and 7.9c are the results with the imposition of a 3rd and 4th order constraint, respectively. It is clear from these figures that the best result or least error in the region $-0.5 < \alpha\Delta,\ \beta\Delta < 0.5$ is realized by enforcing the highest order constraint. On the other

hand, if one is interested in keeping the error small over a larger region in wave number space, then the low order constraint becomes attractive. For point A only the 2nd order constraint interpolation has an error less than 1% over the wave number region of $-1.0 \le \alpha\Delta$, $\beta\Delta < \le 1.0$. Figs. 7.10a,b,c are for interpolation to point D of the irregular stencil. Again, the error contours of these figures point to the benefit of minimizing interpolation error over the low wave number range by using the maximum order constraints. The error is less than ¼ % for $|\alpha\Delta|$, $|\beta\Delta| < 0.55$ (wave length longer than 12.5 mesh points). Again for the larger wave number range, say $-1.0 \le \alpha\Delta$, $\beta\Delta \le 1.0$, the 2nd order constraint has an interpolation error less than 1%. Thus, the choice of order constraints depends on the range of wave number one wishes to have the error below a specified level. For general usage, the imposition of a medium order constraint (say 2nd or 3rd order for a 16-point irregular stencil) may be a good compromise.

Fig. 7.11 shows contours of local interpolation error, E_{local}, at A using the 16-point regular stencil of Fig. 7.7. Figs. 7.11 a,b,c are subjected to 2nd, 3rd and 4th order constraints, respectively. Because of regularity of the stencil points, $x_j = x_k$ and $y_j = y_k$ occur repeatedly, there are only four independent values of x_j and y_j ($j = 1,2,\ldots,16$). This immediately leads to degeneracy in the 4th order constraints. To show this is, indeed, the case, recall that the interpolation coefficients are to be found by solving Eq. (7.35) $\mathbf{BX} = \mathbf{d}$. Here N is 16. Including the last row of submatrix $\mathbf{A}$, the last 15 rows of matrix $\mathbf{B}$ are as follows,

$$
\begin{vmatrix}
1 & 1 & 1 & \cdots & 1 & 0 & \cdots & \cdots & \cdots & 0 \\
x_1 - x_0 & x_2 - x_0 & x_3 - x_0 & \cdots & x_N - x_0 & 0 & \cdots & \cdots & \cdots & 0 \\
y_1 - y_0 & y_2 - y_0 & y_3 - y_0 & \cdots & y_N - y_0 & 0 & \cdots & \cdots & \cdots & 0 \\
(x_1 - x_0)^2 & (x_2 - x_0)^2 & (x_3 - x_0)^2 & \cdots & (x_N - x_0)^2 & 0 & \cdots & \cdots & \cdots & 0 \\
\vdots & \vdots & \vdots & \vdots & \vdots & \vdots & \vdots & \vdots & \vdots & \vdots \\
(y_1 - y_0)^4 & (y_2 - y_0)^4 & (y_3 - y_0)^4 & \cdots & (y_N - y_0)^4 & 0 & \cdots & \cdots & \cdots & 0
\end{vmatrix}.
$$

If there is no degeneracy, the above fifteen row vectors must be linearly independent. But this is not the case as shown below.

Consider the following five of the fifteen row vectors

$$
\begin{vmatrix}
1 & 1 & 1 & \cdots & 1 & 0 & \cdots & \cdots & \cdots & 0 \\
x_1 - x_0 & x_2 - x_0 & x_3 - x_0 & \cdots & x_N - x_0 & 0 & \cdots & \cdots & \cdots & 0 \\
(x_1 - x_0)^2 & (x_2 - x_0)^2 & (x_3 - x_0)^2 & \cdots & (x_N - x_0)^2 & 0 & \cdots & \cdots & \cdots & 0 \\
(x_1 - x_0)^3 & (x_2 - x_0)^3 & (x_3 - x_0)^3 & \cdots & (x_N - x_0)^3 & 0 & \cdots & \cdots & \cdots & 0 \\
(x_1 - x_0)^4 & (x_2 - x_0)^4 & (x_3 - x_0)^4 & \cdots & (x_N - x_0)^4 & 0 & \cdots & \cdots & \cdots & 0
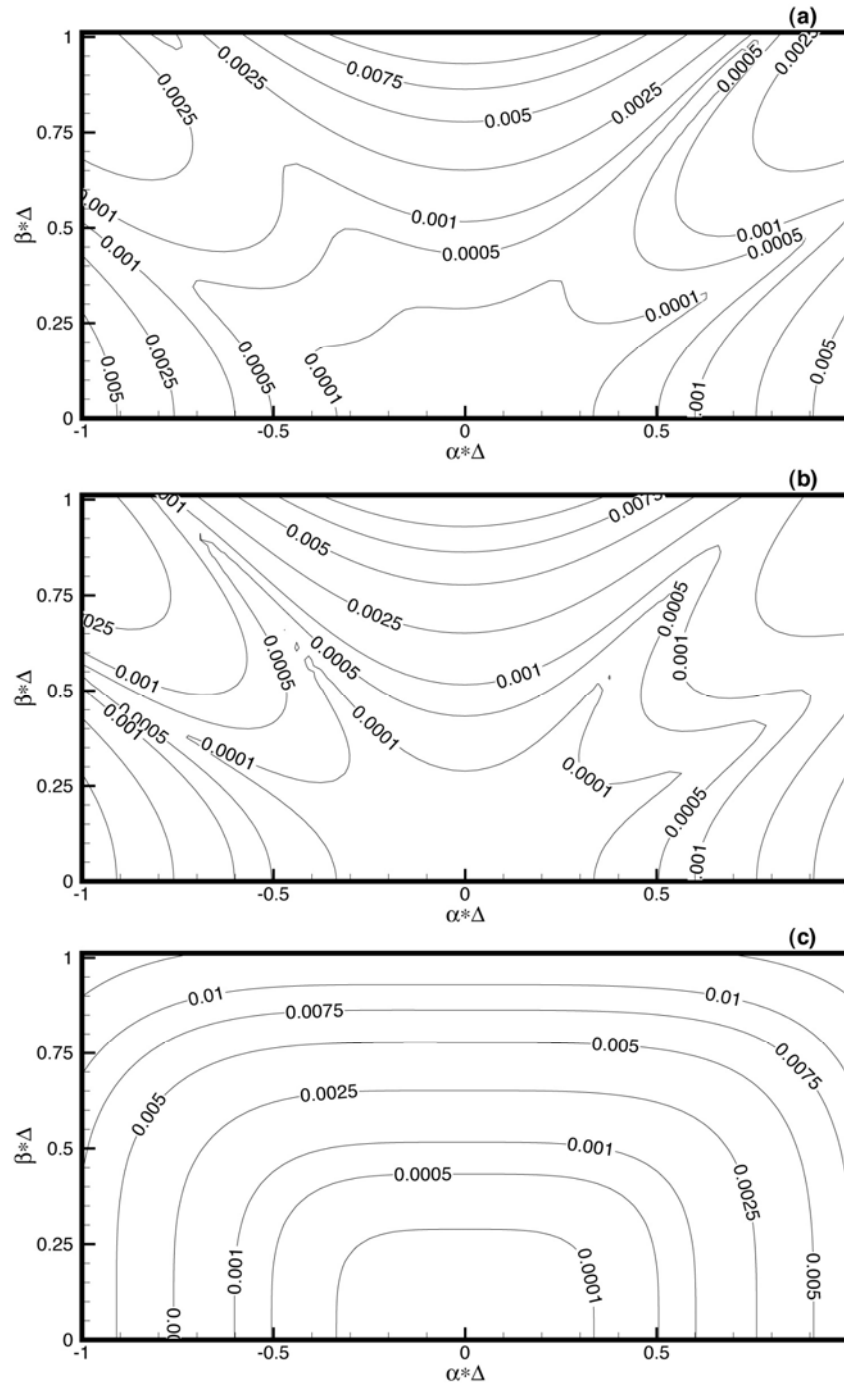\end{vmatrix}.
$$

Fig. 7.11. Contour maps of interpolation error, E_{local}, at A using the regular stencil with order constraints. (a) Second order. (b) Third order. (c) Fourth order.
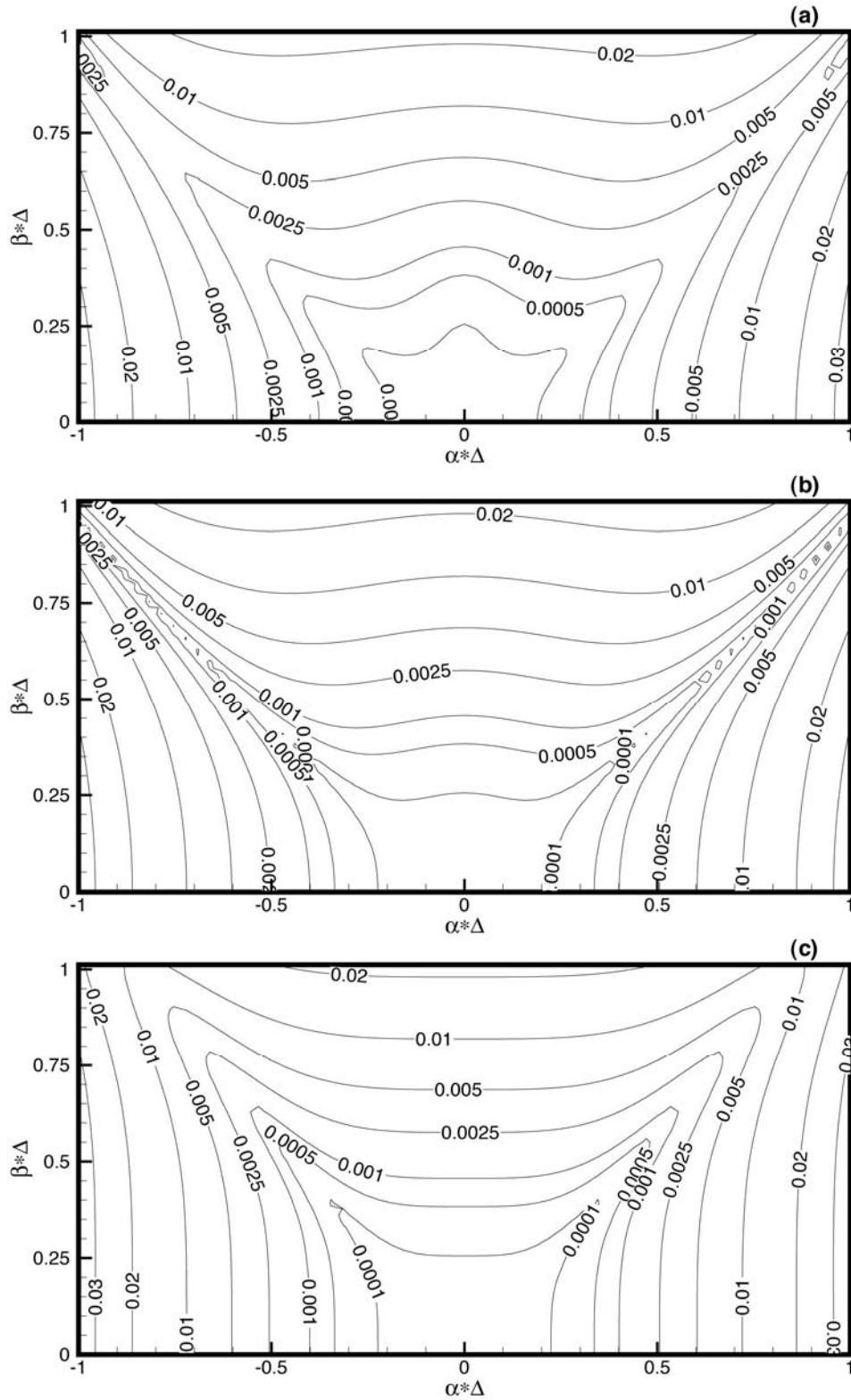
91

Fig. 7.12. Contour maps of interpolation error, E_{local}, at D using the regular stencil with order constraints. (a) Second order. (b) Third order. (c) Fourth order.

92

Since there are only four independent x_j's, there are only four independent column vectors. It follows that there are only four independent row vectors as well. Similarly, there is also one degeneracy due to the fact that there are only four independent values of y coordinates. To impose 4th order constraint on the interpolation scheme, only 13 linearly independent conditions are imposed. Fig. 7.11c is computed with only 13 constraints.

On comparing Figs. 7.11 a,b,c it is clear that the case with 4th order constraints turns out to have slightly more error than those with lower order constraints. On the other hand, the cases with 2nd order and 3rd order constraints are about the same. Figs. 7.12 a,b,c show similar error contours for the point D of Fig. 7.7. Again because of degeneracy with the 4th order constraints only 13 conditions are used in the optimization procedure. An inspection of these figures suggests that there are only minor differences among them. If minor differences in the distribution of interpolation error are acceptable, then the use of the 2nd order constraints would suffice when a highly regular stencil is used.

7.2.3. Global interpolation

An interpolation stencil may be in the form of a regular stencil in a curvilinear coordinate system but would be an irregular stencil when a different coordinate system is used as the frame of reference. For example, Fig.7.4 shows a regular 16-point interpolation stencil of the polar coordinate system. That is if the $r - \theta$ plane is used for computation, the interpolation stencil points form a regular stencil. But, if the computation is done in Cartesian coordinates, namely the coordinates of the stencil points are specified in a Cartesian coordinate system, the interpolation points form an irregular stencil.

In overset grids computation and in other applications, extensive interpolation from one set of mesh points of one curvilinear coordinate system to the mesh points of another coordinate system becomes necessary. Global interpolation of this type may be carried out using either set of coordinate system. As a test case, consider a plane wave with wave vector **k** inclined at 30° to the x-axis in the $x - y$ plane. The wave function Φ may be written as

$$\Phi(x,y) = \text{Re}\left\{ e^{ik[x\cos(\pi/6)+y\sin(\pi/6)]} \right\} \tag{7.39}$$

where Re{ } is the real part of { }. The wave function can also be written in polar coordinates (r,θ) by a straightforward coordinate transformation, thus

$$\Phi(r,\theta) = \text{Re}\left\{ e^{ikr\cos(\theta-\pi/6)} \right\} \tag{7.40}$$

Suppose a mesh of $\Delta x = \Delta y = 1/32$ in the Cartesian coordinates and $\Delta r = 1/32$, $\Delta\theta = \pi/150$ in the polar coordinate as shown in Fig.7.4 are used for interpolation purpose. Let the values of Φ be known on the polar mesh points. The objective is to find Φ at the mesh points of the Cartesian coordinates by interpolation using a 16-point stencil. That is, the aim to interpolate the values of Φ from the polar grid to the Cartesian grid. One obvious way is to refer the coordinates of all points to the polar coordinates system and perform the interpolation in the (r,θ) plane. In the (r,θ) plane the 16-interpolation points form a regular stencil. If the optimized interpolation

scheme is used, it is easy to show that the matrix **A** (for interpolation in polar coordinate, see Eq. (7.15)) is the same for all interpolation stencils. For this reason, the inverse coefficient matrix $\mathbf{A}^{-1}$ needs to be computed only once. On the other hand, if the interpolations are carried out in the Cartesian coordinate system, the stencils are irregular. It follows that the matrix **A** for each point to be interpolated to is different.
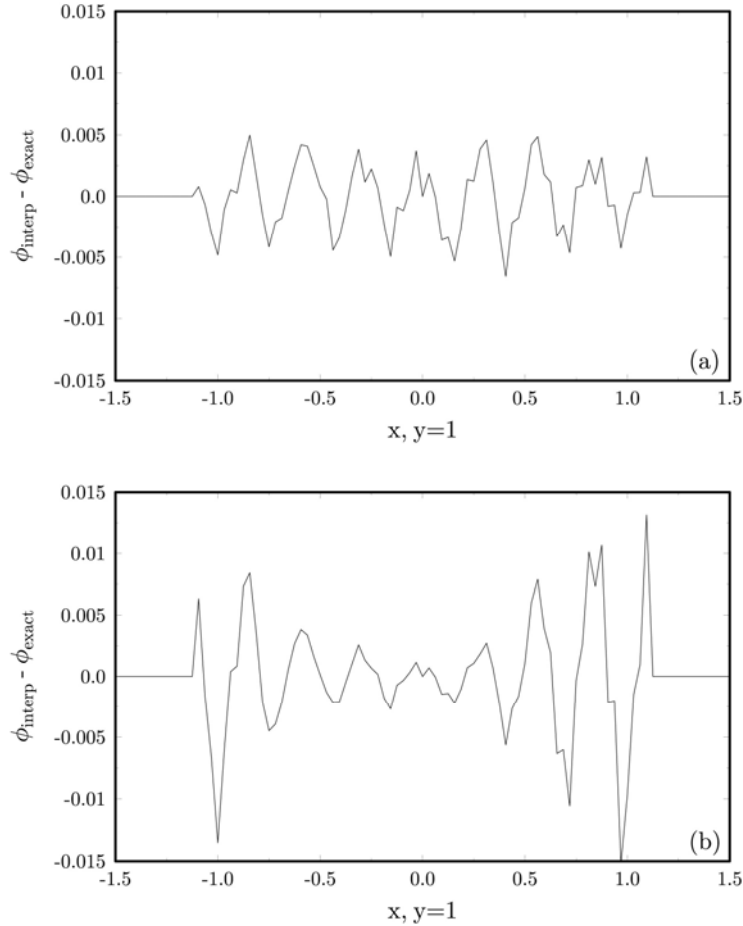

Fig.7.13. Distribution of interpolation error along the line $y = 1$. (a) Using a 16-point regular stencil in the $r - \theta$ plane. (b) Using a 16-point irregular stencil in the $x - y$ plane.

One piece of information one would like to know about global interpolation as described above is which way of interpolation, using regular or irregular stencils, would yield the least global error. For the example under consideration, the exact wave function on the Cartesian mesh is given by Eq. (7.39). Figure7.13a shows the interpolation error for the plane wave along the line $y = 1.0$ using the polar coordinates as the reference coordinates (regular stencils). Figure7.13b shows the corresponding interpolation error when the interpolation is performed in the Cartesian coordinates (irregular stencil). It is evident from these figures that the error in Fig.7.13b is more than twice as large as that in Fig 7.13a. This strongly suggests that when global interpolation is needed, it would be best if regular stencils are used. Figs.7.14 a,b provide similar comparison of global interpolation error arising from the use of regular and irregular stencils along the line $x = 1.0$. Again, the use of irregular stencils results in considerably larger

interpolation error. Although intuitively, the use of a regular stencil may appear to be the preferred choice, yet it is reassuring to see its confirmation by a concrete example.
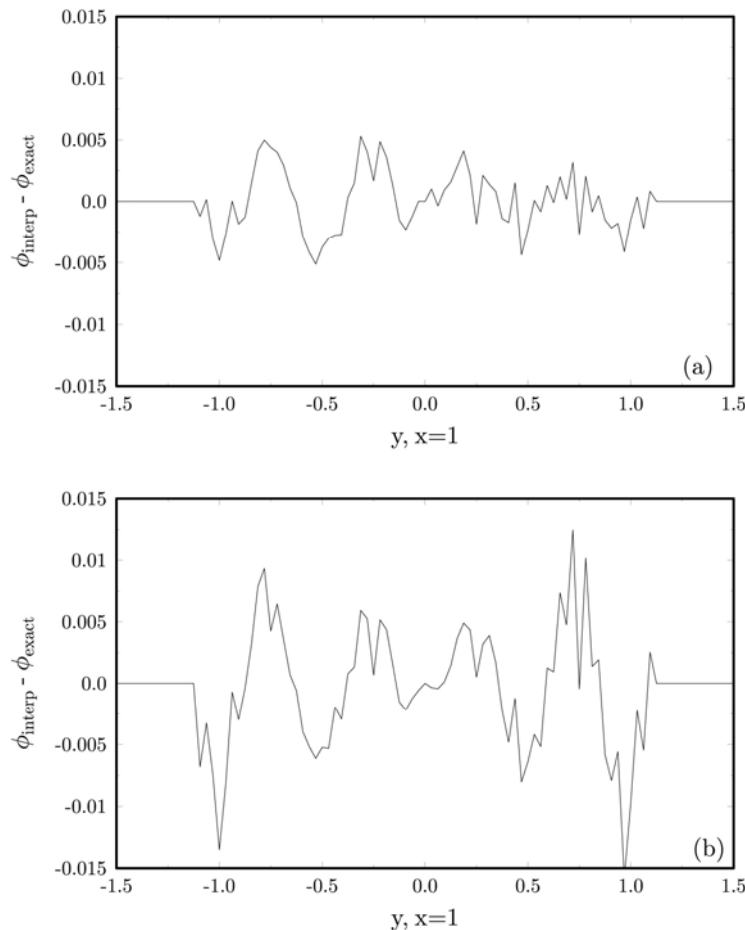
Fig.7.14. Distribution of interpolation error along the line $x = 1$. (a) Using a 16-point regular stencil in the $r - \theta$ plane. (b) Using a 16-point irregular stencil in the $x - y$ plane.

7.3 Numerical Examples: Scattering Problems

As examples to illustrate the use of overset grid method, two problems involving acoustic scattering by a rigid cylinder in two dimensions discussed in section 7.1 above will now be considered. The governing equations in Cartesian and Cylindrical coordinates are given in Eqs. (7.1) and (7.2). They are discretized and the numerical solutions are advanced in time by the 7-point stencil DRP scheme. The ghost point method is used to enforce the no through flow boundary condition.

(A) Transient scattering problem

First consider the scattering of an initial pressure pulse by the cylinder. For this problem, the Euler equations are solved with the initial conditions, $t = 0$

$$u = v = 0, \qquad \rho = \left(1 - \frac{1}{\gamma}\right) + p$$

$$p = \frac{1}{\gamma} + \varepsilon \exp\left[-(\ln 2)\left(\frac{(x-4)^2 + y^2}{0.2^2}\right)\right].$$

$$(7.41)$$

With a very small initial pulse amplitude ($\varepsilon = 10^{-4}$), the computed solution is identical to the solution of the linearized Euler equations. This cylinder scattering problem governed by the linearized Euler equation is a benchmark problem of the 2nd CAA Workshop on Benchmark Problems. The exact solution given in the conference proceedings unfortunately has an error. The correct solution is provided in Appendix B at the end of this chapter.
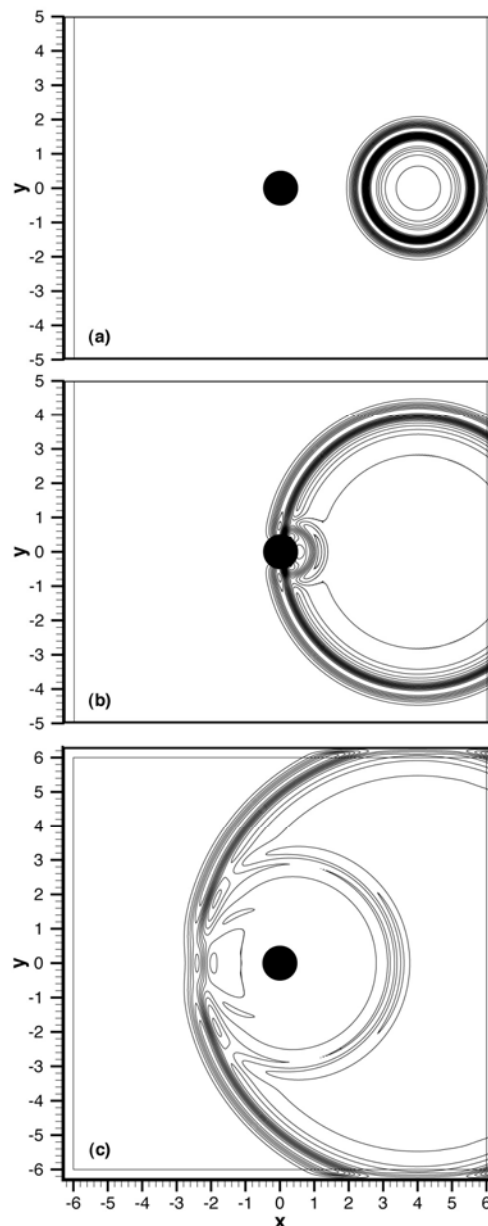
Fig.7.15. Pressure contours showing the scattering of an acoustic wave pulse by a circular cylinder. (a) $t = 1.6$. (b) $t = 4.0$. (c) $t = 6.4$. Dashed lines are the exact solution.
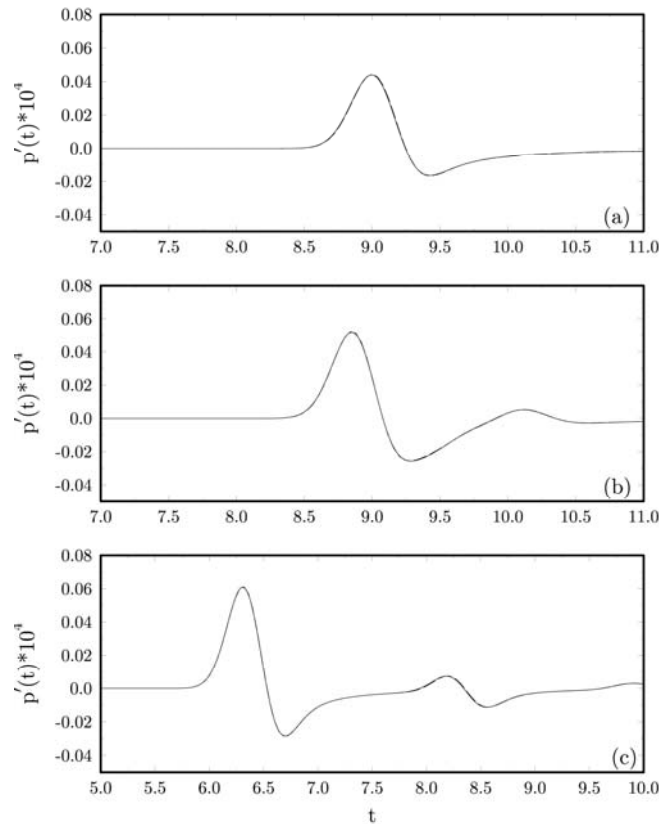
Fig.7.16. Time history of pressure perturbation p' = p–(1/g) at (a) $x = -5$, $y = 0$, (b) $x = -4$, $y = -4$, (c) $x = 0$, $y = -5$. Dashed line is the exact solution.

Fig.7.15 shows the computed pressure contours at $t = 1.6$, 4.0 and 6.4. The computed contours and the contours of the exact solution are indistinguishable (the difference is less than the thickness of the contour lines). The direct acoustic pulse and the scattered pulse can clearly be seen in this figure. For a more comprehensive comparison between the numerical and exact solution, the pressure time-history at three locations with Cartesian coordinates (–5,0), (–4,4) and (0,5) are plotted in Fig.7.16. Plotted in these figures also are the exact solution. The differences between the exact (dashed line) and computed solution are again very small.

(B) Plane wave scattering problem

In a paper by Kurbatskii and Tam (1997) the problem of plane wave scattering by a cylinder was solved using a Cartesian boundary treatment method. Here the same problem is solved using overset grids method. One advantage of the overset grids method in this case is that the simple ghost point method may be used to enforce the wall boundary condition. Again, the 7-point stencil DRP scheme is used to solve the Euler equations. The amplitude of the incoming waves with wave front perpendicular to the x-axis and wavelength equal to 8Dx is set to be small. The problem is, therefore, essentially linear and the accuracy of the computed solution can be ascertained by comparing with exact linear solution.
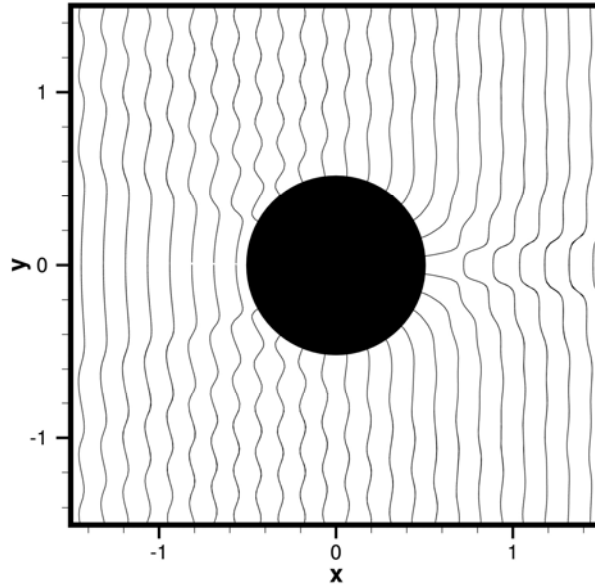
Fig.7.17. Zero pressure contours at the beginning of a cycle. Pressure pattern formed by the scattering of a plane wave by a cylinder. Wavelength equal to quarter diameter of cylinder.

Fig.7.17 shows the computed zero pressure contours at the beginning of a cycle. Plotted in this figure also are the contours of the exact solution in dashed line. The difference between the computed and the exact solution is very small; less than the thickness of the lines. Fig.7.18 shows the computed and the exact scattering cross-section $\sigma(\theta)$, defined by

$$\sigma(\theta) = \lim_{r \to \infty} \left(r \overline{p_s^2} \right)^{\frac{1}{2}} \tag{7.42}$$

where the overbar denotes time average. p_s is the pressure of the scattered acoustic waves. There is good agreement between the two. A major part of the small discrepancies arises because the computed result is measured at a finite distance from the center of the cylinder whereas the exact solution is determined by taking the asymptotic limit $r \to \infty$.
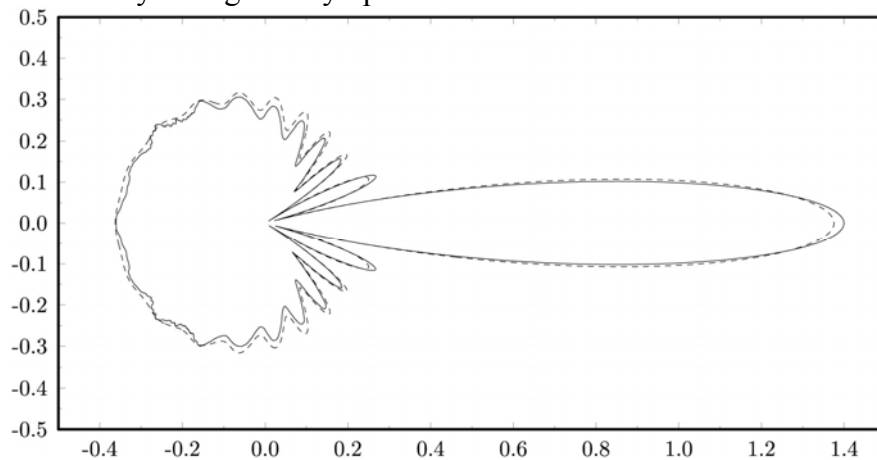
Fig.7.18. Comparison between computed and exact scattering cross-section. Dashed curve is the exact solution.

7.4 Sliding Interface Problems

7.4.1 Sliding interface problem in two dimensions

Aircraft engine noise is a significant environmental and certification issue. Noise generated by the fan rotor wake impinging on the stator is an important noise component at both take-off and landing. In the Second CAA Workshop on Benchmark Problems, a simplified model of this noise mechanism was proposed as a benchmark problem. One important feature of the problem is a sliding interface imitating the relative motion between a fan blade fixed computation domain and a stator blade fixed computation domain. Here a less demanding sliding interface problem is considered. It will be shown that the use of optimized interpolation scheme and overset grids method yields accurate numerical results.

Fig.7.19 shows two computation planes with six columns of overlapping meshes. The left computation plane is stationary. The right computation plane moves upward at a velocity of v_g. The sliding interface is the line at the center of the overlapping meshes. (x_1, y_1) will be used to denote the coordinates of a point in the stationary computation plane on the left and (x_2, y_2) will be used to denote the coordinates of a point in the moving computation plane on the right. The relationships between the two coordinate systems are, $x_2 = x_1$, $y_2 = y_1 - v_g t$. For computation purposes, square meshes are used in each computation plane, i.e. $\Delta x_1 = \Delta y_1$, $\Delta x_2 = \Delta y_2 = 0.78 \Delta x_1$. However, the mesh sizes are not the same in the two computation grids. Dimensionless variables with Δx_1 as length scale, a_0 (the speed of sound) as the velocity scale, $\Delta x_1 / a_0$ as the time scale, ρ_0 (mean flow density) as the density scale and $\rho_0 a_0^2$ as the pressure scale are used. It will be assumed that there is a uniform mean flow at 0.5 Mach number in the x-direction over the entire computation domain. The x-direction is the horizontal direction in Fig.7.19. The sliding interface is at $x = 60$.

The governing equations are the Euler equations. In the stationary computation plane, they are given by Eq. (7.1) with x replaced by x_1 and y by y_1. In the moving computation plane, the governing equations, with respect to a grid fixed frame of reference, are:

$$
\begin{aligned}
\frac{\partial \rho}{\partial t} + u \frac{\partial \rho}{\partial x_2} + \left(v - v_g\right)\frac{\partial \rho}{\partial y_2} + \rho\left(\frac{\partial u}{\partial x_2} + \frac{\partial v}{\partial y_2}\right) &= 0 \\[4pt]
\frac{\partial u}{\partial t} + u \frac{\partial u}{\partial x_2} + \left(v - v_g\right)\frac{\partial u}{\partial y_2} + \frac{1}{\rho}\frac{\partial p}{\partial x_2} &= 0 \\[4pt]
\frac{\partial v}{\partial t} + u \frac{\partial v}{\partial x_2} + \left(v - v_g\right)\frac{\partial v}{\partial y_2} + \frac{1}{\rho}\frac{\partial p}{\partial y_2} &= 0 \\[4pt]
\frac{\partial p}{\partial t} + u \frac{\partial p}{\partial x_2} + \left(v - v_g\right)\frac{\partial p}{\partial y_2} + \gamma p\left(\frac{\partial u}{\partial x_2} + \frac{\partial v}{\partial y_2}\right) &= 0
\end{aligned}
\tag{7.43}
$$

At time equal to zero, a pressure pulse centered at $x_1 = y_1 = 0$ is released. At the same time, a vorticity pulse and an entropy pulse centered at $x_1 = 40$, $y_1 = 0$ are released. Mathematically, the initial conditions at $t = 0$ are,

$$p = \frac{1}{\gamma} + \varepsilon \exp\left[-(\ln 2)\left(\frac{x_1^2 + y_1^2}{9}\right)\right]$$

$$\rho = 1 + \varepsilon \exp\left[-(\ln 2)\left(\frac{x_1^2 + y_1^2}{9}\right)\right] + 0.1\varepsilon \exp\left[-(\ln 2)\left(\frac{(x_1 - 40)^2 + y_1^2}{25}\right)\right]$$

$$u = 0.5 + 0.04\varepsilon y_1 \exp\left[-(\ln 2)\left(\frac{(x_1 - 40)^2 + y_1^2}{25}\right)\right]$$

$$v = -0.04\varepsilon(x_1 - 40)\exp\left[-(\ln 2)\left(\frac{(x_1 - 40)^2 + y_1^2}{25}\right)\right]$$

(7.44)

where $\varepsilon = 0.005$ and $\gamma = 1.4$. In the course of time, the acoustic, the vorticity and the entropy pulse will all be propagating or convected downstream. They will all reach the sliding interface at nearly the same time. They will then move across the sliding interface into the moving grid farther downstream. The exact solution of this problem was given in section 6.4.

In the computation, the 7-point stencil DRP scheme is again used. For points on the stationary grid, the unknowns on every grid point including those on the sliding interface are determined at every time step by solving Eq. (7.1). Similarly, for points on the moving grid, the unknowns on every grid point including those on the sliding interface are updated according to Eq. (7.43). The unknowns of the three extra columns of grid points extending beyond the sliding interface are not calculated by the 7-point stencil DRP scheme. They are found by optimized interpolation using a 16-point stencil from the values of the variables on the other grid. In this way, information of the solution is passed between the two computation grids.

Figs.7.19a,b,c show the computed density contours associated with the acoustic and entropy pulses at time $t = 5.6$, 44.9 and 73.0. In this computation v_g is set equal to 0.4. Also plotted in these figures are contours of the exact solution in dashed lines. Because the difference between the computed and the exact solution is small the dashed lines may not be easily detected. In Fig.7.19a, the two pulses are in the stationary grid. Figure7.19b shows that the acoustic pulse, moving downstream at three times the velocity of the entropy pulse, catches up with the entropy pulse right at the sliding interface. Figure7.19c shows that the entropy pulse has now been convected past the sliding interface onto the moving grid. At this time, the acoustic pulse has already propagated further downstream. Fig.7.20 shows the computed and the exact density waveform along the x-axis at four different times. The sliding interface is located at $x = 60$. It is clear from these figures that the treatment of a sliding interface using optimized interpolation is effective and accurate.
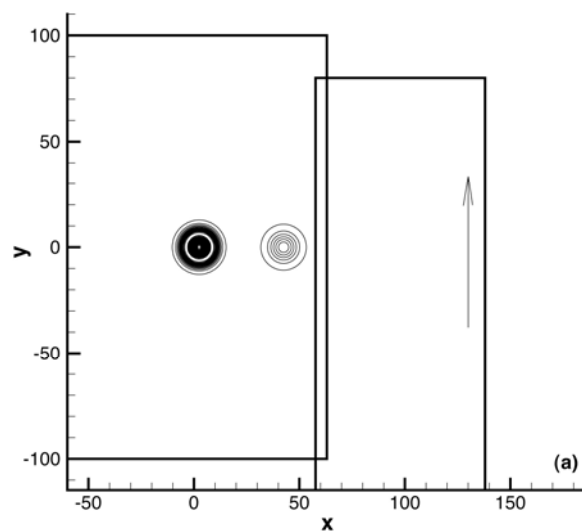
Fig.7.19a. Density contours showing the transmission of an acoustic and an entropy pulse across a sliding interface. Dashed lines are the exact solution. (a) $t = 5.6$. (b) $t = 44.9$. (c) $t = 73.0$.
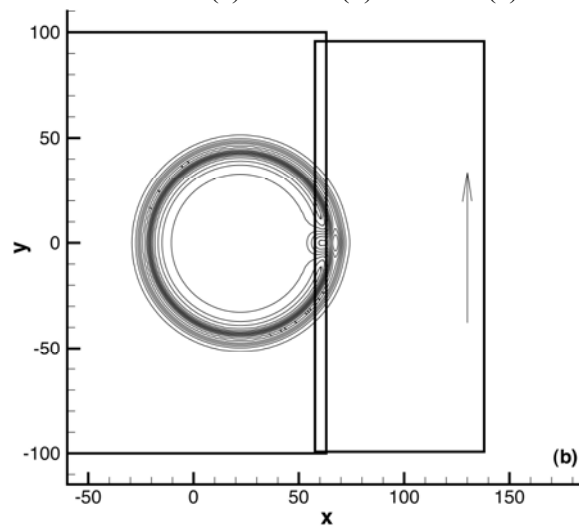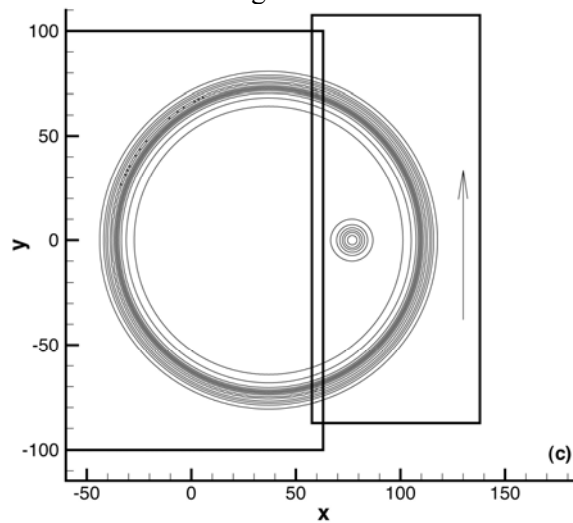

Fig.7.19b.

Fig.7.19c.

Figs.7.21a,b show the computed and the exact fluid velocity excluding the mean flow, $(u'^2 + v'^2)^{1/2}$, contours of the acoustic and vorticity pulses as they propagate through the sliding interface. Again, the difference between the computed and exact contours, being less than the thickness of the contour lines, is difficult to detect. Fig.7.22 shows the waveform along the x-axis at four instances of time. At $t = 29.25$ to $t = 39$ the two pulses merge and propagate across the sliding interface together. At time $t = 68.25$, the acoustic pulse has passed through the entropy pulse and the two pulses are now separated. The computed waveforms are in good agreement with exact solution.

In the above computation, the moving grid moves at a subsonic velocity. In a similar computation the same results are recovered when the moving grid slides past the stationary grid at a supersonic velocity.
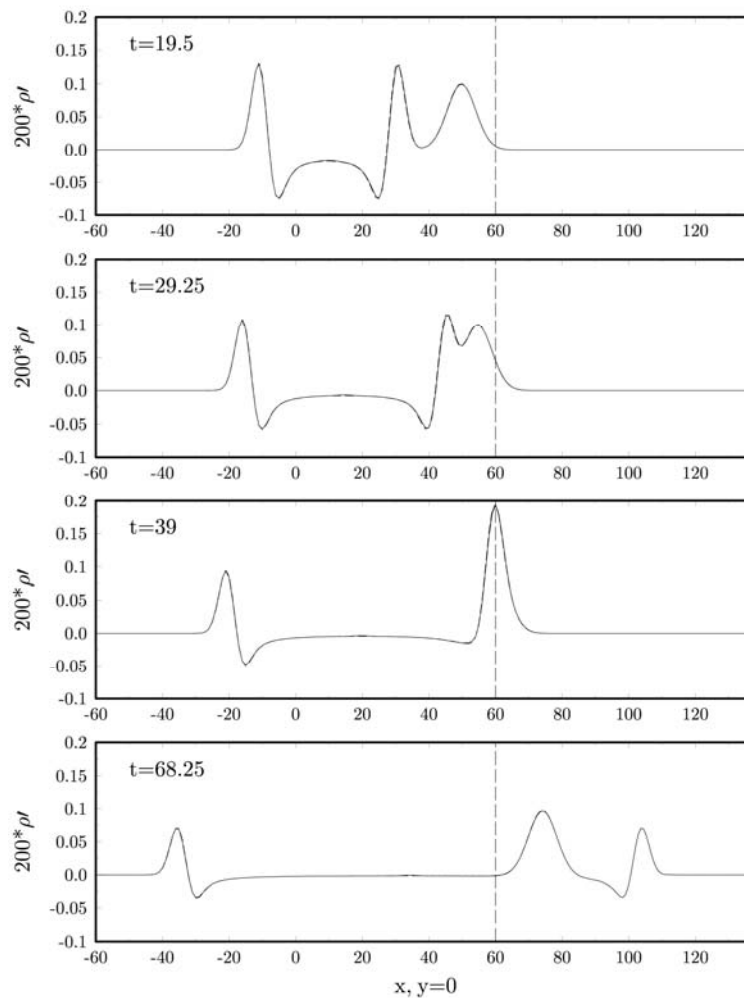
Fig.7.20. Spatial distribution of density perturbation $\rho' = \rho - 1$ associated with an acoustic and an entropy pulse propagating across a sliding interface located at $x = 60$. Dashed line is the exact solution.
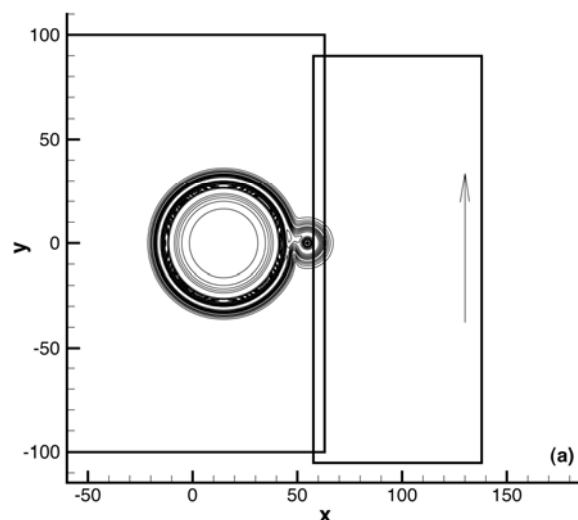
Fig.7.21a. Contours of fluid velocity $(u'^2 + v'^2)^{1/2}$ associated with the transmission of an acoustic and a vorticity pulse across a sliding interface. Dashed lines are the exact solution. (a) $t = 28.1$. (b) $t = 67.3$.
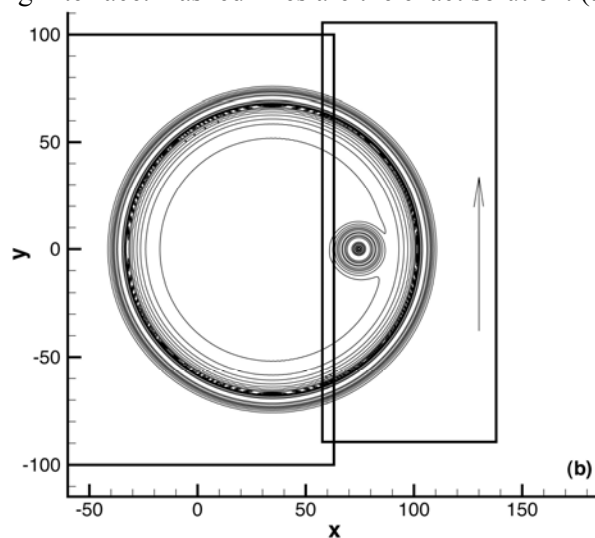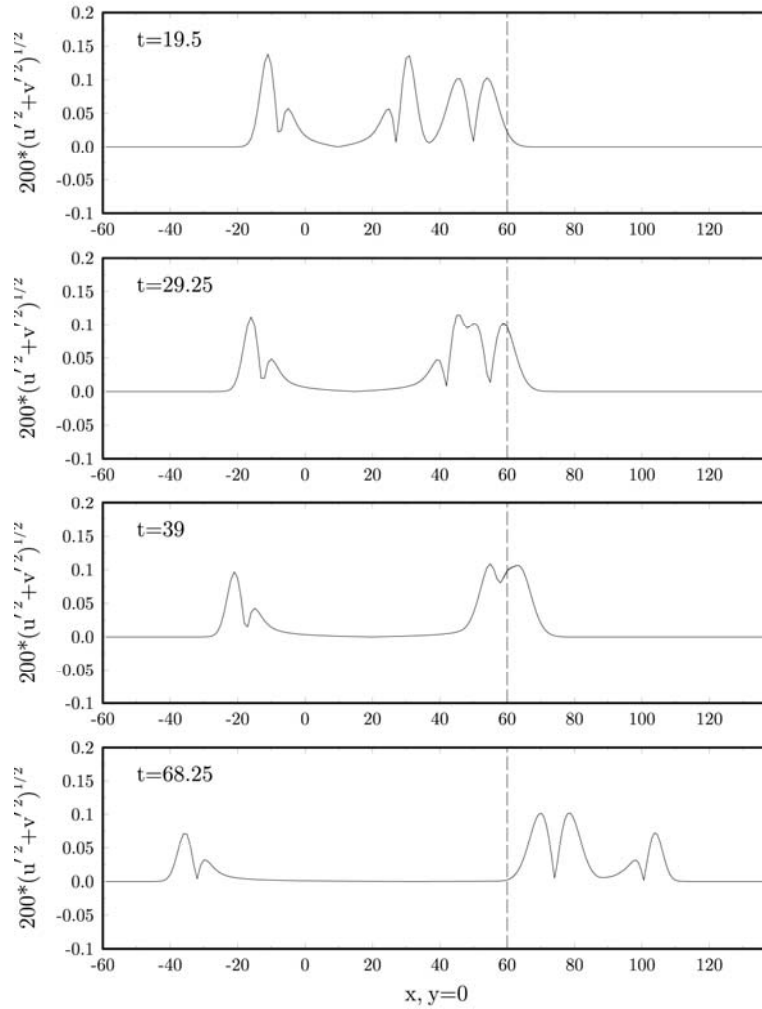

Fig.7.21b.

103

Fig.7.22. Spatial distribution of fluid velocity perturbation $(u'^2 + v'^2)^{1/2}$, where $u' = u - 0.5$, $v' = v$, associated with the transmission of an acoustic and a vorticity pulse across a sliding interface at $x = 60$. Dashed line is the exact solution.

7.4.2. Sliding interface problem in three dimensions

As an example of the use of overset grids in three dimensions, consider the propagation of a small amplitude three dimensional spherically symmetric acoustic pulse across a sliding interface. This problem is chosen because an exact solution (linearized) is available for comparison. On taking into account spherical symmetry, the linearized dimensionless momentum and energy equations are,

$$\frac{\partial v}{\partial t} = -\frac{\partial p}{\partial R} \tag{7.45}$$

$$\frac{\partial p}{\partial t} + \frac{1}{R^2}\frac{\partial}{\partial R}(R^2 v) = 0 \tag{7.46}$$

where R is the radial coordinate and v is the radial velocity. The initial conditions at t = 0 corresponding to a radially symmetric Gaussian pressure pulse with a half-width b are,

$$v = 0 \qquad (7.47)$$

$$p = \varepsilon \exp\left[-(\ln 2)\left(\frac{R}{b}\right)^2\right] \qquad (7.48)$$

The above problem may be recast into a problem involving p alone, that is,

$$\frac{\partial^2 p}{\partial t^2} - \frac{1}{R}\frac{\partial^2}{\partial R^2}(Rp) = 0 \qquad (7.49)$$

$$t = 0 \qquad p = \varepsilon \exp\left[-(\ln 2)\left(\frac{R}{b}\right)^2\right] \qquad (7.50)$$

$$\frac{\partial p}{\partial t} = 0 \qquad (7.51)$$

The exact solution of Eqs. (7.49), (7.50) and (7.51), which is bounded at R = 0, is

$$p = \left[\frac{R-t}{2R}e^{-(\ln 2)\left(\frac{R-t}{b}\right)^2} + \frac{R+t}{2R}e^{-(\ln 2)\left(\frac{R+t}{b}\right)^2}\right] \qquad (7.52)$$

Numerical computation of the above problem in three dimensional Cartesian coordinates using the 7-point stencil DRP scheme and the optimized multi-dimensional interpolation method for data transfer across the sliding interface has been carried out. This may be regarded as a three dimensional extension of the acoustic pulse problem of the previous section. The major difference is that there are now 64 points, 4x4x4, in the interpolation stencil. Again, as in the two dimensional problem, a uniform mean flow at Mach 0.5 in the x-direction is included (the exact solution is obtained by applying a moving coordinate transformation to Eq. (7.52)). The sliding grid is taken to be moving in the z-direction at a Mach number of 0.4. The full Euler equations are computed. The initial conditions are as given in Eqs. (7.47) and (7.48). The initial pressure pulse has a half-width of 6 mesh spacings and an intensity with $\varepsilon = 0.005$. The pulse is centered at the origin of the coordinate system. The sliding interface is located at x = 60.
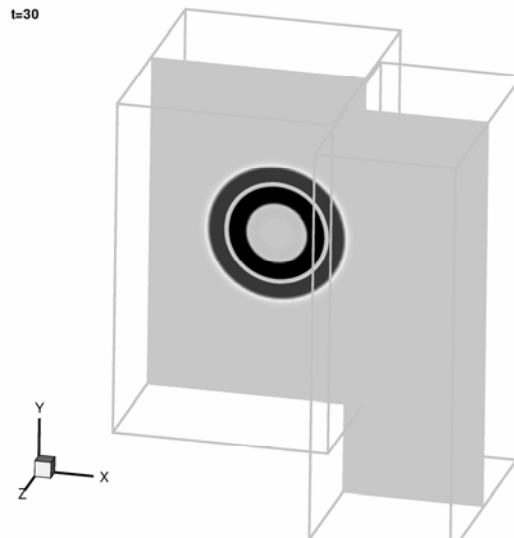
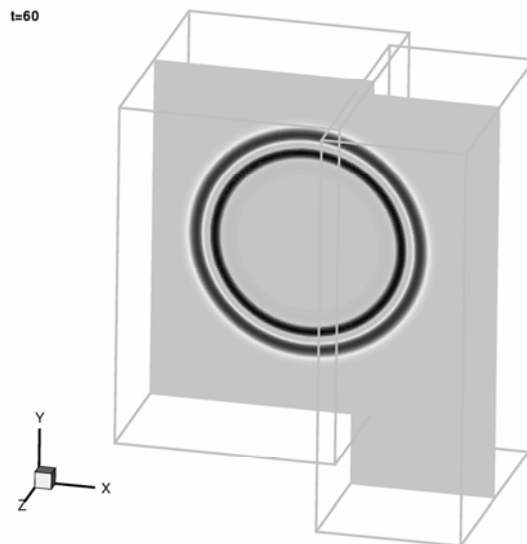Fig.7.23. Computed pressure contours in the x-y plane at t = 30.

Fig.7.24. Computed pressure contours in the x-y plane at t = 60.

Figs. (7.23) and (7.24) show the computed pressure contours in the x-y plane at time t = 30 and 60. The acoustic pulse expands spherically at a dimensionless speed of unity and is simultaneously convected in the downstream direction by the mean flow at a speed of 0.5. At time t = 30, the pulse has not reach the sliding interface. At t = 60, part of the pulse has crossed the sliding interface into the downstream moving grid. The computed pressure contours remain circular. Fig.7.25 shows the pressure contours at t = 60 in the x-z plane. Again, the contours are circles centered at x = 30, z = 0. Fig.7.26 shows the computed wave form in the x-y plane at t = 30, 40 and 60. Plotted in this figure also are the exact wave forms. They, however, cannot be detected because they differ from the computed solution by less than the thickness of the lines.
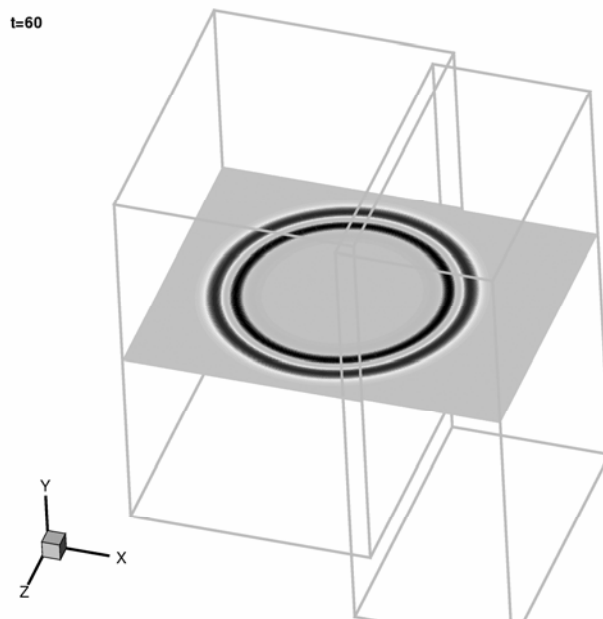
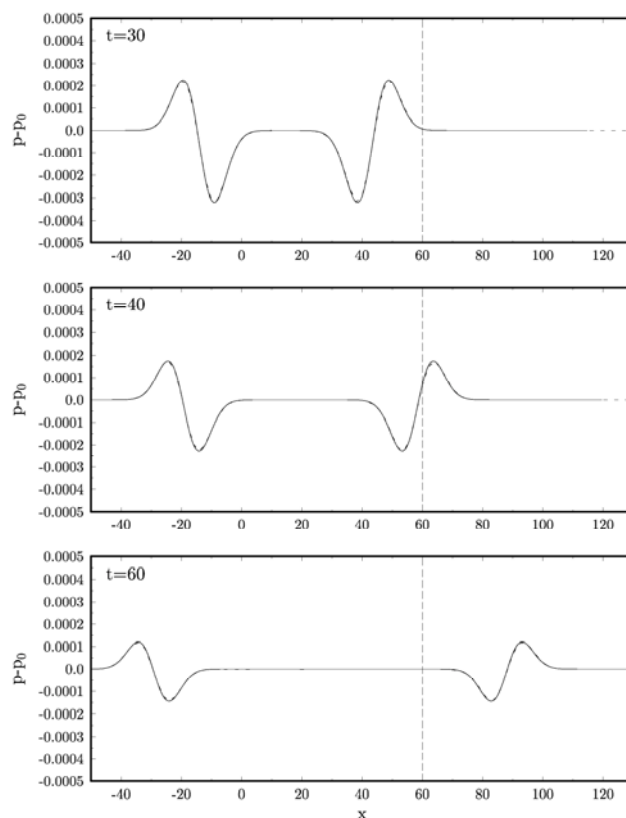Fig.7.25. Computed pressure contours in the x-z plane at t = 60.

Fig.7.26. Comparisons of computed waveforms with exact solution at t = 30, 40 and 60.

Finally, it is worthwhile to point out that overset grids method may also be used for computing the solutions of moving boundary problems. In such applications, a stationary grid and a moving grid

attached to a moving object are used. For this type of problem, the overlapping grids change constantly with time. As a result, a good deal of effort is needed in locating the overlapping grids.

Appendix 7A. Computation of the values of the elements of matrix A as $x_j \rightarrow x_k$

As alluded to before, when the stencil points are aligned on a coordinate line, the limit form of the matrix elements as given by Eqs. (7.16) and (7.20) are to be used; e.g.,

$$\lim_{x_j \rightarrow x_k} \frac{\Delta \sin\left(\frac{\kappa(x_j - x_k)}{\Delta}\right)}{(x_j - x_k)} = \kappa.$$

However, for points very nearly aligned, direct numerical evaluation of the matrix or vector elements is not recommended because of the division by a small number. Instead, we advise that the limit values be used whenever $|x_j - x_k| < \varepsilon$. To find a suitable value of ε, let us consider the error incurred when $(\Delta/(x_j - x_k))\sin(\kappa(x_j - x_k)/\Delta)$ is approximated by its limit value κ where $|x_j - x_k| < \varepsilon$. Let $\zeta = (x_j - x_k)/\Delta$, we have by Taylor series expansion,

$$\sin(\kappa\zeta) = \kappa\zeta - \frac{(\kappa\zeta)^3}{3!} + \frac{(\kappa\zeta)^5}{5!} - \ldots$$

It is easy to establish

$$\left| \sin(\kappa\zeta) - \kappa\zeta \right| \leq \frac{(\kappa\zeta)^3}{3!}$$

or

$$\frac{\left| \frac{\sin(\kappa\zeta)}{\zeta} - \kappa \right|}{\kappa} \leq \frac{(\kappa\zeta)^2}{3!}.$$

Thus the relative error of using the limit value to approximate the relevant parts of a matrix element is less than $(\kappa^2/3!)(\varepsilon/\Delta)^2$. We recommend to take $\varepsilon/\Delta = 10^{-5}$ for $\kappa = 1.2$. In this case, the relative error is less than 2.4×10^{-11}. This is an extremely small error.

Appendix 7B. Derivation of an exact solution for the scattering of an acoustic pulse by a circular cylinder

In this appendix, an exact analytical solution for the scattering of an acoustic pulse by a circular cylinder is derived. The solution provided in the Proceedings of the Second Computational Aeroacoustics Workshop on Benchmark Problems has an error.

Let the cylinder be centered at $(x,y) = (0,0)$ with a radius r_o and the acoustic pulse be initialized as

$$p(x,y,0) = e^{-b[(x-x_s)^2 - (y-y_s)^2]}, \quad u = v = 0 \quad \text{at} \quad t = 0, \tag{7.53}$$

where p is the pressure, (u,v) is the velocity, and $b = (\ln 2)/d^2$. Here d is the half-width of the pulse. The solution will be found in terms of a velocity potential ϕ defined as

$$p = -\frac{\partial \phi}{\partial t}, \quad u = \frac{\partial \phi}{\partial x}, \quad v = \frac{\partial \phi}{\partial y}. \tag{7.54}$$

Let

$$\phi(x,y,t) = \phi_i(x,y,t) + \phi_r(x,y,t)$$

where $\phi_i(x,y,t)$ represents the wave generated by the pulse in the free space and $\phi_r(x,y,t)$ represents the wave reflected by the cylinder. The solution for $\phi_i(x,y,t)$ is,

$$\phi_i(x,y,t) = \text{Im}\left\{ \int_0^\infty A_i(x,y,\omega) e^{-i\omega t} d\omega \right\} \tag{7.55}$$

where

$$A_i(x,y,\omega) = \frac{1}{2b} e^{-\frac{\omega^2}{(4b)}} J_0(\omega r_s) \tag{7.56}$$

and $r_s = \sqrt{(x-x_s)^2 + (y-y_s)^2}$. Here $\text{Im}\{\ \}$ and $\text{Re}\{\ \}$ denote the imaginary and real part of $\{\ \}$, respectively, and J_k denotes the Bessel function of order k.

To find ϕ_r, on following Eq. (7.55), the solution may be taken to have the form,

$$\phi_r(x,y,t) = \text{Im}\left\{ \int_0^\infty A_r(x,y,\omega) e^{-i\omega t} d\omega \right\} \tag{7.57}$$

in which $A_r(x,y,\omega)$ satisfies the Helmholtz equation

$$\left(\frac{\partial^2 A_r}{\partial x^2} + \frac{\partial^2 A_r}{\partial y^2} \right) + \omega^2 A_r = 0$$

and the following solid wall boundary condition on the cylinder,

$$\frac{\partial A_r}{\partial r} = -\frac{\partial A_i}{\partial r} \quad \text{at} \quad r = r_0. \tag{7.58}$$

A_r can be solved by separation of variables in the polar coordinates (r,θ) which gives the following expansion

$$A_r(x,y,\omega)=\sum_{k=0}^{\infty}C_k(\omega)H_k^{(1)}(r\omega)\cos(k\theta).\qquad(7.59)$$

In Eq. (7.59), $H_k^{(1)}$ is the Hankel function of the first kind of order k. The expansion in Eq. (7.59) ensures that ϕ_r will satisfy the far field radiation condition. Then the boundary condition Eq. (7.58) leads to

$$\sum_{k=0}^{\infty}C_k(\omega)\omega H_k^{(1)'}(r_0\omega)\cos(k\theta)=\frac{1}{2b}e^{-\frac{\omega^2}{(4b)}}\omega J_1(\omega r_{s_0})\frac{r_0-x_s\cos\theta-y_s\sin\theta}{r_{s_0}}\qquad(7.60)$$

where

$$r_{s0}=r_s\big|_{r=r_0}=\sqrt{r_0^2-2r_0x_s\cos\theta-2r_0y_s\sin\theta+x_s^2+y_s^2}.$$

On considering the left side of Eq. (7.60) as a Fourier cosine series in θ, it is straightforward to find,

$$C_k(\omega)=\left(\frac{\omega}{2b}e^{-\frac{\omega^2}{(4b)}}\right)\frac{\varepsilon_k}{\pi\omega H_k^{(1)'}(r_0\omega)}\int_0^{\pi}J_1(\omega r_{s0})\frac{r_0-x_s\cos\theta-y_s\sin\theta}{r_{s0}}\cos(k\theta)d\theta$$

where $\varepsilon_0=1$ and $\varepsilon_k=2$ for $k\neq 0$.

Finally, the total pressure field can be found as follows,

$$\begin{aligned}p(x,y,t)&=-\frac{\partial\phi}{\partial t}=-\frac{\partial}{\partial t}(\phi_i+\phi_r)\\&=\mathrm{Re}\left\{\int_0^{\infty}(A_i(x,y,\omega)+A_r(x,y,\omega))\omega e^{-i\omega t}d\omega\right\}\end{aligned}$$

where $A_i(x,y,\omega)$ is given by Eq. (7.56) and $A_r(x,y,\omega)$ by Eq. (7.59).

8. MULTI-SCALES PROBLEMS

Many aeroacoustics problems involve multiple length and time scales. This should not be difficult to understand. For, in addition to the intrinsic sizes and scales of the noise sources, the acoustic wavelength is an inherent length scale of the problem. In many instances, the length scale of the noise source differs greatly from the acoustic wave length. This leads to a large disparity in length scales as in classical multi-scales problems. For example, in supersonic jet noise, Mach wave radiation is generated by the instability waves of the jet flow. The instability waves are supported by the thin shear layer of the jet. In the region near the nozzle exit, the

averaged shear layer thickness is about $0.1D$ where D is the jet diameter. The acoustic wave length, on the other hand, is two or more jet diameters long. Thus there is an order of magnitude difference between those characteristic lengths. In sound scattering problems, the length scale of the surface geometry of the scatterers may be much smaller than the acoustic wave length. This occurs very often in edge scattering and diffraction problems. A concrete example is the radiation of fan noise from a jet engine inlet. The acoustic wave length is much longer than the radius of the lip of the engine inlet. To obtain an accurate numerical solution of the inlet diffraction problem, a fine mesh is needed around the lip region. Oftentimes, an aeroacoustics problem becomes a multi-scales problem because of the change in the physics governing different parts of the Computational domain. An example is the shedding of vortices at the edge of a resonator or a sharp edge of a solid body induced by high intensity incident sound waves. Away from the solid surface, the fluid is nearly inviscid. But close to the wall, viscosity effect dominates. The oscillatory motion of the incident sound waves induces a very thin Stokes layer on the solid surface. The Stokes layer rolls up at the corner of a solid surface to form vortices that shed periodically. To simulate the vortex shedding process, it is, therefore, necessary to use very fine mesh close to the solid surface and around the corner to resolve the Stokes layer. But away from the solid surface, a coarse mesh with 7 mesh points per acoustic wave length is all that is needed to capture the sound waves accurately using the 7-point stencil DRP scheme.

Computationally, a very effective way to treat a multi-scales problem is to use a multi-size mesh. Fig. 8.1 shows a typical multi-size mesh. In this example, the mesh size changes by a factor of two across the mesh-size-change interface. A factor-of-two change in the mesh size is not an absolute necessity. It is recommended because a larger change may result in a very strong artificial discontinuity inside the computational domain. On the other hand, a smaller change may require several steps of changes to achieve the same total change in mesh size. This will give rise to a large number of mesh-size-change interfaces, which is not desirable.

The time step used in a computation is dictated very often by the choice of spatial mesh size. Recall that numerical instability requirements link Δt, the time step, to the mesh size Δx. If a single time step marching scheme such as the Runge-Kutta method is used, then Δt is dictated by the smallest size mesh of the entire computational domain. This results in an inefficient computation. The optimum situation is to use a Δt consistent with the local numerical stability requirement. In such an arrangement, most of the computation is concentrated in regions with fine meshes, as it should be. In the coarse mesh region, the solution is updated only occasionally with a much larger time step. This type of algorithm is referred to as "multi-size-mesh multi-time-step" schemes. If the mesh-size change is a factor of two across mesh block interface, the time step should also change by a factor of two to maintain numerical stability. For multi-level time marching schemes such as the DRP scheme, the use of multiple time steps with a factor of two change between adjacent mesh block is easy to arrange. Fig. 8.2 shows such an arrangement in which the computed solution advanced in steps of Δt in the fine mesh region and in steps of $2 \Delta t$ in the coarse mesh region.
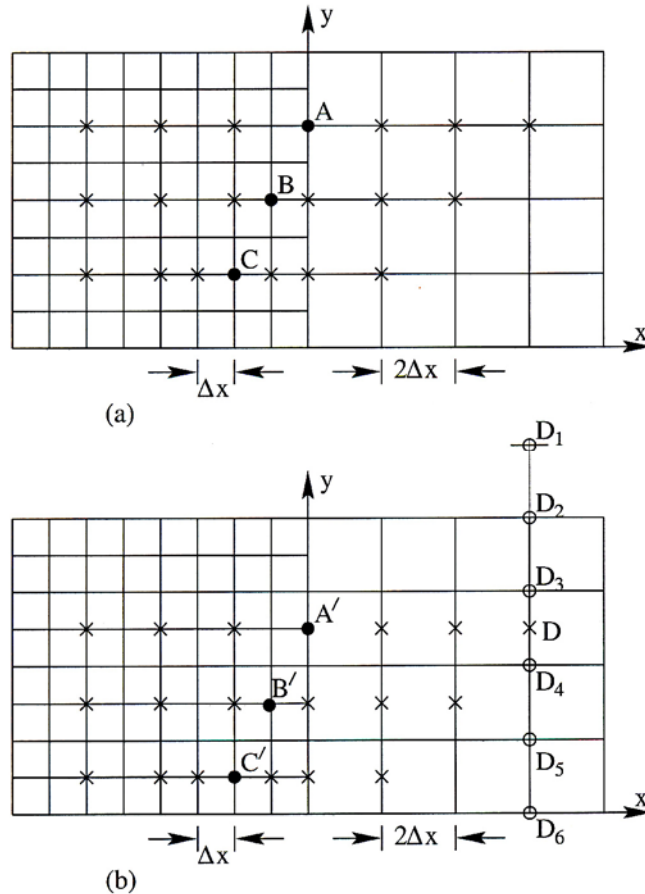
111

Figure 8.1. Special stencils for use in the mesh-size-change buffer regions. ● mesh points at which finite difference approximation of spatial derivative is to be found. × stencil points. ○ points used for interpolation.

In carrying out a multi-size-mesh multi-time-step computation, the computation scheme to be used in each of the uniform mesh block is the same as if there is a single size mesh throughout the entire computation domain. The exception is for a narrow buffer region at the block interface. In the buffer region, special stencils are to be used so that information on the solution can be transmitted through without significant degradation. Also it is to be noted that any surface of discontinuity, no matter if it is a mesh-size-change interface or an internal or external boundary, is a likely source of short spurious numerical waves. To suppress the generation of spurious short waves, special artificial selective damping stencils should be incorporated in the computation scheme for mesh points adjacent to the block interface. The design of these special stencils is given in the next three sections.
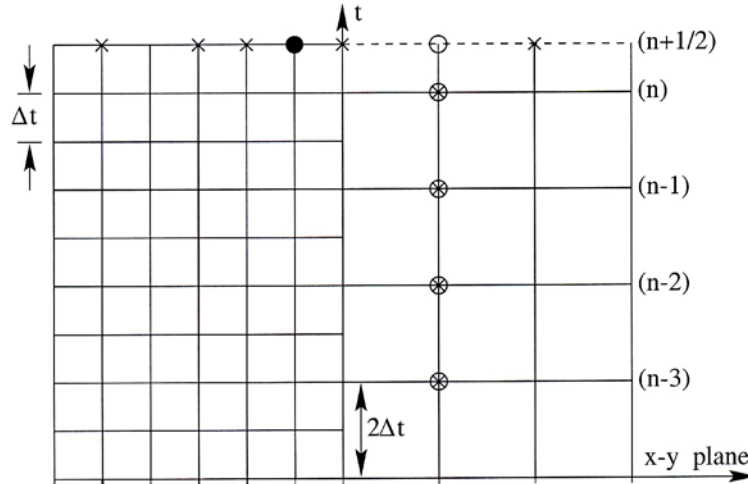
Figure 8.2.   Special time-marching stencil for use in the mesh-size-change buffer region.
○ mesh points at which solution to be found at a half-time level. ⊗ stencil points.

8.1 Spatial Stencils for Use in Mesh-Size-Change Buffer Region

If a factor of two increase in the mesh size between adjacent blocks is used, then every other mesh line in the fine mesh block continues into the coarse mesh block as shown in Fig. 8.1. The remaining set of mesh lines terminates at the mesh-size-change interface. To compute the x-derivative for points on the coarse grid, including points on the interface such as point A, the 7-point central difference DRP scheme may be used even though part of the stencil is extended into the fine mesh region. For mesh points on the fine grid, again the 7-point central difference DRP scheme may be used except for the first three columns (or rows) of mesh points right next to the coarse grid. For points on the continuing mesh lines such as points B and C in Fig. 8.1, special central difference stencils as indicated are to be used. These stencils may be written in the form,

$$\left(\frac{\partial f}{\partial x}\right)_B \cong \frac{1}{\Delta x}\sum_{j=-3}^{3} a_j^B f_j^B \tag{8.1}$$

$$\left(\frac{\partial f}{\partial x}\right)_C \cong \frac{1}{\Delta x}\sum_{j=-3}^{3} a_j^C f_j^C . \tag{8.2}$$

To find the stencil coefficients a_j^B and a_j^C ($j = -3$ to 3), the optimization procedure of section 2.4.1 may be followed. Now, first consider the stencil for point B. It will be assumed that $f(x)$ has a Fourier transform $\tilde{f}(\alpha)$ with absolute value $A(\alpha)$ and argument $\phi(\alpha)$; i.e.,

$$A(\alpha) = |\tilde{f}(\alpha)|, \qquad \phi(\alpha) = \arg[\tilde{f}(\alpha)].$$

The Fourier transform may be written as,

$$f(x) = \int_{-\infty}^{\infty} A(\alpha)e^{i[\alpha x + \phi(\alpha)]}d\alpha . \tag{8.3}$$

In other words, $f(x)$ is made up of a superposition of simple waves, $f_\alpha(x)$, of the form,

$$f_\alpha(x) = e^{i[\alpha x + \phi(\alpha)]}.$$

(8.4)

weighted by $A(\alpha)$. Now the accuracy of finite difference approximation (8.1) of each simple wave component of $f(x)$ is examined. Upon substituting $f_\alpha(x)$ into Eq. (8.1), the finite difference approximation becomes,

$$\alpha f_\alpha(x) \cong \overline{\alpha} f_\alpha(x)$$

where

$$\overline{\alpha} = \frac{2}{\Delta x}\left[a_1^B \sin(\alpha \Delta x) + a_2^B \sin(3\alpha \Delta x) + a_3^B \sin(5\alpha \Delta x)\right]$$

(8.5)

is the wave number of the finite difference stencil. In deriving (8.5), the antisymmetric condition, $a_{-j}^B = -a_j^B$, has been invoked.

On following the steps of section 2.4.1, the condition that Eq. (8.1) or Eq. (8.5) be accurate to order $(\Delta x)^4$ is imposed. By means of Taylor series expansion, this condition yields the following restrictions on the stencil coefficients,

$$\begin{aligned}
2\left(a_1^B + 3a_2^B + 5a_3^B\right) &= 1 \\
a_1^B + 3^3 a_2^B + 5^3 a_3^B &= 0
\end{aligned}$$

(8.6)

The coefficients will now be chosen so that the error of using $\overline{\alpha}\Delta x$ to approximate $\alpha \Delta x$ over the band of wave number $|\alpha \Delta x| < \kappa$, E, is minimum subjected to conditions (8.6). For this purpose, the error is defined as

$$E = \int_0^\kappa \left[\overline{\alpha}\Delta x - \alpha \Delta x\right]^2 d(\alpha \Delta x)$$

(8.7)

The condition for a minimum is given by (after eliminating a_2^B and a_3^B by Eq. (8.6))

$$\frac{dE}{da_1^B} = 0.$$

(8.8)

An extensive numerical study of the effects of the choice of κ on $\overline{\alpha}(\alpha)$ and $d\overline{\alpha}/d\alpha$ has been carried out. Based on the numerical results, it is deemed that a good choice of the values of κ is 0.85. For this choice, the values of the stencil coefficients are,

$$a_0^B \quad = \quad 0.0$$

$$a_1^B \quad = \quad a_{-1}^B = 0.595328177715$$

$$a_2^B \quad = \quad a_{-2}^B = -0.037247422191$$

$$a_3^B \quad = \quad a_{-3}^B = 0.003282817772$$

Figs. 8.3 and 8.4 show the corresponding $\overline{\alpha}(\alpha)$ and $d\overline{\alpha}/d\alpha$ curves. The resolution and dispersion characteristics of the stencil lie in-between those of the central difference DRP scheme on the two sides of the interface.
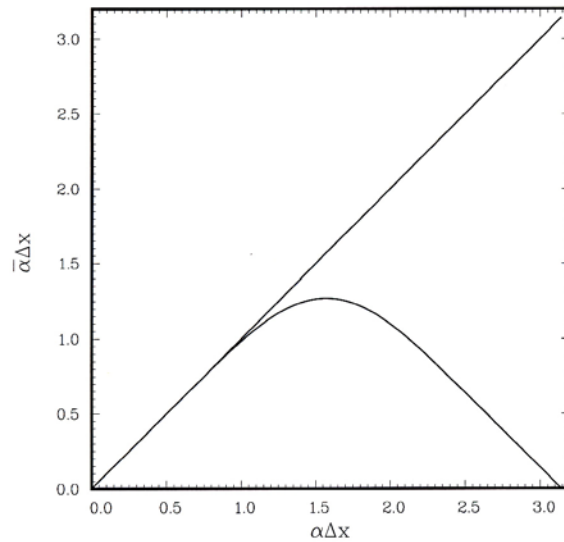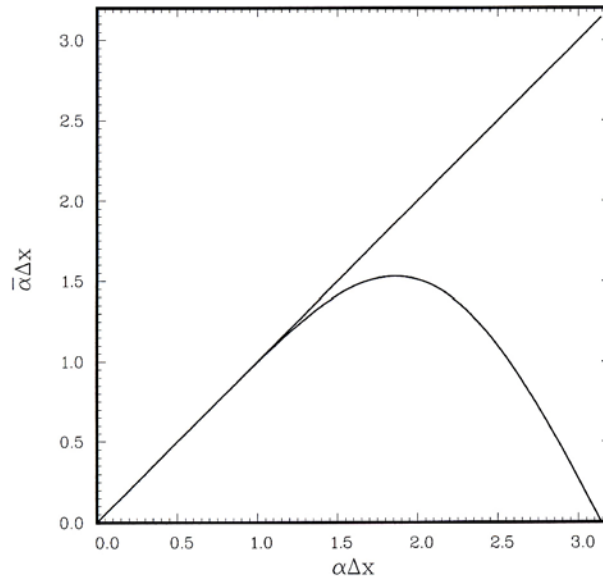

Figure 8.3. Dependence of $\overline{\alpha}\Delta x$ on $\alpha\Delta x$ for stencil B. $\kappa = 0.85$.
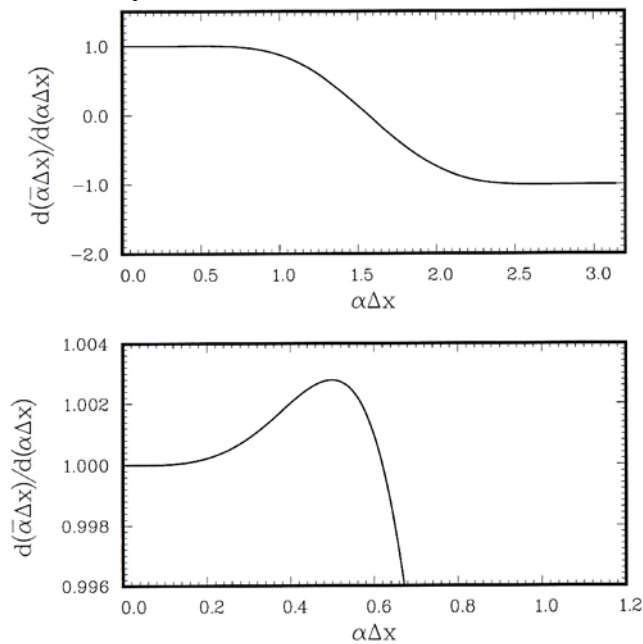
Figure 8.4. The $\dfrac{d(\overline{\alpha}\Delta x)}{d(\alpha\Delta x)}$ curve for stencil B.

On proceeding as for stencil B, the stencil coefficients for stencil C may be found. For stencil C, it is recommended that the value $\kappa = 1.0$ be used. The stencil coefficients are,

$$a_0^C = 0.0$$

$$a_1^C = a_{-1}^C = 0.726325187522$$

$$a_2^C = a_{-2}^C = -0.120619908868$$

$$a_3^C = a_{-3}^C = 0.003728657553$$

Figs. 8.5 and 8.6 show the corresponding $\overline{\alpha}(\alpha)$ and $d\overline{\alpha}/d\alpha$ curves for this stencil. Again the resolution and dispersion characteristics lie in-between those of the central difference DRP scheme on the two sides of the interface.

Figure 8.5. Dependence of $\overline{\alpha}\Delta x$ on $\alpha\Delta x$ for stencil c. $\kappa = 1.0$.

For mesh points lying on the terminating mesh lines such as points A', B' and C' of Fig. 8.1, the same stencils as for A, B and C may be used. However, the stencils extend into points in the coarse mesh region where the solution is not computed. To obtain the values of the solution at these points, such as point D, it is recommended that interpolation be used. The interpolation stencil, a symmetric stencil is preferred, makes use of the values of the adjacent six mesh points, D_1 to D_6, as shown in Fig. 8.1. In actual computation, the interpolation step is executed only after the solution on the coarse mesh region has been advanced by a time step. The interpolated values allow the solution on the fine mesh side to continue advancing in time.
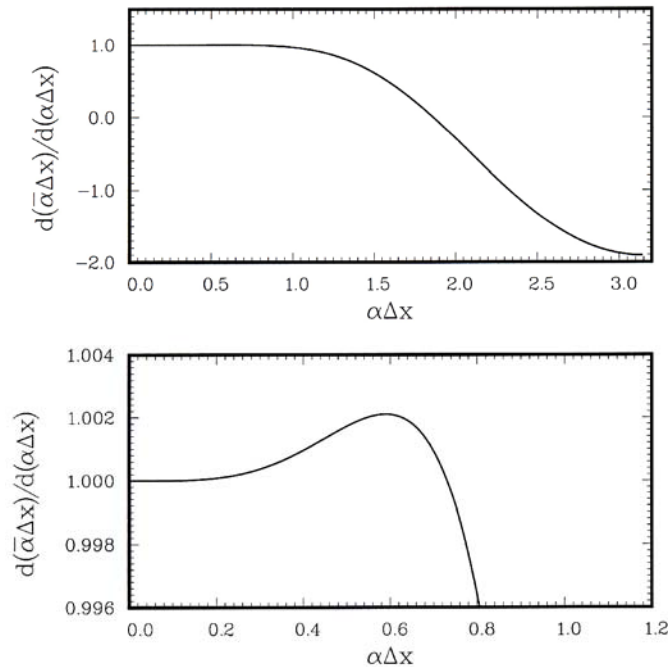
Figure 8.6. The $\dfrac{d(\overline{\alpha}\Delta x)}{d(\alpha\Delta x)}$ curve for stencil C.

8.2 Time-Marching Stencil

The time marching step, Δt, is constrained by the numerical stability or accuracy requirements of a computation scheme. In general, the stability or accuracy requirements link Δt directly to the mesh size Δx. Thus in a region with large mesh size, a larger Δt may be used. When more than one mesh size is used, the optimum strategy is to use the largest time step permissible in each region. It follows, if the mesh size changes by a factor of two in adjacent domains, the time step should also change by the same ratio. Fig. 8.2 shows the time levels of the computation in the mesh-size-change buffer region. In the fine mesh region on the left, the time step is Δt. In the coarse mesh region on the right, the time step is $2\Delta t$. Effectively, the fine mesh region is computed twice as often as the coarse mesh region.

Suppose the solution is known at time level n (see Fig. 8.2), the solution in the fine mesh region may be advanced by a time step Δt to time level $(n+1/2)$ in the usual way. Once this is completed, the next step is to advance the solution to time level $(n+1)$ in both the fine and coarse mesh regions. It is straightforward to carry out this step in the coarse mesh region by using the solution on time levels n, $(n-1)$, $(n-2)$ and $(n-3)$. However, for points in the buffer region on the fine mesh side, the stencils extend into the coarse mesh region. There is no information at the $(n+1/2)$ time level at these points on the coarse mesh side. To provide the needed information of the solution, it is necessary to compute the solution at the time level $(n+1/2)$ for the first two rows or columns of the mesh point on the coarse mesh side based on the solution at time levels n, $(n-1)$, $(n-2)$ and $(n-3)$. To advance the solution by a half time step as shown in Fig. 8.2, the following four level scheme may be used.

$$\mathbf{u}_{|,m}^{(n+\frac{1}{2})} = \mathbf{u}_{|,m}^{(n)} + (2\Delta t)\sum_{j=0}^{3} b_j^* \mathbf{K}_{|,m}^{(n-j)} \tag{8.9}$$

where $\mathbf{K} = d\mathbf{u}/dt$ is given by the governing equation. (ℓ,m) are the spatial indices.

To find the stencil coefficients b_j^* of Eq. (8.9), one may consider $\mathbf{u}$ to be made up of a Fourier spectrum of simple harmonic components of the form $e^{-i\omega t}$ where ω is the angular frequency. The effect of time marching algorithm (8.9) on each Fourier component of frequency ω may be analyzed by substituting $\mathbf{u}_{\ell,m}^{(n)} = \mathbf{u}_{\ell,m}(\mathbf{t}) = \mathbf{A}e^{-i\omega n(2\Delta t)}$ into Eq. (8.9). It is easy to find,

$$\frac{d\mathbf{u}_{|,m}}{dt} = \frac{\left(e^{-i\omega\Delta t} - 1\right)}{(2\Delta t)\sum_{j=0}^{3} b_j^* e^{2ij\omega\Delta t}} \mathbf{u}_{|,m} \tag{8.10}$$

Since $d(\mathbf{u}_{\ell,m}/dt) = i\omega\mathbf{u}_{\ell,m}$, the factor, on the right side of Eq. (8.10) multiplying $\mathbf{u}_{\ell,m}$, must be equal to $-i\overline{\omega}$ where $\overline{\omega}$ is the angular frequency of the time marching finite difference scheme. Thus one finds,

$$\overline{\omega}\Delta t = \frac{i\left(e^{-i\omega\Delta t} - 1\right)}{2\sum_{j=0}^{3} b_j^* e^{2ij\omega\Delta t}} \tag{8.11}$$

There are four coefficients, namely, b_0^*, b_1^*, b_2^* and b_3^*. Here the condition that $\overline{\omega} \cong \omega$ be accurate to order $(\Delta t)^3$ is imposed. On expanding Eq. (8.11) by Taylor series, it is straightforward to find that the four coefficients are related by the following three conditions.

$$\sum_{j=0}^{3} b_j^* = \frac{1}{2} \tag{8.12}$$

$$\sum_{j=0}^{3} jb_j^* = -\frac{1}{8} \tag{8.13}$$

$$\sum_{j=0}^{3} j^2 b_j^* = \frac{1}{24}. \tag{8.14}$$

There is no loss of generality in regarding b_0 as the remaining free parameter. The value of b_0 is chosen so that $\overline{\omega}$ is a good approximation of ω over the frequency band $-\lambda \le \omega\Delta t \le \lambda$. This is done by minimizing the integral

$$E(b_0) = \int_{-\lambda}^{\lambda} \left\{ \sigma\left[\text{Re}(\overline{\omega}\Delta t) - \omega\Delta t\right]^2 + (1-\sigma)\left[\text{Im}(\overline{\omega}\Delta t)\right]^2 \right\} d(\omega\Delta t) \tag{8.15}$$

where σ is the weight parameter. The condition for minimization is $dE/db_0 = 0$.

A numerical study of the real and imaginary parts of $(\overline{\omega}\Delta t - \omega\Delta t)$ for different choices of λ and σ has been carried out. Based on the results of this study, the values $\lambda = 0.5$ and $\sigma = 0.42$ are recommended for use. For this choice of parameters, the optimized coefficients are,

$$b_0^* = 0.773100253426$$

$$b_1^* = -0.485967426944$$

$$b_2^* = 0.277634093611$$

$$b_3^* = -0.064766920092$$

For a given $\overline{\omega}\Delta t$, Eq. (8.11) yields 7 roots of $\omega\Delta t$. As in the original DRP scheme, only one of the roots yields the physical solution. All the other roots are spurious and should be damped if the scheme is to be stable. Fig. 8.7 shows the dependence of the roots on $\overline{\omega}\Delta t$. The scheme is stable if $\overline{\omega}\Delta t < 0.88$. If $\overline{\omega}\Delta t$ is restricted to less than or equal to 0.19, then the damping rate, $Im(\omega\Delta t)$, is less than 0.78×10^{-5}, which is quite small. The accuracy of this scheme when restricted to this range is comparable to that of the standard DRP scheme.
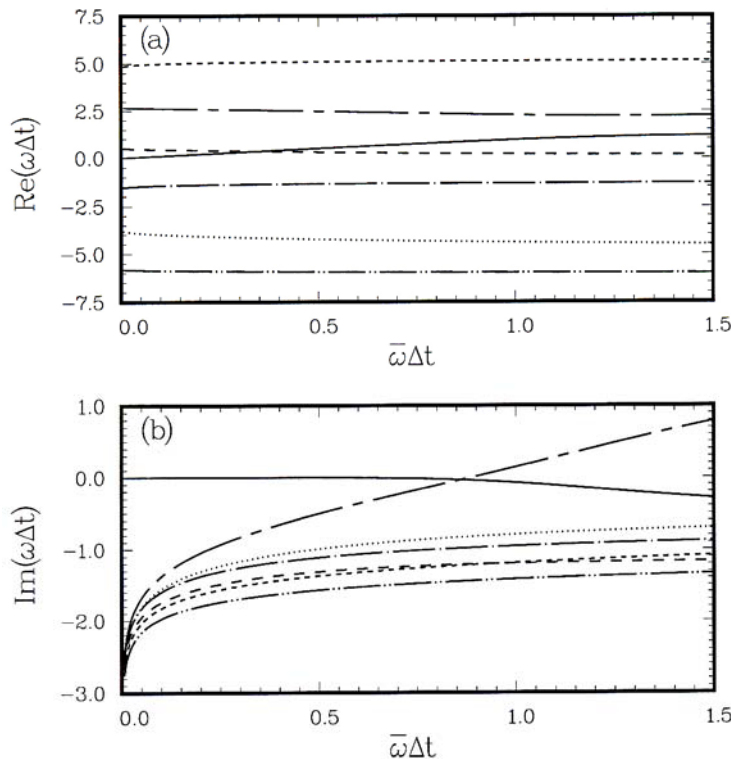

Figure 8.7. The dependence of the seven roots of $\omega\Delta t$ on $\overline{\omega}\Delta t$.

8.3 Damping Stencils

In numerical computation, surfaces of discontinuity, such as mesh-size-change interfaces, are potential sources of spurious numerical waves. For this reason, it is necessary to add artificial selective damping in the buffer region of the interface. For points A and A', the 7-point damping

stencils discussed in section 4.2 may be used. For points B or B', C or C' special damping stencils are needed.

Consider the x-momentum equation of the linearized Euler equations.

$$\frac{\partial u}{\partial t} + K = 0. \tag{8.16}$$

The discretized form of Eq. (8.16) at point C including the artificial selective damping terms is

$$\left(\frac{\partial u}{\partial t}\right)_C + K = \frac{\nu_a}{(\Delta x)^2} \sum_{j=-3}^{3} d_j^C u_{C,j} \tag{8.17}$$

where the damping stencil coefficients satisfy the symmetric condition $d_{-j} = d_j$. ν_a is the artificial kinematic viscosity. Δx is the mesh size at C.

Consider a single Fourier component of u i.e. u $= \hat{u}(t) e^{i\alpha \ell \Delta x}$. Substitution into Eq. (8.17) yields

$$\left(\frac{\partial u}{\partial t}\right)_C + K = -\frac{\nu_a}{(\Delta x)^2} D^C(\alpha \Delta x) u \tag{8.18}$$

where the damping function $D^C(\alpha \Delta x)$ is given by,

$$D^C(\alpha \Delta x) = d_0^C + 2\left[d_1^C \cos(\alpha \Delta x) + d_2^C \cos(2\alpha \Delta x) + d_3^C \cos(4\alpha \Delta x)\right]. \tag{8.19}$$

It is required that there is no damping if u is a constant (or $\alpha \Delta x \rightarrow 0$). This leads to

$$d_0^C + 2\sum_{j=1}^{3} d_j = 0. \tag{8.20}$$

The normalization condition is $D^C(\pi) = 1.0$ or

$$d_j^C + 2\left(-d_1^C + d_2^C + d_3^C\right) = 1. \tag{8.21}$$

In addition, it is intended to select the remaining parameters such that Eq. (8.19) is a good approximation to a Gaussian function of half width σ centered at $\alpha \Delta x = \pi$. Specifically, the integral

$$\int_0^\kappa \left[D^C(\alpha \Delta x) - e^{-(\ln 2)\left(\frac{\alpha \Delta x - \pi}{\sigma}\right)^2}\right] d(\alpha \Delta x)$$

is to be minimized. Numerical experiments suggest that a good choice of κ and σ are:

$$\kappa = 0.7, \qquad \sigma = 0.2\pi. \tag{8.22}$$

This yields the following damping stencil coefficients,

$$
\begin{aligned}
d_0^C &= 0.350576727483 \\
d_1^C &= d_{-1}^C = -0.25 \\
d_2^C &= d_{-2}^C = 0.0788677598279 \\
d_3^C &= d_{-3}^C = -0.004156123569
\end{aligned}
\qquad (8.23)
$$

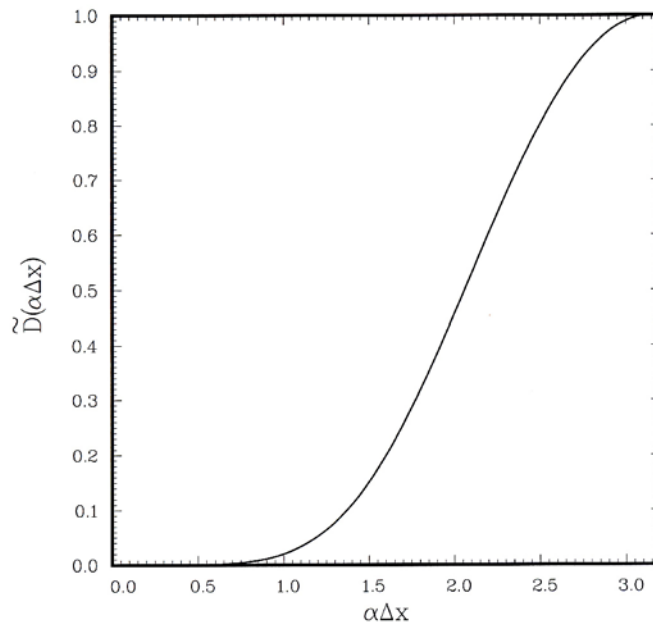The damping function corresponding to this stencil is shown in Fig. 8.8.

Figure 8.8. Damping function for stencil point C. $\kappa = 0.7$, $\sigma = 0.2\,\pi$.

On following the above steps, the coefficients of the damping stencil for points B or B' are found. In this case, numerical experiments suggest the choice of $\kappa = 0.8$ and $\sigma = 0.2\pi$. The damping stencil coefficients are,

$$
\begin{aligned}
d_0^B &= 0.5 \\
d_1^B &= d_{-1}^B = -0.294977493296 \\
d_2^B &= d_{-2}^B = 0.052389707989 \\
d_3^B &= d_{-3}^B = -0.007412214693
\end{aligned}
\qquad (8.24)
$$

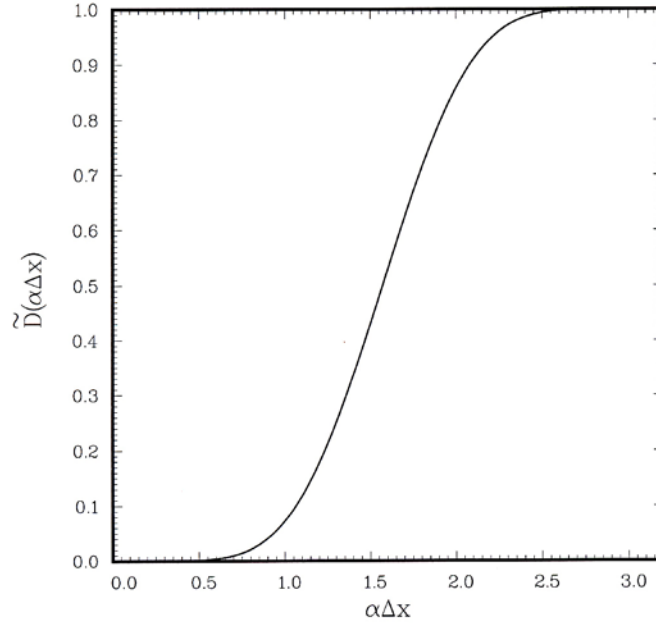The damping function is shown in Fig. 8.9.

Figure 8.9. Damping function for stencil point B. $\kappa = 0.8$, $\sigma = 0.2\,\pi$.

Very often one is required to compute flows with a thin boundary layer adjacent to a wall. To calculate such rapidly changing flows, it is desirable to use higher spatial resolution in regions with rapid changes. Thus the finest mesh is installed right next to the wall. In such a mesh design, one may have a cascade of mesh sizes through several layers from the outermost coarse layer to the finest mesh layer right at the wall. Experience has shown that it is possible for waves corresponding to grid-to-grid oscillations to be trapped in one of the nested mesh layers very close to the wall. This provides an environment for the growth of grid-to-grid oscillations as they bounce from one side of the layer to the other side gaining amplitude at each reflection. It is, therefore, a good practice to impose stronger artificial selective damping in the computation for the fine meshes near a wall. For an estimate of the magnitude of mesh Reynolds number that should be imposed, it is noted that the time, T, needed by the short waves to propagate from one side of the mesh layer to the other side, is equal to the distance traveled divided by the speed of propagation. Here the group velocity of the spurious grid-to-grid oscillations is taken to be approximately equal to twice the speed of sound a_0 (see Fig. 2.4). Hence, one finds,

$$T = \frac{N\Delta x}{2a_0} \tag{8.25}$$

where N is the number of mesh points across the width of the mesh layer, Δx is the mesh size. Since $\tilde{D}(\pi) = 1.0$, the total damping factor is,

$$e^{-\frac{v_a T}{(\Delta x)^2}} = e^{-\frac{N}{2R_\Delta}} \tag{8.26}$$

where $R_\Delta = v_a/(\Delta x)a_0$ is the mesh Reynolds number. It is suggested that this factor should be equal to 10^{-2} or less to avoid accumulation of spurious grid-to-grid oscillations. On setting this factor equal to 10^{-2}, a criterion for the choice of the mesh Reynolds number is established, namely,

$$\frac{N}{R_\Delta} \geq 9.2 \,. \tag{8.27}$$

As an example, if the nested mesh layer has 20 mesh points, i.e. $N = 20$, then $R_\Delta^{-1} \geq 0.46$, say 0.5, should be used. This value is much larger than the value recommended for general background damping, which is $R_\Delta^{-1} \geq 0.05$. (Note: away from the solid boundaries a smaller and smaller inverse mesh Reynolds number should be used.) Formula (8.27) also suggests that any uniform mesh layer in a multi-size-mesh computation should not have fewer than 20 mesh points. This is to avoid the necessity of using excessively large artificial damping.

8.4 Numerical Examples

To illustrate the implementation and the effectiveness of multi-size-mesh multi-time-step computing, two problems from the Third CAA Workshop on Benchmark Problems are considered here. The first is a two-dimensional rotor noise problem. The second is an automobile door cavity tone problem.

First Example: The Sound Field of an Open Rotor

For this problem, it is convenient to use nondimensional variables with respect to the following scales,

> length scale $= b$ (length of blade)
>
> velocity scale $= a_\infty$ (ambient sound speed)
>
> time scale $= b/a_\infty$
>
> density scale $= \rho_\infty$ (ambient gas density)
>
> pressure scale $= \rho_\infty a_\infty^2$
>
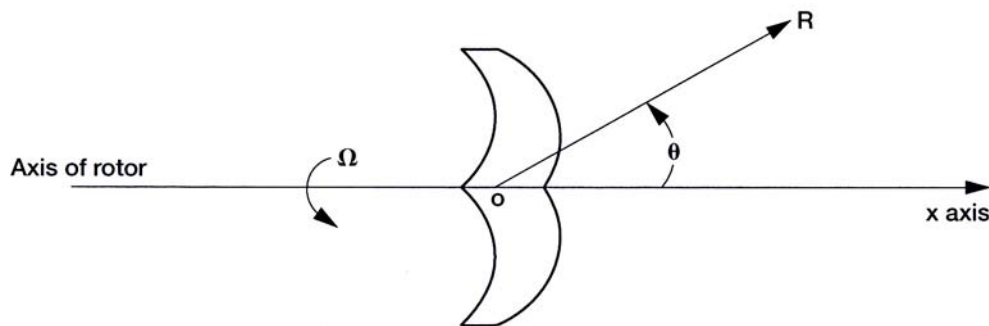> body force scale (per unit volume) $= \rho_\infty a_\infty^2 / b$

Figure 8.10. An open rotor.

A rotor (see Fig. 8.10) exerts a rotating force on the fluid. As a model problem, the rotor is replaced by a distribution of rotating body force. The governing equations are the linearized Euler equations. In cylindrical coordinates (r, ϕ, x), they are,

$$\frac{\partial v}{\partial t} = -\frac{\partial p}{\partial r} + F_r$$

$$\frac{\partial w}{\partial t} = -\frac{1}{r}\frac{\partial p}{\partial \phi} + F_\phi$$

$$\frac{\partial u}{\partial t} = -\frac{\partial p}{\partial x} + F_x \qquad (8.28)$$

$$\frac{\partial p}{\partial t} + \frac{1}{r}\frac{\partial(vr)}{\partial r} + \frac{1}{r}\frac{\partial w}{\partial \phi} + \frac{\partial u}{\partial x} = 0$$

where (F_r, F_ϕ, F_x) are the components of the body force.

For simplicity, F_r is set equal to zero while F_ϕ and F_x are assumed to consist of a single azimuthal and frequency component, i.e.

$$\begin{bmatrix} F_\phi(r,\phi,x,t) \\ F_x(r,\phi,x,t) \end{bmatrix} = \text{Re}\left\{ \begin{bmatrix} \tilde{F}_\phi(r,x) \\ \tilde{F}_x(r,x) \end{bmatrix} e^{im(\phi-\Omega t)} \right\} \qquad (8.29)$$

where Re{ } is the real part of { }. For computation purposes, the following body force distributions in r and x are used.

$$\tilde{F}_\phi(r,x) = \begin{cases} F(x) r J_m(\lambda_{mN} r), & r \le 1 \\ 0 & r > 1 \end{cases} \qquad (8.30)$$

$$\tilde{F}_x(r,x) = \begin{cases} F(x) J_m(\lambda_{mN} r), & r \le 1 \\ 0 & r > 1 \end{cases} \qquad (8.31)$$

$$F(x) = \exp\left[-(\ln 2)(10x)^2\right] \qquad (8.32)$$

where $J_m(\ )$ is the mth-order Bessel function, λ_{mN} is the Nth root of J'_m or $J'_m(\lambda_{mN}) = 0$. In this model, m is the number of blades, Ω is the angular velocity of the rotor. The choice of the Bessel functions in Eqs.(8.30) and (8.31) has no significance other than to make the analytical solution simple.

It is possible to reduce the 3-dimensional problem of Eq. (8.28) to a two-dimensional problem by factoring out the azimuthal dependence. Let

$$\begin{bmatrix} u(r,\phi,x,t) \\ v(r,\phi,x,t) \\ w(r,\phi,x,t) \\ p(r,\phi,x,t) \end{bmatrix} = \text{Re}\left\{ \begin{bmatrix} \tilde{u}(r,x,t) \\ \tilde{v}(r,x,t) \\ \tilde{w}(r,x,t) \\ \tilde{p}(r,x,t) \end{bmatrix} e^{im\phi} \right\} \tag{8.33}$$

The governing equations for $(\tilde{u},\tilde{v},\tilde{w},\tilde{p})$ are found by substituting Eqs. (8.29) to (8.33) into Eq. (8.28). Upon factoring out $e^{im\phi}$, these equations are

$$\frac{\partial \tilde{v}}{\partial t} = -\frac{\partial \tilde{p}}{\partial r}$$

$$\frac{\partial \tilde{w}}{\partial t} = -\frac{im}{r}\tilde{p} + F_\phi(r,x)e^{-im\Omega t}$$

$$\frac{\partial \tilde{u}}{\partial t} = -\frac{\partial \tilde{p}}{\partial x} + F_x(r,x)e^{-im\Omega t} \tag{8.34}$$

$$\frac{\partial \tilde{p}}{\partial t} + \frac{1}{r}\frac{\partial(\tilde{v}r)}{\partial r} + \frac{im\tilde{w}}{r} + \frac{\partial \tilde{u}}{\partial x} = 0$$

For an open rotor solution, it is only necessary to find the outgoing wave solution of Eq. (8.34) in the r–x plane.

Now the benchmark problem is to calculate the directivity, $D(\theta)$, of the radiated sound for a 8-blade rotor ($m = 8$) with $N = 1$ ($\lambda_{8,1} = 9.64742$). In a spherical polar coordinates system (R,θ,ϕ), with the x-axis as the polar axis, the directivity is defined by,

$$D(\theta) = \lim_{R \to \infty} R^2\, \overline{p^2(R,\theta,\phi,t)}$$

where an overbar indicates a time average. The directivity $D(\theta)$ at one degree interval at two rotational speeds,

(a) $\Omega = 0.85$ (subsonic tip speed)
(b) $\Omega = 1.15$ (supersonic tip speed)

are to be computed.

To ensure that the computed solution is accurate, one must make provisions to take into account two important characteristics of this problem. First is that the noise source is discontinuous at the blade tip. This could be a source of short spurious numerical waves. Second is that the blades are slender. That is, the loading is concentrated over a narrow width. Computationally, this requires a finer spatial resolution in the source region than in the acoustic radiation field.

A. *Grid Design*

The half-width of the forcing function in Eqs. (8.30) and (8.31) is 0.2. To resolve this width a minimum of 10 mesh points is necessary. In other words, the maximum mesh size in the source region is 0.02. This high resolution is not needed as one moves away into the acoustic field. The multi-size-mesh multi-time-step DRP algorithm is used for computation. This allows one to use coarser and coarser mesh starting from the source region radially outward. Fig. 8.11 shows the computation domain. The domain is divided into three regions. The mesh size as well as the time step increases by a factor of two each time one crosses into an outer region.
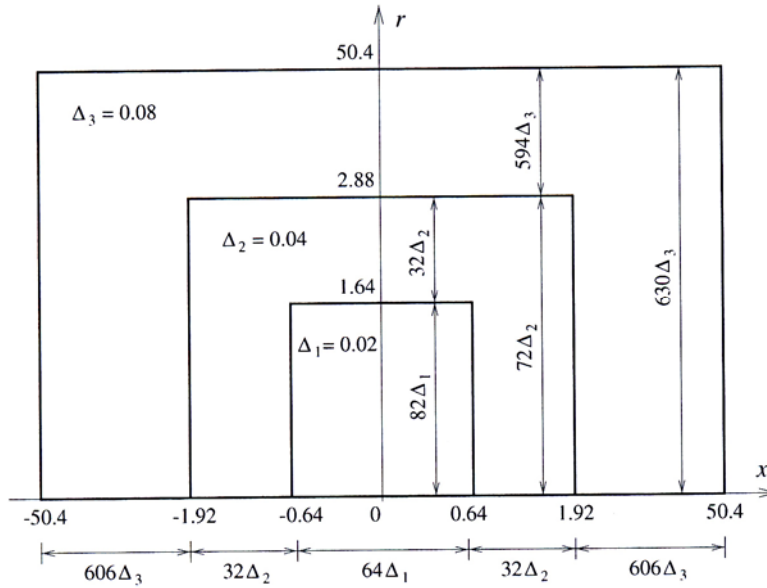
Figure 8.11. Schematic diagram showing the computational domain and mesh design.

B. Numerical Boundary Conditions

Two types of numerical boundary conditions are needed. Along the outer boundary of the computation domain, radiation boundary conditions are required. Along the axis of the cylindrical coordinates, i.e., $r = 0$, a special set of axis boundary condition is needed. Here, the radiation boundary conditions shown below are used.

$$\left(\frac{\partial}{\partial t} + \frac{\partial}{\partial R} + \frac{1}{R}\right)\begin{bmatrix}\tilde{u} \\ \tilde{v} \\ \tilde{w} \\ \tilde{p}\end{bmatrix} = 0 \tag{8.35}$$

where $R = (r^2 + x^2)^{1/2}$.

As $r \rightarrow 0$, Eq. (8.34) has a numerical singularity and cannot be used as it is. One way to deal with the singularity is to extend the solution to the negative-r part of the x–r-plane as follows,

$$\tilde{u}(-r,x) = (-1)^m \tilde{u}(r,x)$$
$$\tilde{v}(-r,x) = (-1)^{m-1} \tilde{v}(r,x)$$
$$\tilde{w}(-r,x) = (-1)^{m-1} \tilde{w}(r,x)$$
$$\tilde{p}(-r,x) = (-1)^m \tilde{p}(r,x)$$

(8.36)

Formula (8.36) allows one to extend the computed solution into the lower half of the x–r-plane as indicated in Fig. 8.12. In this way, computation stencils for points near the axis (but not on the axis such as point A) may be extended into the negative r half-plane as shown. For the points on the axis, such as point B, they will not be calculated by the time marching DRP scheme. They are to be found, after the values at all the other points have been updated to a new time level, by symmetric interpolation. A 7-point interpolation stencil for point B is shown in Fig. 8.12.
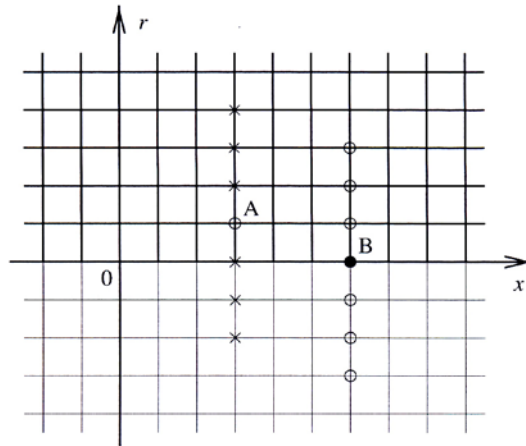

Figure 8.12. Extension of the computational domain, the upper part of the x-r plane, to the non-physical lower half plane.

C. Artificial Selective Damping

As discussed before, artificial selective damping is incorporated into the DRP computational algorithm for two purposes. First, it is used to provide background damping to eliminate short spurious waves to prevent them from propagating across the computation domain. Generally speaking, small amplitude short spurious waves are just low-level pollutants of the numerical solution. But if these waves are allowed to impinge on an internal or external boundary of the computational domain, they could lead to the reflection of large amplitude long waves. These spurious long waves are sometimes not distinguishable from the physical solution and are, therefore, extremely undesirable. The second reason to add artificial selective damping is to stabilize the numerical solution at a discontinuity. The damping prevents the build-up of spurious short waves, which are generated by the discontinuity, and this promotes stability.

In the present problem, the forcing functions are discontinuous at the blade tip. Thus, in addition to the general background damping with an inverse mesh Reynolds number 0.05, extra

damping is added around the blade tip region. The mesh size change interface as well as the external boundary of the computation domain are also a form of discontinuity. Extra damping is added around these boundaries as well. To impose extra damping, a distribution of inverse mesh Reynolds number in the form of a Gaussian function with a half-width of 4 mesh spacing normal to the boundary is used. The maximum of the Gaussian is on the discontinuity with an assigned value of 0.05. At the tip of the blade, where the forcing function is discontinuous, more damping is required. A maximum value of 0.75 is used instead.

D. Asymptotic Solution

An asymptotic solution of the present problem may be found by a straightforward application of Fourier Transform. Details of the analysis are given in the Proceedings of the Third CAA Workshop on Benchmark Problems (NASA CP-2000-209790, Aug. 2000). The directivity of sound radiation with respect to a spherical polar coordinate system (R, θ, ϕ) with the polar axis coinciding with the axis of the rotor is,

$$D(\theta) = \underset{R \to \infty}{Lim} R^2 \overline{p^2} = \left(\frac{\pi}{400 \ln 2}\right)^{1/2} \frac{m^2 (1 + \Omega \cos \theta) \Omega \sin \theta}{\lambda_{mN}^2 - m^2 \Omega^2 \sin^2 \theta} J_m(\lambda_{mN}) J_m'(mR \sin \theta) e^{-\frac{m^2 \Omega^2 \cos^2 \theta}{400 \ln 2}}$$

E. Numerical Results

Eq. (8.34) are discretized according to the multi-size-mesh mult-time-step DRP scheme and marched in time to a time periodic state. To start the computation, a zero initial condition is used. Fig. 8.13 shows a comparison of the directivity at $R = 50$ obtained computationally against the asymptotic solution for $\Omega = 0.85$, the subsonic tip speed case. As expected, most of the acoustic radiation is concentrated in the plane of rotation. There is good agreement between the numerical results and the asymptotic solution. Fig. 8.14 shows the directivity at supersonic tip speed with $\Omega = 1.15$. At higher frequency, the acoustic wavelength is shorter. This case, therefore, offers a more stringent test of the accuracy of the entire computational algorithm. The agreement with asymptotic solution is reasonably good.
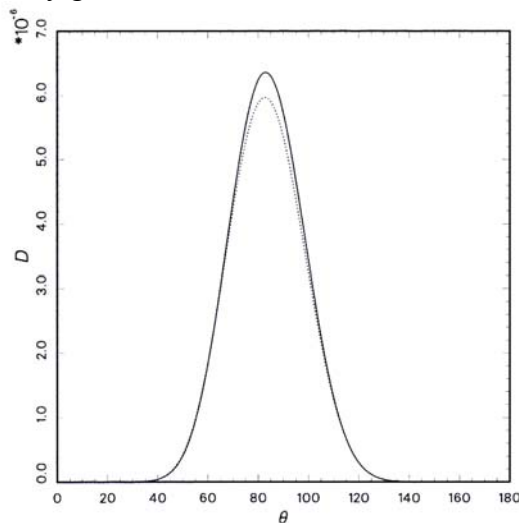

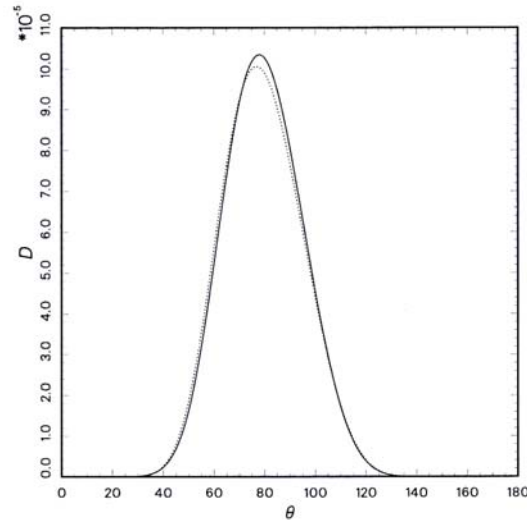Figure 8.13. Directivity of sound field at R = 50, Ω = 0.85, —— numerical, $\cdots\cdots$ asymptotic.

Figure 8.14. Directivity of sound field at R = 50, Ω = 1.15, —— numerical, · · · · · · asymptotic.

Second Example : Acoustic Resonances Induced by Flow over an Automobile Door Cavity

This problem is to compute the resonance tones induced by a turbulent boundary layer flow outside a scaled model automobile door cavity. To properly model and compute the turbulent boundary layer flow and its interaction with the cavity is a task that will require extensive time and effort. Here a laminar boundary layer is considered instead. It is believed that the cavity tone frequencies would most likely be about the same whether the flow is turbulent or laminar. But the tone intensities are expected to be different.

A boundary layer flow will definitely be laminar if $R_{\delta*}$ < 600. $R_{\delta*}$ is Reynolds number based on displacement thickness. This is the Reynolds number below the stability limit of the Tollmien-Schlichting waves. In modern facilities with low free stream turbulence and sound, a boundary layer may remain laminar if $R_{\delta*}$ is larger than 600 but less than 3400. For a free stream velocity of 50.9m/s and 26.8m/s (velocities prescribed by the benchmark problem), these correspond to a boundary layer thickness of 2.9 mm and 5.5 mm, respectively. In this example, consideration will be restricted to a boundary layer thickness of 2 mm and 1 mm at flow velocities of 50.9m/s and 26.8m/s respectively.

A. Computation Domain and Grid Design

The computation domain is shown in Fig. 8.15. It is designed primarily for the case U = 50.9 m/s and a boundary layer thickness δ = 2 mm. In the cavity opening region, viscous effects are important. To capture these effects, a fine mesh is needed. Away from the cavity, the disturbances are mainly acoustic waves. By using the Dispersion-Relation-Preserving (DRP) scheme in the computation, only a very coarse mesh would be necessary in the acoustic region. The mesh design is dictated by these considerations. The computation domain is divided into a number of subdomains as shown in Fig 8.15. The finest mesh with $\Delta x = \Delta y$ = 0.0825 mm is used in the cavity opening region. The mesh size increases by a factor of 2 every time one crosses into the next subdomain. The mesh size in the outermost subdomain is 32 times larger than the finest mesh.
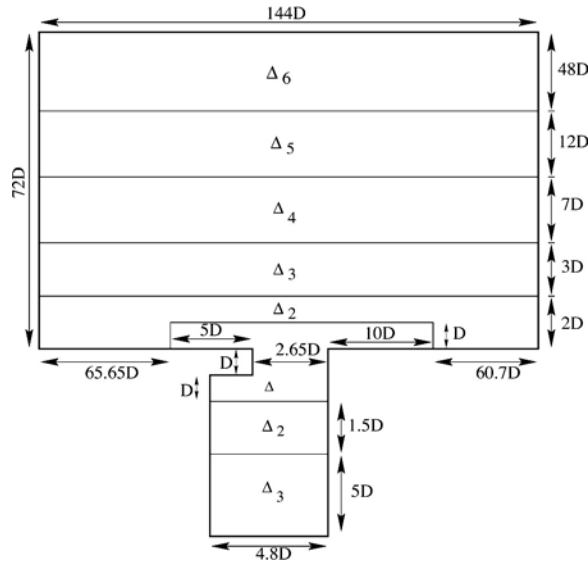
Figure 8.15. Computational domain showing the division into sub-domains and their mesh size.
$D = 3.3mm$.

B. The Governing Equations and the Computational Algorithm

The governing equations are the compressible Navier-Stokes equations in two-dimensions. In dimensionless form with D (D = 3.3 mm is the thickness of the cavity overhang) as length scale, U, the free stream velocity (from left to right), as velocity scale, D/U as the time scale, ρ_0, the ambient gas density, as the density scale and $\rho_0 U^2$ as the pressure scale, they are

$$\frac{\partial \rho}{\partial t} + \rho \frac{\partial u_j}{\partial x_j} + u_j \frac{\partial \rho}{\partial x_j} = 0 \tag{8.37}$$

$$\frac{\partial u_i}{\partial t} + u_j \frac{\partial u_i}{\partial x_j} = -\frac{\partial p}{\partial x_i} + \frac{\partial \tau_{ij}}{\partial x_j} \tag{8.38}$$

$$\frac{\partial p}{\partial t} + u_j \frac{\partial p}{\partial x_j} + \gamma p \frac{\partial u_j}{\partial x_j} = 0 \tag{8.39}$$

$$\tau_{ij} = \frac{1}{R_D} \left(\frac{\partial u_i}{\partial x_j} + \frac{\partial u_j}{\partial x_i} \right) \tag{8.40}$$

where R_D is the Reynolds number based on D.

The above equations are solved in time by the multi-size-mesh multi-time-step DRP algorithm. In each subdomain of Fig. 8.15, the equations are discretized by the DRP scheme. At the mesh size change boundaries, special stencils as given in Section 8.1 are used. The time-steps of adjacent subdomains differ by a factor of two just as the mesh size. By using the multi-size-mesh multi-time-step algorithm most of the computation effort and time are spent in the opening

region of the cavity where the resolution of the unsteady viscous layers is of paramount importance.

C. Numerical Boundary Conditions

Along the solid surfaces of the cavity and the outside wall, the no-slip boundary condition is enforced by the ghost point method. Along the vertical external boundary regions (3 mesh points adjacent to the boundary), the flow variables are split into a mean flow and a time dependent component. The mean flow, with a given boundary layer thickness, is provided by the Blasius solution. The time dependent part of the solution is the only portion of the solution that is computed by the time marching scheme. The boundary conditions used for the computation are as follows. Along the top and left external boundaries the asymptotic radiation boundary conditions are imposed. Along the right boundary, the outflow boundary conditions are used.

D. Artificial Selective Damping

Artificial selective damping is added to the time marching DRP scheme to eliminate spurious short waves and to prevent the occurrence of numerical instability. The damping stencil with a damping curve of half-width 0.2π is used for background damping. Near the solid walls or the outer boundaries where a 7-point stencil does not fit, a 5- or 3-point stencil is used instead. For general background damping an inverse mesh Reynolds number of 0.05 is used everywhere. Along walls and mesh change interfaces, additional damping is included. The added damping has an inverse mesh Reynolds number distribution in the form of a Gaussian function with the maximum value at the wall or interface and a half-width of four mesh points as in the first example. On the wall, the maximum value of R_Δ^{-1} is set equal to 0.15. The corresponding value at a mesh-size-change interface is 0.3. There are three external corners at the cavity opening. They are likely sites at which short spurious waves are generated. To prevent numerical instability from developing at these points, additional artificial selective damping is imposed. Again a half-width of 4 mesh point Gaussian distribution of the inverse mesh Reynolds number centered at each of these points is used. The maximum value of R_Δ^{-1} at these points is set equal to 0.35. By implementing artificial selective damping distribution as described, no numerical instability nor excessive short spurious waves have been found in all the computations.

E. Numerical Results

To start the computation, the time independent boundary layer solution without the cavity is used as the initial condition. The solution is time-marched until a time periodic state is reached.
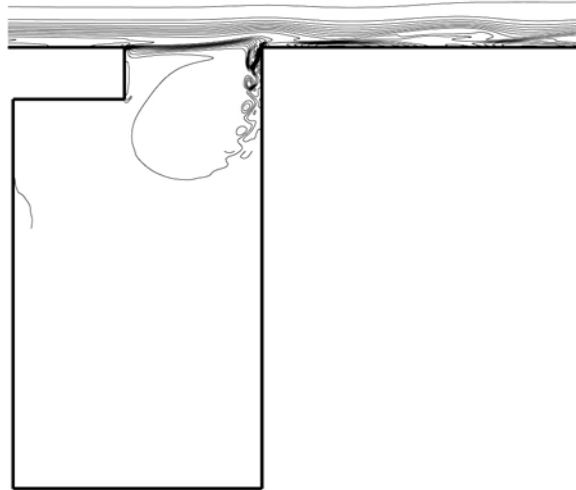
Figure 8.16. Instantaneous vorticity contours showing the shedding of small vortices at the trailing edge of the cavity. U=50.9m/s, δ=2mm.

The characteristic features of the flow in the vicinity of the cavity opening and the acoustic field are found by examining the instantaneous vorticity, steamlines and pressure contours. Fig. 8.16 shows a plot of the instantaneous vorticity contours for the case $U = 50.9$ m/s and $\delta = 2.0$ mm. As can easily be seen, vortices are shed periodically at the trailing edge of the cavity. Some shed vortices move inside the cavity. Other vortices are shed into the flow outside. The shed vortices outside are convected downstream by the boundary layer flow. These convected vortices are clearly shown in the pressure contour plot of Fig. 8.17. They form the low pressure centers. These vortices persist over a rather long distance and eventually are dissipated by viscosity. Fig. 8.18 shows the instantaneous streamline pattern. It is seen that the flow at the mouth of the cavity is completely dominated by a single large vortex. Below the large vortex, another vortex of opposite rotation often exists. The position of this vortex changes from time to time and does not always attach to the cavity wall. The far field pressure contour pattern is shown in Fig. 8.19. This pattern is the same as that of a monopole acoustic source in a low subsonic stream. That the noise source is a monopole and not a dipole is consistent with the model of Tam and Block (1978). The sound is generated by flow impinging periodically at the trailing edge of the cavity.
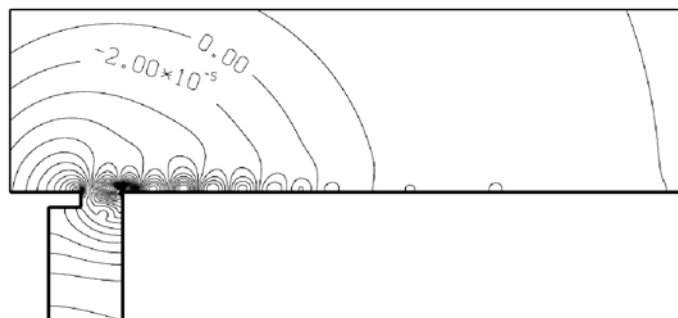

Figure 8.17. Near field pressure contours showing the convection of shed vortices along the outside wall. $U = 50.9$ m/s, $\delta = 2$mm.
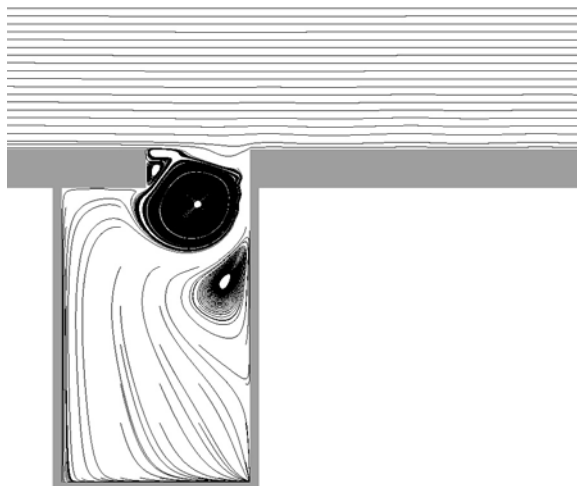
Figure 8.18. Instantaneous streamline pattern. $U = 50.9$ m/s, $\delta = 2$ mm.
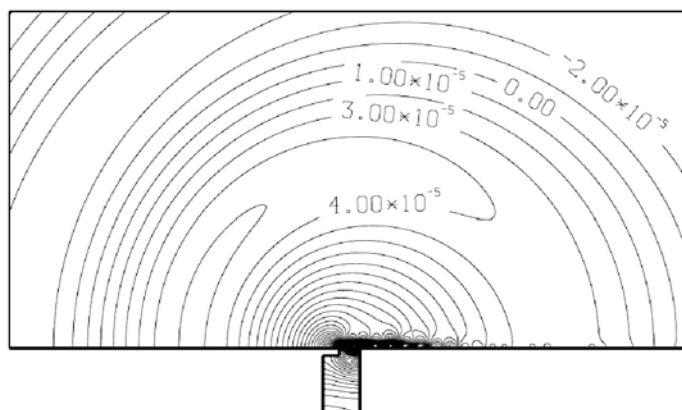

Figure 8.19. Far field pressure contours showing a monopole acoustic field. $U = 50.9$ m/s, $\delta = 2$ mm.

Experiments indicate that cavity resonance may consist of a single tone or multiple tones. The number of tones occured depend on the flow conditions and the cavity geometry. Fig. 8.20 shows the noise spectrum measured at the center of the left wall of the cavity at $U = 50.9$ m/s, $\delta = 2$ mm. The spectrum consists of a single tone at 1.99KHz.
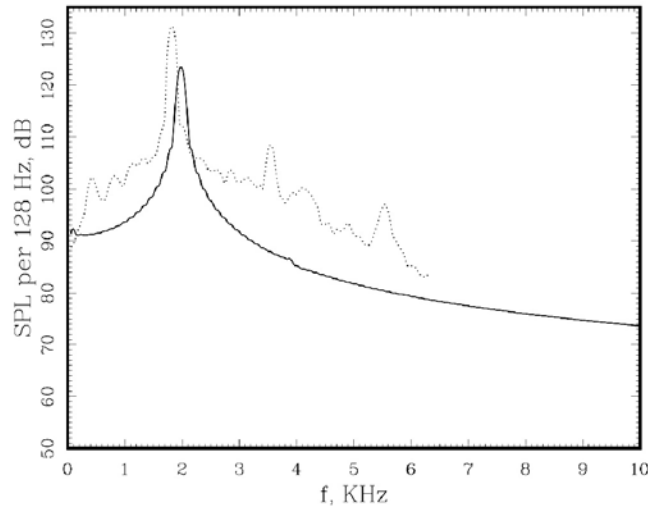
Figure 8.20. Noise spectrum at the center of the left wall of the cavity. $U = 50.9$ m/s, $\delta = 2$mm
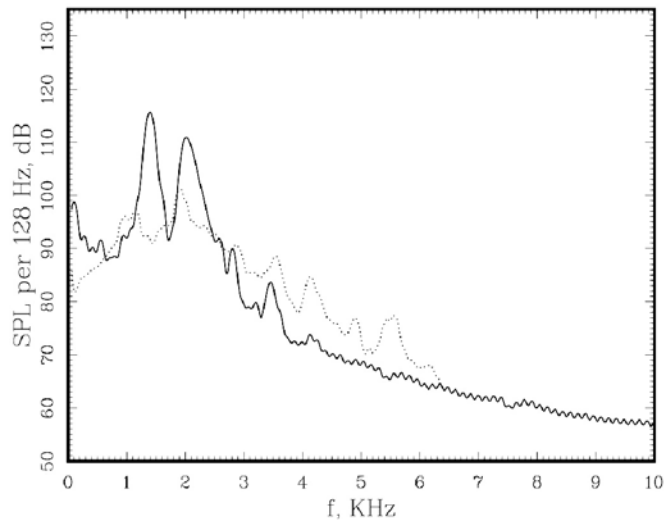——— numerical simulation, ……… experiment (Henderson).

Figure 8.21. Noise spectrum at the center of the left wall of the cavity. $U = 26.8$ m/s, $\delta = 1$ mm
——— numerical simulation, ……… experiment (Henderson).

Shown in Fig. 8.20 also is the spectrum measured experimentally by Henderson (2000). There is good agreement between the tone frequency of the numerical simulation and that of the physical experiment. In the experiment, the boundary layer is turbulent, therefore, it is not expected that there would be good agreement in the tone intensity. Fig. 8.21 shows the noise spectrum at the lower speed $U = 26.8$ m/s and $\delta = 1$ mm. In this case, there are two tones. One is at a frequency of 1.32KHz and the other at 2.0KHz. This is in fair agreement with the experimentally measured spectrum. Again, the tone frequencies are reasonably well reproduced in the numerical simulation, but the tone intensities are different. Figs. 8.20 and 8.21 together suggest that as the flow velocity increases, one of the tones disappears. The strength of the remaining tone intensifies with flow speed.

9. IMPEDANCE BOUNDARY CONDITION

Nowadays, acoustic treatment is, invariably, used on the inside surface of commercial aircraft jet engines for fan noise reduction. Acoustic treatment panels or liners, when properly toned, are extremely effective noise suppressors. Because of structural integrity requirement, the acoustic liners are usually of the Helmholtz resonator type. Fig. 9.1 shows a single layer acoustic liner. The liner consists of a face sheet with holes at a regular pattern. Underneath the face sheet are cavities. The cavities control the frequency range within which damping is most effective. The dominant damping mechanism of this type of liners is attributed to the dissipation arising from vortex shedding at the mouths of the holes. The vortex shedding process converts acoustic energy iinto the rotational kinetic energy of the shed vortices. These vortices are subsequently dissipated by molecular viscosity. In the absence of vortex shedding, which is the case at low sound pressure level, the principal damping mechanism is associated with viscous dissipation of the oscillatory flow at the mouths of the Helmholtz resonators. The flow and acoustic fields around the Helmholtz resonators of acoustic liners are exceedingly complicated, especially when there is a mean flow over the liner.
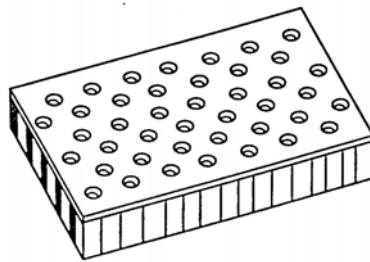

Figure 9.1 A single layer Helmholtz resonator type acoustic liner.

For engineering purposes, a gross macroscopic description of the effects of the acoustic liners on incident acoustic waves is definitely preferred over a more demanding microscopic description of the actual phenomenon. In the aeroacoustic community, it is an accepted practice to characterize the macroscopic properties of an acoustically treated surface by a single quantity Z called the impedance. Impedance is defined as the ratio of the acoustic pressure p to the acoustic velocity component normal to the treated surface v_n (positive when pointing into the surface). That is,

$$p = Z\, v_n. \tag{9.1}$$

Impedance is a complex quantity, $Z = R - iX$ ($e^{-i\omega t}$ time dependence is assumed). The use of a complex quantity is needed to account for the damping and phase shift imparted on the sound waves by the acoustically treated surface. The acoustic resistance R and the acoustic reactance X are generally frequency dependent. They also vary with the intensity of the incident sound waves and the adjacent mean flow velocity. These quantities are usually measured empirically, although some semi-empirical formulas are available for their estimates. It has been found experimentally that R is positive and does not vary much with frequency. On the other hand, X may be both positive or negative depending on the frequency. For many acoustic liners, the dependence of X

on angular frequency ω can be represented adequately by a simple analytical expression of the form,

$$\frac{X}{\rho a_0} = \frac{X_{-1}}{\omega} + X_1 \omega \tag{9.2}$$

where X_{-1} and X_1 are two parameters. ρ is the gas density and a_0 is the speed of sound. Fig. 9.2 shows an accurate representation of the data of Motsinger and Kraft (1991) by the two-parameter formula. The values of X_{-1} and X_1 obtained by mean-least-square fit are -13.48 and 0.0739, respectively, where ω is measured in kilo radian per second.
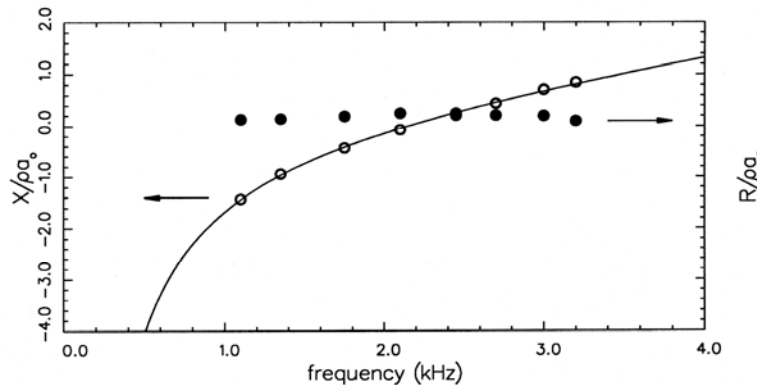

Figure 9.2 Measured dependence of the resistance and reactance of a 6.7% perforate treatment panel on frequency at low sound intensity from Motsinger and Kraft (1991). ○ reactance, ● resistance

Impedance boundary condition (9.1) is basically a boundary condition established for frequency-domain analysis. As it is, it cannot be used in time-domain computation. For time-marching computation, a suitable equivalent of the impedance boundary condition in the time-domain is needed. One significant advantage of time-domain methods over frequency-domain methods is that broadband noise problems can be handled relatively easily, almost without extra effort. For broadband noise problems, frequency-domain methods are computationally intensive and laborious. In addition, if the problem is nonlinear, frequency-domain methods would be exceedingly difficult to carry out.

Time-domain problems can be solved only if they are well posed and stable. In the presence of a mean flow, standard formulation of the impedance boundary condition is known to support spurious unstable solutions of the Kelvin-Helmholtz type. It turns out for acoustic liner problems such instability is rather weak. It can be suppressed by the imposition of artificial selective damping at the liner surface.

9.1 A Three-Parameter Broadband Model

A simple model for broadband impedance boundary condition is to take the resistance R to be a constant and the reactance X to be given by Eq. (9.2). That is,

$$Z = R_0 - i \left[\frac{X_{-1}}{\omega} + X_{-1}\omega \right]. \tag{9.3}$$

For this model, the time domain impedance boundary condition maybe written as follows,

$$\frac{\partial p}{\partial t} = R_0 \frac{\partial v_n}{\partial t} - X_{-1}v_n + X_1 \frac{\partial^2 v_n}{\partial t^2}. \tag{9.4}$$

It is straightforward to show by assuming time dependence of the form $e^{-i\omega t}$ for all variables that Eq. (9.4) is equivalent to the frequency-domain impedance boundary condition with impedance given by Eq. (9.3).

For a single frequency sound field of frequency Ω ($\Omega > 0$), the above three-parameter model may still be used. Let $Z_0 = R_0 - iX_0$ be the impedance of the acoustic liner at frequency Ω, then the following choice of X_{-1} and X_1 will transform the broadband model to a single frequency model.

$$X_{-1} = \frac{-\left(1 - \dfrac{X_0}{|Z_0|}\right)^2 \Omega}{\left[\dfrac{2}{|Z_0|} - \dfrac{X_0}{|Z_0|^2}\right]} \tag{9.5a}$$

$$X_1 = \frac{1}{\left[\dfrac{2}{|Z_0|} - \dfrac{X_0}{|Z_0|^2}\right]\Omega} \tag{9.5b}$$

9.2 Stability of the Three-Parameter Time-Domain Impedance Boundary Condition

Time-domain impedance boundary condition (9.4) may not be used unless it leads to stable solution. To show that an acoustic problem with Eq. (9.4) as boundary condition is computationally stable, consider a plane acoustic liner adjacent to a sound field as shown in Fig. 9.3. For simplicity, let the surface of the liner be the $x-z$-plane. In terms of dimensionless variables with L (a typical length of the problem) as the length scale, a_0 (the sound speed) as the velocity scale, L/a_0 as the time scale, ρ_0 (the gas density) as the density scale, $\rho_0 a_0^2$ as the pressure scale and $\rho_0 a_0$ as the scale for impedance, the acoustic field equations (the linearization momentum and energy equations) are,

$$\frac{\partial \mathbf{v}}{\partial t} = -\nabla p \tag{9.6}$$

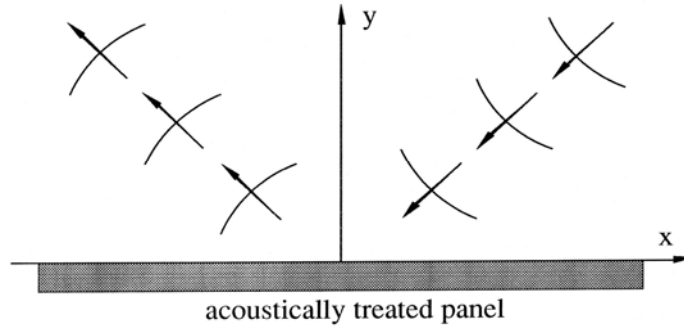$$\frac{\partial p}{\partial t} = -\nabla \cdot \mathbf{v} \tag{9.7}$$

Figure 9.3 Sound field adjacent to an acoustically treated panel

Let $\bar{f}(\alpha,\beta,\omega)$ be the Fourier-Laplace transform of a function $f(x,z,t)$. The functions f and $\tilde{f}$ are related by,

$$\tilde{f}(\alpha,\beta,\omega) = \frac{1}{(2\pi)^3} \int\int\limits_{-\infty}^{\infty} \int\limits_{0}^{\infty} f(x,z,t)\, e^{-i(\alpha x + \beta z - \omega t)} dt\, dx\, dz \tag{9.8a}$$

$$f(x,z,t) = \int\int\limits_{-\infty}^{\infty} \int\limits_{\Gamma} \tilde{f}(\alpha,\beta,\omega)\, e^{i(\alpha x + \beta z - \omega t)} d\omega\, d\alpha\, d\beta. \tag{9.8b}$$

By applying Fourier-Laplace transforms to Eqs. (9.6) and (9.7), it is easy to find that the solution that satisfies radiation and boundedness condition as $y \to \infty$ is,

$$\begin{bmatrix} \tilde{p} \\ \tilde{v} \end{bmatrix} = A \begin{bmatrix} 1 \\ \dfrac{\left(\omega^2 - k^2\right)^{\frac{1}{2}}}{\omega} \end{bmatrix} e^{i\left(\omega^2 - k^2\right)^{\frac{1}{2}} y} \tag{9.9}$$

where $k = (\alpha^2 + \beta^2)^{1/2}$, and v is the velocity component in the y direction (note that $v = -v_n$). The branch cuts of the function $(\omega^2 - k^2)^{1/2}$ are taken to be $0 \le \arg(\omega^2 - k^2)^{1/2} \le \pi$, the left (right) equality is to be used if ω is real and positive (negative). The branch cut configuration in the ω-plane is shown in Fig. 9.4.
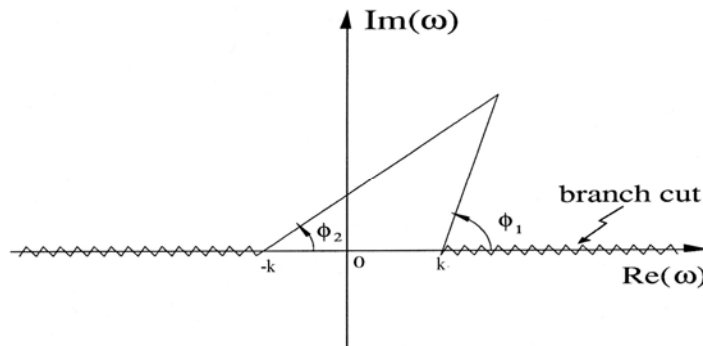
Figure 9.4 Branch cut configuration for $(\omega^2 - k^2)^{1/2}$. Argument of $(\omega^2 - k^2)^{1/2} = \frac{1}{2}(\phi_1 + \phi_2)$

138

The Fourier-Laplace transform of Eq. (9.4) is,

$$-\omega\tilde{p} = \left[-\omega R_0 + i\left(X_{-1} + \omega^2 X_1\right)\right]\tilde{v}_n \tag{9.10}$$

Substitution of Eq. (9.9) into Eq. (9.10), results in the dispersion relation,

$$\frac{\omega^2}{\left(\omega^2 - k^2\right)^{\frac{1}{2}}} + \omega R_0 - iX_1\omega^2 = iX_{-1} \tag{9.11}$$

Let

$$F(\omega) = \frac{\omega^2}{\left(\omega^2 - k^2\right)^{\frac{1}{2}}} + \omega R_0 - iX_1\omega^2. \tag{9.12}$$

That is, $F(\omega)$ is the left side of Eq. (9.11). By tracing over the contour *ABCDEFGH* in the upper half ω-plane, it is easy to establish that the upper half ω-plane is mapped into the shaded region in the *F*-plane as shown in Fig. 9.5. The mapped region does not include the negative imaginary axis. Now X_{-1}, on the right side of Eq. (9.11), is negative. This means that no value of ω in the upper half ω-plane would satisfy dispersion relation (9.11). Thus, the solutions of the initial value problem can only have ω with a negative imaginary part. These solutions are numerically stable.
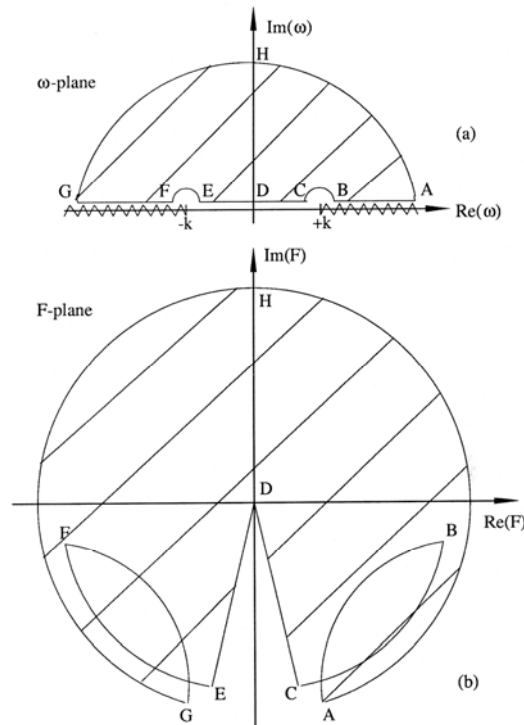

Figure 9.5 Map of the upper half ω–plane in the F-plane. (a) ω–plane, (b) F-plane.

9.3 Impedance Boundary Condition in the Presence of a Subsonic Mean Flow

In jet engines, there is, invariably, a mean flow adjacent to the acoustic liners. Traditionally, impedance boundary condition in the presence of a mean flow is formulated with the assumption of the existence of a very thin zero-velocity fluid layer at the surface of the acoustic liner (see Fig. 9.6). At the interface of the zero-velocity fluid layer and the mean flow, the condition of continuity of particle displacement is used. In dimensionless variables, the frequency-domain impedance boundary condition, after simplification, may be written as,

$$-i\omega p + M\frac{\partial p}{\partial x} = -i\omega Z v_n. \tag{9.13}$$
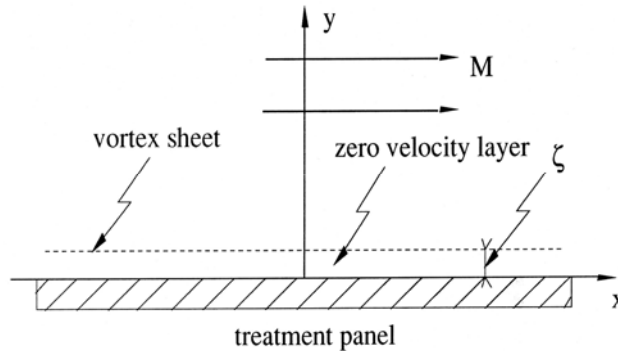

Figure 9.6 Schematic diagram showing a postulated zero velocity fluid layer adjacent to an acoustically treated panel in the presence of a mean flow.

In an extensive numerical study of the normal modes of a duct with acoustic liners, it was found by Tester (1973) that boundary condition (9.13) led to unstable solution. The unstable solution is of the Kelvin-Helmholtz type instability arising from the vortex sheet interface between the mean flow and the zero-velocity fluid layer. In standard duct acoustics analysis using frequency-domain approach, this instability is either not mentioned or totally bypassed and ignored. Now, it is easy to show that the use of boundary condition (9.13) always gives rise to an unstable solution.

The linearized momentum and energy equations governing the sound field superimposed on a uniform mean flow of Mach number M in the x-direction (see Fig. 9.6) are,

$$\frac{\partial \mathbf{v}}{\partial t} + M\frac{\partial \mathbf{v}}{\partial x} = -\nabla p \tag{9.14}$$

$$\frac{\partial p}{\partial t} + M\frac{\partial p}{\partial x} + \nabla \cdot \mathbf{v} = 0. \tag{9.15}$$

By applying Fourier-Laplace transforms to Eqs. (9.14) and (9.15), it is easy to find that the solution that satisfies outgoing wave and boundedness conditions at $y \to \infty$ is,

$$\begin{bmatrix} \tilde{u} \\ \tilde{v} \\ \tilde{w} \\ \tilde{p} \end{bmatrix} = A \begin{bmatrix} \alpha/\tilde{\omega} \\ k(\hat{\omega}^2-1)^{\frac{1}{2}}/\tilde{\omega} \\ \beta/\tilde{\omega} \\ 1 \end{bmatrix} \exp\left[ik\left(\hat{\omega}^2-1\right)^{\frac{1}{2}} y \right] \tag{9.16}$$

where $\tilde{\omega} = \omega - M\alpha$, $k = (\alpha^2 + \beta^2)^{1/2}$, and $\hat{\omega} = \tilde{\omega}/k$. The branch cuts of the square-root function $(\hat{\omega}^2-1)^{1/2}$ are the same as those stipulated in Fig. 9.4 with $\hat{\omega}$ replacing ω and k set equal to 1.

Substitution of Eq. (9.16) into the Fourier-Laplace transforms of boundary condition (9.13) yields the following dispersion relation:

$$\frac{\hat{\omega}^2}{\left(\hat{\omega}^2-1\right)^{\frac{1}{2}}} + Z\hat{\omega} = -\frac{\alpha}{k} MZ. \tag{9.17}$$

Now, let the left side of Eq. (9.17) be denoted by $\bar{f}(\hat{\omega})$:

$$\bar{f}(\hat{\omega}) = \frac{\hat{\omega}^2}{\left(\hat{\omega}^2-1\right)^{\frac{1}{2}}} + Z\hat{\omega}. \tag{9.18}$$
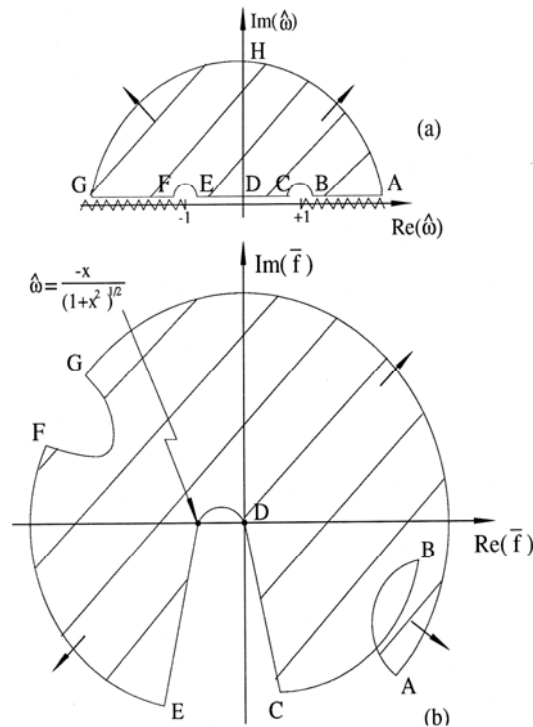

Figure 9.7 Map of the upper half $\hat{\omega}$ plane in the $\bar{f}$ plane (X > 0): (a) $\hat{\omega}$ plane, (b) $\bar{f}$ plane.

Fig. 9.7 shows the map of the upper half-$\hat{\omega}$-plane in the $\bar{f}$-plane (shaded region) for $X > 0$. Since α can be positive or negative, there will always be values of α for which the point representing the right side of Eq. (9.17) lies in the shaded region of the $\bar{f}$-plane. Therefore, there will always be an unstable solution. If X is negative, a similar mapping procedure will show that there is always an unstable solution.

The existence of a Kelvin-Helmholtz type instability renders the boundary value problem ill-posed for the time-domain solution. The instability is, however, nonphysical. Its origin is in the postulate of a vortex sheet discontinuity right next to the impedance boundary. In reality, no such vortex sheet exists in the flow. For time domain problems, the instability is weak. It can be effectively suppressed by the addition of artificial selective damping near and at the surface of the acoustic liner. With the weak instability suppressed, boundary condition (9.13) has yielded solutions that are in agreement with frequency-domain calculations.

9.4 Numerical Implementation

On incorporating the effect of convection (see Eq. (9.13)) the time domain impedance boundary condition (9.4) becomes,

$$\frac{\partial p}{\partial t} + M\frac{\partial p}{\partial x} = R\frac{\partial v_n}{\partial t} - X_{-1}v_n + X_1\frac{\partial^2 v_n}{\partial t^2}. \tag{9.19}$$

The numerical implementation of this boundary condition will now be considered.

Let a large acoustically treated panel be lying on the x–z-plane as shown in Fig. 9.3. It will be assumed that there is a uniform flow adjacent to the panel. The governing equations of the acoustic field are the linearized Euler equations. In dimensionless form, these equations are,

$$\frac{\partial \rho}{\partial t} + M\frac{\partial \rho}{\partial x} + \frac{\partial u}{\partial x} + \frac{\partial v}{\partial y} + \frac{\partial w}{\partial z} = 0 \tag{9.20}$$

$$\frac{\partial u}{\partial t} + M\frac{\partial u}{\partial x} = -\frac{\partial p}{\partial x} \tag{9.21}$$

$$\frac{\partial v}{\partial t} + M\frac{\partial v}{\partial x} = -\frac{\partial p}{\partial y} \tag{9.22}$$

$$\frac{\partial w}{\partial t} + M\frac{\partial w}{\partial x} = -\frac{\partial p}{\partial z} \tag{9.23}$$

$$\frac{\partial p}{\partial t} + M\frac{\partial p}{\partial x} + \frac{\partial u}{\partial x} + \frac{\partial v}{\partial y} + \frac{\partial w}{\partial z} = 0. \tag{9.24}$$
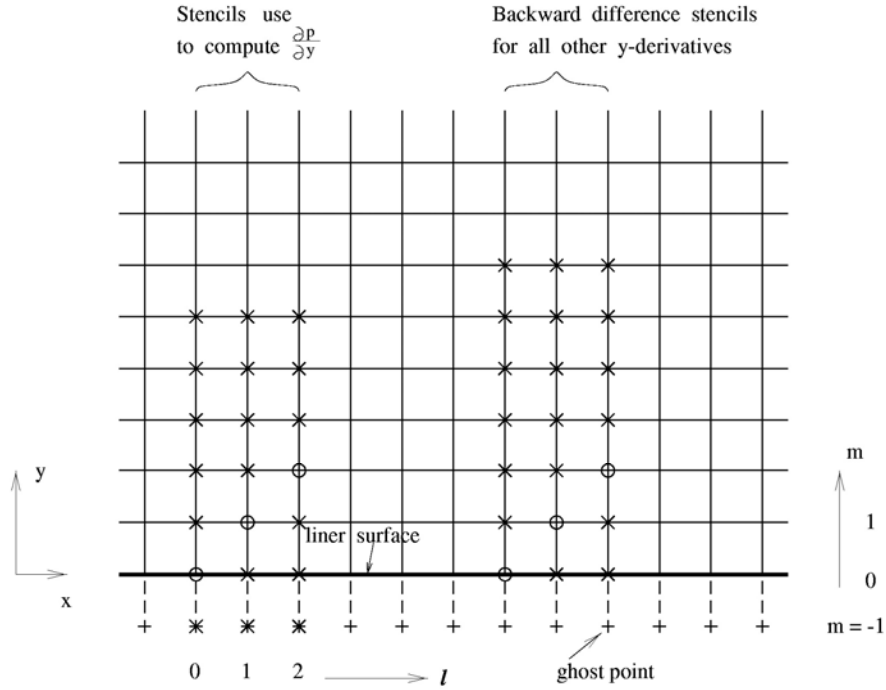
Figure 9.8 Backward difference stencils used in the boundary region adjacent to the liner surface.

Now consider a computational domain as shown in Fig. 9.8. $y = 0$ is the surface of the acoustically treated panel. Eqs. (9.20) to (9.24) apply to every grid point on the mesh. This includes the boundary points at $y = 0$ or $m = 0$, where m is the mesh index in the y-direction. However, boundary condition (9.19) also applies to the boundary mesh point at $y = 0$ or $m = 0$. This means that there are more equations than unknowns. To resolve this problem of an over-determined system, a row of ghost values of pressure, $p_{\ell,-1,k}$ is introduced at $m = -1$, the ghost point. Here subscript ℓ and k are the mesh indices in the x- and z-directions, respectively. Including the ghost values, the number of equations and unknowns are exactly equal. Since the ghost values are not governed by a time dependent equation, it is necessary to combine boundary condition and equations of motion to reduce one of the equations effectively to a form without time derivative. This form of the boundary condition is then used to determine the ghost values.

To facilitate the implementation of the time-domain impedance boundary condition (9.19), an auxiliary variable $q(x,z,t)$, defined at $y = 0$ by

$$q = \frac{\partial v_n}{\partial t} = -\left. \frac{\partial v}{\partial t} \right|_{y=0}.$$
(9.25)

is introduced. q is only defined on the acoustic liner surface; i.e., $y = 0$. Note: $v_n = -v$ for the flow configuration of Figure 9.3. Boundary condition (9.19) may be rewritten as, after eliminating $\partial p / \partial t$ by Eq. (9.24).

$$\frac{\partial q}{\partial t} = -\frac{1}{X_1}\left[Rq + X_{-1}v + \frac{\partial u}{\partial x} + \frac{\partial v}{\partial y} + \frac{\partial w}{\partial z} \right].$$
(9.26)

Now, at $y = 0$ or $m = 0$, Eq. (9.22) may be rewritten in the form

$$\frac{\partial p}{\partial y} = q - M\frac{\partial v}{\partial x}.$$

(9.27)

Eq. (9.27) does not contain time derivative. It is in a suitable form for use to determine the ghost value $p_{\ell,-1,k}$.

The discretized form of Eq. (9.27) using the backward difference stencil of Fig. 9.8 is

$$\frac{1}{\Delta y}\sum_{j=-1}^{5}a_j^{51}p_{\ell,j,k}^{(n)} = q_{\ell,k}^{(n)} - \frac{M}{\Delta x}\sum_{j=-3}^{3}a_j v_{\ell+j,0,k}^{(n)}$$

where Δx, Δy are the mesh sizes. On solving for the ghost value, it is straightforward to find,

$$p_{\ell,-1,k}^{(n)} = \frac{\Delta y}{a_{-1}^{51}}\left[q_{\ell,k}^{(n)} - \frac{M}{\Delta x}\sum_{j=-3}^{3}a_j v_{\ell+j,0,k}^{(n)} - \frac{1}{\Delta y}\sum_{j=0}^{5}a_j^{51}p_{\ell,j,k}^{(n)}\right].$$

(9.28)

On choosing the ghost value by Eq. (9.28), the governing equation (9.27) or its progenitor (9.22) is automatically satisfied. To compute the entire sound field, the values of ρ, u, w and p at every mesh point (ℓ,m,k) are calculated by Eqs. (9.20), (9.21), (9.23) and (9.24). For velocity component v at all mesh points except those on the acoustically treated panel surface; i.e., $m = 0$, the value is updated by means of Eq. (9.22). For mesh points at $m = 0$, $v_{\ell,0,k}$ are computed by Eq. (9.25). The auxiliary variable q is to be calculated by Eq. (9.26). In discretizing the spatial derivatives in y for mesh points in rows $m = 0,1,2$ the backward difference stencils shown in Fig. 9.8 are to be used. Finally, artificial selective damping must be added to each time dependent equation to suppress the weak instability of the impedance model.
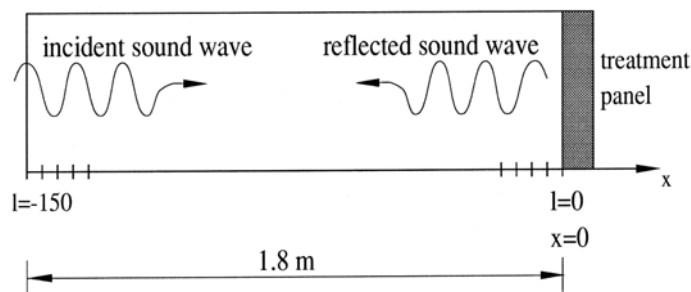
Figure 9.9 A normal-incidence impedance tube.

9.5 Numerical Example

To illustrate how well the time-domain impedance boundary condition works, consider an initial value problem associated with the normal-incidence impedance tube (see Fig. 9.9). An impedance tube is designed to measure the impedance of an acoustic liner sample. Let the length of the impedance tube be 1.8 m. The speed of sound at room temperature is 340 m/s. To ensure

that there are at least seven mesh points per wavelength in the computation for sound frequency up to 4 kHz, the impedance tube is divided into 150 mesh spacings yielding $\Delta x = 0.012$ m. In this example Δx is used as the length scale; i.e., $L = \Delta x$. The impedance of the treatment panel is taken to be $R = 0.18$, $X_{-1} = -0.47567$ and $X_1 = 2.09236$ (ω is non-dimensionalized by $a_0/\Delta x$). These are values corresponding to those of Fig. 9.2. At time $t = 0$, a transient acoustic pulse is generated. This produces a broadband pressure field in the frequency domain. A part of the acoustic pulse propagates down the tube and impinges on the acoustic treatment panel on the right. This leads to a partially reflected pulse. It will be assumed that the disturbance is generated by the following initial conditions at $t = 0$:

$$u = 0, \qquad p = e^{-0.00444(x+83.333)^2} \cos\left[0.444(x + 83.333)\right]. \tag{9.29}$$

This choice of initial conditions ensures that the center of the acoustic spectrum of the incident wave at the surface of the acoustic treatment panel has a frequency of 2 kHz and a spectrum half-width of 0.5 kHz. The impedance tube problem has an exact solution, which may be derived as follows.

The governing equations for the acoustic field are the one-dimensional version of Eqs. (9.6) and (9.7). They are,

$$\frac{\partial u}{\partial t} = -\frac{\partial p}{\partial x} \tag{9.30}$$

$$\frac{\partial p}{\partial t} = -\frac{\partial u}{\partial x} \tag{9.31}$$

upon eliminating u, the governing equation for p is,

$$\frac{\partial^2 p}{\partial t^2} = \frac{\partial^2 p}{\partial x^2}. \tag{9.32}$$

The solution of Eq. (9.32) satisfying initial condition (9.29) is

$$p = \frac{1}{2}e^{-0.00444(x-t+83.333)^2} \cos\left[0.444(x - t + 83.333)\right] \\ + \frac{1}{2}e^{-0.00444(x+t+83.333)^2} \cos\left[0.444(x + t + 83.333)\right] \tag{9.33}$$

The first term of Eq. (9.33) is the part of the pulse that propagates in the positive x-direction. This is the sound pulse that impinges on the acoustically treated panel at $x = 0$. For convenience, a subscript 'inc' will be used to label the incident acoustic field, a subscript 'ref' will be used to label the reflected field. Thus

$$p_{\text{inc}} = u_{\text{inc}} = \frac{1}{2}e^{-0.00444(x-t+83.333)^2} \cos\left[0.444(x - t + 83.333)\right] \tag{9.34}$$

and let

$$p_{\text{ref}} = -u_{\text{ref}} = \Phi(x + t). \tag{9.35}$$

Eq. (9.35) is a general solution of Eq. (9.32). At the impedance surface, $x = 0$, the Laplace transforms of the incident and reflected acoustic field variables are,

$$\widetilde{p}_{\text{inc}} = \widetilde{u}_{\text{inc}} = 2.11677 \left[e^{-\frac{(\omega-0.444)^2}{0.01776}} + e^{-\frac{(\omega-0.444)^2}{0.01776}} \right] e^{i83.333\omega} \tag{9.36}$$

$$\tilde{p}_{\text{ref}} = -\tilde{u}_{\text{ref}} = \tilde{\Phi}(\omega). \tag{9.37}$$

On imposing the impedance boundary condition (9.1), one finds,

$$(\tilde{p}_{\text{inc}} + \tilde{p}_{\text{ref}}) = Z(\tilde{u}_{\text{inc}} + \tilde{u}_{\text{ref}}). \tag{9.38}$$

On using Eqs. (9.36) and (9.37), it is found,

$$\tilde{\Phi} = \frac{Z-1}{Z+1} \tilde{p}_{\text{inc}}. \tag{9.39}$$

The exact solution is obtained by taking the inverse transform of Eq. (9.39) and adjusting the argument according to Eq. (9.35). This gives,

$$\begin{aligned}
p_{\text{ref}}(x,t) &= \int_{-\infty}^{\infty} \frac{(Z-1)}{(Z+1)} 2.116 \left[e^{-56.265(\omega+0.444)^2} + e^{-56.265(\omega-0.444)^2} \right] e^{-i\omega(x+t-83.333)} d\omega \\
&= 4.232 \, \text{Re} \left\{ \int_{0}^{\infty} \frac{(Z-1)}{(Z+1)} \left[e^{-56.265(\omega+0.444)^2} + e^{-56.265(\omega-0.444)^2} \right] e^{-i\omega(x+t-83.333)} d\omega \right\}.
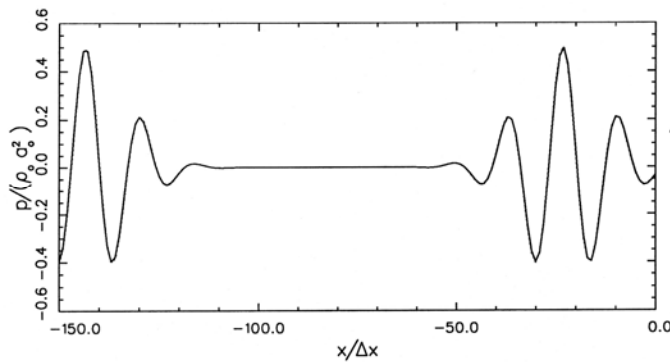\end{aligned} \tag{9.40}$$

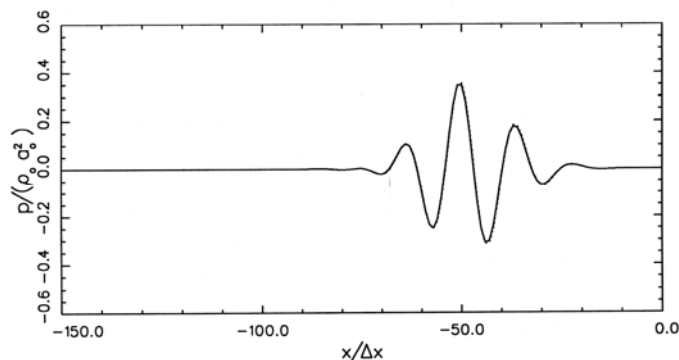Figure 9.10 Pressure waveform of the incident acoustic pulse at t = 60.1.

Figure 9.11 Pressure waveform of the reflected acoustic pulse at t = 140.1.

Fig. 9.10 shows the computed pressure distribution at time $t = 60.1$. At this time, the left half of the initial pulse is about to exit the computational domain, whereas the right half of the pulse is about to impinge on the surface of the treatment panel. The dotted curve is the exact solution. Fig. 9.11 shows the reflected pulse propagating away from the impedance boundary of the tube at $t = 140.1$. The amplitude of the reflected pulse is considerable smaller than that of the incident pulse. Part of the acoustic energy is dissipated during the reflection process off the impedance surface. The exact solution is represented by the dotted curve (the dotted curve is difficult to see as it is almost identical to the computed result). There is excellent agreement between numerical results and the exact solution. This is true for both the wave amplitude and phase. This example provides confidence in the use of time-domain impedance boundary condition.

REFERENCES

Ablowitz, M.J. and Fokas, A.S. (1997) *Complex Variables: Introduction and Applications*, Cambridge University Press.

Atkins, H., and Casper, J. (1994) Nonreflective Boundary Conditions for High-Order Methods, *AIAA J.*, **32** 512-518.

Atkins, H.L. (1997a) "Continued Development of Discontinuous Galerkin Method for Computational Aeroacoustics Applications", *AIAA Paper 97-1581*.

Atkins, H.L. (1997b) "Application of the Discontinuous Galerkin Method to Acoustic Scatter Problems", *2nd CAA Workshop on Benchmark Problems, NASA CP 3352* 45-56.

Atkins, H. L., and Lockard, D. P. (1999) A High-Order Method Using Unstructured Grids for the Aeroacoustic Analysis of Realistic Aircraft Configurations, *AIAA Paper 99-1945, AIAA, 5th AIAA/CEAS Aeroacoustics Conference and Exhibit, Bellevue, Washington.*

Balakrishnan, N. and Fernandez, B. (1998) Wall Boundary Conditions for Inviscid Compressible Flows on Unstructured Meshes, *Int. J. for Num. Meth. in Fluids*, **28** 1481-1501.

Baum, M., Poinsot, T., and Thevenin, D. (1994) Accurate Boundary Conditions for Multicomponent Reactive Flows, *J. Comp. Physics*, **116** 247.

Bayliss, A. and Turkel, E. (1980) Radiation Boundary Conditions for Wave-Like Equations, *Comm. Pure and Appl. Math.*, **33** 707-725.

Bayliss, A., and Turkel, E. (1982a) Far Field Boundary Conditions for Compressible Flows, *J. Comp. Physics*, **48** 182-199.

Bayliss, A. and Turkel, E. (1982b) Outflow Boundary Conditions for Fluid Dynamics, *SIAM J. Sci. and Stat. Comp.*, **3** 250-259.

Bayliss, A., Parikh, P., Maestrello, L. and Turkel, E. (1985) "Fourth Order Scheme for the Unsteady Compressible Navier-Stokes Equation", *ICASE Report 85-44.*

Becache, B. Fauqueux, S. and Joly, P. (2003) Stability of perfectly matched layers, group velocity and anisotropic waves, *Journal of Computational Physics*, **188**, 270-296.

Berenger, J. P. (1994) A perfectly matched layer for the absorption of electromagnetic waves, *Journal of Computational Physics*, **114**, 185-200.

Berenger, J. P. (1996) Three dimensional perfectly matched layer for the absorption of electromagnetic waves, *Journal of Computational physics,* **127**, 363.

Berthet, R., Astruc, D., and Estivalezes, J. L. (2000) Assessment of Numerical Boundary Conditions for Simulation of Sound Scattering by Vorticity, *AIAA Paper 2000-2005, AIAA, 6th AIAA/CEAS Aeroacoustics Conference and Exhibit, Lahaina, Hawaii.*

Bismuti, P.J. and Kopriva, D.A. (1997) "Solution of Acoustic Scattering Problems by A Staggered-Grid Spectral Domain Decomposition Method", *2nd CAA Workshop on Benchmark Problems, NASA CP 3352* 69-78.

Bogey, C. and Bailly, C. (2002) Direct Computation of the sound of a high Reynolds number subsonic jet, *CEAS Workshop from CFD to CAA*, 7-8 Novernber , Athens, Greece.

Bogey, C., Bailly, C. and Juve, D. (2003a) Noise investigation of a high subsonic, moderate Reynolds number jet using a compressible LES, *Theoretical and Computational Fluid Dynamics*, **16**, 273-297.

Bogey, C. and Bailly, C. (2003b) LES of a high Reynolds number high subsonic jet : effects of the inflow conditions on flow and noise. AIAA paper 2003-3170.

Bogey, C. and Bailly, C. (2003c) LES of a high Reynolds number high subsonic jet : effect of sub-grid scale modeling on flow and noise, AIAA Paper 2003-3557.

Bruneau, C. H. and Creuse, E. (2001) Towards a Transparent Boundary Condition for Compressible Navier-Stokes Equations, *Int. J. Num. Meth. in Fluids*, **36** 807-840.

Canuto, C., Hussaini, M., Quarteroni, A. and Zang, T. (1987) *Spectral Methods in Fluid Dynamics,* Springer-Verlag, New York.

Chakravarthy, S. R. (1983) Euler Equations -- Implicit Schemes and Boundary Conditions, *AIAA J.*, **21** 699-706.

Chang, S.C. (1995) "The Method of Space-Time Conservation Element and Solution Element – A New Approach for Solving the Navier-Stokes and Euler Equations", *J. Comput. Phys.,* **119** 295-324.

Chang, S.C., Wang, X.Y. and Chow, C.Y. (1999) "The Space-Time Conservation Element and Solution Element Method – A New High-Resolution and Genuinely Multidimensional Paradigm for Solving Conservation Laws", *J. Comput. Phys.,* **156** 89-136.

Choi, D., Barber, T.J., Chiappta, L.M. and Nushimura, M. (1999) Large eddy simulation of high Reynolds number jet flows, AIAA paper 99-0230.

Chung, C., and Morris, P. J. (1995) Acoustic Scattering from Two and Three-Dimensional Bodies, *Proceedings of the First Joint CEAS/AIAA Aeroacoustics Conference*, Munich, 55-63.

Colonius, T., Lele, S. K., and Moin. P. (1993) Boundary Conditions for Direct Computation of Aerodynamic Sound Generation, *AIAA J.*, **31** 1574-1582.

Constantinescu, G.S. and Lele, S.K. (2001) Large eddy simulation of a near sonic turbulent jet and its radiated sound field, AIAA paper 2001-0376.

Dadone, A. and Grossman, B. (1994) Surface Boundary Conditions for the Numerical   Solution of the Euler Equations, *AIAA J.*, **32** 285-293.

Dadone, A. (1998) Symmetry Techniques for the Numerical Solution of the 2D Euler Equations at Impermeable Boundaries, *Int. J. for Num. Meth. in Fluids*, **28** 1093-1108.

Davis, S. (1991) "Low-Dispersion Finite Difference Methods for Acoustic Waves in a Pipe", *J. Acoust. Soc. Amer.,* **90(5)** 2775-2781.

Davis, S. (1995) "Computational Aeroacoustics Using Hyperbolic Wave Primitives", *ICASE/LaRC Workshop on Benchmark Problems in CAA, NASA CP 3300* 27-33.

Dong, T. Z. (1997) On Boundary Conditions for Acoustic Computations in Non-Uniform Mean Flows, *J. Comp. Acoustics*, **5** 297-315.

Dyson, R. W. and Hixon, R. (2002) Towards Arbitrary Accuracy Inviscid Surface Boundary Conditions, *AIAA Paper 2002-2438, AIAA, 8th AIAA/CEAS Aeroacoustics Conference and Exhibit, Breckenridge, Colorado*.

Engquist, B. and Majda, A. (1977) Absorbing Boundary Conditions for the Numerical Simulation of Waves, *Math. of Comp.*, **31** 629-651.

Engquist, B. and Majda, A. (1979) Radiation Boundary Conditions for Acoustic and Elastic Wave Calculations, *Comm. on Pure and Appl. Math.*, **32** 313-357.

Ferm, L. (1995) Non-Reflecting Boundary Conditions for the Steady Euler Equations, *J. Comp. Physics*, **122** 307-316.

Freund, J.B., Lele, S.K. and Moin, P. (2000) Numerical simulation of a Mach 1.92 turbulent jet and its sound field, *AIAA Journal*, **38**, 2023-2031.

Freund, J.B. (2001) Noise sources in a low Reynolds number turbulent jet at Mach 0.9, *J. Fluid Mech*, **438**, 277-305.

Fung, K.-Y., Man, R.S.O. and Davis, S. (1996) "Implicit High-Order Compact Algorithm for Computational Acoustics", *AIAA J.,* **35(10)** 2029-2037.

Fung, K.-Y., Ju, H.B. and TallaPragada, B. (2000) Impedance and its Time-Domain Extensions, *AIAA Journal*, **38**(1), 30-38.

Gaitonde, D. and Shang, J.S. (1997) "Optimized compact-difference-based finite-volume schemes for linear wave phenomena", *Journal of Computational Physics* **138**, 617–643.

Giles, M. B. (1990) Nonreflecting Boundary Conditions for Euler Equation Calculations, *AIAA J.*, **28** 2050-2058.

Goodrich, J. W., and Hagstrom, T. (1996) Accurate Algorithms and Radiation Boundary Conditions for Linearized Euler Equations, *AIAA Paper 96-1660, AIAA, 2nd AIAA/CEAS Aeroacoustics Conference, State College, Pennsylvania*.

Goodrich, J. W., and Hagstrom, T. (1997) A Comparison of Two Accurate Boundary Treatments for Computational Aeroacoustics, *AIAA Paper 97-1585, AIAA, 3rd AIAA/CEAS Aeroacoustics Conference and Exhibit, Atlanta, Georgia.*

Gotleib, D. and Turkel, E. (1976) "Dissipative Two-Four Methods for Time-Dependent Problems", *Mathematics of Comput.,* **30** 703-723.

Hagstrom, T. and Goodrich, J. (1998) Experiments with Approximate Radiation Boundary Conditions for Computational Aeroacoustics, *Appl. Num. Math.*, **27**, 385-402.

Hagstrom, T. and Hariharan, S. I. (1988) Accurate Boundary Conditions for Exterior Problems in Gas Dynamics, *Math. of Comp.*, **51** 581-597.

Hagstrom, T. (1996) On High-Order Radiation Boundary Conditions, *IMA Volume on Computational Wave Propagation*, eds. Engquist, B. and Kriegsmann, G., Springer-Verlag, 1-22.

Hagstrom, T. and Hariharan, S. I. (1997) Progressive Wave Expansions and Open Boundary Problems, *Computational Wave Propagation*, eds. B. Engquist and G. A. Kriegsmann, IMA Volumes in Mathematics and its Applications, 86, Springer, New York, 23-43.

Hagstrom, T. and Hariharan, S. I. (1998) A Formulation of Asymptotic and Exact Boundary Conditions using Local Operators, *Appl. Num. Math.*, **27** 403.

Hagstrom, T. and Nazarov, I. (2003) Perfectly matched layers and radiation boundary conditions for shear flow calculations, AIAA paper 2003-3298.

Haras, Z. and Ta'asan, S. (1994) "Finite-Difference Schemes for Long-Time Integration", *J. Comput. Phys.,* **114** 265-279.

Hariharan, S. I., and Hagstrom, T. (1990) Far Field Expansion for Anisotropic Wave Equations, *Comp. Acoustics*, **2** 283-294.

Hayder, M. and Turkel, E. (1995) Nonreflecting Boundary Conditions for Jet Flow Computations, *AIAA J.,* **33** 2264-2270.

Hedstrom, G. W. (1979) Non-Reflecting Boundary Conditions for Nonlinear Hyperbolic Systems, *J. Comp. Physics*, **30** 222-237.

Hendeson, B. (2000) Category 6 automobile noise involving feedback-sound generation by low speed cavity flow, *Proceedings of the Third Computational Aeroacousitcs (CAA) Workshop on Benchmark Problems,* pp. 95-100.

Higdon, R. L. (1986) Absorbing Boundary Conditions for Difference Approximations to the Multidimensional Wave Equation, *Math. of Comp.,* **47** 437-459

Higdon, R. L. (1987) Numerical Absorbing Boundary Conditions for the Wave Equation, *Math. of Comp.,* 49, 1987, p. 65-90.

Hixon, R., Shih, S.-H., and Mankbadi, R. R. (1995) Evaluation of Boundary Conditions for Computational Aeroacoustics, *AIAA J.*, **33** 2006-2012.

Hixon, R., Shih, S.-H. and Mankbadi, R.R. (1997a) "Application of an Optimized MacCormack-Type Scheme to Acoustic Scattering Problems"*, 2nd CAA Workshop on Benchmark Problems, NASA CP* 3352, 101-110.

Hixon, R. (1997b) "On Increasing the Accuracy of MacCormack Schemes for Aeroacoustic Applications", *AIAA Paper 97-1586.*

Hixon, R. (1998a) "A New Class of Compact Schemes", *AIAA Paper 98-0367.*

Hixon, R. and Turkel, E. (1998b) "High-Accuracy Compact MacCormack-Type Schemes for Computational Aeroacoustics", *AIAA Paper 98-0365*.

Hixon, R. (1999) "Curvilinear Wall Boundary Conditions for Computational Aeroacoustics", *AIAA Paper 99-2395, AIAA, 35th AIAA/ASME/SAE/ASEE Joint Propulsion Conference and Exhibit, Los Angeles, California*.

Hixon, R. (2000) 3-D Characteristic-Based Boundary Conditions for CAA, *AIAA Paper 2000-2004, AIAA, 6th AIAA/CEAS Aeroacoustics Conference and Exhibit, Lahaina, Hawaii*.

Hu, F.Q. (1996a) "On absorbing boundary conditions of linearized Euler equations by a perfectly matched layer", Journal of Computational Physics, **129**, 201-219.

Hu, F.Q. (1996b) "On perfectly matched layer as an absorbing boundary condition", AIAA paper 96-1664.

Hu, F.Q. (2001) "A stable perfectly matched layer for linearized Euler equations in unsplit physical variables", *Journal of Computational Physics*, **173**, 455-480.

Hu, F.Q., Hussaini, M.Y. and Rasetarinera, P. (1999) "An Analysis of the Discontinuous Galerkin Method for Wave Propagation Problems", *J. Comput. Phys.,* **151** 921-946.

Hu, F. Q. (2004) "Absorbing boundary conditions (a review)", *International Journal of Computational Fluid Dynamics,* **18**, 513-531.

Hu, F. Q. (2005) "A perfectly matched absorbing boundary condition for linearized Euler equations with a non-uniform mean flow", *Journal of Computational Physics,* **208**, 469-492.

Ju, H.B. and Fung, K.-Y. (2000) "A Time-Domain Method for Duct Acoustics", *Journal of Sound and Vibration*, **237**(4), 667-681.

Ju, H. B. and Fung, K.-Y. (2001) "Time-Domain Impedance Boundary Conditions with Mean Flow Effects", *AIAA Journal*, **39** (9), 1683-1690.

Ju, H.B. and Fung, K.-Y. (2002) "Time-Domain Simulation of Acoustic Sources over an Impedance Plane", *Journal of Computational Acoustics*, **10**(3), 311-329.

Kim, J.W. and Lee, D.J. (1996) "Optimized Compact Finite Difference Schemes with Maximum Resolution", *AIAA J.,* **34(5)** 887-893.

Kim, J. W. and Lee, D. J. (1997) "Implementation of Boundary Conditions for the Optimized High-Order Compact Schemes', *J. Comp. Acoustics*, **5** 177-191.

Kim, J. W. and Lee, D. J. (2000) "Generalized Characteristic Boundary Conditions for Computational Aeroacoustics", *AIAA J.*, **38** 2040-2049.

Kopriva, D.A. (1986) "A Spectral Multidomain Method for the Solution of Hyperbolic Systems", *Appl. Num. Math., 2* 221-241.

Kopriva, D.A. (1990) "Spectral Solution of Acoustic Wave-Propagation Problems", *AIAA Paper 90-3916.*

Kopriva, D.A. and Kolias, J.H. (1995) "Solution of Acoustic Workshop Problems by a Spectral Multidomain Method", *ICASE/LaRC Workshop on Benchmark Problems in CAA, NASA CP 3300* 117-124.

Kopriva, D.A. and Kolias, J.H. (1996a) "A Conservative Staggered-Grid Chebyshev Multidomain Method for Compressible Flows", *J. Comput. Phys., 125* 244-261.

Kopriva, D.A. (1996b) "A Conservative Staggered-Grid Chebyshev Multidomain Method for Compressible Flows. ii. A Semi-Structured Method", *J. Comput. Phys., 128* 475-488.

Kurbatskii, K. A., and Tam, C. K. W. (1997) "Cartesian Boundary Treatment of Curved Walls for High-Order Computational Aeroacoustics Finite-Difference Schemes", *AIAA J.,* **35** 133-140.

Lau, J.C. (1981) "Effect of exit Mach number and temperatures on mean flow and turbulence characteristics in round jets", *Journal of Fluid Mechanics* **105**, 193–218.

Lee, C. and Seo, Y. (2002) "A new compact spectral scheme for turbulence simulation", *Journal of Computational Physics* **183**, 438–469.

Lele, S.K. (1992) "Compact Finite Difference Schemes with Spectral-like Resolution", *J. Comput. Phys., 103* 16-42.

Li, Y. (1997) "Wavenumber-Extended High-Order Upwind-Biased Finite-Difference Schemes for Convective Scalar Transport", *J. Comput. Phys.*, **133** 235-255.

Li, X. and Thield, F. (2004) Numerical computation of sound radiation from liner ducts by a time-domain impedance boundary condition, AIAA paper 2004-2902.

Lockard, D.P., Brentner K.S. and Atkins, H.L. (1995) "High-Accuracy Algorithms for Computational Aeroacoustics", *AIAA J.*, **33(2)** 246-251.

Lockard, D. P. and Morris, P. J. (1998) Radiated Noise from Airfoils in Realistic Mean Flows, *AIAA J.*, **36** 907-914.

Lockard, D.P., Brentner K.S. and Atkins, H.L. (1995) "High-Accuracy Algorithms for Computational Aeroacoustics", *AIAA J.*, **33(2)** 246-251.

Lockard, D.P. and Atkins, H.L. (2000) "An Application of the Quadrature-Free Discontinuous Galerkin Method", *3rd CAA Workshop on Benchmark Problems, NASA/CP 2000-209790* 331-337.

Loh, H.T., Smith-Kent, R., Perkins, F. and Chwalowski, P. (1996) "Evaluation of Aft Skirt Length Effects on Rocket Motor Base Heat, Using Computational Fluid Dynamics", *AIAA Paper 96-2645*.

Loh, C.Y. and Zaman, K.B.M.Q. (2002) "Numerical investigation of transonic resonance with a convergent-divergent nozzle", *AIAA Journal* **40**, 2393–2401.

Lupoglazoff, N. Biancherin, A., Vuillot, F. and Rahier, G. (2002) Comprehensive and superconic hot jet flow fields. Part 1: aerodynamics analysis, AIAA paper 2002-2599, Part 2: acoustic analysis, AIAA paper 2002-2600.

Manning, T.A. and Lele, S.K. (1998) "Numerical simulations of shock vortex interactions in supersonic jet screech", *AIAA Paper* 1998-0282.

Motsinger, R. E. and Kraft, R. E., (1991) "Design and performance of duct acoustic treatment", *Aeroacoustics of Flgiht Vehicles: Theory and Practice*, NASA RP-1258, chapter 14.

Nance, D.V., Viswanathan, K. and Sankar, L.N. (1996) "A Low Dispersion Finite Volume Scheme for Aeroacoustic Applications", *AIAA Paper 96-0278*.

Norum, T.D. and Brown, M.C. (1993) "Simulated high-speed flight effects on supersonic jet noise", *AIAA Paper* 93-4388.

Orlin, P.A., Perkins, A.L. and Heburn, G. (1997) "A frequency accurate temporal derivative finite difference approximation", *Journal of Computational Acoustics* **5**, 371–382.

Özyörük, Y. and Long, L.N. (2000) Time-Domain Calculation of Sound Propagation in Lined Ducts with Sheared Flows, *AIAA Journal*, **38**(5), 768-773.

Özyörük, Y., Long, L.N. and Jones, M.G. (1998) Time-Domain Numerical Simulation of a Flow-Impedance Tube, *Journal of Computational Physics*, **146**(1), 29-57.

Patera, A. (1984) "A Spectral Element Method for Fluid Dynamics", *J. Comput. Phys.,* **54** 468-488.

Poinsot, T. J. and Lele, S. K. (1992) Boundary Conditions for Direct Simulations of Compressible Viscous Reacting Flows, *J. Comp. Physics*, **101** 104-129.

Porter, R. W. and Coakley, J. F. (1972) Use of Characteristics for Boundaries in Time Dependent Finite Difference Analysis of Multidimensional Gas Dynamics, *Int. J. for Num. Meth. in Eng.*, **5** 91-101.

Rasetarinera, P., Kopriva, D.A. and Hussaini, M.Y. (2000) "Discontinuous Spectral Element Solution of Aeroacoustic Problems", *3rd CAA Workshop on Benchmark Problems, NASA/CP 2000-209790* 103-115.

Roe, P. L. (1989) Remote Boundary Conditions for Unsteady Multidimensional Computations, *Computers and Fluids*, **17** 221-231.

Rowley, C. W., and Colonius, T. (2000) Discretely Nonreflecting Boundary Conditions for Linear Hyperbolic Systems, *J. Comp. Physics*, **157** 500-538.

Roe, P. (1998) "Linear Bicharacteristic Schemes Without Dissipation", *SIAM J. Sci. Comput.*, **19(5)** 1405-1427

Scott, J. N. and Hankey, W. L. (1985) Boundary Conditions for Navier-Stokes Solutions of Unsteady Flow in a Compressor Rotor, *Three-Dimensional Flow Phenomena in Fluid Machinery, Fluids Engineering Technical Session, Vol. 42.* ASME, New York.

Scott, J. N., Mankbadi, R. R., Hayder, M. E., and Hariharan, S. I. (1993) Outflow Boundary Conditions for the Computational Analysis of Jet Noise, *AIAA Paper 93-4366, AIAA, 15th AIAA Aeroacoustics Conference, Long Beach, California*.

Shen, H. and Tam, C.K.W. (1998) "Numerical simulation of the generation of axisymmetric mode jet screech tones", *AIAA Journal* **36**, 1801–1807.

Shen, H. and Tam, C.K.W. (2000) "Effects of jet temperature and nozzle-lip thickness on screech tones", *AIAA Journal* **38**, 762–767.

Shen, H. and Tam, C.K.W. (2002) "Three-dimensional numerical simulation of the jet screech phenomenon", *AIAA Journal* **40**, 33–41.

Stanescu, D., Ait-Ali-Yahia, D., Habashi, W.G. and Robichaud, M. (1999) "Multidomain Spectral Computations of Sound Radiation from Ducted Fans", *AIAA J.,* **37** 296-302

Tam, C. K. W. and Block, P. J. W. (1978) "On the tones and pressure oscillations induced by flows over rectangular cavities", *Journal of Fluid Mechanics*, **89**, 373–399.

Tam, C. K. W. and Webb, J. C. (1993) "Dispersion-Relation-Preserving Finite-Difference Schemes for Computational Acoustics", *J. Comp. Physics*, **107** 262-281.

Tam, C.K.W., Webb, J.C. and Dong, Z. (1993) "A study of the short wave components in computational acoustics", *Journal of Computational Acoustics* **1**, 1–30.

Tam, C. K. W. and Dong, Z. (1994) Wall Boundary Conditions for High-Order Finite-Difference Schemes in Computational Aeroacoustics, *Theoretical and Comp. Fluid Dynamics*, **6** 303-322..

Tam, C. K. W., and Dong, Z. (1996) "Radiation and Outflow Boundary Conditions for Direct Computation of Acoustic and Flow Disturbances in a Nonuniform Mean Flow", *J. Comp. Acoustics*, **4** 175-201.

Tam, C.K.W. and Auriault, L. (1996) "Time-Domain Impedance Boundary Conditions for Computational Acoustics", *AIAA Journal*, **34**(5), 917-923.

Tam, C. K. W., Auriault, L. and Cambulli, F. (1998) Perfectly matched lyaer as an absorbing boundary condition for the linearized Euler equations in open and ducted domain, *Journal of Computational Physics,* **144**, 213-234.

Tam, C.K.W. and Kurbatskii, K.A. (2003) "Multi-size-mesh multi-time-step dispersion-relation-preserving scheme for multiple-scales aeroacoustics problems", *International Journal of Computational Fluid Dynamics* **17**, 119–132.

Tam, C.K.W. and Shen, H. (1993) "Direct computation of nonlinear acoustic pulses using high-order finite difference schemes", *AIAA Paper* 93-4325.

Tam, C.K.W. (2004) "Computational Aeroacoustics : an overview of computational challenges and applications", *International Journal of Computational Fluid Dynamics*, **18,** 547-567.

Tam, C.K.W. and Ju, H. (2004) "Computation of the aliasing and the interface transmission benchmark problems by the dispersion-relation-preserving scheme", *Proceedings of the 4th CAA Workshop on Benchmark Problems*, NASA CP-2004-212954, pp. 371-382.

Thomas, J.P. and Roe, P.L. (1993) "Development of Non-Dissipative Numerical Schemes for Computational Aeroacoustics", *AIAA Paper 93-3382.*

Thompson, K. W. (1987) Time Dependent Boundary Conditions for Hyperbolic Systems, *J. Comp. Phys.*, **68** 1-24.

Thompson, K. W. (1990) Time Dependent Boundary Conditions for Hyperbolic Systems II, *J. Comp. Phys.*, **89** 439-461.

Uzun, A. Blaisdell, G.A. an dLyrintzis, A.S. (2003) 3-D large eddy simulation for jet aeroacoustics. AIAA paper 2003-3322.

Visbal, M.R. and Gaitonde, D.V. (2001) "Very high-order spatially implicit schemes for computational acoustics on curvilinear meshes", *Journal of Computational Acoustics* **9**, 1259–1286.

Wang, Z. J., and Sun, Y. (2002) A Curvature-Based Wall Boundary Condition for the Euler Equations on Unstructured Grids, *AIAA Paper 2002-0966, AIAA, 40th Aerospace Sciences Meeting and Exhibit, Reno, Nevada*.

Whitham, G.B. (1974) *Linear and Nonlinear Waves,* Wiley-Interscience, New York.

Zheng, S. and Zhuang, M. (2002) Application and Verification of Time Domain Impedance Boundary Conditions in Multi-Dimensional Acoustic Problems, *AIAA 2002-2593, 8th AIAA/CEAS Aeroacoustics Conference &Exhibit, 17-19 June*.

Zhao, W. Frankel, S.H. an dMongeau, L. (2001) Large eddy simulations of sound radiation from subsonic turbulent jets. AIAA Journal, **39**, 1469-1477.

Zheng, S. and Zhuang, M. (2003) A computational aeroacoustics tool for duct acoustics with analytical and experimental variations, AIAA paper 2003-3248.

Zhuang, M. and Chen, R. (1998) "Optimized upwind dispersion-relation-preserving finite difference scheme for computational aeroacoustics", *AIAA Journal* **36**, 2146–2148.

Zhuang, M. and Chen R.F. (2002) "Applications of High-Order Optimized Upwind Schemes for Computational Aeroacoustics", *AIAA J.* **40(3)** 443-449.

Zingg, D.W., Lomax, H. and Jurgens, H.M. (1993) "An Optimized Finite-Difference Scheme for Wave Propagation Problems", *AIAA Paper 93-0459*.

Zingg, D.W., Lomax, H. and Jurgens, H.M. (1996) "High-Accuracy Finite-Difference Schemes for Linear Wave Propagation", *SIAM J. Sci. Comput.* **17(2)** 328-346.

Zingg, D.W. (2000) "Comparison of High-Accuracy Finite-Difference Methods for Liner Wave Propagation", *SIAM J. Sci. Comput.*, **22(2)** 476-502.